Magnetic and Mechanical Properties of Magnetostrictive FeGaSiB Films

By

Qayes Abdullah Abbas Aldulaim

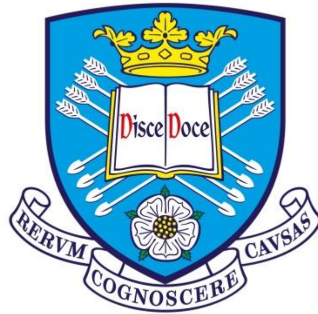

University of Sheffield

Submitted for the award of the degree

of

Doctor of Philosophy

(PhD)

from the

Department of Materials Science and Engineering

University of Sheffield

October 2018

Abstract

Novel magnetostrictive FeGaSiB thin films are of interest for potential applications such as magnetostrictive sensors. The growth parameters of the fabrication method and adding non-magnetic elements such as Ga can influence the structural, magnetic, and mechanical properties of the amorphous FeSiB thin films.

This thesis investigates experimentally the effect of the growth parameters and adding Ga into amorphous FeSiB films on these properties. Both the amorphous magnetostrictive FeGaSiB and FeSiB films were fabricated on Si (100) substrates using a co-sputtering and evaporation technique. The differences in the structural, magnetic, and mechanical properties of magnetostrictive FeGaSiB and FeSiB films were investigated and compared.

It was found that for all the films, changing the growth parameters and adding Ga did not affect the morphology of the films, as they all had amorphous structures. The magnetic properties and the saturation magnetostriction constants of both the FeGaSiB and FeSiB films were influenced by the film thickness, growth parameters, and the Ga content.

It was found that the highest magnetostriction constant of FeGaSiB film was deposited at the lowest Ar gas pressure, p_{Ar}, (4 µbar), lowest power P_{FeSiB}, (20W), and Ga rate (0.2 a.u.) for a 50nm thick film. The magnetostrictive FeGaSiB films had mechanical properties lower than the magnetostrictive FeSiB films and for both films, the mechanical properties were influenced by the film thickness and type of substrate.

Qayes A. Abbas, 2018 & Email: qayes.a.abbas@gmail.com

Publications

The work presented in this thesis is published in the two Journals:

1. Qayes A. Abbas, Nicola A. Morley, "Fabrication and characterization of magnetostrictive amorphous FeGaSiB thin films", Journal of Magnetism and Magnetic Materials, vol, 439, pp. 353–357, 2017.
2. Qayes A. Abbas, Nicola A. Morley, August Johansson, and Tom Thomson, "Influence of Ar Pressure on the Magnetic Properties of Amorphous FeGaSiB Thin Films", IEEE Transactions on Magnetics, vol. 53, no. 11, 2017.

A further paper published, which the author was involved in is:

3. E. Miskevich, F. K. Alshammari, W-G Yang, J. Sharp, S. Baco, Z. Leong, Q. A. Abbas, and N A Morley, "Artificial multiferroic structures using soft magnetostrictive bilayers on Pb ($Mg_{1/3}Nb_{2/3}$) –$PbTiO_3$", Journal of Physics D: Applied Physics, 51, 085001, 2018.

Conferences

The work in this thesis has been presented as posters and oral presentations at the conferences below;

a- Posters

1. Qayes A. Abbas, Nicola A. Morley, "Fabrication and Characterization of Magnetostrictive Amorphous FeGaSiB thin films", Conference on **Magnetism 2016** at the Cutler's Hall, Sheffield, UK, 4-5 April 2016.
2. Qayes A. Abbas, Nicola A. Morley, "Study the effect of Growth parameters on magnetostrictive amorphous FeGaSiB thin films", International Conference of the 8th Joint European Magnetic Symposia (**JEMS 2016**), 21-26 August 2016, Scottish Exhibition and Conference Centre SECC), Glasgow, UK,
3. Qayes A. Abbas, Nicola A. Morley, "Effect of growth parameters on magnetostrictive amorphous FeGaSiB thin films", Conference on **Magnetism 2017** at the University of York, York, UK, 3rd – 4th April 2017.
4. Qayes A. Abbas, Nicola A. Morley, "Effect of growth parameters on magnetostrictive amorphous FeGaSiB thin films", 1st Iraqi student Conference at University of Sheffield, the Firth Hall, Firth Court, University of Sheffield, Sheffield, UK, 29th September 2017.
5. Qayes A. Abbas, Nicola A. Morley, Tom J. Hayward, Tom Thomson, "Effect of growth parameters on Magnetostrictive Amorphous thin films", Conference of **Magnetism 2018**, University of Manchester, Manchester, UK, 9-10 April 2018,

6. S. Baco, Qayes. A. Abbas, Z. Leong, T. J. Hayward, T. Thomson, N. A. Morley, “Effect of growth conditions on the Soft Magnetostrictive properties of thin Fe-Co-Cr films”, Conference of **InterMag 2018**, Singapore 23- 27 April 2018.

b- Oral Presentation

1- Qayes A. Abbas, Nicola A. Morley, August Johansson, Tom Thomson, “Development of amorphous FeGaSiB films”, International conference of **InterMag 2017** at the Convention Centre Dublin, Ireland, 24-28 April 2017.

Acknowledgements

First of all, I would like to thank my God (**Allah**) to help me in my life, to finish this study, and for I have been a PhD student under the supervision of Dr. Nicola A. Morley. I would like to express my honest appreciation to my supervisor Dr. Nicola Morley for her support and guidance during the years of my PhD study, for her help to analyses the XPS measurements, and for her helps many times to fix the problems which I had with the co-sputtering evaporation technique. I would like to thank my second supervisor Dr. Thomas J Hayward for his help in my study.

I am deeply grateful to my family (my father “Abdullah”, my mother, my brothers “Ziad”& “Oday”, and my sister with her husband “Hasan”) for their help and support me during my study. Also, I owe my deepest gratitude to my wife “Hind” for her help in my life during my study in the UK. Also, my heartfelt appreciation goes to my son “Rayan” for granting me great happiness after his birth in the final year of my study. I would like to express the deepest appreciation to all the magnetics group members, SCAMMD group, especially for Prof. Dan Allwood, Dr. Ghaiath A Fadhil, Dr. Ruth C. Bradley, Dr. Jonathan M. Wood, Alaa K. Alasadi, and Richard WS Dawidek, in the department of Materials Science and Engineering/ University of Sheffield for their help to me during my study. I would like to thank Dr. Precious Shamba for her help to me in the first two years of my study. I would like to thank Prof. Thomas Thomson from the School of Computer Science, University of Manchester, Manchester/UK, for his help to use the VSM technique to measure the magnetic properties of my samples. I would like to thank Dr. Richard J. Frith in the Cleanroom/ University of Sheffield for his help with fixing problems which I had with the co-sputtering evaporation technique. I would like to thank Dawn Bussey, in the department of Materials Science and Engineering/ the University of Sheffield, for her help with AFM and nanoindentation techniques. I would like to thank Dr. David Morgan/ Cardiff University and the XPS data collection was performed at the EPSRC National Facility for XPS (‘HarwellXPS’), operated by Cardiff University. I would like to thank Mr. Righdan Mohsen Namus for his help to analyze the yield strength.

Finally, I would like to show my greatest appreciation to the Iraqi Ministry of Higher Education & Scientific Research (MOHESR) for the financial support of this study and the Iraqi cultural attaché in London/ UK for their support of my PhD. Also, I would like to offer my special thanks to the University of Anbar for candidating me to the doctoral study.

List of Symbols and Acronyms

H	Magnetic Field
μ_B	Bohr Magneton
L	Quantum Number of Orbital,
S	Quantum Number of Spin
J	Total Angular Momentum
g	Landé g-factor
$\vec{B}$	Magnetic Flux Density
χ	Susceptibility
μ_o	Magnetic Permeability
μ_r	Relative Permeability
M	Magnetization
M_s	Saturation Magnetization
M_r	Remanence
H_c	Coercive Field
H_k	Anisotropy Field
H_s	Saturation Field
E_{Total}	Total Magnetic Energy
E_{ex}	Exchange Energy
E_a	Magnetocrystalline Energy
E_{ms}	Magnetostatic Energy
E_{me}	Magnetoelastic Energy
E_z	Zeeman Energy
J_{ex}	Exchange Constant
φ_{ij}	Angle Between Two Spins
$\vec{S}_i, \vec{S}_j$	Spin Vectors of Electrons

Qayes A. Abbas, 2018 & Email: qayes.a.abbas@gmail.com

$\alpha_{1,}\ \alpha_{2,}\ \alpha_3$	Direction Cosines of Magnetization Vector
K_a, K_1, K_2	Cubic Anisotropy Constants
k_{uo}, k_{u1}, k_{u2}	Uniaxial Anisotropy Constants
H_d	Demagnetizing Field
N_d	Demagnetization Factor
σ	Stress
λ_s	Saturation Magnetostriction Constant
k_{total}	Total Anisotropy
t	Thickness
k_v	Bulk Anisotropy Constant
k_s	Surface Anisotropy Constant
K_u	Anisotropy constant
N	Atomic Layers
N_{tu}	Number of Turns in the Coil
σ_{dw}^{ex}	Exchange Energy of Domain Wall
σ_{dw}^{an}	Anisotropy Energy of Domain Wall
δ_{dw}	Thickness of Domain Wall
σ_{dw}	Total Energy Domain Wall
π	Pi Symbol
E_s	Young’s Modulus
v_s	Poisson’s Ratio
σ_x	Stress Compenent in x Direction
σ_y	Stress Component in x Direction
t_f	Film Thickness,
t_s	Substrate Thickness
$\varepsilon_x, \varepsilon_y$	Strain Components in x,y Directions
R	The Radius

Qayes A. Abbas, 2018 & Email: qayes.a.abbas@gmail.com

k_σ Induced Anisotropy Under Applied Stress

λ_{100} Magnetostriction Constants in <100> Direction

λ_{111} Magnetostriction Constants in <111> Direction

λ_{iso} Isotropic Magnetostriction Constant

λ_θ Saturation Magnetostriction with Angle θ along with Magnetization

λ_{total} Total Magnetostriction Constant

λ_v Volume Magnetostriction

λ_{su} Surface Magnetostriction Constant

$\beta_1, \beta_2, \beta_3$ Direction Cosines of Crystal Axes

h_c Contact Depth

A Area

h Total Displacement

h_s Displacement of the Surface at the Boundary of the Contact

P Applied Load

P_{max} Maximum Applied Load

h_{max} Maximum Displacement

E_r Reduced Modulus

S Stiffness

H_r Hardness

$A_{contact}$ Contact Area

v_i Poisson’s Ratio of Indenter Tip

E_i Young’s Modulus of Indenter Tip

σ_{ys} Yield Strength

Q Loading Curvature

h_f Residual Depth of Penetration

n_ϵ Strain Hardening

C Capacity

H_{ll}	Longitudinal Direction of Magnetic Field
$H_{\perp}$	Perpendicular Direction of Magnetic Field
W	Weight
W_T	Weight the Pendulous Part of the Ribbon
G_e, G_s	Gains of the Amplifier Systems
m_e	Magnetic Field Modulation Depth
I_s, I_e	Intensities of the Strain Modulated
λ	Wavelength
a	Lattice Constant
D_{grain}	Grain Size
d	Inter-Plan Spacing
β	Full Width of the Half Maximum of the Peak
BE	Binding Energy
KE	Kinetic Energy
ϕ	Work Function
hv	Photon Energy
V_{ind}	Induced Voltage
Φ	Flux in the Coil
D	Strength of Uniaxial Anisotropy
l	Mean Free Path
P_{FeSiB}	FeSiB Target Power
p_{Ar}	Argon Gas Pressure
R_{Ga}	Ga Evaporation Rate
x	Composition
BCC	Body Centre Cubic
HCP	Hexagonal Close-Packed
AFM	Atomic Force Microscopy

Qayes A. Abbas, 2018 & Email: qayes.a.abbas@gmail.com

PVD	Physical Vapour Deposition
PLD	Pulsed Laser Deposition
MBE	Molecular Beam Epitaxy
RF or rf	Radio Frequency
DC	Direct Current
Ar	Argon Gas
CVD	Chemical Vapour Deposition
LPCVD	Low Pressure Chemical Vapour Deposition
MEMS	Micro-Electro-Mechanical Systems
MOKE	Magneto-Optical Kerr Effect
VSM	Vibrating Sample Magnetometer
XRD	X-ray Diffraction
FWHM	Full Width Half Maximum
XPS	X-Ray Photoelectron Spectroscopy
EXAFS	X-ray Absorption Fine Structure
CEMS	Conversion Electron Mössbauer Spectroscopy
FMR	Ferromagnetic Resonance
SAMR	Small Angle Magnetization Rotation
SMFMR	Strain modulated Ferromagnetic Resonance
IPA	Isopropanol
PMMA	PolyMethyl Methacrylate

Contents

Abstract .... **I**
Publications .... **II**
Conferences .... **II**
Acknowledgements .... **IV**
List of Symbols and Acronyms .... **V**
Chapter 1 Introduction **1**
1.1 Outline of the thesis 2
1.2 References 3
Chapter 2 Background Theory **5**
2.1 Introduction 5
2.2 Fundamentals of Magnetism and Magnetic Materials 5
2.3 Classification of Magnetic Materials 7
2.4 Overview of Magnetic Anisotropies and Associated Energies 9
2.4.1 Exchange Energy 10
2.4.2 Magnetocrystalline Energy 10
2.4.3 Magnetostatic Energy 11
2.4.4 Zeeman Energy 11
2.4.5 Magnetoelastic Energy 12
2.4.6 Growth Induced Anisotropy 12
2.4.7 Surface Anisotropy of Thin Film 12
2.5 Magnetic Domains and Domain Walls 13
2.6 Magnetization Process 16
2.7 Magnetostriction of Ferromagnetic Materials 16
2.7.1 Villari Effect (Magnetization-Dependent Stress) 17
2.7.2 Magnetostriction of Cubic Crystals 21
2.7.3 Magnetostriction of Polycrystalline 22
2.7.4 Magnetostriction of Thin Films 22
2.8 Mechanical Characterization of Thin Films 23
2.9 References 30
Chapter 3 Literature Review **32**
3.1 Introduction 32
3.2 Magnetostriction Phenomenon in Ferromagnetism 32

Qayes A. Abbas, 2018 & Email: qayes.a.abbas@gmail.com

3.3 Magnetostriction Materials 32
3.4 Methods of Measuring the Magnetostriction 34
3.4.1 Direct Measurement Methods 34
3.4.2 Indirect Measurement Methods 39
3.5 Magnetic Properties in Magnetostrictive Polycrystalline Films 42
3.5.1 Magnetic Properties of Magnetostrictive FeGa Films 42
3.5.2 Magnetic Properties of Magnetostrictive FeCo Films 49
3.6 Magnetic Properties in Magnetostrictive Ribbons 51
3.7 Magnetic Properties of Magnetostrictive Amorphous Films 54
3.7.1 Magnetic Properties of Magnetostrictive Amorphous FeSiB Films 54
3.7.2 Magnetic Properties of Magnetostrictive Amorphous FeGaB Films. 56
3.7.3 Magnetic Properties of Magnetostrictive Amorphous FeB Films 57
3.8 Mechanical Properties of Magnetostrictive Materials 60
3.9 References 64
Chapter 4 Experimental Techniques 69
4.1 Thin Film Fabrication Techniques 69
4.2 Thin Film Growing Mechanism 71
4.3 Film Thickness Uniformity 72
4.4 Film Purity 73
4.5 Thermal Evaporation Mechanism 73
4.6 Sputtering Mechanism 74
4.7 Growth Parameters Which Effect Film Properties 77
4.7.1 Gas Pressure 77
4.7.2 Target-Substrate Distance 77
4.7.3 Sputtering Target Power 77
4.7.4 Sputtering Rate 78
4.8 Co-Sputtering and Evaporation Technique at Sheffield 78
4.8.1 Co-Sputter-Evaporation Deposition Chamber 78
4.8.2 Co-Sputtering and Evaporation 79
4.9 Sample Preparation and Target 80
4.9.1 Growth of Amorphous FeSiB Thin Films 81
4.9.2 Growth of Amorphous FeGaSiB Thin Films 81
4.10 Characterization Techniques 82
4.10.1 X-Ray Diffraction 82
4.10.2 Atomic Force Microscopy 85

Qayes A. Abbas, 2018 & Email: qayes.a.abbas@gmail.com

4.10.3 X-Ray Photoelectron Spectroscopy 87
4.10.4 Magneto-Optical Kerr Effect (MOKE) Magnetometer 91
4.10.5 Vibration Sample Magnetometer (VSM) 92
4.11 Magnetostriction Measurement 94
4.12 Nanoindentation Technique 97
4.13 References 102
Chapter 5 Fabrication and Characterization of Magnetostrictive Amorphous FeSiB and FeGaSiB Films as a Function of Thickness 104
5.1 Introduction 104
5.2 Fabrication of The Films 104
5.2.1 Fabrication of FeSiB Thin Film 104
5.2.2 Fabrication of FeGaSiB Thin Films 105
5.3 Thickness Calibration 105
5.4 Films Characterization 106
5.5 Structural Properties 108
5.5.1 XRD Results 108
5.5.2 XPS Results 111
5.5.3 AFM Results 112
5.6 Magnetic Properties 113
5.6.1 Magnetic Properties Measured by MOKE 113
5.6.2 Magnetic Properties Measured by VSM system. 118
5.7 Magnetostriction Properties 121
5.8 Summary 123
5.9 References 124
Chapter 6 Influence of Growth Parameters on The Structure, Magnetic Properties, and Magnetostriction Constants of FeSiB and FeGaSiB Films. 125
6.1. Introduction 125
6.2 Fabrication of The Films 126
6.2.1 Fabrication of FeSiB Thin Film 126
6.2.2 Fabrication of FeGaSiB Thin Films 126
6.3 Characterization of The Films 127
6.4 Influence of Ar Gas Pressure on The Structure, Magnetic Properties, and Magnetostriction Constants of Amorphous FeGaSiB Thin Films 128
6.4.1 Structural Properties 129
6.4.2 Magnetic Properties 133
6.4.2.1 Magnetic Properties Measured by MOKE 133

Qayes A. Abbas, 2018 & Email: qayes.a.abbas@gmail.com

6.4.2.2 Magnetic Properties Measured by VSM System 138
6.4.3 Magnetostriction Properties 140
6.5 Influence of Sputtering Target Power on The Structure, Magnetic Properties, and Magnetostriction Constants of Amorphous FeGaSiB Thin Films 142
6.5.1 Structural Properties 142
6.5.2 Magnetic Properties 146
6.5.2.1 Magnetic Properties Measured by MOKE 146
6.5.2.2 Magnetic Properties Measured by VSM System 150
6.5.3 Magnetostriction Properties 151
6.6 Influence of Ga Evaporation Rate on The Structure, Magnetic Properties, and Magnetostriction Constants of Amorphous FeGaSiB Thin Films 153
6.6.1 Structural Properties 153
6.6.2 Magnetic Properties 156
6.6.2.1 Magnetic Properties Measured by MOKE 156
6.6.2.2 Magnetic Properties Measured by VSM 160
6.6.3 Magnetostriction Properties 161
6.7 Comparison of Fabrication Parameters 162
6.8 Summary 166
6.9 References 167
Chapter 7 Investigation of Mechanical Properties of Magnetostrictive Thin Films By Nanoindentation. 169
7.1 Introduction 169
7.2 Fabrication of The Films 171
7.2.1 Fabrication of Thick FeSiB Films 171
7.2.2 Fabrication of Thick FeGaSiB Films 171
7.3 Characterization of The Films 172
7.4 Structural Properties 174
7.5 Nanoindentation Test of Magnetostrictive Thin Films 175
7.6 Material Influences 196
7.7 Summary 200
7.8 References 202
Chapter 8 Summary and Future Work 205
8.1 Summary 205
8.2 Future Work 209
Appendix 1 i

Qayes A. Abbas, 2018 & Email: qayes.a.abbas@gmail.com

Chapter 1 Introduction

Recently, the development of magnetic amorphous materials for Micro-Electro-Mechanical System (MEMS) applications such as low field sensing devices [1, 2] has become of interest. The requirements of sensor devices that include a magnetostrictive thin film is a high magnetostriction constant induced under low saturation field. Thus to improve the efficiency of these devices, these properties have to be investigated [3]. One of the main materials of interest is magnetostrictive Fe-based amorphous thin films [4, 5], such as FeSiB (Metglas) and FeSiBC (Metglas) [6-8].

There has been a wide range of experimental research carried out on ferromagnetic amorphous materials in ribbon form [9], [10], which show unique magnetic properties such as a large magnetostriction constant, low saturation field and soft coercivity. These properties are an encouragement, such that amorphous ribbons are promising materials for applications such as sensors and actuator devices. In spite of their unique magnetic properties, these materials have high stresses in random orientations, which lead to complex domain structures. Further disadvantages of these amorphous ribbons are that they can become brittle after annealing and because of their large dimensions (microns), they are not suitable for use in nano dimension devices.

For example, FeSiB ribbons with thickness 23 μm, magnetostriction constant 27 ppm, saturation field <20 kA/m, and magnetization 1241 kA/m are useful in applications such as low core loss at high frequencies >1kHz, transformers, magnetic sensors, and motors [11-13]. However, MEMS applications often require a larger magnetostriction constant (λ_S> 50 ppm) and a smaller anisotropy field (H_k < 10 kA/m). Therefore, FeSiB ribbon alloys do not achieve these requirements. Thus the interest in FeSiB thin films has increased, with many studies being carried out to investigate their soft magnetic properties, so that they can be used in MEMS applications such as low field sensors [14].

Adding non-magnetic elements such as Al, Be, Ga [15-17] into crystalline Fe-based alloys have helped to improve their magnetic properties and magnetostriction constant. For example, the addition of Al in the percentage of 17% into Fe produced a magnetostriction constant of about 140 ppm [15], while Be addition of 6.8% into Fe produced a

Qayes A. Abbas, 2018 & Email: qayes.a.abbas@gmail.com

magnetostriction constant of about 101ppm [18]. Further, adding Ga into Fe with a Ga percentage between 4% and 27% [19] causes a considerable increase in magnetostriction constant, λ_{100}, which reaches two maximum values; 265 ppm at the Ga content of about 19% and 235 ppm at the Ga content of 27%. However, as these films are polycrystalline, they have magnetocrystalline anisotropy, thus have a high saturated field, which is not suitable for low field applications. Therefore, amorphous thin films, such as FeSiB, which have no magnetocrystalline anisotropy, could be a better candidate to study their magnetic properties by adding non-magnetic elements. Thus the investigation of gallium, Ga, which is a non-magnetic material, has been chosen as an additive element into FeSiB films, to answer the main questions of this thesis. These include how the addition of Ga to FeSiB films influences the structure, magnetic properties, magnetostriction constant and mechanical properties of these films under different growth parameters. Therefore, it was necessary to investigate the effect of growth parameters on the properties of FeSiB film before adding Ga, using the same growth technique. Hence, studying the effect of growth parameters on the properties of FeSiB and FeGaSiB films allows a comparison of the results.

For the fabrication of FeGaSiB thin films, a co-sputtering- evaporation technique was used with a range of growth parameters. The chamber for this technique is designed to allow the sputtered atoms of the FeSiB Metglas target and evaporated Ga atoms to move together through the plasma toward the substrate. Changing the growth parameters, such as FeSiB target power, sputtering Ar gas pressure, and the Ga evaporation rate, allows films to be grown with a range of compositions. Using this technique achieved the addition of Ga into the FeSiB thin films and the successful fabrication of FeGaSiB thin films. Therefore, changing the growth parameters and adding Ga were the main sources, which influenced the magnetic properties of the magnetostrictive amorphous thin films.

1.1 Outline of the thesis

This thesis involves eight chapters, which can be briefly presented as follows:

Chapter 2 presents the fundamentals of magnetism and magnetic materials, an overview of the different magnetic anisotropies and associated energies, and the magnetostriction effect including the magnetization-dependent stress is included.

Chapter 3 presents a detailed literature review of the previous research work carried on magnetostrictive materials, including polycrystalline thin films such as FeGa and amorphous thin films such as FeSiB, FeGaB, and FeB.

Chapter 4 covers the major experimental techniques used to fabricate and characterize the samples. It includes sample preparation, structural techniques and magnetic techniques used to characterize the samples.

Chapter 5 presents the experimental result obtained from adding Ga to FeSiB film as a function of film thickness on the structure, magnetic properties, and magnetostriction constant of both FeSiB and FeGaSiB thin films. The results for both film sets are compared.

Chapter 6 presents the investigation of the influence of the growth parameters on the composition, structure, magnetic properties, and magnetostriction constant of amorphous FeSiB and FeGaSiB films.

Chapter 7 presents the investigation of mechanical properties such as hardness, elastic modulus, and yield strength, by nanoindentation technique, on magnetostrictive amorphous films

Chapter 8 gives the summary of the conclusions and future works.

1.2 References

[1] M.R.J. Gibbs, R. Watts, W.J. Karl, A.L. Powell, and R.B. Yates, *Sensors Actuators* A, 59, 229, 1997.

[2] H. Chiriac, M. Pletea and E. Hristoforou, *Sensors Actuator*, 81,166-169, 2000.

[3] M. R. J. Gibbs, *IEEE Trans. Magn.* 43, 2666, 2007.

[4] J. Nowak, J. Wenda, *J. Magn. Magn. Mater*. 124,119, 1993.

[5] M. Vazquez, D. Garcıa, C. Prados, A. Asenjo, F.J. Castano, K. Mandal, J.M. Garc!ıa, M. Tera, A. Hernando, *IEEE Trans. Magn*. 136, 3968, 2000.

[6] Z.G. Sun, H. Kuramochi, M. Mizuguchi, F. Takano, Y. Semba, H. Akinaga, *J. Magn. Magn. Mater.* 272–276, 1160–1161, 2004.

[7] Maria Neagu, M. Dobromir, G. Popa, H. Chiriac, Gh. Singurel, Cornelia Hison, *Sensors and Actuators A*, 129, 172–175, 2006.

[8] M. Coïsson, F. Vinai, P. Tiberto, F. Celegato, *J. Magn. Magn. Mater*., 321, 806–809, 2009.

[9] G.S. Mogilny, B.D. Shanina, V.V. Maslov, V.K. Nosenko , A.D. Shevchenko , V.G. Gavriljuk, *Journal of Non-Crystalline Solids* 357, 3237–3244, 2011.

[10] O. Zivotsky, A. Hendrych, L. Klimˇsa, Y. Jira´ skova´, J. Burˇsı´k, J.A.M. Go´mez, D. Janicˇkovic, *J. Magn. Magn. Mater.* 324, 569–577, 2012.

[11] M. Mouhamad, C. Elleau, F. Mazaleyrat, C. Guillaume, and B. Jarry, *IEEE Trans. Magn*, vol. 47, no. 10, p.3192, 2011.

[12] R. Hasegawa, *J. Magn. Magn. Mater.*, vol. 304, pp. 187–191, 2006.

[13] R. Hasegawa, *J. Magn. Magn. Mater*. vol. 215–216, pp.240-245, 2000.

[14] S. Thomas, J. Mathew, P. Radhakrishnan, V.P.N. Nampoori, A.K. George, S.H. Al-Harthi, R.V. Ramanujan, M.R. Anantharaman, *Sensors Actuators A: Phys.*, 161,83-90, 2010.

[15] S. F. Xu, H. P. Zhang, W. Q. Wang, S. H. Guo, W. Zhu, Y. H. Zhang, X. L. Wang, D. L. Zhao, J. L. Chen, and G. H. Wu, *J. Phys. D: Appl. Phys*. 41, 015002, 2008.

[16] N. Srisukhumbowornchai and S. Guruswamy, *J. Appl. Phys*. 90, 5680, 2001.

[17] H. Okamoto, Materials Park, Ohio, p.147, 1993.

[18] N. Srisukhumbowornchai and S. Guruswamy, *J. Appl. Phys*. 90 (2001) 5680.

[19] A. E. Clark, K. B. Hathaway, M. Wun-Fogle and J. B. Restorff, T. A. Lograsso, V. M. Keppens, G. Petculescu, and R. A. Taylor, *J. Appl. Phys*., 93, 10, 2003.

Chapter 2 Background Theory

2.1 Introduction

This chapter consists of two parts. In the first part, the fundamentals of magnetism, the classification of magnetic materials, overview of magnetic anisotropies and their associated energies, magnetostriction of ferromagnetism, and Villari effect are briefly covered. The second part of this chapter presents the calculation of mechanical properties of thin films. The properties include the hardness, reduced modulus, Young's modulus, and yield strength are presented.

2.2 Fundamentals of Magnetism and Magnetic Materials

Magnetism arises originally from the motion of an electron in an orbit around a nucleus and the electron spin. The electron movement around a nucleus generates an orbital magnetic moment and due to the electron self-spinning, a spin magnetic moment is generated.

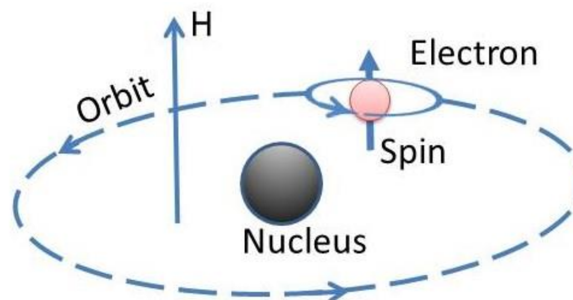

Figure 2.1 Schematic of motion of electron for both spin and orbital moments.

Due to the electronic structure present in the free atom [1], as shown in **Fig. 2.1**, this leads to the atom possessing a magnetic dipole moment, even in the absence of an external magnetic field [2]. The smallest unit of magnetic moment due to the motion an electron is called the Bohr Magneton (μ_B) (9.274 X 10^{-24} A m^2) as defined by ($e\hbar/2m_e c$) where e is the electron charge, ħ is the Planck constant, m_e is the electron mass, and c is the speed of light [2]. The motion of individual electrons, around the nucleus, is similar to the motion of charged particles of a current in a wire loop to produce a magnetic field **Fig. 2.2**.

Qayes A. Abbas, 2018 & Email: qayes.a.abbas@gmail.com

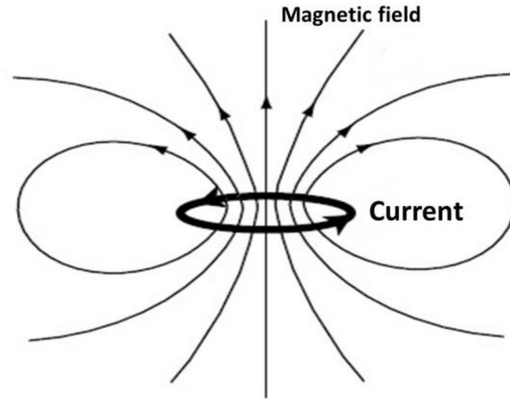

Figure 2.2 a magnetic field of a wire loop with a current flowing through it.

The orbital magnetic moment and the spin magnetic moment of every single electron in an atom can be coupled with each other to produce spin-orbit interaction [1, 3, and 4]. Also, there are other types of interactions, which contribute to a total atomic magnetic moment, produced in magnetic materials: orbit-orbit interaction and spin-spin interaction among electrons. The relative contribution of the orbital and spin magnetic moments is defined by the quantum mechanics using the Landé g-factor, which is given by:

$$g = 1 + \frac{J(J+1)+S(S+1)-L(L+1)}{2J(J+1)} \tag{2.1}$$

Where J =L+S is the total angular momentum and L, S are the quantum numbers which refer to the orbital, spin of an atom.

In this equation, when $g = 1$, this means there is a pure orbital motion contribution and $S = 0$ and when $g = 2$, hence there is pure spin motion contribution and $L = 0$, [5, 6].

Before describing magnetic materials, in the next section, it is important to define the relation between the magnetic field ($\vec{H}$), magnetic flux density ($\vec{B}$), and the susceptibility (χ) of a material, to understand the response of these materials to a magnetic field $\vec{H}$. For free space, the magnetic permeability is $\mu_o = 4\pi \times 10^{-7}$ Hm^{-1}, thus the magnetic flux density, which is measured in units of Wm^{-2}, is given by:

$$\vec{B} = \mu_o \vec{H} \tag{2.2}$$

In case of placing the magnetic material in a magnetic field, $\vec{H}$, the magnetic flux density is given by:

$$\vec{B} = \mu_o(\vec{H} + \vec{M}) \tag{2.3}$$

Where $\vec{M} = \chi\vec{H}$, measured in units of Am^{-1}, is the magnetization of the material.
After substituting the $\vec{M}$ into equation 2.3 with $\chi\vec{H}$, then $\vec{B}$ will be:

$$\vec{B} = \mu_o(\vec{H} + \chi\vec{H}) \quad (2.4)$$

After solving the equation 2.4, then $\vec{B}$ will be:

$$\vec{B} = \mu_o\vec{H}(1 + \chi) \quad (2.5)$$

Thus the relative permeability of a material is $\mu_r = (1 + \chi)$, therefore the magnetic flux density is given by:

$$\vec{B} = \mu_o\mu_r\vec{H} \quad (2.6)$$

2.3 Classification of Magnetic Materials

After describing the relations above, magnetic materials can be classified depending on their response to the external magnetic field $\vec{H}$.

Diamagnetic materials indicate materials, which have a very weak magnetism due to the alignment of the magnetic moments in the opposite direction to an applied magnetic field $\vec{H}$. The magnetic moment arises due to the motion of electrons in orbits around the nucleus, being generated by the electromagnetic induction of the magnetic field, to induce magnetism. In the absence of the magnetic field, these materials do not have magnetism and their net magnetic moment goes back to zero. The susceptibility (χ) of these materials is less than zero and very small about (-10^{-6}). Therefore, their relative permeability μ_r is less than 1. A diamagnetic response is found in materials such as Cu, Bi and Be [7].

Paramagnetic materials refer to materials that have in the absence of the field a random orientation of their atomic magnetic moments. On the application of a magnetic field, these materials have a net atomic magnetic moment (net magnetization) due to their weak interaction, and their magnetic moments align parallel to the direction of the magnetic field. These materials have a positive magnetic susceptibility greater than zero and smaller than the range (10^{-3} to 10^{-5}) and their relative permeability is above 1. A paramagnetic response is found in materials such as Al and Mn [8].

Ferromagnetic materials refer to materials that have magnetism even without an external magnetic field due to the alignment of unpaired spins, for the atomic magnetic moment. As a result of the internal interactions, the thermal energy influences are overcome and the magnetic moments are forced to align in a parallel direction to each other, which creates a

spontaneous magnetization even without a magnetic field. The response of ferromagnetic materials under a magnetic field is different from the response of both diamagnetic and paramagnetic materials. Changing the magnetism of these materials in the magnetic field is nonlinear and increases with increasing the magnitude of magnetic field until the saturation state is reached, where all the magnetic moments align with the direction of the magnetic field. After removing the magnetic field, the magnetization of ferromagnetic materials does not go to zero, instead, it reduces to the remanence magnetization (M_r, point in **Fig. 2.3**). The magnetization is decreased to zero by applying an opposite magnetic field. The coercive field, (H_c, point in **Fig. 2.3**) is the field required for the magnetization to reach zero. The response of the magnetization (M) under magnetic field (H) is shown in **Fig. 2.3**. This response is called a hysteresis loop, which has the interest points of technological applications. The saturation magnetization M_s, the coercivity H_c, the remanence magnetization M_r, and the saturation field, H_s in the case of isotropic materials or anisotropy field H_k in the case of anisotropic materials are shown in **Fig. 2.3**. The ferromagnetic response is found in materials such as Fe, Co, and Ni and their alloys. [9]

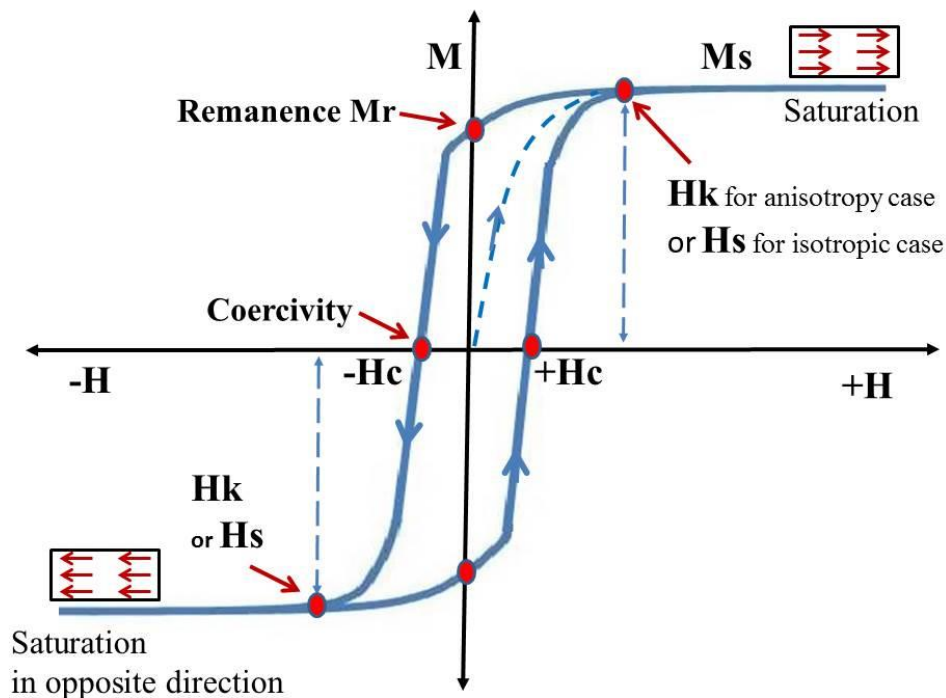

Figure 2.3 A hysteresis loop. The important points for the response of ferromagnetic materials under magnetic field (H).

Antiferromagnetic materials are materials that have a spontaneous magnetization arising from an opposite spins of the same magnitude on alternating atomic locations or due to the anti-parallel orientation of atomic magnetic moments on a sub-lattices arrangement. In these materials, the net spontaneous magnetization is zero in the absence of a magnetic field, due to opposite magnetic moment directions cancelling each other out. Antiferromagnetic materials exhibit a similar linear response of paramagnetic materials when they are placed under a magnetic field. This response is found in materials such as FeO, MnO, and NiO [6].

Ferrimagnetic materials refer to materials which have a spontaneous magnetization generated from the atomic magnetic moment of a different magnitude with anti-parallel alignment on sub-lattices. This provides a net magnetism, as although the magnetic moments in opposite directions will cancel out, as one direction has a larger magnetic moment compared to the other direction, this gives a net magnetization. The ferrimagnetic response is found in materials such as cubic and hexagonal ferrites [10].

2.4 Overview of Magnetic Anisotropies and Associated Energies

Magnetic anisotropy means that the magnetic moments of a ferromagnetic material prefer to reduce their energy by aligning in preferred directions. The anisotropy can be generated from two sources: the first is the intrinsic influence, which comes from the structural effects such as crystallographic, grains, intrinsic strain, and defects. The second type occurs from the induced anisotropy, which comes from different external effects such as an annealing field. The magnetic energy is the energy associated with the magnetic anisotropy and it can be in different forms depending on the type of anisotropy. The total energy, E_{Total} of the magnetic system, where the unit of total energy is J/m^3, can be expressed as:

$$E_{Total} = E_{ex} + E_a + E_{ms} + E_z \tag{2.7}$$

Where E_{ex}, E_a, E_{ms}, and E_z denote to the energy density of exchange, magnetocrystalline energy, magnetostatic energy, and Zeeman energy of a magnetic material, respectively. The unit of the terms in this equation is J/m^3, where the energy density of exchange, E_{ex}, is a local volume average of the exchange energy, ε_{ex}, in equation 2.8. The source of these energies is briefly indicated below.

2.4.1 Exchange Energy

Exchange energy, ε_{ex}, originates as a result of the interaction between two adjoining spins, i.e. the spin-spin interaction. For a ferromagnet, the exchange energy is reduced to a minimum when the exchange interaction aligns the magnetic moments parallel to each other. When two nearest neighbouring electrons possess spins S_i and S_j. The unit of the exchange energy ε_{ex} is Jouls and it is given by [11]:

$$\varepsilon_{ex} = -2J_{ex}\vec{S}_i.\vec{S}_j = -2J_{ex}\,S_iS_j\cos\varphi_{ij} \qquad (2.8)$$

Where J_{ex} refers to the exchange constant and φ_{ij} is the angle between $\vec{S}_i$ and $\vec{S}_j$.

In the case where J_{ex} is positive, the exchange energy is at a minimum value when the spins are parallel ($\varphi_{ij} = 0^o$) and this occurs in ferromagnetic materials. When the two spins are in anti-parallel alignment ($\varphi_{ij} = 180^o$), the exchange energy is a maximum value. If, on the other hand, the exchange constant, J_{ex}, is negative, the minimum exchange energy arises from anti-parallel spins as is the case for antiferromagnetic materials.

2.4.2 Magnetocrystalline Energy

Magnetocrystalline anisotropy is the orientation of the magnetic moments along preferred particular crystalline axes, which is affected by the temperature. When the temperature is approaching the Curie temperature, the material's crystal turns magnetically isotropic. The origin of magnetocrystalline anisotropy is from the spin-orbit interaction, which represents the coupling of an electron magnetic moment to the crystalline lattice. The magnetocrystalline energy is the energy needed to align magnetic moments along the specific directions of a crystalline ferromagnetic material. In amorphous materials, as there is no crystalline structure, there is therefore no magnetocrystalline anisotropy. In the absence of a magnetic field, the magnetic moments of a crystalline ferromagnetic material will prefer to align along one crystalline direction, which is recognized as the easy axis, as it is easy to magnetize along it. Applying a magnetic field along a different direction, forces the magnetic moments to align along non-preferred crystalline directions. The crystalline direction, which requires the largest magnetic field to align the moments along is recognized as the hard axis.

For a cubic structure, for example, the BCC Fe structure, **Fig. 2.4**, the magnetocrystalline anisotropy energy E_a is given by [2]:

$$E_a = K_a + K_1(\alpha_1^2\alpha_2^2 + \alpha_2^2\alpha_3^2 + \alpha_3^2\alpha_1^2) + K_2(\alpha_1^2\alpha_2^2\alpha_3^2) + \cdots \qquad (2.9)$$

Where α_1, α_2, α_3 are the direction cosines in three dimensions of the magnetization vector ($\bar{M}$) and K_a, K_1, and K_2 are the cubic anisotropy constants.

For uniaxial systems, for example, the HCP Co structure, **Fig. 2.4**, E_a , is given by:

$$E_a = k_{uo} + k_{u1}sin^2\theta + k_{u2}sin^4\theta + \cdots \quad (2.10)$$

Where θ is the angle between the magnetization direction with the easy axis direction and k_{uo}, k_{u1}, and k_{u2} are the uniaxial anisotropy constants.

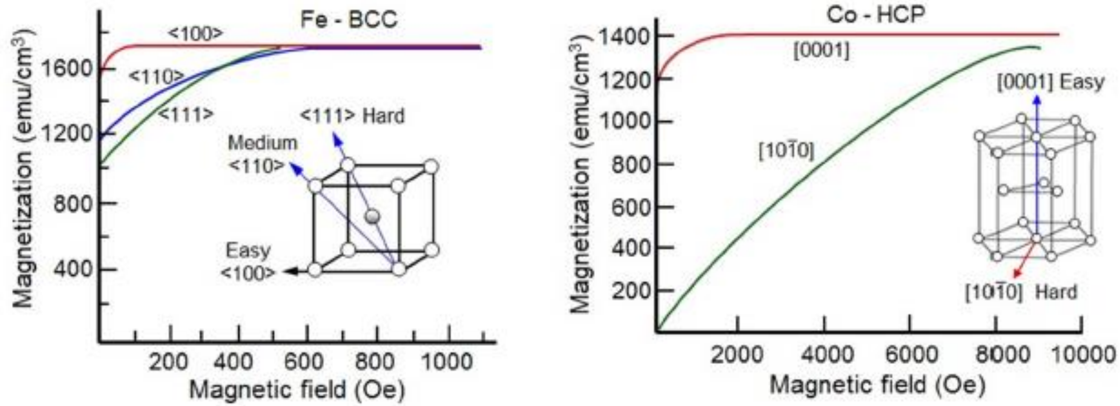

Figure 2.4 the easy, medium, and hard axis directions in Fe and Co, taken from reference [2]

2.4.3 Magnetostatic Energy

The magnetostatic energy originates as a result of the interaction between the magnetization of the ferromagnetic material under a magnetic field and the opposed magnetic field produced due to the magnetization distribution. This opposed magnetic field is identified as the demagnetizing field. The magnetostatic energy, E_{ms}, is calculated from the equation [12]:

$$E_{ms} = \frac{1}{2} \mu_o H_d M \quad (2.11)$$

Where M is the magnetization of the magnetic material and H_d, is the demagnetizing field produced by the magnetization, M, and is given by $H_d = -N_d M$, where N_d refers to the demagnetization factor. This factor depends strongly on the shape and geometry of the sample. In addition, the demagnetization factor can have values ≤ 1 for any sample geometry [13].

2.4.4 Zeeman Energy

The Zeeman energy originates as a result of the interaction between the applied magnetic field and the magnetization of material and it can be calculated by :

$$E_z = -\mu_o MH \cos\theta \quad (2.12)$$

Where θ is the angle between the vector of an applied field and the magnetization direction of the material.

2.4.5 Magnetoelastic Energy

Magnetoelastic energy, E_{me}, originates as a result of the interaction between the magnetization and the mechanical strain generated in the lattice structure. The magnetoelastic energy, E_{me}, can be given by [12] :

$$E_{me} = -\frac{3}{2}\lambda_s \sigma \cos^2\theta_\sigma \tag{2.13}$$

Where σ is the externally applied stress, θ_σ is the angle between the direction of magnetization and the applied stress, and λ_s is the saturation magnetostriction constant.

2.4.6 Growth Induced Anisotropy

The growth of thin films can affect the anisotropy in different ways. For example, in magnetostrictive materials, the stress induced during film growth affects the anisotropy [14]. In this case, the magnetization is coupled with the stress through the inverse magnetostriction effect [14]. In addition, the misfit between the substrate and the film produces a stress due to the difference between the thermal expansion coefficients of the film and substrate. Also, induced anisotropy can be achieved by applying mechanical stress to the substrate during the growth [14]. Further applying a magnetic field during the film growth induces anisotropy along with the direction of the magnetic field and making this direction the easy axis [15]. The alignment of the atoms in the same direction of the field leads to a reduction in the interaction energy between the pairs of atoms. Also, the interaction energy is influenced by the type of nearest neighbour atoms [15].

2.4.7 Surface Anisotropy of Thin Film

The surface of thin films also has an anisotropy associated with them. Nèel [16] presented a phenomenological model, suggesting that the total anisotropy, k_{total}, of a thin film is represented by the sum of the two terms as given in equation,

$$k_{total} = k_v + \frac{k_s}{t} \qquad (2.14)$$

Where t is the thickness of the film, k_v is the bulk anisotropy, and k_s is the surface anisotropy.

On the surface, the anisotropy changes as a result of reducing the symmetry of the atoms [17]. Due to the absence of any layer of atoms in a bond with the surface atoms, the bond lengths are changed. This will lead to a change in the magnetoelastic property on the surface in proportion to the bulk. Another effect of the surface on the anisotropy arises from the surface roughness.

2.5 Magnetic Domains and Domain Walls

The magnetic moments in a ferromagnetic material distribute in small regions, which are known as magnetic domains [18], and are spontaneously magnetized. In each domain, the magnetic moments align parallel to each other and in the same direction [1], but this alignment direction differs from one magnetic domain to another [19]. In the absence of a magnetic field, the net magnetization is zero, this is due to the formation of magnetic domains so that the energy of the ferromagnet is minimized. Whilst the domain structure of a ferromagnetic material lead to an increase in the exchange energy as a result of the non-parallel alignment of the magnetic moments between the adjacent domains, the magnetostatic energy is significantly reduced due to the decreased demagnetizing field. Hence, the total energy in the magnetic system is reduced. Any two adjacent domains are separated by a transition area or boundary, which is named the domain wall. The creation of domain walls is determined by equalization between the various magnetic energy contributions. A broad domain wall will minimize the exchange energy contribution where there is a progressive variation between the magnetic moment directions instead of changing sharply. For instance, a 180° domain wall involves rotating the alignment of the magnetic moments gradually from 0° to 180°. Nevertheless, the broad domain wall can also lead to an increase in the magnetocrystalline energy contribution as a consequence of increasing the alignment of the magnetic moments along non-preferred crystalline directions. On the contrary, a narrow domain wall can lead to an increase in the exchange energy, but a reduction in the magnetocrystalline energy, hence the overall magnetic energy is considered by optimizing both two energies [6].

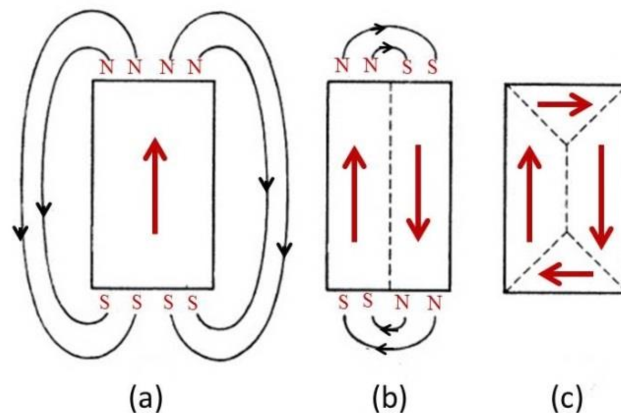

Figure 2.5 (a) single domain (b) formation of 180° domains, and (c) the formation of 90° closure domains. Adapted from references [13, 20]

In the case of a single magnetic domain, **Fig. 2.5 (a)** which is magnetized uniformly, the exchange energy reduces to a minimum while the magnetostatic energy reaches the highest state due to a very large demagnetizing field. To reduce the demagnetizing field influence, magnetic moments change their alignment in opposite directions as a result of the configuration of magnetic domains in **Fig. 2.5 (b)**. The formation and configuration of closure domains, **Fig. 2.5 (c)**, lead to cancelling the demagnetisation field effect. The configuration of closure domains takes place in cubic anisotropy materials such as the total magnetization, which defines as a magnetic moment per unit volume, of a material, is the summation of the individual domain structures [8].

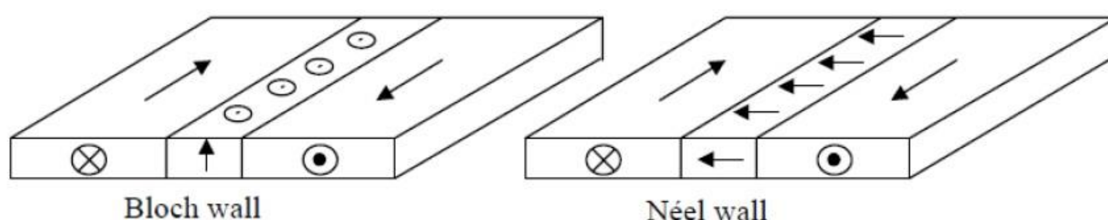

Figure 2.6 domain wall, Bloch and Neel walls taken from reference [8].

The domain walls can be in many categories [18]. The most common classes are Bloch wall and Néel wall. The Bloch and Néel walls in magnetic thin films form due to the orientation of magnetic moments as shown in **Fig. 2.6**. The magnetic moments in a Bloch wall are aligned perpendicular to the film plane, which increases the demagnetizing energy, while the magnetic moments in a Néel wall align in the plane of the film.

Returning to Eq. (2.8), the exchange energy can be rewritten as:

$$E_{ex} = J_{ex}S^2\varphi_{ij}^2 \tag{2.15}$$

From this equation, it can be seen that the exchange energy, E_{ex}, is proportional to φ_{ij}^2 and the directions of the spins in the domain wall will change gradually. In the case of uniform rotation of the spins by 180º over *N* atomic layers in a 180º wall (Bloch wall), the angle between the neighbouring spins is $\varphi_{ij} = \frac{\pi}{N}$. For instance, if it is considered that the structure is BCC for a simple cubic lattice, the surface density of atoms for the (100) plane is $1/a^2$, where a refers to the lattice constant. Consequently, the corresponding exchange energy per unit area over N atomic layers can be written as[6]:

$$\sigma_{dw}^{ex} = \frac{N}{a^2}E_{ex} = \frac{J_{ex}S^2\pi^2}{a^2N} \tag{2.16}$$

This equation illustrates that the exchange energy per unit area, σ_{dw}^{ex}, reduces with increasing *N* atomic layers. Hence σ_{dw}^{ex} leads to an increase in the thickness δ_{dw} of the domain walls, where the domain wall thickness is $\delta_{dw}= Na$ for N atoms.

Also, another energy present in the formation of a domain wall comes from rotating of the spins far from the magnetocrystalline easy directions. This rotation leads to an increase in the anisotropy energy through anisotropy constant per unit volume, and hence the anisotropy energy per unit area, σ_{dw}^{an} presented in the domain wall can be given by :

$$\sigma_{dw}^{an} = K_u\left(\frac{N}{a^2} \times a^3\right) = K_uNa \tag{2.17}$$

Where K_u refers to the anisotropy constant.

Summed together the distributed energies in the domain wall, which represented both the exchange energy and the anisotropy energy, the total energy per unit area of the domain wall of N atoms is given by :

$$\sigma_{dw} = \sigma_{dw}^{ex} + \sigma_{dw}^{an} = \frac{J_{ex}S^2\pi^2}{Na^2} + K_uNa \tag{2.18}$$

From the equation of total energy, there is competition between the exchange energy, which tends to increase the domain wall thickness, δ_{dw}, and the magnetocrystalline anisotropy energy, which tends to decrease it. Therefore, from the relation between δ_{dw} and N atoms, the δ_{dw} is determined from the given equation :

$$\frac{d\sigma_{dw}}{dN} = -\frac{J_{ex}S^2\pi^2}{N^2a^2} + K_ua = 0 \tag{2.19}$$

This gives the expression,

$$N = \sqrt{\frac{J_{ex}S^2\pi^2}{K_u a^3}} \tag{2.20}$$

Hence, the domain wall thickness will be given by :

$$\delta_{dw} = Na = \pi\sqrt{\frac{J_{ex}S^2}{K_u a}} \tag{2.21}$$

Therefore, a larger exchange energy produces a wider domain wall while a higher anisotropy constant produces a thinner domain wall.

From equation (2.18), the total energy of the wall can be rewriten for N as :

$$\sigma_{dw} = 2\pi\sqrt{\frac{J_{ex}S^2K_u}{a}} \tag{2.22}$$

2.6 Magnetization Process

When a ferromagnetic material is placed in a magnetic field, the magnetization is saturated in two ways. The first is the motion of domain walls. When the domains are placed in a magnetic field and their magnetic moments align parallel to the applied magnetic field, an increase in the domain area occurs due to the motion of domain walls. The second is the rotation of domains when applying a strong magnetic field. All the domains are rotated parallel along with the direction of the magnetic field.

2.7 Magnetostriction of Ferromagnetic Materials

Magnetostriction or Joule effect refers to the phenomenon of a ferromagnetic material when it changes dimensions on the application of a magnetic field. The origin of this phenomenon arises from the spin-orbit-lattice coupling. As a result of the strong coupling between the lattice and the orbit, a large magnetic anisotropy arises due to any change of the lattice. The magnetostriction can be explained by the concept of the relation between the atomic magnetic moments and their tendency to minimize their energy. In a ferromagnetic material, the magnetic moment orientation and the distance between adjoining moments can alter. Changing the distance between the magnetic moments or the angle of alignment of the moments can affect the interaction energy of the magnetic system. When the orientation of moments is changed by an angle along with applying a magnetic field along with an easy

direction, this leads to an increase in the interaction energy. Therefore, to minimize this energy there is a response to change the distance between the magnetic moments. In contrast to this concept, the Villari effect [21] can be understood, as explained in more details in section (2.7.1).

2.7.1 Villari Effect (Magnetization-Dependent Stress)

Applying a mechanical stress to a ferromagnetic material affects its magnetic properties. The interaction between the strain and the magnetization of a magnetic material leads to creating the magnetoelastic effect. Any bending, stretching, and twisting stresses can achieve this influence of mechanical deformation on the magnetization of a ferromagnetic material. For bending tools used in this work, applying different stress values changes the magnetization for a given direction, which is observed in the shape of hysteresis loops as shown in **Fig. 2.7**, where M_1, M_2, M_3 refer to the magnetization under applying $stress_1$ of first bending tool (Radius = 300 mm), $stress_2$ of second bending tool (Radius = 400 mm), $stress_3$ of third bending tool (Radius = 500 mm) respectively, . This response of the magnetization to the applied stress is known as the Villari effect [21], which is inverse to the Joule effect which is defined in section 2.7. The Villari effect is described as changing the domain structure of a ferromagnetic material by applying a mechanical force.

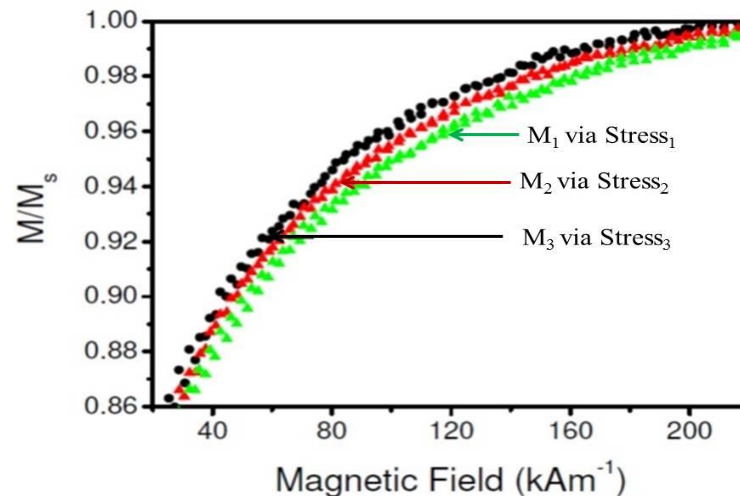

Figure 2.7 Magnetic hysteresis loops for by applying different mechanical stress values adapted from reference [22].

In this thesis, the magnetostriction measurement was measured via the Villari effect by using bending tools. To create a uniform effect over the whole of the film, a uniform strain should

be generated over the whole sample using a suitable bending tool. To achieve this a cylindrical section was needed to bend the substrate. The uniform strain is produced in the film and substrate, as the curvature is constant over the surface of the cylindrical section. In this method, the mechanical properties of the substrate were taken into consideration such as Young's modulus, E_s, and Poisson's ratio, v_s.

Depending on the theoretical principles of bending [23], the relationship between the applied stress and strain was derived. Appling an in-plane stress, **Fig. 2.8**, induces an in-plane strain in two dimensions x and y.

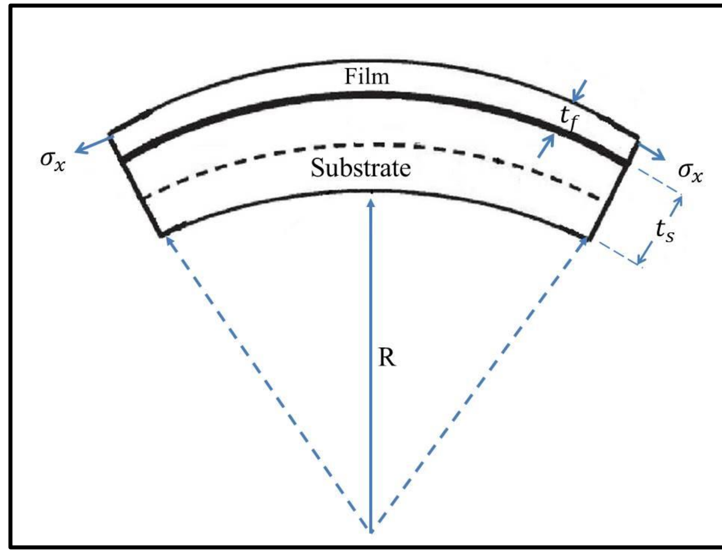

Figure 2.8 Schematic diagram of the stress applied on a film/substrate system.

Figure 2.8 shows the schematic diagram of a bending film/substrate system by applying stress, where σ_x is the applied stress in the x direction, where y direction set to be zero, t_f, is the film thickness, t_s is the substrate thickness, and R is the radius of curvature of bending.

The relations between the stress and strain in the x and y directions are :

$$\varepsilon_x = \frac{\sigma_x}{E_s} - \frac{v_s \sigma_y}{E_s} \qquad (2.23)$$

$$\varepsilon_y = \frac{\sigma_y}{E_s} - \frac{v_s \sigma_x}{E_s} \qquad (2.24)$$

Where ε_x and ε_y are referring to the strain components, σ_x and σ_y are referring to the stress in x and y directions, and E_s, v_s are the Young's modulus and Poisson's ratio of the substrate respectively.

To preserve continuity in the material during bending, the strain in the y-direction, ε_y, has to be zero, $\varepsilon_y = 0$ [23]. From equation (2.24) this leads to:

$$\sigma_y = \nu_s \sigma_x \tag{2.25}$$

Now substituting equation (2.25) into equation (2.23).

$$\varepsilon_x = \frac{(1-\nu_s{}^2)\sigma_x}{E_s} \tag{2.26}$$

It is possible to rewrite equation (2.26) to find an expression for σ_x, therefore,

$$\sigma_x = \frac{\varepsilon_x E_s}{1-\nu_s{}^2} \tag{2.27}$$

The strain component along the x-direction of the bent substrate is:

$$\varepsilon_x = \frac{t_s}{2R} \tag{2.28}$$

Where t_s is the substrate's thickness and R is the radius of curvature of the bending tool.

In this case, it is assumed that the thickness of the substrate is greater than the film thickness. By substituting equation (2.28) into equation (2.27) to get the dependence of the stress component on the radius, *R*, of bending tool:

$$\sigma_x = \frac{t_s E_s}{2(1-\nu_s{}^2)} \frac{1}{R} \tag{2.29}$$

From the magnetic theoretical principles, the relation between the thin film magnetic properties and the strain was derived [24]. For the magnetic properties of films under an applied stress, the uniaxial anisotropy field of a magnetic material under applied stress is given by:

$$H_k = \frac{2K_u}{\mu_o M_s} \tag{2.30}$$

Where $M_s$is the saturation magnetization and K_u is the anisotropy constant.

The anisotropy constant, k_σ, of induced anisotropy in a magnetic material under applied stress is given by:

$$K_\sigma = \frac{3}{2}\lambda_s \sigma \tag{2.31}$$

Where λ_s is the saturation magnetostriction constant and σ is the component of stress.

By assuming that $K_u = K_\sigma$ and substituting equation (2.31) into equation (2.30), the magnetic anisotropy field depends on the applied stress is given by:

$$H_k = \frac{3\lambda_s\sigma}{\mu_o M_s} \tag{2.32}$$

From equations (2.30) and (2.32), assuming the stress is along the x-direction, then the magnetic anisotropy field can be expressed as:

$$H_k = \frac{2K_u}{\mu_o M_s} = \frac{3\lambda_s\sigma}{\mu_o M_s} \tag{2.33}$$

From equations (2.29) and (2.32), the expression of magnetic anisotropy field can be rewritten to get the relationship between the anisotropy field and the radius of bending tool:

$$H_k = \frac{3\lambda_s t_s E_s}{2\mu_o M_s(1-\nu^2)}\frac{1}{R} \tag{2.34}$$

The magnetostriction constant λ_s can be determined from the derivation of equation (2.34) for H_k with 1/R:

$$\frac{\partial H_k}{\partial(^1/_R)} = \frac{3t_s E_s}{2\mu_o M_s(1-\nu^2)}\lambda_s \tag{2.35}$$

The value of $\frac{\partial H_k}{\partial(^1/_R)}$ can be found by plotting H_k as a function of *1/R* and applying a linear fitting equation to the data and finding the slope, **Fig. 2.9**. Therefore, the slope will represent the value of $\frac{\partial H_k}{\partial(^1/_R)}$. Hence the magnetostriction constant λ_s can be given as:

$$\lambda_s = \left(\frac{\partial H_k}{\partial(^1/_R)}\right)\frac{2\mu_o M_s(1-\nu^2)}{3t_s E_s} \tag{2.36}$$

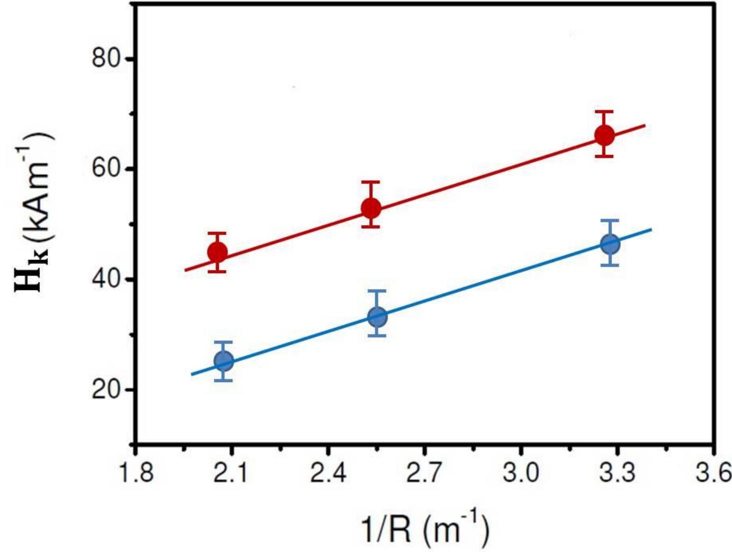

Figure 2.9 Example of the linear relation of anisotropy field, H_k, as a function of the inverse of the bending radius (1/R) adapted from reference [22].

Figure 2.9 presents the linear fitting of the anisotropy field as a function of the inverse of bending radius (*1/R*). Where the two data lines represent the anisotropy field values at the positive and negative parts of a hysteresis loop for three different bending tools.

2.7.2 Magnetostriction of Cubic Crystals

The cubic crystal of solid materials has anisotropic magnetic properties, therefore the saturation magnetostriction is defined along with a specific crystalline axis. In these materials there are two specific directions of the saturation magnetostriction constant: λ_{100} and λ_{111}. Therefore, the saturation magnetostriction constant, λ_s, of a cubic crystalline material can be written as,

$$\lambda_s = \frac{3}{2}\lambda_{100}\left(\alpha_1^2\beta_1^2 + \alpha_2^2\beta_2^2 + \alpha_3^2\beta_3^2 - \frac{1}{3}\right) + 3\lambda_{111}(\alpha_1\alpha_2\beta_1\beta_2 + \alpha_2\alpha_3\beta_2\beta_3 + \alpha_3\alpha_2\beta_3\beta_1) \quad (2.37)$$

Where λ_{100} and λ_{111} are the magnetostriction constants in the <100> and <111> directions of the cubic crystal. $\beta_1\,\beta_2\,\beta_3$ are the direction cosines o the strain which are related to the crystal axes, and change the magnetic state of a material from the demagnetizing state to magnetic saturation in orientation described by cosines $\alpha_1, \alpha_2, \alpha_3$.

In the case where the strain has oriented in the same direction as the magnetization, this will lead to a state that α_1=β_1, α_2=β_2, and α_3=β_3, therefore:

$$(\alpha_1^2 + \alpha_2^2 + \alpha_3^2) = 1 \quad (2.38)$$

From equation (2.38) and equation (2.37):

$$\lambda_s = \lambda_{100} + 3(\lambda_{111} - \lambda_{100})(\alpha_1^2\alpha_2^2 + \alpha_2^2\alpha_3^2 + \alpha_3^2\alpha_1^2) \quad (2.39)$$

In the case where the magnetostriction is isotropic, the terms in equation (2.37) can be stated to give $\lambda_{iso} = \lambda_{100} = \lambda_{111}$. If the angle θ is between two directions related to the direction cosines as in:

$$Cos\,\theta = \alpha_1\beta_1 + \alpha_2\beta_2 + \alpha_3\beta_3 \quad (2.40)$$

Then the result will be

$$\lambda_\theta = \frac{3}{2}\lambda_{iso}(cos^2\theta - \frac{1}{3}) \quad (2.41)$$

Where λ_θ refers to the saturation magnetostriction at the angle θ along with the direction of magnetization.

2.7.3 Magnetostriction of Polycrystalline

A polycrystalline material contains crystalline grains arranged in different directions. The total magnetostriction of these materials depends on the individual magnetostriction of each grain and their arrangement. When the grains orientation arrangement is completely random the magnetostriction, in this case, is the average of all the individual magnetostriction of grains. Therefore, the total magnetostriction over all grain orientations is given by [25]:

$$\lambda_s = \frac{2\lambda_{100} + 3\lambda_{111}}{5} \quad (2.42)$$

2.7.4 Magnetostriction of Thin Films

Similar to the relation between the magnetic anisotropy and film thickness, Szymczak [26, 27] found an equivalent formula for the saturation magnetostrictive constants in equation (2.14) to present the magnetostriction in thin films and give the total expression as given by:

$$\lambda_{total} = \lambda_v + \frac{\lambda_{su}}{t} \quad (2.43)$$

In a thick film, when the thickness increases, the second term will be very small and the volume magnetostriction, λ_v, dominates so that λ_{total} is independent of thickness. For films with small thickness (i.e. <10nm), the surface term, λ_{su}, will dominate and λ_{total} depends on the thickness.

2.8 Mechanical Characterization of Thin Films

The mechanical properties of thin films are determined by using the nanoindentation method and the data analyzed using the standard Oliver & Pharr method [28]. The technique involves applying a load in mN or μN onto an indenter, which consists of a very small hard tip (usually diamond) used for making an indentation into a thin film or solid, by penetrating the surface. From the nanoindentation test a load-displacement curve can be obtained, which gives the required applied load to penetrate a certain displacement (depth) in the material surface. Further, the elastic and plastic properties can be determined during the indentation procedure. In the case of thin films, it was found that there was no influence of the substrate on the measurement up to 10 % of the film thickness [28]. The load-displacement curve includes loading the indenter, rest, and unloading the indenter as shown in **Fig. 2.10**. Also the curve provides the maximum load and maximum displacement. Fitting the slope of the unloading curve represents the stiffness. From the parameters presented in the load-displacement curve, both the hardness and elastic modulus can be determined.

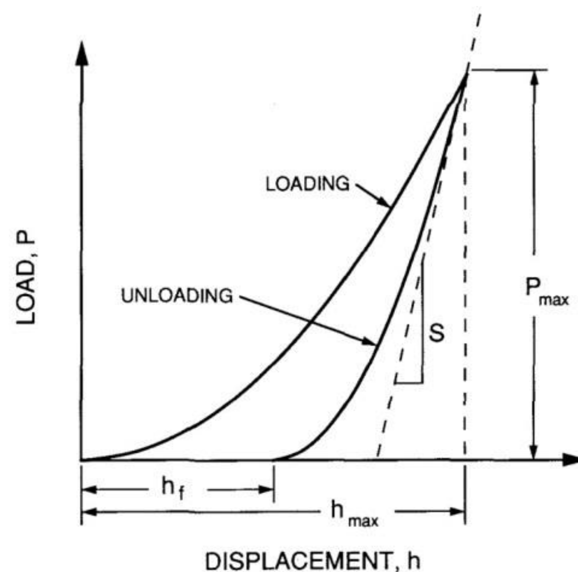

Figure 2.10 Example of the cycle of the load as a function of the displacement of nanoindentation taken from reference [28].

Before starting to present the hardness and elastic modulus definitions, it is necessary to define the contact area between the material and the indenter tip, which depends on the area function of the tip. The contact area is the real contact area between the removed material surface with the tip. Therefore, for the Berkovich indenter tip used in this study, the contact

area is estimated as an experimental function of the displacement of the indenter tip, (h_c), and can be given by [28]:

$$A(h_c) = 24.5h_c^2 \tag{2.44}$$

From **Fig. 2.11**, the contact depth, h_c, is determined from the experimental data as:

$$h_c = h - h_s \tag{2.45}$$

Where h is the total displacement at any time during applied load and h_s is the displacement of the surface at the boundary of the contact.

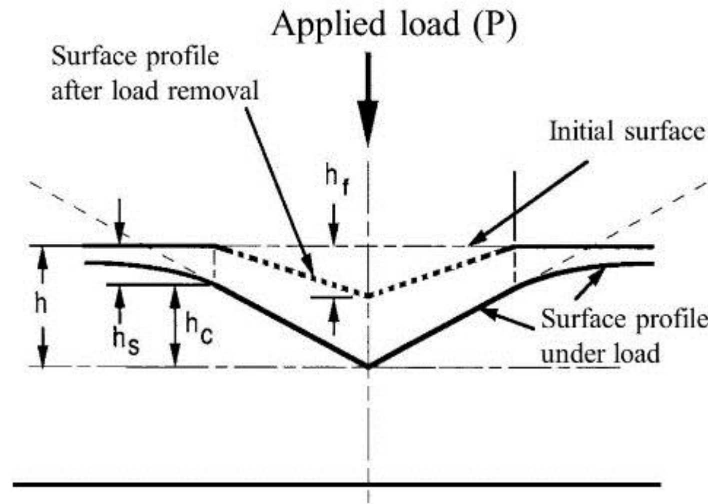

Figure 2.11 Cross section of the indenter and parameters taken from reference [28].

At the peak of the load, **Fig. 2.10**, the P_{max} represents the maximum load applied at the maximum displacement h_{max}. The area function is describing the indenter geometry and it represents the cross-section area of the indenter along the distance starting from the tip. The Berkovich indenter area function, A_f, which is used in this thesis data by fitting the relation of A_f and h_c using equation:

$$A_f(h_c) = 24.5h_c^2 + C_1h_c^1 + C_2h_c^{1/2} + C_3h_c^{1/4} + \cdots + C_8h_c^{1/128} \tag{2.46}$$

Where $C_1$to C_8 are constants and they are related with the indenter geometry.

Therefore, the contact area can be calculated as given by:

$$A_{contact} = \frac{\pi}{4}\frac{1}{E_r^2}\frac{1}{(C-C_f)^2} \tag{2.47}$$

Where $A_{contact}$ is the contact area, E_r is the reduced modulus, and $C - C_f$ are constants, where C refers to the total measured compliance while C_f refers to the compliance of the load frame.

From the load-displacement curve in **Fig. 2.10**, the measurement of the initial unloading stiffness is determined. The unloading stiffness is measured from the unloading data curve by using a straight line fit to the unloading curve and finding the slope to measure the stiffness. The expression of the stiffness, S, can be given by:

$$S = \frac{dP}{dh} = \frac{2}{\sqrt{\pi}} E_r \sqrt{A_{contact}} \tag{2.48}$$

Where $\frac{dP}{dh}$ is the change in the load to the change of displacement, $A_{contact}$ is the contact area of the elastic contact, and E_r is the reduced modulus.

The hardness, H_r, normally indicates resistance forced to localize plastic deformation. The hardness is calculated from the fraction of the applied load to the contact area, therefore by dividing the maximum applied load, P_{max}, by the contact area of the tip used, the hardness, H_r, can be given by:

$$H_r = \frac{P_{max}}{A_{contact}} \tag{2.49}$$

Where $A_{contact}$ is the contact area and P_{max} is the maximum applied load.

Therefore, the hardness, H_r, is inversely proportional to the contact area. The relation between the reduced modulus, E_r, and the contact area, $A_{contact}$, and calculated stiffness, S, is given by:

$$E_r = \frac{\sqrt{\pi}}{2} \frac{S}{\sqrt{A_{contact}}} \tag{2.50}$$

The reduced modulus measurement includes the compliance of the indenter and the elastic modulus of the material by the following expression:

$$\frac{1}{E_r} = \frac{(1 - v_s{}^2)}{E_s} + \frac{(1 - v_i^2)}{E_i} \tag{2.51}$$

Where v_s and E_s are the Poisson ratio and Young's modulus of the material respectively, and v_i and E_i are Poisson ratio and Young's modulus of the indenter tip respectively.

The Young's modulus (E_S) is inversely proportional to the square root of the contact area and can be measured from rewriting equation (2.51).

There are many factors, which can affect the measurement of these parameters and thus create an error in the calculations. The elastic modulus and hardness can be affected by the equipment, the substrate material, and the material under study. The substrate can affect the measurement if the depth of the tip reaches near the substrate through the film. To avoid the effect of the substrate on the elastic modulus and hardness, the indentation depth is kept to less than 10% of the total film thickness. While the material effect occurs due to the response of the material to the applied load and this includes material either piling-up or sinking-in. The pile-up occurs in the indentation of soft films around the indenter because of the incompressibility of plastic deformation, where some materials tend to flow up to the surface of the indenter sides after the indenter penetrates into the surface of the material **Fig. 2.12 (a)**. While the sink-in occurs in the indentation of hard films, when the plastic deformation area is moved out from the indenter with the imprint sinking, lower down the original surface level **Fig. 2.12 (b)**.

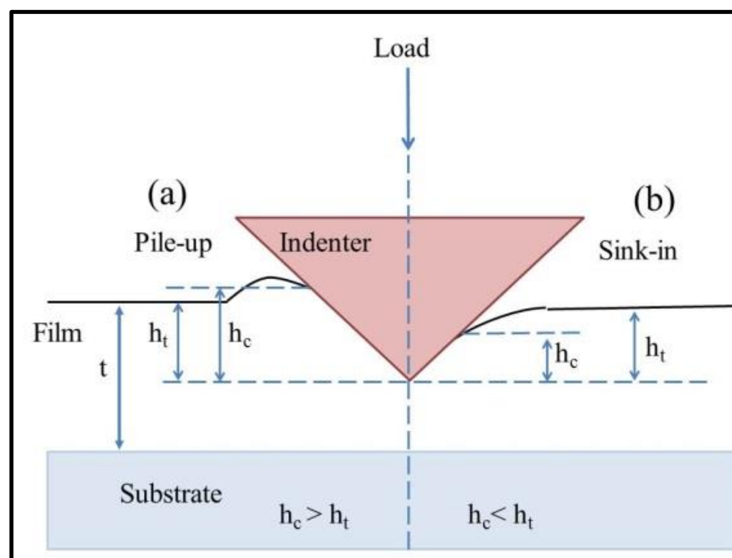

Figure 2.12 Schematic illustrations (a) the pile-up and (b) the sink-in of the material surface under applying the load of the indenter.

As a result of a material pile-up or sink-in under the measurement, the contact area is influenced and a large difference can occur between the real contact area and the apparent contact area, which is normally noticed after the indentation.

The yield strength, σ_{ys}, of a material can be described as the maximum stress applied to the material before it begins to change its shape or without producing plastic deformation. Also, the yield point is the point of the elastic deformation when the material returns to the original shape after removing the applied stress.

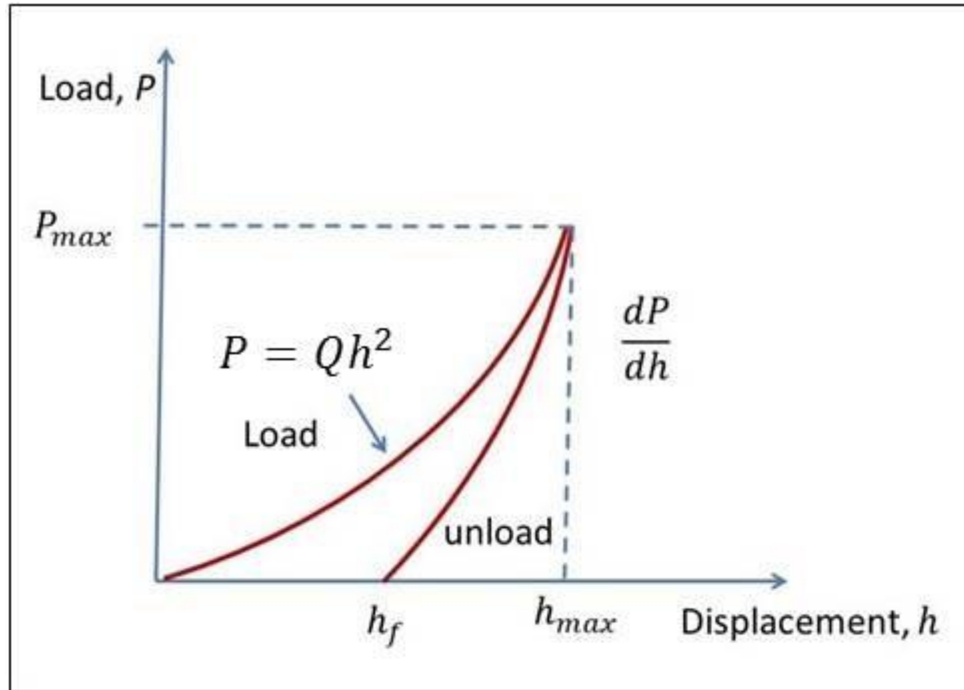

Figure 2.13 The load-displacement (P-h) curve for loading and unloading cycle adapted from reference [29].

The yield strength of thin films is determined from the hardness data utilizing the method established by Giannakopoulos and Suresh [29]. The data are analyzed by using the approach based on the load-depth (P-h) relations and displacement. In this method, the effective elastic modulus (reduced modulus), E_r, of the indenter with the material being studied, is calculated using the equation:

$$\frac{h_f}{h_{max}} = 1 - d^* \frac{H_r}{E_r} \qquad (2.52)$$

Where h_{max} is the maximum depth of penetration, h_f is the residual depth of penetration, H_r *is* the hardness of the thin films, and d* is a constant. In the case of a Berkovich indenter d* =4.678.

From both of the load-displacement curve and the maximum indentation load ($P_{max} \approx Qh_{max}^2$), the value Q is estimated. where Q refers to the indentation curvature.

From this model [29], the yield strength, σ_{ys}, and the flow stress, $\sigma_{0.29}$, which is the stress conforming to the plastic strain of 0.29 for the used material in uniaxial compression, **Fig. 2.14**, which used to determine yield strength in this study, can then be estimated by simultaneously solving the following two equations derived by Giannakopoulos and Suresh [29]:

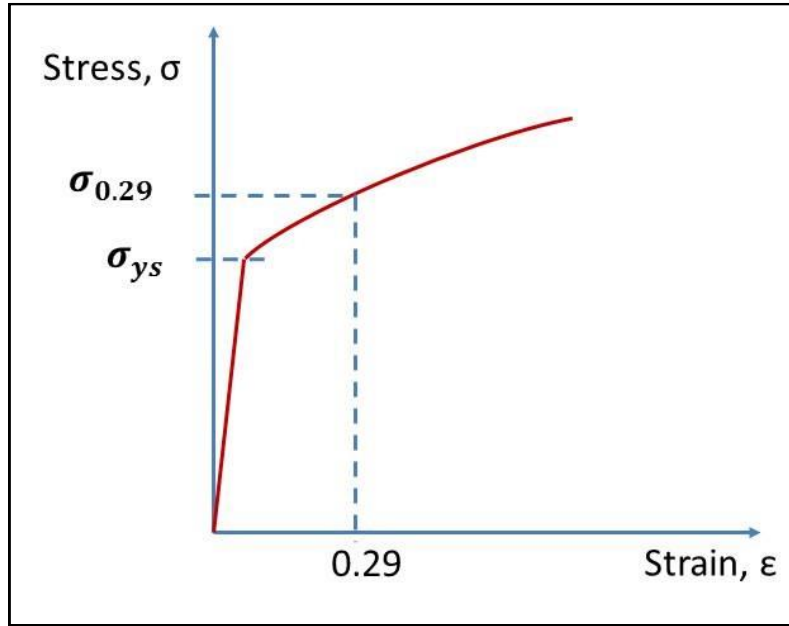

Figure 2.14 Example stress-strain curve and the characteristic strain adapted from reference [29].

From defining the plastic stress-strain reaction of the material under the indenter, the ratio of residual depth of displacement to the maximum displacement is symptomatic to the amount of plastic deformation and strain hardening as given by:

$$\frac{\sigma_{0.29}-\sigma_{ys}}{0.29E_r} = 1 - 0.142\frac{h_f}{h_{max}} - 0.957\left(\frac{h_f}{h_{max}}\right)^2 \tag{2.53}$$

It can be noticed that this equation can describe the strain hardening behaviour occurring in a material, which appears as a pile-up effect or sink-in based around the sides of the indenter. When h_f approaches zero, this will lead to make the right side of equation (2.53) equal to 1 and the left side will represent a linear response $\sigma_{0.29} - \sigma_{ys} = 0.29E_r$. In the case of $h_f = h_{max}$, the right side of this equation approaches zero, this will indicate that strain hardening is

not occurring and the yield strength, σ_{ys} is equal to $\sigma_{0.29}$ indicating that the material is perfectly plastic. Further, it is found that if h_f/h_{max} is equal to 0.875 this indicates that there is no pile-up and/or sink-in occurring in the material. It is found that pile-up occurs when the ratio, $h_f/h_{max} \geq 0.875$ and sink-in occurs when the ratio, h_f/h_{max} is ≤ 0.875. [29]

From **Fig. 2.14**, the data of the loading curve follows the formula, $P = Qh^2$, were Q refers to the indentation curvature, the loading curvature, which can be measured by providing equation (2.54) is a result of the elastoplastic indentation deformation along with research [30, 31].

$$Q = \frac{P}{h^2} = u_1\sigma_{0.29}\left\{1 + \frac{\sigma_{ys}}{\sigma_{0.29}}\right\}\left\{u_2 + ln\left(\frac{E_r}{\sigma_{ys}}\right)\right\} \tag{2.54}$$

Where in the case of Berkovich tip $u_1 = 6.618$ and $u_2 = -0.875$ for a tip with angle 130.6°.

Finally, the strain hardening, n_ϵ, can be calculated by using:

$$n_\epsilon = \ln\{\sigma_{0.29} - \ln(\sigma_{ys})\}/5 \tag{2.55}$$

2.9 References

[1] N.A. Spaldin, Magnetic Materials Fundamentals and Applications, Cambridge University Press, 2011.

[2] B.D. Cullity, Introduction to Magnetic Materials, Addison-Wesley Publishing Company, 1972.

[3] A. Beiser, Concepts of Modern Physics, 5th Ed., McGraw-Hill, Inc., New York, USA, 1995.

[4] R. B. Leighton, Principles of Modern Physics, McGraw Hill, New York, 1959.

[5] C. Kittel, Introduction to Solid State Physics, 2nd Ed., John Wiley and Sons, Inc., New York, USA, 1956.

[6] S. Chikazumi, Physics of Magnetism, John Wiley and Sons, Inc., New York, USA, 1964.

[7] R. M. Bozorth, Ferromagnetism, Published by IEEE Magnetic Society, IEEE, Inc., New York, USA, 1993.

[8] D. C. Jiles, Introduction to Magnetism and Magnetic Materials, 2nd Ed., Chapman and Hall, London, UK, 1998.

[9] S. Chikazumi, and C. D. Graham, Physics of Ferromagnetism 3e. Oxford University Press on Demand, 2009.

[10] C. Kittel, Introduction to Solid State Physics, 7th Ed., John Wiley and Sons, Inc., New York, USA, 1996.

[11] J.P. Jakubovics, Magnetism and Magnetic Materials, The Institute of Metals, 1987.

[12] B.D. Cullity, C.D. Graham, Introduction to Magnetic Materials, Hoboken: Wiley, 2009.

[13] R. C. O' Handley, Modern Magnetic Materials: Principles and Applications, John Wiley & Sons, Inc., 1999.

[14] M. Ali, PhD thesis, University of Sheffield, UK, 1999.

[15] M. P. Hollingworth, PhD thesis, University of Sheffield, UK, 2004.

[16] L. Neel, Journal Physics Radium, 15, 1954.

[17] R. C. O' Handley, Modern Magnetic Materials: Principles and Applications, Wiley, 2000.

[18] A. Hubert, R. Schäfer, Magnetic Domains The Analysis of Magnetic Microstructures, Springer, 1998.

[19] D. Jiles, Introduction to Magnetism and Magnetic Materials, Chapman & Hall,1991.

[20] C. Kittel, Rev. Mod. Phys. 21, 541, 1949.

[21] E. Villari, Annu. Rev. Phys. Chem. 126, 87, 1865.

[22] A. Javed, Ph.D. dissertation, Dept. of Materials Science and Engineering, Univ. Sheffield, Sheffield, U.K, 2010.

[23] Timoshenko and Woinowski-Krieger, Theory of plats and Shells, McGraw-Hill, 1959.

[24] C. S. Gudeman, IEEE Trans Mag, 26 (5), p. 2580-2582, 1990.

[25] R. C. O' Handley, Modern Magnetic Materials: Principles and Applications, John Wiley & Sons, Inc., 2000.

[26] H. Szymczak, J. Appl. Phys., 81 (8) p. 5411, 1997.

[27] H. Szymczak, and R. Zuberek, ACTA Physica Polonica A, 83 (5), p. 651-659, 1993.

[28] W. C. Oliver, G. M. Pharr, J. Mater. Res., Vol. 7, No. 6, 1992.

[29] A. E. Giannakopoulos and S. Suresh, Scripta Materialia, Vol. 40, No. 10, pp. 1191–1198, 1999.

[30] S. Suresh and A. E. Giannakopoulos, Acta Mater. 46,5755, 1998.

[31] S. Suresh and A. E. Giannakopoulos, and J. Alcala, Acta Mater. 45, 1307, 1997.

Chapter 3 Literature Review

3.1 Introduction

In this chapter, a brief description of magnetostrictive materials with crystalline and amorphous morphology is presented. Also included is a literature review about nanoindentation measurements of thin films and the importance of studying the mechanical properties of magnetostrictive thin films.

3.2 Magnetostriction Phenomenon in Ferromagnetism

In general, magnetostriction or the magnetostrictive effect is when a change occurs in dimensions or shape of magnetic materials in bulk or ribbon or thin film under an applied magnetic field. The magnetostrictive effect was initially described in 1842 by the physicist Joule [1]. He detected this phenomenon in a piece of iron material when it altered its length along the direction of an applied magnetic field (longitudinal magnetostriction). Since that time researchers have worked to apply this phenomenon on other materials to discover new magnetostrictive materials. Later, an opposite longitudinal magnetostriction phenomenon to the Joule effect was discovered in 1865 by Villari, the phenomenon was named the magnetoelastic Villari effect. Villari found that applying a bending stress can change the magnetization of a magnetic material. In this thesis, the magnetostriction constant was measured via the Villari effect by straining the films using bending tools with different radii (Chapter 4).

3.3Magnetostriction Materials

Magnetostrictive materials in either bulk alloys or thin films are being developed, after being discovered, to achieve the required properties for micro-electro-mechanical system (MEMS) applications such as sensors and actuators [2] [3]. The requirements of these applications focus on the particular characteristics needed, which are a considerable magnetostrictive constant greater than 50ppm that works under a low applied magnetic field. Many efforts have focused on finding new magnetostrictive Fe-based alloys in the forms of crystalline, polycrystalline, and amorphous structures. For Fe-based materials used in applications the necessary properties of design and technology for these applications are high magnetostrictive responses under low saturation magnetic field, good mechanical properties,

Qayes A. Abbas, 2018 & Email: qayes.a.abbas@gmail.com

good flexibility, operation under high temperatures, the potential to work under stress, and low cost [4]. As applications require a low saturation field, methods are needed to decrease the magnetocrystalline anisotropy to achieve a value close to zero. There are two possible methods, the first method includes making the alloy from positive and negative magnetocrystalline phases [5], while the second method includes fabricating an amorphous structure. The suitable requirements for magnetostrictive sensors would be a magnetostrictive material with saturation magnetostriction constant $\lambda_s >$ 50 ppm and magnetocrystalline anisotropy < 10 kA.m^{-1}, respectively.

As noted, that magnetostrictive materials with a large value of magnetostriction are important for technological applications. Rare earth materials first discovered in the 1960's, for example, Dy and Tb were shown at low temperatures to have very high magnetostrictive properties. However, one drawback of these elements compared with our study is their low Curie temperatures. This mean that the magnetostriction constant reaches zero near room temperature, which is not suitable for most magnetostrictive applications. Rare earth Fe-based alloys such as $TbFe_2$ and $SmFe_2$ [5] on the other hand were shown at room temperature to have the largest magnetostriction. For example, the magnetostriction in $TbFe_2$ alloy was measured along the direction [111] at different temperatures. It was found that at room temperature, it had a positive magnetostriction value of about 2000 ppm under a magnetic field of 800 kA/m. However, one drawback of these alloys is related to the high magnetic field magnitude required, where 800 kA/m is very high for applications compared with our study, which focuses on preparing thin films saturated under low magnetic field, making it a disadvantage. This means these alloys require a high magnetic field to reach the saturate state to measure their magnetostriction, due to their high magnetocrystalline anisotropy.

Another example of large magnetostriction rare earth alloys is $SmFe_2$ which shows at room temperature a large magnetostriction constant of -1258 ppm at 300 K. It was found that the alignment of the magnetization in these alloys changes from the [110] direction at low temperatures to the [111] direction at temperatures greater than 195 K. Another drawback of these alloys is the high magnetocrystalline anisotropy, which leads to difficulty in saturating this alloy.

The ferromagnetic transition elements such as Iron, Fe, Cobalt, Co, and Nickel, Ni, which have Curie temperatures of 1044 K, 1388 K, and 628 K respectively, have been studied to determine their magnetic and magnetostrictive properties. The studies showed that Iron,

Cobalt, and Nickel have soft ferromagnetic properties, and have a spontaneous magnetization due to a parallel alignment of their magnetic moments in the absence of an external magnetic field. A material can be classified as a soft magnetic material when its coercivity is less than 1kA/m. Typically, amorphous materials are classified as very soft magnetic materials as they have low coercivity, therefore, to achieve this the Iron, Cobalt, and Nickel elements are alloyed with metalloid elements such as B, Si, P, and C. To search for soft magnetic materials, which have good magnetic properties and high magnetostriction better than the transition elements such as iron, experimental work has been done to create new alloys by adding non-magnetic elements and different magnetic elements to iron. In general, the addition of non-magnetic elements such as Ga, Al, Be, and Si can lead to an increase in the interatomic distance in the Fe-based structure that leads to an increase in the magnetostriction magnitude. For example, it was reported that the magnetostriction of bcc Fe is significantly improved by addition of Ga [6] (see section 3.5.1).

3.4 Methods of Measuring the Magnetostriction

Techniques for measuring the magnetostriction properties can be generally categorized into direct and indirect methods. Magnetostrictive techniques cannot measure the magnetostriction for all different types of the samples because the limitations of the techniques. The measurements can depend on many factors such as the size of the sample, substrate nature, and the physical principle of the technique. Briefly, a discussion is made in this chapter of the techniques.

3.4.1 Direct Measurement Methods

Direct measurement methods include the strain gauge, the dilatometer, and the cantilever, which are able to measure the strain of magnetostrictive materials depending on the applied magnetic field. In this case, the strain will be measured directly.

3.4.1.1 Strain Gauge Method

The strain gauge method is extensively used over a wide temperature range to measure the magnetostriction in crystalline and amorphous bulk materials. It involves a wire being attached in a certain direction on an area of a material. One variation of this method involves the electrical resistance of the wire varying as a function of the strain. The wire resistance increases when the strain gauge is flexed. Also, by applying a large enough magnetic field to

saturate the magnetic material along the crystalline axis, the change in length of the sample is measured as the strain by the gauge. A schematic diagram of this method is shown in **Fig. 3.1**. This measurement of the magnetostriction is given by [7]:

$$\lambda_s = \varepsilon[1 + \frac{2A_g\ E_{s,g}}{A_m\ E_{s,m}}] \tag{3.1}$$

Where A is the cross sectional area of the gauge and sample, ε is the induced strain, E_s is the Young's modulus of the gauge and sample, where g indicates the gauge subscripts and m the magnetic sample.

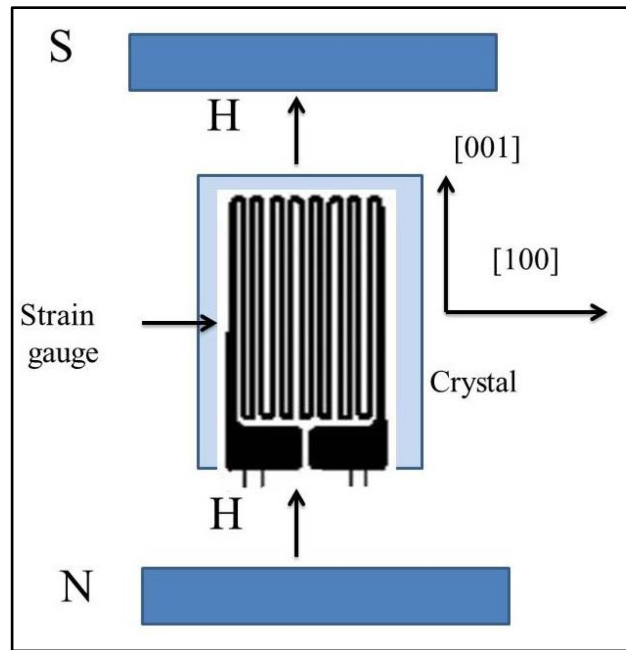

Figure 3.1 Schematic diagram of a strain gauge adapted from reference [8].

In summary, the main features of this method are that it is more suitable for ribbon and bulk samples. The measurements can be done under a wide range of temperatures and applied stresses. A small cross-sectional area of the gauge can be chosen to reduce the mechanical loading effect. The glue used to attach the gauge to the sample can also affect the measurement. The sensitivity of this method is typically about 10^{-8}.

3.4.1.2 Dilatometry Methods

A. Tunnelling Tip Dilatometry

In general, the tunnelling tip method involves many parts (the tunnelling tip, magnetostrictive specimen, the solenoid coils, and feedback electronic system), which are described elsewhere [8]. The schematic diagram of this method is shown in **Fig. 3.2**. In this method the tunnelling tip is used as a position-sensing detector, the magnetostrictive material can be in ribbon, wire, or rod form. The magnetostrictive sample is held in a quartz tube, which is placed inside the solenoid coils. By using a piezoelectric activator, the tunnelling tip location can be controlled. From the feedback data to the tunnelling current, which works to control the piezoelectric actuator, the distance between the magnetostrictive sample and the tunnelling tip is preserved. Hence, any changing in the length of the sample can be measured by the control signal in the feedback system.

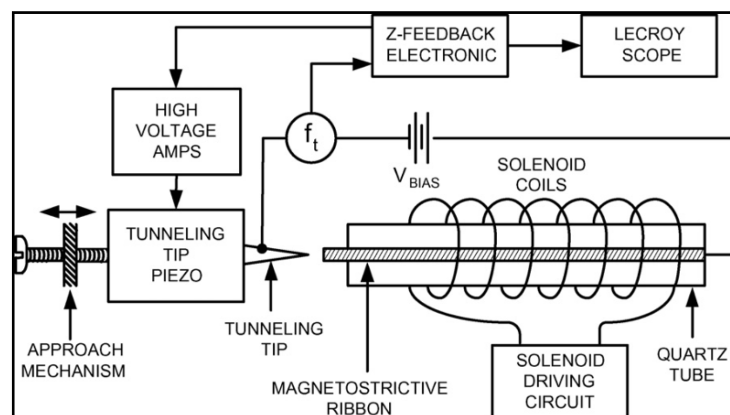

Figure 3.2 Schematic diagram of the tunnelling tip dilatometry method taken from reference [8].

B. Capacitance Dilatometry.

Capacitance dilatometry is a sensitive method to measure small variations in length of samples. The variation in the materials' dimension is detected as a difference in the capacitance between two electrodes. The capacitance dilatometers method involves a capacitor with parallel plates, where one plate is a fixed plate, and another one is a moving plate. Any change in the sample length will move the moving plate, which changes the space between the plates. Thus the capacitance is changed proportional to the space between the plates. The normal design of the capacitance dilatometry method is shown in **Fig. 3.3**.

Research studies such as Tsuya et al [9], Boley et al [10], Briss et al [11], and Heremans et al [12] have developed different types of capacitance methods. For example, Tsuya [9] designed a three terminal capacitance dilatometer to measure the magnetostriction of 0.5–10 mm diameter spherical specimens. Boley [10] developed the method by using a high oscillating magnetic field to generate the magnetostriction. When a material reaches the saturation state, this is sensed by the variation in capacitance. Also, this method was developed by Briss [11] for calculating a series of magnetostriction values of disc shaped samples under a range of temperatures from room temperature to 4 K using a superconductive split-coil magnet. Further, Heremans [12], usedu3 2 the capacitance method in pulsed fields. In general, in the capacitance methods the magnetostriction λ_s is proportional to the change in the capacitance, ΔC. The sensitivity of capacitance methods is about 10^{-10}.

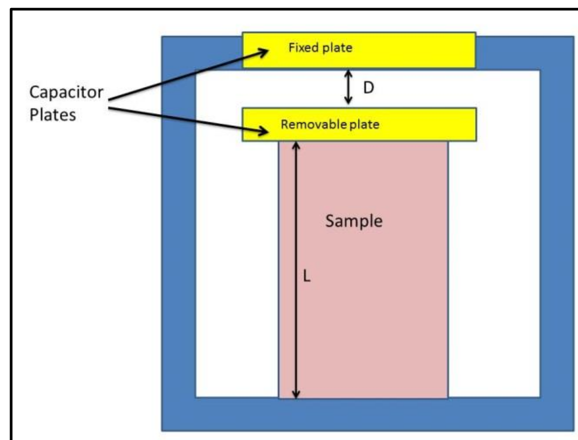

Figure 3.3 Schematic diagram of normal capacitance dilatometry method adapted from reference [13].

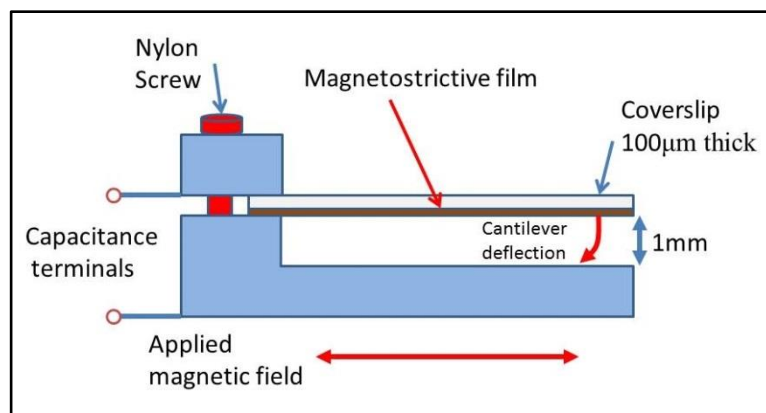

Figure 3.4 Schematic diagram of the cantilever capacitance dilatometry method adapted from reference [14].

Another type of the capacitance method is based on the change of capacity by using a cantilever as shown schematically in **Fig. 3.4**. The film to be measured is deposited on the cantilever, where an applied magnetic field on the film can produce strain in the film. The induced bending moment leads to a deflection of the cantilever and creates a change in the capacitance ΔC. [14]

3.4.1.3 Optical Interferometry

In the optical interferometry method, an optical lever, which represents an arm can measure displacement by attaching a mirror to determine small changes in length, and thus deformation of magnetic materials. This material deformation is related to the percentage of both the incident and reflected beam intensities. By attaching a mirror to the optical lever, the variation in dimension can be determined as a variation in the angle of the reflected beam. The optical lever is rotated due to the deformation in the sample, which increases with increasing applied magnetic field. This method is suitable for large samples, one drawback of this method is that it is not suitable for samples of dimensions < 1 mm. A new method, optical fiber displacement measurement, was developed to measure the magnetostriction. This method uses an optical fiber displacement detector and a measurement probe. The main parts of this method are shown in **Fig. 3.5**.

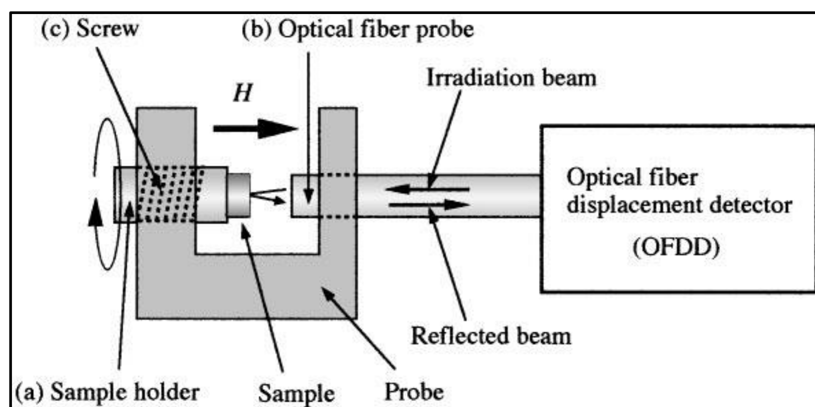

Figure 3.5 Schematic diagram of an optical interferometry method taken from reference [15].

In this method, the reflected light is measured by use of an optical fibre displacement detector and measurement probe. To avoid any magnetic effects the sample holder is made from duralumin material, which is a mixture of aluminium and copper. A rotated screw is used to regulate the sample position. The optical fibres are separated into two parts, irradiation and receiving fibres. The light is transmitted through the irradiation fibres to the sample and the

reflected light from the surface of sample passes in the receiving fibres and is detected by a photodetector. The main principle of this method is that the received optical power depends on the distance between the surface of the sample and the optical fiber. An increase in this distance leads to an increase in the optical power. Therefore, when the magnetic sample changes its dimension using a magnetic field, the distance between the optical fiber probe and the tested sample will change. The change in the ratio of the incident and reflected light intensities is analysed by computer to measure the magnetostriction of the sample in the range of 10^{-6} to 10^{-5}, which suitable to test small samples <1 mm. The sensitivity of this method is about 10^{-11}.

3.4.2 Indirect Measurement Methods

Indirect measurement methods are able to measure the saturation magnetostriction indirectly. The magnetostriction is determined from a measurement of parameters, which depend on the strain. Most indirect measurement techniques are methods based on the Villari effect.

3.4.2.1 Small Angle Magnetization Rotation (SAMR)

The small angle magnetization rotation (SAMR) method was first described by Narita et al [16]. This method is based on Villari effect. This technique involves applying together two different magnetic fields in different directions: the first is a dc magnetic field ($H_{\parallel}$) generated by a solenoid, in longitudinal direction of the sample axis to reach magnetic saturation and the second is an ac magnetic field ($H_{\perp}$), generated by driving coils, in a perpendicular direction. A third sensing coil contains the sample and measures the induced voltage caused by rotating the sample magnetization. The application of a variable tensile stress is used to affect the anisotropy within the sample, and hence changing the anisotropy is proportional to the magnetostriction of material, equation (3.2). The main parts of this method are shown in **Fig. 3.6**. This method has a sensitivity of about 10^{-9}.

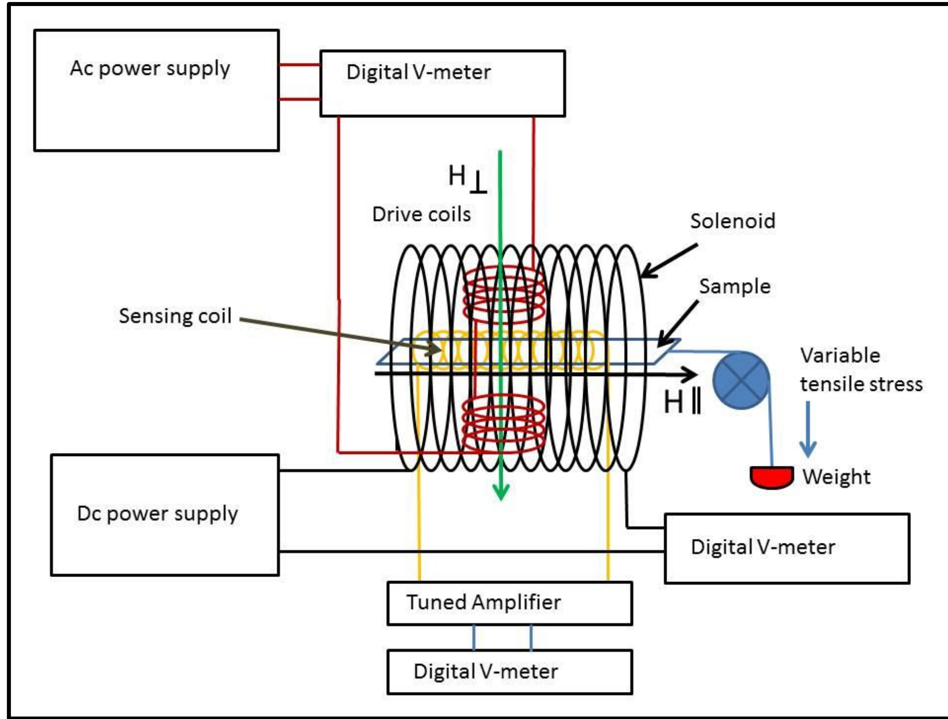

Figure 3.6 Schematic diagram of Small-angle magnetization rotation (SAMR) method adapted from reference [16].

The magnetization rotation angle is influenced by the dc magnetic field and the applied tensile stress. Applying a stationary ac drive field together with a variable tensile stress, results in a readuction of the rotation angle as a result of increasing anisotropy field (H_k). Both the applied stress and dc magnetic field are changed to control the induced voltage in the sensing coil. The magnitude of saturation magnetostriction can be obtained from the applied stress and the measured H_k as follows:

$$\lambda_s = -\left[\frac{M_s}{3}\right]\left[\frac{dH_k}{d\sigma}\right] \tag{3.2}$$

Where λ_s is the saturation magnetostriction, M_s is the saturation magnetization, H_k is the anisotropy field, and σ is the applied stress.

When the induced anisotropy field is measured, the saturation magnetostriction can be determined from the constant magnetization rotation:

$$\lambda_s = \frac{1}{3}\frac{H_k}{\sigma}M_s \tag{3.3}$$

Experimentally, by applying an arrangement of weights, the applied stress can be determined, thus the saturation magnetostriction can be determined from the weights

$$\lambda_s = \frac{1}{3}\frac{H_k}{W_T} M_s W \quad (3.4)$$

Where W is the weight per the long dimension of the samples and W_T is a weight the pendulous part of the ribbon

3.4.2.2 Strain Modulated Ferromagnetic Resonance (SMFMR)

This method involves a periodic strain applied using an ultrasonic transducer on a ferromagnetic sample located inside a microwave cavity (resonator) [17], which can be oscillated to a high-frequency value. Also, this method is based on Villari effect. The signal strength found after phase sensitive detection is related to the value of the strain modulation depth, m_s. The position of the ferromagnetic resonance line can be modulated as a result of the magnetoelastic coupling. While the magnetic field modulated FMR signals are recorded together, the amplitude of the strain modulation depth, m_s, can be determined when the intensities of two FMR signals are compared. When the gain of the amplifier channels of both the FMR (Ge) and the SMFMR (Gs) are identified, the strain modulation depth, m_s, can be found by:

$$m_s = m_e \frac{I_s}{I_e}\frac{G_e}{G_s} \quad (3.5)$$

Where G_e and G_s are the gains of the amplifier systems, m_e is the magnetic field modulation depth, while I_s and I_e refer to the intensities of the strain modulated FMR signal and H-modulated signal respectively. The magnetostriction value can be determined by comparison of the high signal of the SMFMR versus the signal of the FMR line. The main parts of this method are shown in **Fig. 3.7**. This method is generally used for samples in thin film form as a result of the slight skin depth of microwave frequencies. The method has a sensitivity about 10^{-9}.

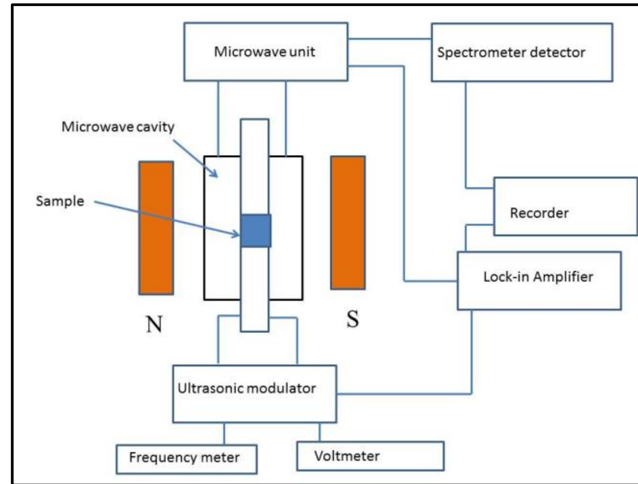

Figure 3.7 Schematic diagram of strain modulated ferromagnetic resonance (SMFMR) adapted from reference [18].

3.5 Magnetic Properties in Magnetostrictive Polycrystalline Films

Magnetic properties of polycrystalline thin films are different from their bulk alloys and amorphous structures. The magnetic properties of polycrystalline thin films can be affected by many factors, such as the growth parameters, film thickness, fabrication methods, composition, stress within the film, and substrate material. Other factors such as the texture, texture orientation, phase transfer, grain size, and grain boundary, which are missing in amorphous films, can affect the magnetic properties of polycrystalline thin films. This part of the review will present the advantages and disadvantages of some polycrystalline thin films to compare them with amorphous thin films.

3.5.1 Magnetic Properties of Magnetostrictive FeGa Films

The magnetic properties and magnetostriction of polycrystalline FeGa thin films have been studied by many researchers and developed by changing the composition of Ga within the films or by changing the film thickness. In Fe-Ga, a number of things can affect the magnetoelastic properties of these films, these include the many phases present such as A2, DO_3, Ll2, B2, and $D0_{19}$ as described by Ikeda et al [19] and shown in **Fig. 3.8**.

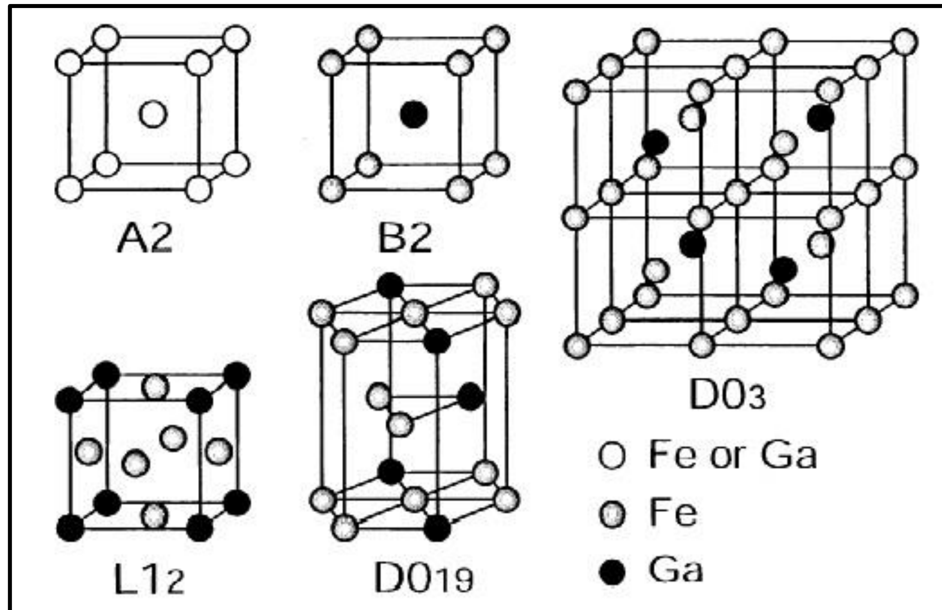

Figure 3.8 The locations of the Fe and Ga atoms of the crystalline structures of A2, B2, D0$_3$, L12 and D0$_{19}$, taken from reference [19].

The phase diagram of crystalline FeGa alloy as shown in **Fig. 3.9**, it can be seen that these crystalline phases are changed by the effect of temperature and Ga content.

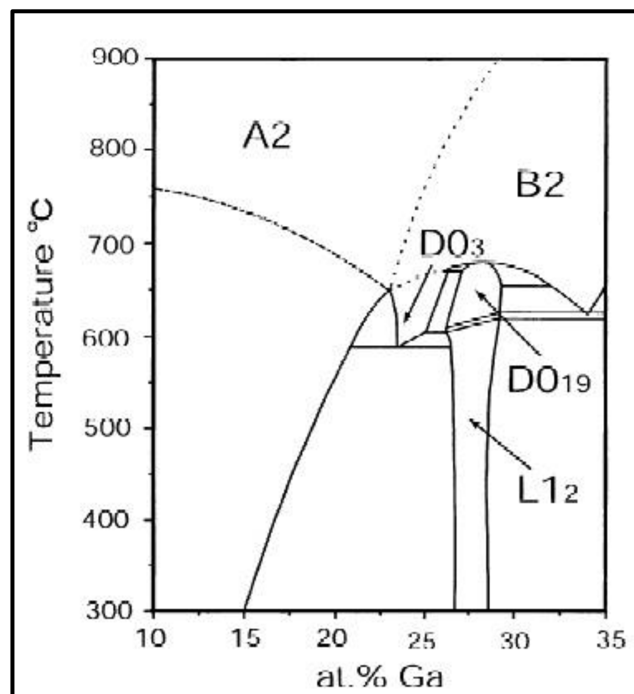

Figure 3.9 Binary phase diagram of FeGa crystalline taken from reference [19].

The XRD pattern of FeGa phases are shown in **Figs. (3.10 and 3.11)**, it can be seen that there are adiffernce between the XRD pattrens of these phases.

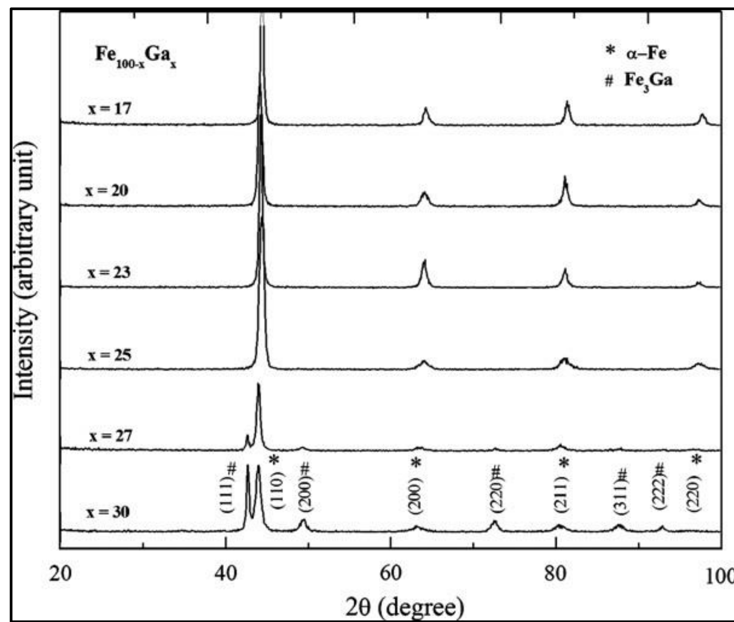

Figure 3.10 XRD pattern of FeGa phases taken from reference [20].

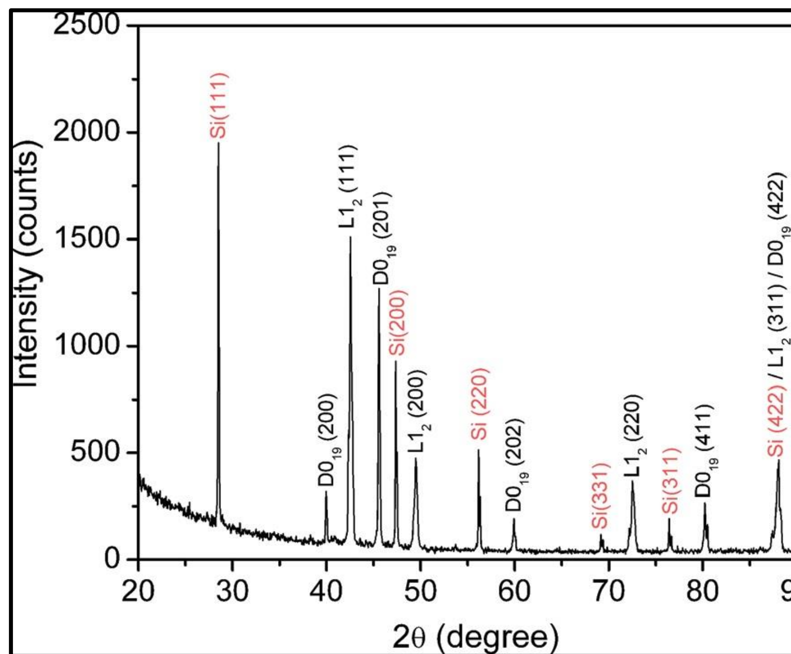

Figure 3.11 XRD pattern of FeGa phases taken from reference [21].

Dunlap et al [22] investigated the structural properties of polycrystalline $Fe_{100-x}Ga_x$ films by two different techniques: Mössbauer spectroscopy and XRD. The films were grown to a large thickness equal to 0.8 μm by the sputtering from Fe and $Fe_{50}Ga_{50}$ targets. The XRD results showed that all the films had a large (110) peak of the bcc A2 phase and they found that the increase of Ga composition leads to an increase in the lattice constant. The results of the Mössbauer spectroscopy on the other hand showed a short-range order of DO_3 when ($x > 20$). The Fe probe atoms of the Mössbauer spectroscopy are sensitive to the local environment and using this technique can investigate the classes of short-range structures that can affect the magnetostrictive properties of FeGa films. One drawback of this work was the absence of the effect of increasing the Ga content and the short-range order of DO_3 phase on the magnetostriction constant of polycrystalline FeGa films. Basantkumar et al [14] investigated the effect of changing the Ga composition and the thickness on the magnetic properties of $Fe_{100-x}Ga_x$ thin films, fabricated by rf sputtering technique using a target of composition $Fe_{81.6}Ga_{18.4}$. The thickness and the Ga composition were changed by changing the sputtering growth parameters. For example, they succeeded to control the Ga composition ($15 \leq x \leq 30$) by changing the forward power of the sputtering. The XRD results showed that all the films had <110> texture and there was no DO_3 phase peak detected. The magnetic properties were measured on a vibrating sample magnetometer (VSM). They found that the coercive field of these films was reduced from 1989 A/m to 1193 A/m and the Ga composition was decreased from 27% to 19% with increasing the forward power from 60 to 100W. From the result of the cantilever capacitance method, they showed that the largest magnetostrictive constant 147 ppm was presented in films with forward power of 80 W, thickness 146.5 nm, and Ga content 23.8%. A minimum value of 16.3 ppm was found in films with forward power of 100 W, thickness 133 nm, and Ga content 19.4%. Their results showed that the magnetostriction constant changed with the growth parameters, but they did not mention which parameter affected the film properties, i.e either the thickness or Ga content.

Hattrick-Simpers et al [23] investigated the magnetostriction properties of $Fe_{100-x}Ga_x$ alloy films with thickness 500 nm. The films were fabricated on silicon substrates by co-sputtering using two targets: Fe at power 75 W and Fe_2Ga_3 at power 40 W; for both targets the Argon pressure was 6μbar. These parameters allowed them to change the composition of the films ($0 < x < 45$). The result of the XRD and TEM showed that the films had a random nano-polycrystalline orientation structure with an average grain size of about 25 nm. For the magnetostriction measurements, they used the cantilever method to determine the λ_{100}, by using $\lambda_{eff} = (3/5)\ \lambda_{100}$, as a function of the Ga composition and ignorins the λ_{111}. From their

magnetostriction data, they found that the magnetostriction had two peaks, the first one at (x = 21) with magnetostriction value about 64 ppm and the second one at (x = 32) with magnetostriction value about 74 ppm. In addition to these two peaks, they also presumed that the results presented another peak of magnetostriction about 23 ppm at Ga content 4.5%. They compared the result of magnetostriction, λ_{100} with the result of bulk FeGa studied by Clark et al [6] **Fig. 3.12**. They found a difference in the results, as the peaks had shifted and the magnetostriction constants were lower. They suggested that the difference in the comparison comes from the residual stress in the films due to the deposition process. The lack of the relation between the chemical ordering of FeGa phases with the magnetostriction results was the one drawback of their study.

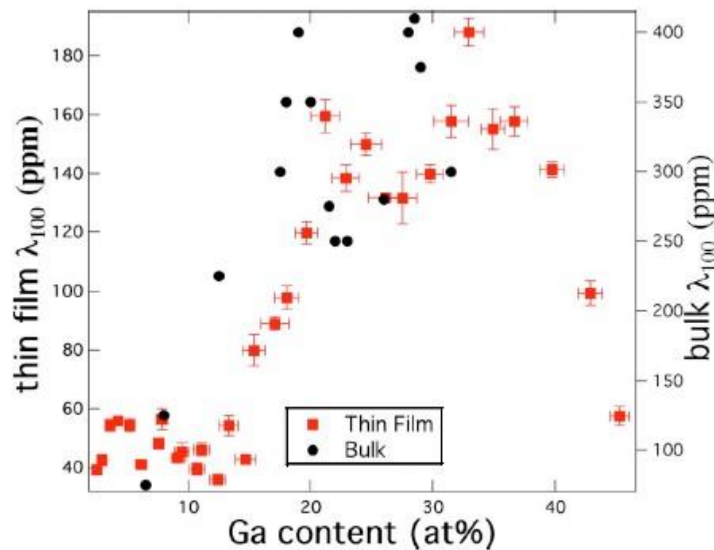

Figure 3.12 Comparison between the magnetostriction, λ_{100} of the thin film and bulk alloy of FeGa, taken from reference [23].

Clark et al [6] found that the magnetostriction properties of $Fe_{100-x}Ga_x$ alloys were affected by changing the Ga concentration and two peaks were observed, the first one λ_{100} = 265 ppm at x = 19 and the second one λ_{100} = 235 ppm at x = 28. Their result is presented in **Fig. 3.13**. The measurements were obtained by the strain gauge technique at room temperature.

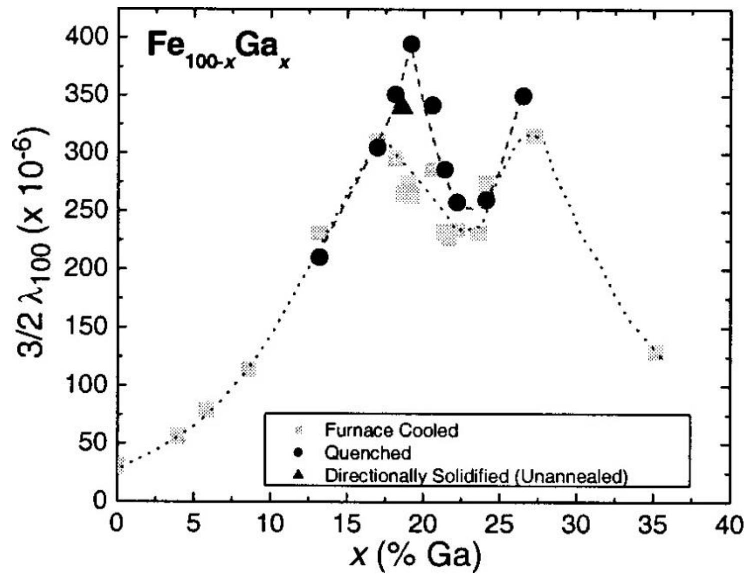

Figure 3.13 Magnetostriction, (3/2) λ_{100} of FeGa alloy as a function of Ga content taken from reference [6].

Morley et al [24] developed a deposition chamber that used co-sputtering and evaporation to deposit Fe_{100-x} Ga_x thin films. The films were fabricated by sputtering a Fe target and evaporating Ga, as it has a too low melting point to sputter. Changing of the growth parameters allowed them to control the composition of the films in the range $0 < x < 40$. They studied the structure, magnetic properties, and magnetostriction of Fe-Ga films and compared the results with those of pure Fe films with the same thickness. They designed this chamber to overcome the problem of low melting point of the Ga and to give better control of the Ga composition compared to sputtered Fe-Ga targets. One problem to overcome was they had to evaporate the Ga through the Ar gas plasma to the substrate. The substrate in this growth chamber was rotated to avoid the effect of the magnetron fields, to achieve thickness uniformity upon the substrate and uniform Fe-Ga composition across the film. They presented the effect of the pressure-distance (pd) product on the magnetic properties of the films and the effect of growth parameters on the composition of the Ga within the film. For example, they found that changing the pressure can strongly affect the amount of Ga to reach the substrate. Another factor, which influenced the Ga composition was the Fe magnetron power. They found that increasing the Ga content reduced the magnetic saturation field, increased the remanent magnetization, and reduced the coercive field compared with the Fe films that were fabricated under the same conditions. They found that the large magnetostriction constant was 17 ppm with film of comsition of $Fe_{76}Ga_{24}$. They found an

increase in magnetostriction constant with an increase in the Ga percentage within the Fe films.

Morley et al [25] studied the effect of a forming field on the magnetic properties of magnetostrictive $Fe_{100-x}Ga_x$ films ($0 \leq x \leq 30$) thin films with thickness 75 nm prepared by the co-sputtering-evaporation technique, which is described in Ref. [24]. Two types of films were fabricated on Si substrates, the films grown with and without a forming field (65 kAm^{-1}), produced by two permanent magnets placed along the short axis of the substrate connected on the substrate holder. Rotating the substrate holder during the growth was necessary to avoid any effect from the stray fields of the magnetron, which can induce anisotropy within the films. From the XRD results, they found that the forming field did not affect the structure of the films and all the films had a texture in the direction <110> perpendicular to the substrate. They found that the films grown with a forming field had uniaxial anisotropy. Also, they found that maximum value of the effective magnetostriction constant at a Ga percentage of ≈ 23%, for the forming field film.

Javed et al [26] studied the effect of a forming field during growth on the structural and magnetic properties of polycrystalline $Fe_{100-x}Ga_x$ ($10 \leq x \leq 35$) thin films with thickness 50 nm. The films fabricated by the technique presented in Ref [24] on Si substrates. From the XRD result, they found that all the films had texture < 110 > perpendicular to the film plane. Also, they found that all the films had a disordered A2 phase. For the magnetostriction result, they found that the values of results without forming field were higher than the value with forming field by a factor of about 50%.

Javed et al [27] investigated the effect of changing the Ga composition as a function of pressure on the structure and magnetic properties of magnetostrictive $Fe_{100-x}Ga_x$ ($19 \leq x \leq 23$) thin films. The films were fabricated on Si substrate using the co-sputtering-evaporation technique Ref. [24], by changing the pressure from 3 to 7 μbar. From the XRD result, they found that all the films had bcc phase of FeGa, with the <110> direction out of plane. Magnetically, they found that most of the films were isotropic except the film grown at 3 μbar, which presented a weak uniaxial anisotropy. Experimentally, the effective saturation magnetostriction constants was kept constant at around 60 ppm, although the Ga% increased.

Javed et al [28] studied the effect of the growth parameters such as the sputter target power, chamber gas pressure, and Ga evaporation rate on the magnetic properties of $Fe_{100-x}Ga_x$ thin films ($14 \leq x \leq 32$). The films were fabricated by co-sputtering-evaporation technique defined in Ref. [24] on Si substrates. From the XRD, they found that all the films had a

texture < 110 > perpendicular to the film plane. From the Mössbauer spectroscopy results, they found that all the films had disordered A2 phase. From the magnetostriction result, they found that: for the samples with different sputtering target power, the maximum value of the magnetostriction was about 85 ppm at 24% Ga. For samples with different chamber pressure, the magnetostriction constant kept around 60 ppm for 19 < Ga % < 24; and for the samples with different Ga evaporation rate, the magnetostriction constant increased to around 50 ppm at 26% of Ga. From their study, they inferred that the effective saturation magnetostriction constants in the case of changing the target power films were greater than those for different gas pressure and Ga evaporation rate films.

Javed et al [29] studied the effect of changing the thickness on the magnetic properties of polycrystalline $Fe_{80}Ga_{20}$ thin films, which were fabricated in the thickness range from 20 nm to 200 nm, by co-sputtering-evaporation described in Ref. [24] on Si substrates. From the XRD result, they found that all the films had texture with < 110 > direction perpendicular to the film plane. They found that the magnetostriction constant increased with increasing the thickness. They reported that the saturation magnetic field, the grain size, the surface roughness, and the magnetostriction constant of the films increased with film thickness. Szumiata [30] studied the effect of annealing temperature (350°C for 1 hour) and forming field (about 65 kA/m) on the magnetic properties of $Fe_{100-x}Ga_x$ ($10 \leq x \leq 35$) thin films prepared by the co-sputtering-evaporation technique [24] with thickness 50 nm on Si substrate. They found that the saturation field reduced with increasing Ga composition for both as-deposited and annealed samples. One effect of annealing was that it reduced the saturation field in comparison with the as-deposited films. While the saturation magnetostriction constant of the as-deposited films was larger than the annealed films.

3.5.2 Magnetic Properties of Magnetostrictive FeCo Films

In bulk form, the FeCo alloy is similar to the FeGa alloy and exhibits one of the largest saturation magnetostriction constants among other non-rare earth bulk alloys [31]. For example, the magnetostriction constant of bulk single crystal $Fe_{50}Co_{50}$ was shown to have a maximum value of λ_{100} = 150 ppm and a small anisotropy constant 10^4 $J.m^{-3}$ [32]. Experimentally, FeCo thin films are affected by the growth parameters and the thickness, which can be controlled to produce good magnetic properties, which are suitable for many applications. For example, Morley et al [33] studied the effect of rotation and stationary substrates along with the growth parameters on the structure and magnetic properties of polycrystalline $Fe_{50}Co_{50}$ thin films with thickness ranging from 10 nm to 100 nm, prepared

by two different sputtering techniques (DC and rf sputtering) on Si substrate. The substrate was rotated during the growth in the DC sputtering technique, while for the rf sputtering the substrate was fixed. From the XRD result, they found that the DC sputtered films, under rotation, with thickness less than 30 nm had <110> peak, whereas for the stationary samples in both DC and rf sputtering systems the films had an absence of <110> peak until the thickness was greater than 35 nm. They found that the magnetic results showed that the rotated films had anisotropic magnetic field in-plane, whereas the stationary films presented uniaxial anisotropy. By using the Villari effect method, they found that the magnetostriction constants were affected by the growth parameters, for example, the films sputtered by DC sputtering under rotation had magnetostriction constants of 11 ppm across all thicknesses. While for the non-rotated films in the DC system, the magnetostriction constant had an increasing linear relation with the thickness. Coïsson et al [34] studied the effect of annealing temperatures, 300 and 350 ^oC for 20 to 120 min and 100 Oe forming field on the magnetic properties of $Fe_{50}Co_{50}$ thin films, with two thicknesses 4 nm and 30 nm, fabricated on glass substrate by rf sputtering. They found that the 30 nm thick films, annealed at 350 ^oC with forming field of 100 Oe with different times had magnetic properties different from the 4 nm thick films of the same growth conditions. The 4 nm thick films showed coercivity lower than the 30 nm thick films. One drawback of this work was the lack of information about how the magnetostriction changed with these parameters. Cooke et al [35] studied the effect of the composition gradient from x=0.67 to x=0.40 on the magnetic properties of $Fe_xCo_{(1-x)}$ thin films prepared by rf sputtering. The magnetostriction constants were measured by two methods. The first method was strain based and the second one was an optical dynamic cantilever. They found that the coercive field of the as-deposited films with increasing Co at% composition reached the highest value at about 55at%. Also, they found that annealing reduced the coercivity of the films. For both methods, the magnetostriction constant increased with increasing the composition and the maximum value was 82 ppm for the strain method. Takashi et al [36] studied the influence of annealing on the magnetic properties and the magnetostriction constant of 240 nm thick $Fe_{32}Co_{68}$ thin films fabricated by sputtering system on glass substrates. They found that with increasing the annealing temperature from 673 K to 1073 K the saturation magnetostriction increased by a factor of three from 56 ppm to reach the maximum at 159 ppm with the presence of bcc (110) texture. However, increasing the annealing temperature more than 1093 K led to a decrease in the magnetostriction constant, which was associated with the formation of the fcc (111) phase. Cooke et al [37] studied the influence of three parameters (annealing temperature, substrate material, and the film

composition) on the structure and magnetic properties of magnetostrictive FeCo films with thickness 300 nm, fabricated by rf sputtering. They found that for all substrate types, the as-deposited films had hard magnetic properties and all films showed coercive field more than 10 kA m^{-1}; The annealed films, in H and Ar gases, showed a significant decrease in the coercivity to about 300Am^{-1}. They clarified that the decrease in the coercive field, could be due to a number of reasons, including relaxation of intrinsic stress, changing in texture, increase in the grain size, effect of the anisotropy constant, K as a result of the presence of short-range order of Fe or Co. Therefore, all of above issues impact the magnetic properties of the films. They found that the composition of films between 49% and 52% affected the coercivity with the lowest coercive field about 281 A m^{-1}. They noticed that the $Fe_{50}Co_{50}$ composition had the lowest coercivity, maximum anisotropy field, and largest saturation magnetostriction constant. Vopsaroiu et al [38] studied the effect of growth rate on the magnetic properties of CoFe films with thickness 20 nm, prepared by sputtering technique. They controlled the growth rate by changing the dc bias sputtering voltage. The films were grown from two different targets in composition $Co_{35}Fe_{65}$ and $Co_{60}Fe_{40}$. Two sets of films with different growth rate (0.1 and 0.8) were fabricated from the first target in composition of $Co_{35}Fe_{65}$ and another two set of films with different growth rate (0.1and 0.8) were grown from the second target in the composition of $Co_{60}Fe_{40}$. They found that for both sets of films, the slow growth rate produced a small grain size of about 10 nm while the fast growth rate produced an average grain size around 150 nm. From the XRD result, they found that the films had a bcc (110) structure. Magnetically, they found that the films with small grain size from both targets, with low growth rate, had in-plane magnetic anisotropy, and soft magnetic properties, while the films with large grain size from both targets, with high growth rate, had hard magnetic properties with coercive fields about 9549 A/m with a maximum magnetization about 1914 kA/m. One drawback of their work was the lack of the effect of either the growth rate or the grain size on the magnetostriction properties.

3.6 Magnetic Properties in Magnetostrictive Ribbons

After the discovery of amorphous magnetic materials, their structure, magnetic, and magnetostriction properties have been widely investigated because of their significant potential in technological applications such as: distribution and power transformers, high-frequency inductors, motors, low loss at low frequencies, current transformers, and devices requiring high permeability [39-41]. The structural investigation of amorphous magnetic material in ribbon form has shown that the magnetic properties and microstructure are

different from bulk form [42]. Two types of ribbons, FeGa and FeSiB, are discussed in this section, to compare their magnetic properties with this thesis study. For example, a massive magnetostriction of about -1300 ppm was observed in the $Fe_{85}Ga_{15}$ ribbons under external magnetic field along the length of ribbon [43]. Zhang et al [44] studied the effect of ribbon thickness on the microstructure and magnetostriction constant for the ribbon composition $Fe_{83}Ga_{17}$ prepared by melt-spinning in a range of thicknesses (45μm, 55μm, 75μm and 100μm). They found that the largest magnetostriction constant of about -2100 ppm was observed for the 75 μm ribbon. They found that the $D0_3$ structure was present in the ribbon as a result of faster cooling rate, but did not decrease the magnetostriction constant. They theorised that the increase in magnetostriction was due to presence of the short-range order of Ga atoms, which adjusted the $D0_3$ phase.

Liu et al [45] prepared, by melt-spinning, ribbons with the composition $Fe_{100-x}Ga_x$ ($15 \leq x \leq 30$) and studied their structural and magnetic properties. They detected, by XRD, the structure of all the ribbons, which included the disordered A2 phase structure. By applying a high magnetic field 1591.5 kA/m to measure the magnetostriction constant, they found that the largest magnetostriction constant was about -750 ppm for the composition range of $15 \leq x \leq 20$. While for composition of $x > 20$, there was a reduction in value of magnetostriction due to increase in Ga percentage. They found that the wheel speed influenced the structure and magnetic properties. They studied the effect of wheel speed on the magnetostriction of $Fe_{85}Ga_{15}$ ribbon and found that the magnetostriction decreased for the wheel speeds greater or lower than 12 m/s, which was also the best wheel speed for the $Fe_{80}Ga_{20}$ ribbon. They detected formation of Ga clusters due to the slow wheel speed and low cooling rate. From their work, it found that the magnetostriction constant was influenced by wheel speed and Ga content.

Zhang et al [46] prepared a melt-spun ribbon at different wheel speed from 8 to 30 m/s with the composition $Fe_{81}Ga_{19}$ and thickness range from 35 μm to 110 μm. They studied the influence of annealing temperature on the structural and magnetostrictive properties. From the XRD results, they found that the ribbons, at room temperature, showed disordered A2 phase. Also, they studied the influence of annealing temperature of 800 ^{o}C for 3 hours and slow cooled at 2 and 0.5 ^{o}C/min on 110 μm thick ribbons. They detected for the slow cooled (2˚C/min) ribbon $D0_3$ phase with peaks (311) and (200) confirming the Fe_3Ga structure was included with the disordered A2 structure. While they found decreasing the cooling rate to about 0.5˚C/min led to the ordered $L1_2$ Fe_3Ga structure presented with the disordered A2

structure. For the magnetostriction measurements, they studied the magnetostrictive properties along the ribbon length direction with composition of $Fe_{81}Ga_{19}$ and thickness 110 μm. They found that using a vertical magnetic field to the sample plane of about 1150 kA/m was enough to induce a negative magnetostriction constant of about -163 ppm while applying a parallel field of about 98 kA/m was enough to induce negative magnetostriction constant of about -21 ppm. They determined that the magnetostrictive properties of $Fe_{81}Ga_{19}$ ribbon can be affected by the heat treatment. For example, they observed a larger magnetostriction around -189 ppm in a quenched sample, which was reduced to -143 ppm for the slow cooled sample at 2˚C/min and -125 ppm for the sample slow cooled at 0.5˚C/min.

Magnetic properties and magnetostriction of amorphous FeSiB ribbons have also been studied and developed. For example, Sun X. et al [47] studied the magnetic properties of amorphous $Fe_{78}Si_9B_{13}$ ribbons with thickness at 25 μm, which were manufactured by the melt spinning method. They found that the annealing of the ribbons led to growing nanocrystalline Fe_2B and α-Fe (Si) phases. They observed that increasing the annealing temperature caused a decrease in the magnetization of the amorphous phase faster than the nanocrystalline phases present.

Brouha and Borst [48] studied the influence of the thermal treatment and in-plane applied magnetic field on the magneto-mechanical properties in three types of ribbons having different compositions, $Fe_{80}B_{10}Si_{10}$, $Fe_{80}B_{15}Si_5$, and $Fe_{80}B_{20}$. The ribbons were annealed at different temperatures for half an hour under an applied magnetic field of about 150 kA/m, within the in-plane direction of the ribbon's width. They found that for all the ribbons the annealing field led to an induced in-plane anisotropy field, which reached a maximum value in all the ribbons at the same annealing temperature of 250 ^oC. They found that the $Fe_{80}B_{10}Si_{10}$ ribbon had an effective magneto-mechanical factor in the range of about 0.4-0.55, while the $Fe_{80}B_{20}$ ribbon had a range of 0.5-0.6. Also, they found that the maximum value of the effective magneto-mechanical factor in composition $Fe_{80}B_{15}Si_5$ was about 0.86 under annealing magnetic field of 60 A/m and a temperature of 350 ^oC with annealing time of 30 minutes.

Tsuya and Arai [49] studied the effect of composition and annealing temperature on the magnetic and magnetostriction properties of crystalline structure ribbons with compositions $Fe_{100-x}Si_x$ and $Fe_xSi_yAl_z$ and amorphous structure ribbons with compositions $Fe_{100-x}B_x$ and $(Fe_{1-x}Co_x)_{78}Si_8B_{14}$. They found that the magnetostriction constants reach zero value for

ribbons with compositions of $Fe_{84.74}Si_{9.71}Al_{5.55}$ and $Fe_{92.5}Si_{7.5}$. Also, they found that the amorphous structure $Fe_{100-x}B_x$ ribbon had a larger magnetostriction constant of about 50 ppm at x=12% after heat treatment at 300 ^oC for 3 hours, which decreased with increasing of B%. While for this ribbon the magnetostriction constant at room temperature had a maximum peak value ≈ 42 ppm at B%=16. For the crystalline ribbon $Fe_{100-x}Si_x$, they found that the ribbon had a maximum magnetostriction constant value of ≈ 8 ppm at Si% = 3.6 and the magnetostriction decreased with increasing of Si% and reached zero at Si%= 7.5.

3.7 Magnetic Properties of Magnetostrictive Amorphous Films

Amorphous materials have a short range order structure and a random distribution of the atoms. Thus, they are missing magnetocrystalline anisotropy, grains, and grain boundaries, which lead to then having soft ferromagnetic properties. The magnetic properties of amorphous material are different from crystalline and polycrystalline materials.

3.7.1 Magnetic Properties of Magnetostrictive Amorphous FeSiB Films

In general, amorphous thin films are developed as they have importance in applications due to their soft magnetic properties. Kobliska et al [50] have stated that the amorphous thin films fabricated by sputtering have similar magnetic properties to the ribbons, which were formed by a rapid quench from their melting points. Therefore, many efforts have been carried out to develop and study the structure, magnetic, and magnetostrictive properties of amorphous FeSiB thin films.

Naoe et al [51] studied amorphous FeSiB thin films fabricated by co-sputtering at room temperature and the effect of annealing temperature on magnetic properties such as the magnetization, coercive field, and permeability. They found that the annealing of the films up to 470 ^oC did not change the magnetization of films. The permeability of the films changed from 850 to 3000 when the films were annealed at 450 ^oC, while the coercive field was changed from 5 to 0.6 Oe when the films were annealed at over 370 ^oC. For the saturation magnetostriction constant, they found that most of the films had a value of ~30 ppm.

In many studies, they found that some of the amorphous films can contain a nanocrystalline phase within the films' amorphous matrix. This phase can affect the magnetic properties of the amorphous films both positively and negatively. For example, Sun et al [52] used the rf sputtering technique to fabricate partial amorphous thin films with the composition $Fe_{78}Si_{10}B_{12}$ containing nanocrystalline α-Fe(Si). These films had a magnetostriction constant

of about 6.5 ppm. The films were annealed for 1 hour at about 540 ^{o}C. This annealing process increased the percentage of α-Fe (Si) within the film, which led to a decrease in the magnetostriction constant to 0.45 ppm because the nanocrystalline α-Fe (Si) had negative magnetostrictive properties. Also, Coïsson et al [53] studied the magnetic properties of FeSiB thin films prepared by rf sputtering using a $Fe_{78}Si_{13}B_9$ target to fabricate films with thickness 80 nm and 305 nm. The XRD results showed that the films were partially amorphous and the crystalline fraction increased with thickness. The other technique that can be used to fabricate amorphous FeSiB thin films is evaporation, for example, Neagu et al [54] fabricated amorphous FeSiB thin films with different thicknesses from 100 to 300 nm by evaporating ribbon with the composition $Fe_{77.5}Si_{7.5}B_{15}$ under vacuum. They used MOKE magnetometry to study the surface magnetic properties of these films. They found that annealing the films under magnetic field reduced the coercive field from 350 A/m to 18 A/m because the structure relaxed. Also, fabrication of not fully amorphous FeSiB thin films using the thermal evaporator was done by Satalkar et al [55]. They deposited three films with thicknesses (110, 160, and 170nm) from evaporated amorphous ribbon with composition $Fe_{79}Si_8B_{13}$. From the XRD results, they found that the amorphous matrix had a nanocrystalline phase of α-Fe in the range from 30-34 nm. The phenomenon of spin reorientation transition, which is detected in ultrathin multilayer magnetic films, can be observed in amorphous thin films such as FeSiB.

Coïsson et al [56] detected the phenomenon of spin reorientation transition in amorphous FeSiB thin films and found that it could be affected by the films' thickness and the thermal treatment temperature. The films were fabricated in a range of thicknesses 25-600 nm by rf sputtering from a Fe_{78} Si_9 B_{13} target. The samples were annealed for about 60 min in a range of temperatures from 200 to 375 ^{o}C. A phase change in amorphous FeSiB thin films during the annealing is produced by increasing the annealing temperature. Study of the growth of nanocrystalline phases in amorphous FeSiB thin films due to increasing the annealing temperature was done by Jang et al [57]. They deposited amorphous FeSiB thin films by DC magnetron sputtering from amorphous $Fe_{84}Si_6B_{10}$ ribbons. The XRD results before the annealing showed that the films were amorphous and after annealing the α-Fe phase started to grow when the temperature reached 723 K. Annealing the films for 1 h at a temperature of about 823 K led to an observed crystalline α-(Fe, Si) phase, while the Fe_2B phase was not formed because its activation energy was higher than the α-(Fe, Si) crystalline phases [58], [59].

3.7.2 Magnetic Properties of Magnetostrictive Amorphous FeGaB Films.

Addition of metalloid elements such as boron into soft magnetic thin films such as FeGa and FeCo can affect the structure, magnetic and magnetostrictive properties. For example, Xuexu et al [60] found that the addition of 1% boron into polycrystalline $Fe_{83}Ga_{17}$ alloy, led to an increase in the magnitude of the magnetostriction constant from 42ppm to 50 ppm, and increased the saturation magnetic field by about 3 time compare with $Fe_{83}Ga_{17}$ binary alloy. The effect of boron on the structural properties was to produce three peaks in the XRD pattern, with the A2 phase of bcc Fe (Ga) as a major phase and one peak for Fe_2B phase, which appear in the result of $(Fe_{83}Ga_{17})_{99}B_1$ alloy.

Lou et al [61] found that increasing the boron percentage from 0 to 21 during fabrication of FeGaB films led to the formation of an amorphous structure and the absence of a polycrystalline structure when the percentage of B was more than 9%. While for the B percentage from 0 to 6.5, a broad bcc (100) peak was observed. This work included changing the Ga from 9–17%, hence there were changes in the Ga:Fe ratio from the target composition of $Fe_{80}Ga_{20}$ but they did not discuss the effect of changing the Ga:Fe ratio in their work. It was found that the saturation magnetization decreased with increasing of Boron, the film had coercivity about 1 Oe when B content ≥ 9 at. % and reduced to 0.4 Oe for B content 21 at. %. Also, the anisotropy field, H_k, reduced dramatically from 120 to 30 Oe when B content of 9 at. % and reaches 15 Oe at B content 21 at. %. while the result of the magnetostriction showed that the films had a peak magnetostriction constant of 70 ppm at 12% of Boron. From the explanation of Clark et al [62], a minimum amount of metalloid atoms may be causing Ga-Ga pair atoms or B-B pair atoms to form, which can affect the magnetostriction properties and the maximum amount of these atomic pairs can produce clusters leading to a reduction in the magnetostriction properties. Cristina et al [63] worked to improve the magnetostriction properties of $Fe_{72}Ga_{28}$ alloys by adding amounts of boron (0.5. 1. 1.5, and 2 at %) to produce FeGaB alloys. The structural investigation showed that all the samples had Fe_2B phase along with the expected FeGa DO_3 and A2 phases. They found that adding the boron to the $Fe_{72}Ga_{28}$ alloy in 1 at% improved the magnetostriction constant to reach a maximum value 92 ppm, which was 2.2 times higher than the sample without boron.

3.7.3 Magnetic Properties of Magnetostrictive Amorphous FeB Films

The binary system of amorphous FeB thin films has been studied to understand the effect of adding boron to the magnetic properties of Fe. For example, Aboaf and Klokholm [64] studied the effect of adding boron on the structural and magnetic properties of FeB films and compared the results for amorphous and crystalline FeB structures. They found that as the structure transitioned from crystalline to amorphous, the magnetostriction was discontinuous with increasing boron percentage. The results showed that the value of magnetostriction in the amorphous structure was 2 times larger than the crystalline value, the magnetostriction then reduced when large amounts > 25 at% of boron were added. The maximum positive magnetostriction value reached was about 50.3 ppm at the boron percentage of 25 at% and then dropped with increasing boron amount greater than 25 at%. The films had perpendicular magnetic anisotropy with low coercive field of about 0.2 Oe after annealing at 300°C. After annealing the films between 400 and 450°C, they found that the coercive field increased quickly because the structure changed from amorphous to crystalline.

Aboaf et al [65] prepared different amorphous thin films by the rf sputtering technique. One of these films was FeB fabricated with a boron content range from 0 to 40 at %. The films had an amorphous structure when the boron content was about 26 at%. Unfortunately, they did not present the magnetic and magnetostriction data of the FeB films, but they did present the magnetic properties of amorphous FeSi films which had discontinuous magnetostriction when the amount of Si was about 26 at%. The films reached the maximum magnetostriction value of about 29 ppm and then decreased with the addition of more Si. They also found that the crystalline structure of these films was created between 180 and 250 ^{o}C.

Kobliska et al [50] fabricated many amorphous magnetic thin films with thickness range from 0.3 to 0.5 μm. The films were grown at room temperature using the sputtering technique. They studied the magnetic and magnetostriction properties for the films and they found that a field of about 500 Oe was enough to saturate the films, which had a perpendicular anisotropy. This anisotropy was removed when the films were annealed at 250 °C for 1 hour; the annealing was needed to achieve a very low coercive field. The amorphous FeB films showed larger magnetostriction constant compared with the other films. For example, the film with composition $Fe_{73}B_{27}$ had a maximum magnetostriction constant of about 50 ppm, which was larger than the amorphous $Fe_{73}Si_6B_{21}$ and $Fe_{62}Si_{19}B_{19}$ films. The coercive field of FeB thin films was slightly lower than amorphous FeSiB thin films.

Chien and Unruh [66] fabricated crystalline and amorphous FeB thin films by sputtering two different composition targets (amorphous FeB and crystalline FeB) and compared the result of the two structures. Kawai et al [67] studied the influence of film thickness on the magnetostriction constant of Fe and $Fe_{98}B_2$ thin films relative to the strain within the films. The study showed that the magnetostriction constant changed from negative to positive i.e. from -4 ppm to +3 ppm when the thickness was reduced from 40 to 10 nm. They considered that changing the saturation magnetostriction constant from negative to be positive was due to the effect of the strain within the films when the thickness was between 10 and 20 nm. Tsunashima et al [68] fabricated two different types of amorphous films FeB and CoFeB by sputtering technique with thicknesses ranging from 1 μm to 1.2 μm and with fixed boron concentration at 20 at%. For the FeB films, they found that the magnetic anisotropy of the films decreased after annealing the film at 300 ^{o}C for 1 hour under rotating field. The effect of annealing on the FeB films was to produce inhomogeneous anisotropy and low permeability, while the coercive field of the FeB films which was 0.5 Oe decreased after annealing.

Table 3.1 Summary of magnetostriction constant of some materiasls presented in the literature review.

Material	Thickness	λ_s (ppm)	Direction	Form	Notes	Refrences
$Fe_{76.2}$ $Ga_{23.8}$	146.5 nm	147	110	Film		Basantkumar et al [14]
Fe_{68} Ga_{32}	500 nm	74	100	Film		Hattrick-Simpers et al [23]
Fe_{81} G_{19}	---------	265	100	Bulk		Clark et al [6]
$Fe_{76}Ga_{24}$	50 nm	17	110	Film		Morley et al [24]
$Fe_{77.5}$ $Ga_{22.5}$	75 nm	75	110	Film	Forming field (65 kA m^{-1})	Morley et al [25]
$Fe_{86.4}Ga_{13.6}$	50 nm	31	110	Film	Forming field (65 kA m^{-1})	Javed et al [26]
Fe_{77} Ga_{23}	50 nm	60	110	Film		Javed et al [27]
Fe_{76} Ga_{24}	50 nm	85	110	Film		Javed et al [28]
$Fe_{80}Ga_{20}$	100 nm	80	110	Film		Javed et al [29]
$Fe_{72.5}Ga_{27.5}$	50 nm	60	110	Film	as-deposited	Szumiata [30]
$Fe_{50}Co_{50}$	10-100 nm	11	110	Film	Room temperature	Morley et al [33]
$Fe_{35}Co_{65}$	300 nm	82	--------	Film		Cooke et al [35]
$Fe_{32}Co_{68}$	240 nm	159	110	Film	Annealing (673-1073) K	Takashi et al [36]
$Fe_{50}Co_{50}$	300 nm	70	110	Film	as-deposited	Cooke et al [37]
$Fe_{85}Ga_{15}$	50 µm	-1300	Amorphous	Ribbon		G. D. Liu et al [43]
$Fe_{83}Ga_{17}$	75 µm	-2100	Amorphous	Ribbon		Zhang et al [44]
$Fe_{80}Ga_{20}$	40–50 µm	-750	Amorphous	Ribbon		Liu et al [45]
$Fe_{81}Ga_{19}$	110 µm	-189	Amorphous	Ribbon	Quenched process	Zhang et al [46]
$Fe_{88}B_{12}$	40 µm	50	Amorphous	Ribbon	Heat treatment at 300 °C for 3 h	Tsuya and Arai [49]
FeSiB	1–2 µm	30	Amorphous	Film		Naoe et al [51]
$Fe_{78}Si_{10}B_{12}$	100 nm	6.5	Amorphous	Film	Contains α-Fe (Si)	Sun et al [52]
$(Fe_{83}Ga_{17})_{99}B_1$	---------	50	--------	Bulk		Xuexu et al [60]
FeGaB	100 nm	70	Amorphous	Film	12% of Boron	Lou et al [61]
$Fe_{0.72}Ga_{0.28})_{99}B_1$	---------	92	---------	Bulk	Fe_2B phase	Cristina et al [63]
$Fe_{75}B_{25}$	---------	50.3	----------	Film		Aboaf and Klokholm [64]
$Fe_{74}Si_{26}$		29		Film		Aboaf et al [65]
$Fe_{73}B_{27}$	0.3-0.5 µm	50	Amorphous	Film		Kobliska et al [50]
$Fe_{98}B_2$	10 nm	3	110	Film		Kawai et al [67]

3.8 Mechanical Properties of Magnetostrictive Materials

The nanoindentation method is the most common methods to measure the mechanical properties such as hardness and modulus of bulk alloy, ribbon, and film or coating. It involves creating a very small indentation in the surface of the film, usually achieved by a Berkovich indenter. There is little information and investigations presented on the mechanical properties of magnetostrictive Fe-based amorphous thin films. The mechanical properties of bulk/ribbon magnetostrictive Fe-based amorphous alloys have been studied.

Lashgari et al [69] investigated the mechanical properties of amorphous $Fe_{80.75}Si_8B_{11.25}$ alloy prepared by melt- spinning. Three specimens were prepared (amorphous specimen, stress-relaxed specimen (400 °C for 0.5 h), and annealed specimen (500 °C for 1h). The polishing of the specimen surface was necessary to get a 0.04 μm surface roughness for nanoindentation measurements. TriboIndenter and UMIS devices were used with a Berkovich tip. They used an applied load 8 mN in the case of TriboIndenter and 10–90 mN in the case of UMIS device. In their study a single loading and multiple unloading–reloading investigations were undertaken. To prevent the effect of the indentations on each other, they set a distance between indentations of about 20 μm. For each specimen, they took the average of the data for 20 indents.

They found that in the single-step nanoindentation method, the heat treatment at 500 °C for 1 h reduced the displacement of the amorphous specimen from a maximum value ≈178.58 nm to ≈159.45 nm. While the heat treatment at 500 °C for 1 h increased the hardness from 10 GPa to ≈11.2 GPa and the reduced elastic modulus from ≈160 GPa to ≈238 GPa. Additional annealing times of about 3 h reduced both values of the hardness and reduced elastic modulus to ≈8.8 GPa and ≈200 GPa respectively.

For the multi-step method, which used different cycles (3, 5, 8, 10), they found in the amorphous specimen there was a small increase in the hardness, while the reduced modulus was unchanged. They found that the stress-relaxed specimen showed softer properties, for example, they found the maximum value of penetration was higher in comparison with the single-step method. While for the amorphous specimen, the maximum value of penetration found in the single-step method was slightly bigger than the multi-step method.

From their result, they mentioned that in the crystalline specimen due to the heat treatment, the decreasing value of the maximum penetration represents a higher hardness in the case of the multi-step method. This decrease in penetration depth was presented as a result of the

strain-hardening response. Also, they found that this strain-hardening reaction presented in crystalline specimen was extremely different compared with both the amorphous and stress-relaxed specimens. Further, they explained that in the crystalline specimen, the behaviour of hardening is due to the entanglement and interaction of dislocations with each other and also due to grain boundaries which lead to increasing the hardness.

Lashgari et al [70] studied the effect of the presence of Cu and annealing temperature on the mechanical properties of three types of Fe-based alloy ribbons in compositions $Fe_{80.75}Si_8B_{11.25}$ (specimen 1), $Fe_{85.2}Si_{0.9}B_{12.62}Cu_{1.28}$ (specimen 2), and $Fe_{78.6}Si_{1.8}B_{17.75}Cu_{1.85}$ (specimen 3) prepared by the melt-spinning method.

Nanoindentation technique type UMIS device with a pyramid Berkovich tip was used with a range of loads (10-90 mN) at increments of 20 mN at room temperature. To avoid the creep effect, three seconds were enough to hold the indenter at the peak load. Also to avoid the effect of indentations on each other, the distance between them was about 20 mm. Their results were averaged at about 75 for each sample. In a diamond solution, the samples were polished to 1 μm surface roughness. They studied the effect of indentation load on the hardness and reduced modulus.

They found, in all three types of amorphous alloy specimens, the hardness and reduced modulus reduced with the increase in the load from 10 to 70 mN and further loading > 70 mN did not noticeably affect the variables. The reduction of the hardness in $Fe_{80.75}Si_8B_{11.25}$ alloy was 7.6%, which was harder than the others, while the hardness of the alloys $Fe_{85.2}Si_{0.9}B_{12.62}Cu_{1.28}$, and $Fe_{78.6}Si_{1.8}B_{17.75}Cu_{1.85}$, reduced by 25.3% and 23.3% respectively. Also, they found the elastic modulus of the $Fe_{80.75}Si_8B_{11.25}$ alloy in amorphous structure was greater than both $Fe_{85.2}Si_{0.9}B_{12.62}Cu_{1.28}$, and $Fe_{78.6}Si_{1.8}B_{17.75}Cu_{1.85}$ alloys. After annealing the samples, they found that the hardness and elastic modulus were larger than the as-fabricated amorphous samples. They found the heat treatment for 1 h of $Fe_{80.75}Si_8B_{11.25}$ alloy at 500 ^oC improved the hardness and elastic modulus in percentages of 35 and 40 respectively. Also, the heat treatment for 1 h of $Fe_{85.2}Si_{0.9}B_{12.62}Cu_{1.28}$ alloy at 470 ^oC improved the hardness (61%) and reduced modulus (141%). While the heat treatment for 1 h of $Fe_{78.6}Si_{1.8}B_{17.75}Cu_{1.85}$ alloy at 460 ^oC caused an increase in the hardness (42%) and elastic modulus (90%).

Chan et al [71] studied the effect of both the thickness and the surface properties of the substrate on the mechanical properties (hardness, elastic modulus, and yield strength) of magnetostrictive FeCo thin films. The films with thickness 0.9, 1, 4, and 4.1 μm were deposited on either Si with thicknesses 2 and 7 μm or Ti–6Al–4V substrate with dimensions 19x19 mm and thickness 6.4 mm. The Ti–6Al–4V substrates were manufactured by electrical

discharge machining (EDM) method. Two Ti–6Al–4V substrates without polishing were used for FeCo films with thicknesses 0.9 µm and 4.1 µm.

Two mechanically polished Ti–6Al–4V substrates were used for FeCo films with thicknesses 1 µm and 4 µm. Two electro-polished Ti–6Al–4V substrates were used for FeCo films with thicknesses 0.9 and 4.1 µm. NanoIndenter technique with a diamond Berkovich tip were used to measure the mechanical properties of these films. They set the surface approach velocity at 5 nm per second and the limitation of indentation depth was 2000 nm. For all the samples, they used an array of 5 indents with a spacing of 3 – 4 mm.

They analyzed the result by MTS® data software, which follows the method of Giannakopoulos and Suresh [72] to measure the yield strength, σ_{ys}.

They found that the hardness, Young's Modulus, and yield strength of FeCo films of different thicknesses and substrates as summarized in the table (3.1):

Table 3.2 summarize the results of Chan et al [71] work.

Film/substrate	Polishing	Thickness (µm)	Hardness (GPa)	Young's Modulus (GPa)	yield strength (MPa)
FeCo/Si	______	2	5.5	165.5	1830
FeCo/Si	______	7	5.4	170	1800
FeCo/Ti-6Al-4V	______	0.9	10.4	164.8	3470
FeCo/Ti-6Al-4V	______	4.1	8.7	206.1	2830
FeCo/Ti-6Al-4V	mechanical	1	8.8	187.3	2930
FeCo/Ti-6Al-4V	mechanical	4	8.2	176	2730
FeCo/Ti-6Al-4V	electro	0.9	10.7	167.7	3570
FeCo/Ti-6Al-4V	electro	4.1	8.5	201.4	2900

They measured the mechanical properties of FeCo/Si and FeCo/ Ti–6Al–4V films, which are good data for magnetostriction FeCo films, but they did not discuss the effect of thickness and the substrate surface on these properties and they focused on the effect of thickness and substrate surface on the interface toughness of the FeCo/Ti–6Al–4V samples.

Jen et al [73] studied the mechanical properties such as Young's modulus, E_s and hardness, H_r of magnetostrictive $Fe_{81-x}Co_xGa_{19}$ films where x is in the range 0, 3, 7, 11, 15, and 19. The films were grown by the dc magnetron sputtering technique with thickness 2500 Å. They

used a nanoindenter to measure the Young's modulus and hardness. They found that both of E_s and H_r of the $Fe_{81-x}Co_xGa_{19}$ films were affected by increasing the percentage of *x*.

They found the Young's modulus reduced from 130 GPa, at x =0, to 115 GPa, at x =7 at%, and after that increased from 115 GPa to 145 GPa, at x = 19 at%. While the hardness increased from 6.5 GPa, at x =0 to 7.5 GPa, at x = 7 at%, and after that decreased from 7.5 GPa to 5.7 GPa, at x =19 at%. Further, they reported that the film with composition $Fe_{62}Co_{19}Ga_{19}$ showed the optimum properties from all the FeCoGa samples investigated.

3.9 References

[1] M.R. Gibbs, Physica Scripta, Vol. T45, 115-119,1992.

[2] M.R.J. Gibbs, R. Watts, W.J. Karl, A.L. Powell, and R.B. Yates, *Sensors Actuators* A, 59, 229, 1997.

[3] H. Chiriac, M. Pletea and E. Hristoforou, *Sensors Actuator*, 81,166-169, 2000.

[4] A.G. Olabi, A. Grunwald, Materials and Design, vol. 29, p. 469–483, 2008.

[5] T. Honda, K. I. Arai, and M. Yamaguchi, *J. Appl. Phys*., vol. 76, no. 10, pp. 6994–6999, 1994.

[6] A. E. Clark, K. B. Hathaway, M. Wun-Fogle, J. B. Restorff, T. A. Lograsso, V. M. Keppens, G. Petculescu, and R. A. Taylor, *J. Appl. Phys*., vol. 93, no. 10 3, pp. 8621–8623, 2003.

[7] P. T. Squire, *Meas. Sci. Technol*., vol. 5, no. 2, pp. 67–81, 1994.

[8] N. B. Ekreem, A. G. Olabi, T. Prescott, A. Rafferty, and M. S. J. Hashmi, *J. Mater. Process. Technol.*, vol. 191, no. 1–3, pp. 96–101, 2007.

[9] N. Tsuya, K. I. Arai, K. Ohmori, and Y. Shiraga, Jpn. *J. Appl. Phys*., vol. 13, no. 11, pp. 1808–1810, 1974.

[10] M. S. Boley, W. C. Shin, D. K. Rigsbee, and D. A. Franklin, *J. Appl. Phys*., vol. 91, no. 101, pp. 8210–8212, 2002.

[11] R. R. Birss, G. J. Keeler, P. Pearson, and R. J. Potton, *J. Phys. E: Sci. Instrum*., vol. 11, no. 11, 1978.

[12] J. Heremans, J. P. Michenaud, Y. Iye, N. Miura, G. Kido, K. Nakamura, and S. Tanuma, *J. Phys. E*., vol. 16, no. 5, pp. 382–386, 1983.

[13] S. Kanagaraj and S. Pattanayak, *Cryogenics*, vol. 43, no. 7, pp. 399–424, 2003.

[14] R. R. Basantkumar, B. J. Hills Stadler, W. P. Robbins, and E. M. Summers, *IEEE Trans. Magn.*, vol. 42, no. 10, 2006.

[15] H. Samata, Y. Nagata, T. Uchida, and S. Abe, *J. Magn. Magn. Mater*., vol. 212, no. 3, pp. 355–360, 2000.

[16] K. Narita, J. Yamasaki, and H. Fukunaga, *IEEE Trans. Magn.*, vol. 16, no. 2, pp. 435–439, 1980.

[17] J. C. M. Henning and J. H. den Boef, *Appl. Phys*., vol. 16, no. 4, pp. 353–357, 1978.

[18] M. D. Cooke, thesis, Department of Physics and Astronomy, University of Sheffield, UK, 2000.

[19] O. Ikeda, R. Kainuma, I. Ohnuma, K. Fukamichi, and K. Ishida, *Journal of Alloys and Compounds,* 347, 198, 2002.

[20] Himalay Basumatary, Mithun Palit, J. Arout Chelvane, S. Pandian, M. Manivel Rajaand V. Chandrasekaran, Scripta Materialia 59, 878–881, 2008.

[21] G. Petculescu, K. L. Ledet, M. Huang, T. A. Lograsso, Y. N. Zhang, R. Q. Wu, M. Wun- Fogle, J. B. Restorff, A. E.Clark, and K. B. Hathaway, Journal of Applied Physics 109, 07A904, 2011.

[22] R. A. Dunlap, N. C. Deschamps, R. E. Mar, and S. P. Farrell, *J. Phys. Condens. Matter*, vol. 18, no. 20, pp. 4907–4920, 2006.

[23] J. R. Hattrick-Simpers, D. Hunter, C. M. Craciunescu, K. S. Jang, M. Murakami, J. Cullen, M. Wuttig, I. Takeuchi, S. E. Lofland, L. Benderksy, N. Woo, R. B. Van Dover, T. Takahashi, and Y. Furuya, *Appl. Phys. Lett.*, vol. 93, no. 10, pp. 10–13, 2008.

[24] N. A. Morley, S. L. Yeh, S. Rigby, A. Javed, and M. R. J. Gibbs, *J. Vac. Sci. Technol. A*, vol. 26, no. 4, pp. 581–586, 2008.

[25] N. A. Morley, A. Javed, and M. R. J. Gibbs, *J. Appl. Phys.*, vol. 105, no. 7, pp. 9–12, 2009.

[26] A. Javed, N. A. Morley, T. Szumiata, and M. R. J. Gibbs, *Appl. Surf. Sci.*, vol. 257, no. 14, pp. 5977–5983, 2011.

[27] A. Javed, N. A. Morley, and M. R. J. Gibbs, *J. Magn. Magn. Mater.*, vol. 321, no. 18, pp. 2877–2882, 2009.

[28] A. Javed, T. Szumiata, N. A. Morley, and M. R. J. Gibbs, *Acta Mater.*, vol. 58, no. 11, pp. 4003–4011, 2010.

[29] A. Javed, N. a. Morley, and M. R. J. Gibbs, *J. Appl. Phys.*, vol. 107, no. 9, p. 09A944, 2010.

[30] T. Szumiata, B. Górka, K. Brzózka, M. Gawroński, M. Gzik-Szumiata, A. Javed, N. A. Morley, and M. R. J. Gibbs, *Nukleonika*, vol. 58, no. 1, pp. 27–30, 2013.

[31] L. C. Wang, H. J. Hatton, M. D. Cooke, M. R. J. Gibbs, W. M. Rainforth, and C. J. D. Hetherington, *J. Appl. Phys.*, vol. 89, no. 11 II, pp. 7511–7513, 2001.

[32] R. C. Hall, *J. Appl. Phys.*, vol. 157, no. 5, pp. 199–201, 1960.

[33] N. A. Morley, S. Rigby, M. R. J. Gibbs, *J. Opto. and Advan.Mater.*, vol. 1, no. 2, pp. 109–113, 2009.

[34] M. Coïsson, F. Celegato, P. Tiberto, and F. Vinai, *J. Magn. Magn. Mater.*, vol. 320, no. 20, pp. 739–742, 2008.

[35] M. D. Cooke, M. R. J. Gibbs, and R. F. Pettifer, *J. Magn. Magn. Mater*., vol. 237, no. 2, pp. 175–180, 2001.

[36] T. Nakajima, T. Takeuchi, I. Yuito, K. Kato, M. Saito, K. Abe, T. Sasaki, T. Sekiguchi, and S. Yamaura, *Mater. Trans.*, vol. 55, no. 3, pp. 556–560, 2014.

[37] M. D. Cooke, L.-C. Wang, R. Watts, R. Zuberek, G. Heydon, W. M. Rainforth, and G. A. Gehring, J. Phys. D. Appl. Phys., vol. 3333, no. 3300, pp. 1450–1459, 2000.

[38] M. Vopsaroiu, K. O'Grady, M. T. Georgieva, P. J. Grundy, and M. J. Thwaites, *IEEE Trans. Magn.*, vol. 41, no. 10, pp. 3253–3255, 2005.

[39] S. Atalay, N. Bayri, T. Izgi, F. E. Atalay, and V. S. Kolat, *Sensors Actuators A: Phys*., vol. 158, no. 1, pp. 37–42, 2010.

[40] C. Manassis, D. Bargiotas, and V. Karagiannis, *Sensors Actuators A: Phys*., vol. 106, no. 1–3, pp. 30–33, 2003.

[41] M. M. Trexler and N. N. Thadhani, *Prog. Mater. Sci*., vol. 55, no. 8, pp. 759–839, 2010.

[42] O. Životský, A. Hendrych, L. Klimša, Y. Jirásková, J. Buršík, J. A. M. Gómez, and D. Janičkovič, *J. Magn. Magn. Mater*., vol. 324, no. 4, pp. 569–577, 2012.

[43] G. D. Liu, L. B. Liu, Z. H. Liu, M. Zhang, J. L. Chen, J. Q. Li, G. H. Wu, Y. X. Li, J. P. Qu, and T. S. Chin, *Appl. Phys. Lett*., vol. 84, no. 12, pp. 2124–2126, 2004.

[44] M. C. Zhang, H. L. Jiang, X. X. Gao, J. Zhu, and S. Z. Zhou, *J. Appl. Phys*., vol. 99, no. 2, p. 23903, 2006.

[45] G. D. Liu, X. F. Dai, Z. H. Liu, J. L. Chen, and G. H. Wu, *J. Appl. Phys.*, vol. 99, no. 9, 2006.

[46] J. Zhang, T. Ma, and M. Yan, *Phys. B Condens. Matter,* vol. 404, no. 21, pp. 4155–4158, 2009.

[47] X. Sun, A. Cabral-Prieto, M. Jose Yacaman, J. Reyes-Gasga, R. Hernandez-Reyes, A. Morales, and W. Sun, *Phys. B Condens. Matter*, vol. 291, no. 1–2, pp. 173–179, 2000.

[48] M. Brouha and J. Van Der Borst, *J. Appl. Phys*., vol. 50, no. B11, pp. 7594–7596, 1979.

[49] N. Tsuya and K. I. Arai, *J. Appl. Phys*., vol. 50, no. B3, pp. 1658–1663, 1979.

[50] R. J. Kobliska, J. A. Aboaf, A. Gangulee, J. J. Cuomo, and E. Klokholm, *Appl. Phys. Lett*, vol.33,5 p. 473, 1978.

[51] M. Naoe, H. Yamamoto, and S. Yamanaka, *J. Appl. Phys.,* vol. 50, p. 7606, 1979.

[52] Z. G. Sun, H. Kuramochi, M. Mizuguchi, F. Takano, Y. Semba, and H. Akinaga, *J. Magn. Magn. Mater.*, vol. 272–276, pp. 1160–1161, 2004.

[53] M. Coïsson, C. Appino, F. Celegato, A. Magni, P. Tiberto, and F. Vinai, *Phys. Rev.,* vol. 77, no. 21, pp. 1–11, 2008.

[54] M. Neagu, M. Dobromir, G. Popa, H. Chiriac, G. Singurel, and C. Hison, *Sensors Actuators, A Phys.*, vol. 129, no. 1–2, pp. 172–175, 2006.

[55] M. Satalkar, S. N. Kane, A. Pasko, A. Apolinário, C. T. Sousa, J. Ventura, J. J. Belo, J. M. Teixeira, J. P. Araujo, F. Mazaleyrat, and E. Fleury, *AIP Conf. Proc.*, vol. 1512, pp. 654–655, 2013.

[56] M. Coïsson, F. Vinai, P. Tiberto, and F. Celegato, *J. Magn. Magn. Mater.*, vol. 321, no. 7, pp. 806–809, 2009.

[57] T. S. Jang, D. H. Lee, J. W.Hong, J. W. Park, *Journal of Magnetics,* vol. 10, no. 4, pp. 145–148, 2005.

[58] X. D. Liu, K. Lu, B. Z. Ding, and Z. Q. Hu, *Mater. Sci. Eng. A*, vol. 179–180, P, pp. 386–389, 1994.

[59] Z. Lai, H. Conrad, G. Teng, and Y. Chao, *Mater. Sci. Eng. A,* vol. 287, no. 2, pp. 238–247, 2000.

[60] X. Gao, J. Li, J. Zhu, J. Li, and M. Zhang, *Mater. Trans.*, vol. 50, no. 8, pp. 1959–1963, 2009.

[61] J. Lou, R. E. Insignares, Z. Cai, K. S. Ziemer, M. Liu, and N. X. Sun, *Appl. Phys. Lett.*, vol. 91, no. 18, pp. 10–13, 2007.

[62] A. E. Clark, M. Wun-Fogle, J. B. Restorff, T. A. Lograsso, and J. R. Cullen, *IEEE Trans. Magn.*, vol. 37, no. 4, pp. 2678–2680, 2001.

[63] C. Bormio-Nunes, C. Teodoro Dos Santos, I. Fernandes Leandro, R. Sato Turtelli, R. Grssinger, and M. Atif, *J. Appl. Phys.*, vol. 109, no. 7, pp. 2009–2012, 2011.

[64] J. A. Aboaf and Klokholm E., *J. Magn. Magn. Mater.*, vol. 18, pp. 1385–1386, 1980.

[65] J. Aboaf, R.J. Kobliska, *IEEE Trans.Magn.*, vol. 14, no. 5, pp. 941–943, 1978.

[66] C. I. Chien. and K. M. Unruh, *Phys. Rev. B,* vol. 29, no. 1, 1984.

[67] T. Kawai, S. Ouchi, M. Ohtake, and M. Futamoto, *IEEE Trans. Magn.*, vol. 48, no. 4, pp. 1585–1588, 2012.

[68] Y. M. and S. U. S. Tsunashima, IEEE Trans. Magn., vol. MAG-17, no. 6, pp. 3314–3316, 1981.

[69] H. R. Lashgari, J. M. Cadogan, D. Chu, and S. Li, *Mater. Des.*, vol. 92, pp. 919–931, 2016.

[70] H. R. Lashgari, Z. Chen, X. Z. Liao, D. Chu, M. Ferry, and S. Li, *Mater. Sci. Eng. A*, vol. 626, pp. 480–499, 2015.

[71] K. S. Chan, H. Ji, X. Wang, S. J. Hudak, and B. R. Lanning, *Mater. Sci. Eng. A*, vol. 422, no. 1–2, pp. 298–308, 2006.

[72] A. E. Giannakopoulos and S. Suresh, Scripta Materialia, Vol. 40, No. 10, pp. 1191–1198, 1999.

[73] S. U. Jen, T. L. Tsai, P. C. Kuo, W. L. Chi, and W. C. Cheng, *J. Appl. Phys.*, vol. 107, no. 1, 2010.

Chapter 4 Experimental Techniques

This chapter describes the main experimental techniques used in this study, which involves four main sections. First is a brief description of the common thin film fabrication techniques and the growth mechanism. Second is a brief description of the co-sputtering-evaporation technique, which is used to fabricate the magnetostrictive amorphous FeSiB and FeGaSiB thin films, and describes in details the growth of FeSiB and FeGaSiB films under different growth parameters. The third part includes the sample preparation. In the fourth part of this chapter, the experimental characterization techniques used to determine the structure, film composition, magnetic properties, magnetostriction constant, and mechanical properties are described. The characterization techniques used include X-Ray Diffraction (XRD), X-ray photoelectron spectroscopy (XPS), Magneto-Optical Kerr Effect (MOKE) magnetometer, vibrating sample magnetometer, and nanoindentation technique. Also, this chapter includes a brief description of the Villari effect method which used to measure the magnetostriction in this study.

4.1 Thin Film Fabrication Techniques

In general, there are several fabrication techniques designed for the growth of thin films. The technique used depends on the requirements of the application for the sample and the behaviour of the source material to be used. These techniques have some limitations, including the size of the substrate, low melting point materials, and the nature of the target. The fabrication of thin films can be categorized into two classes: the first class is the Physical Vapour Deposition (PVD) technique and the second class is the Chemical Vapour Deposition (CVD) technique.

For PVD techniques, the basic fabrication of the thin films is by the physical transportation of atoms directly from a source material (target) to the substrate in a gas phase. The PVD techniques can be classified in the block diagram as seen in **Fig. 4.1.**

Qayes A. Abbas, 2018 & Email: qayes.a.abbas@gmail.com

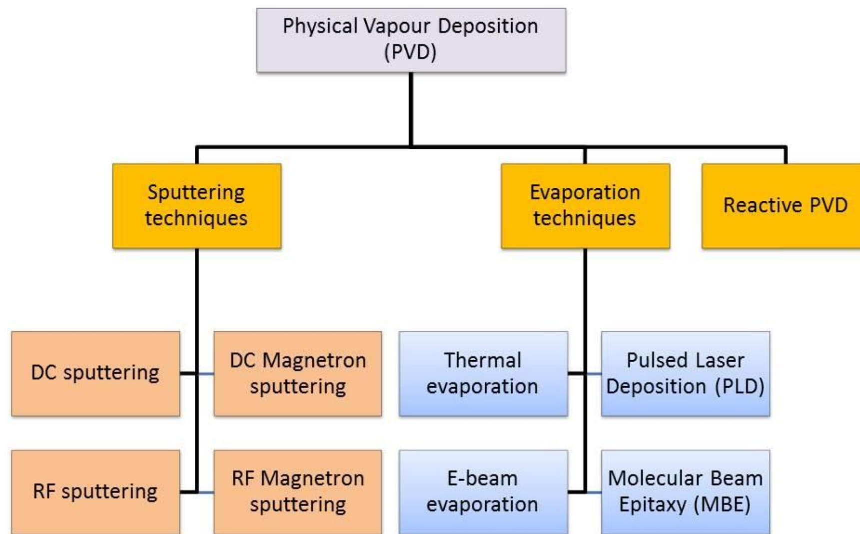

Figure 4.1 Block diagram classifying the types of PVD techniques.

For the CVD techniques, the fabrication of thin films is achieved by reacting the atoms chemically upon the surface of the substrate. CVD techniques can be classified as shown in the block diagram as seen in **Fig. 4.2** below;

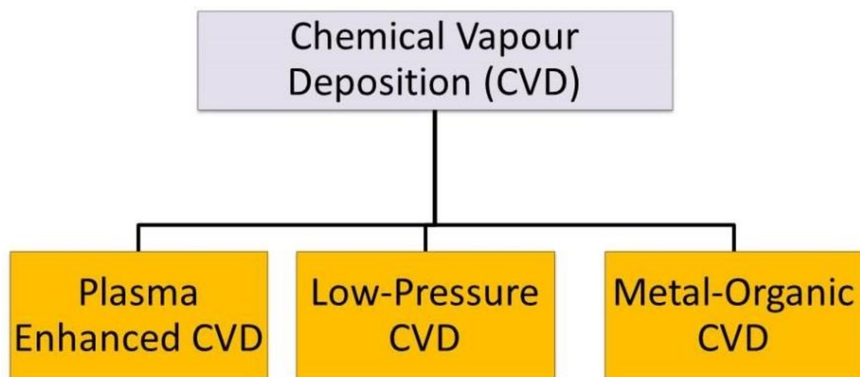

Figure 4.2 Block diagram classifying the types of CVD techniques.

The growth of thin films is normally achieved under vacuum. To achieve high quality thin films, they need to be fabricated in a high vacuum to avoid contamination. The base pressure of these systems is 10^{-6} mBar. Also, the quality of thin films can be affected by fabrication technique, which can affect the stress within the film, adhesion of the film to the substrate, the density of the film, the grain size and the thickness uniformity.

4.2 Thin Film Growing Mechanism

Thin films produced by PVD techniques grow via different growth mechanisms on the substrate. These mechanisms consist of nucleation, adsorption, surface diffusion, and interdiffusion upon the substrate surface [1]. These mechanisms can also be affected by the properties of the substrate and material source to be deposited as a thin film. **Figure 4.3** shows the common mechanisms for film growth.

Venables et al [2] explained the nucleation process and films growth. Their explanation focused on the quantitative nucleation theories, the formation of films thermodynamically, and they used experimental data with physics mechanisms to check these theories. For the deposition process, the adsorption reaction process occurs, which includes the surface adsorption when impinging atoms interact as a gas phase with the substrate surface. The adsorption process can be either a physical or chemical process. Physical adsorption occurs when any particle is bound or stretched but keeps its identity and bonds to the surface by van der Waals force, while chemical adsorption happens when the identity of the particle changes and bonds to the surface in either an ionic bond or a covalent bond.

Venables et al [2], showed that the growth of films can occur via three different processes. The surface diffusion process is the initial stage to start the nucleation and cluster formation to grow the film. This happens due to the strong bonding between the atoms and a weak bond to the substrate. The process, in this case, is identified as an island or Volmer-Weber mode. The stability of forming clusters, at any site on the surface, is not stable and the clusters have an ability to rearrange themselves through the diffusion of atoms, mixing the species, and by the coalescence process. The diffusion process depends on the surface mobility and it takes place in many stages as the film is formed. The surface mobility is affected by the temperature of the substrate and the energy of the atoms. The movement of an individual atom leads to building of small clusters and then by the coalescence process and the re-arrangement of these small clusters into large clusters (islands).

In the sputtering technique, the sputtering gas pressure is a parameter that can affect this growth mode because a higher gas pressure can affect high energy atoms thermally by scattering. This will influence the diffusion mechanism of the atoms on the substrate surface, which leads to defects such as voids within the film. The growth mode of layer by layer is known as Frank-van der Merwe mode. This mode happens if the atoms are strongly bonded to the substrate surface more than to themselves. This leads to creating a whole monolayer on

the substrate surface, which will be covered with a second layer that is less strongly bound to the first layer. Another mode for film growth can be in both modes of layers and islands. This growth mode is known as Stranski-Krastanov. In this mode, the growth will be started by deposition of a monolayer and then the next layer will be unfavourable, therefore, islands are created as a second layer. The reasons for Stranski-Krastanov mode could be due to many factors, which lead to the decrease in binding energy.

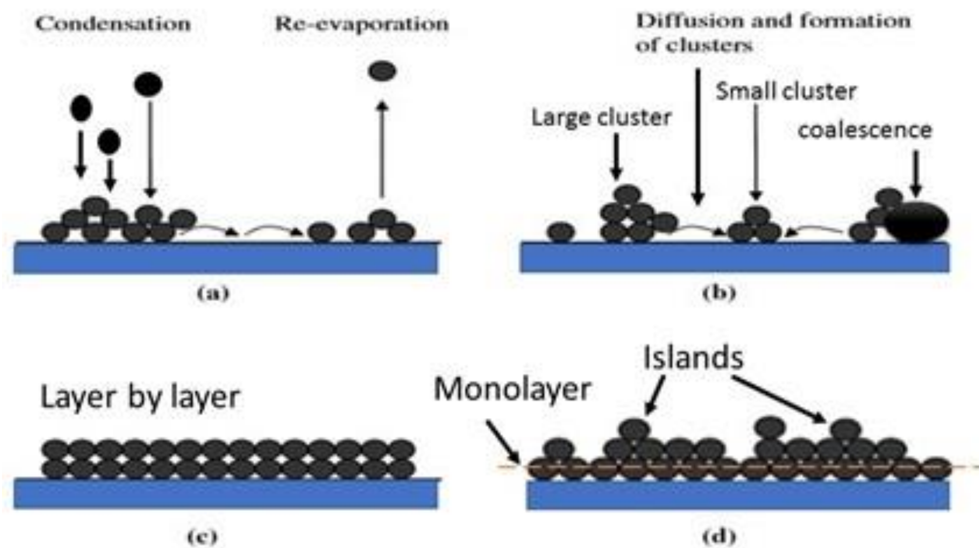

Figure 4.3 Schematic diagrams of thin film growth mechanisms deposited by PVD techniques (a) diffusion of atoms and re-evaporation (b) nucleation, clusters, and coalescence (c) layer by layer mode (d) monolayer with islands mode adapted from reference [3].

4.3 Film Thickness Uniformity

Film thickness uniformity is very important for applications and can change the properties of the film. The thickness uniformity can be affected by the substrate roughness, growth mechanisms and the substrate size. Also, film thickness uniformity [4] can be affected by the target-substrate distance, the sputtering power and gas temperature, which leads to change in the deposition rate. While the substrate size is important, as in sputtering the film thickness decreases across of the sample length. It is found that for the sputtering system used in Ref. [4], there is a 5% reduction in thickness far from the centre of the sample [5] which can be different for different techniques; therefore, a large sample size leads to a big difference in thickness across the surface.

4.4 Film Purity

The film purity can be affected by many factors depending on the type of deposition technique. For example, in the evaporation technique, the chemical purity of the film depends on the percentage of contamination present in the source material, the heater, and the crucible. The residual gases in the chamber such as O_2, CO, H_2O, and CO_2 can also be a source of contamination in the film. Also, the chemical purity of the film deposited by the sputtering technique can be affected by many factors such as the purity of the used gas, the purity of the target material, and the residual gases in chamber mentioned above. In this work, the films deposited by the co-sputtering-evaporation technique can suffer from all the factors presented above.

4.5 Thermal Evaporation Mechanism

Thermal evaporation systems are used to fabricate thin films from materials, which are evaporated. The basic principle of the thermal evaporation process is to heat the source materials within crucibles, in a vacuum chamber until the atoms have enough energy to leave the crucible and transfer to the substrate. The thermal evaporation process is shown schematically in **Fig. 4.4**. The source materials are placed either on a boat or crucible, which are heated to a suitable temperature through providing power to the crucible by a filament or supplying an electrical current across the boat or wire. The source materials can be evaporated at different deposition rates. The deposition rate is influenced by many parameters, including the distance between the source material and the substrate, the chamber geometry and pressure, the source material temperature and evaporation pressure. The film may be contaminated by the reaction of the evaporated material with the bulk material of the crucible or boat. Thus the quality of the deposited film can be influenced by the material of the boat or crucible. Generally, the way to avoid the contamination of the source materials, are to use boats manufactured from refractory materials, which have a high melting point such as molybdenum (Mo), tantalum (Ta), and tungsten (W), or use crucibles manufactured from refractory ceramic materials such as alumina (Al_2O_3), graphite (C), boron nitride (BN), and zirconium.

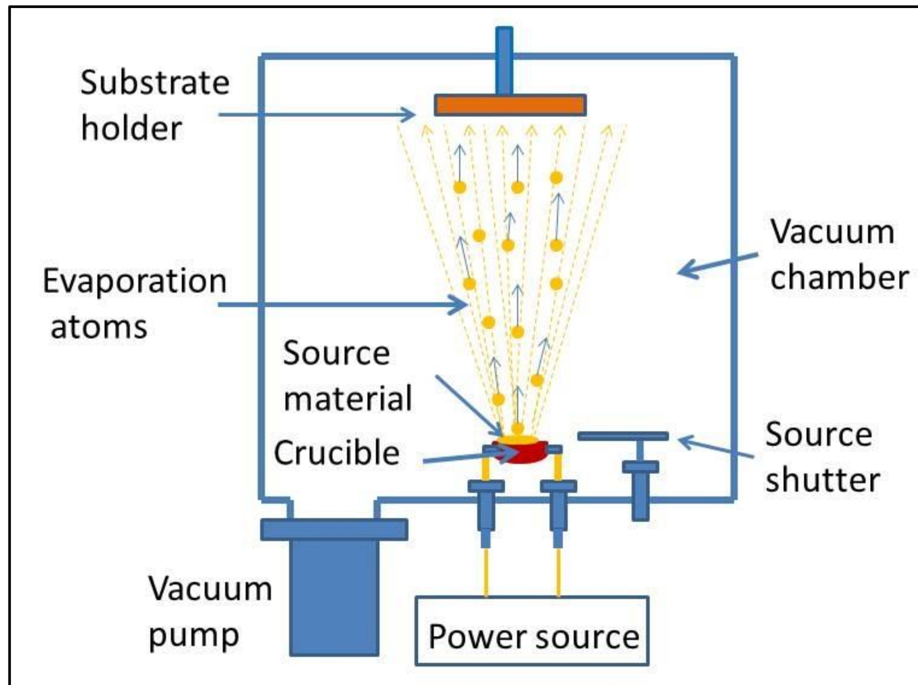

Figure 4.4 Schematic diagram of the thermal evaporation mechanism.

4.6 Sputtering Mechanism

The sputtering technique is a physical vapour deposition (PVD) technique used for the fabrication of thin films under vacuum. The main parts of this technique are; the anode and the cathode poles, which used to generate the potential base of the plasma, DC voltage or radio frequency (RF) supply, vacuum pump, vacuum chamber, magnetron, inert gas and substrate holder, as shown in **Fig. 4.5**. The basic principle of sputtering is that the sputtered atoms are physically removed from the surface of the sputtering target by a bombardment process using ions of the inert gas in plasma **Fig. 4.5.** The removed atoms then travel from the target to the substrate to start the film deposition. The sputtering mechanism is characterized as a mechanical process rather than thermal or chemical, to form the target material into the vapour phase [6].

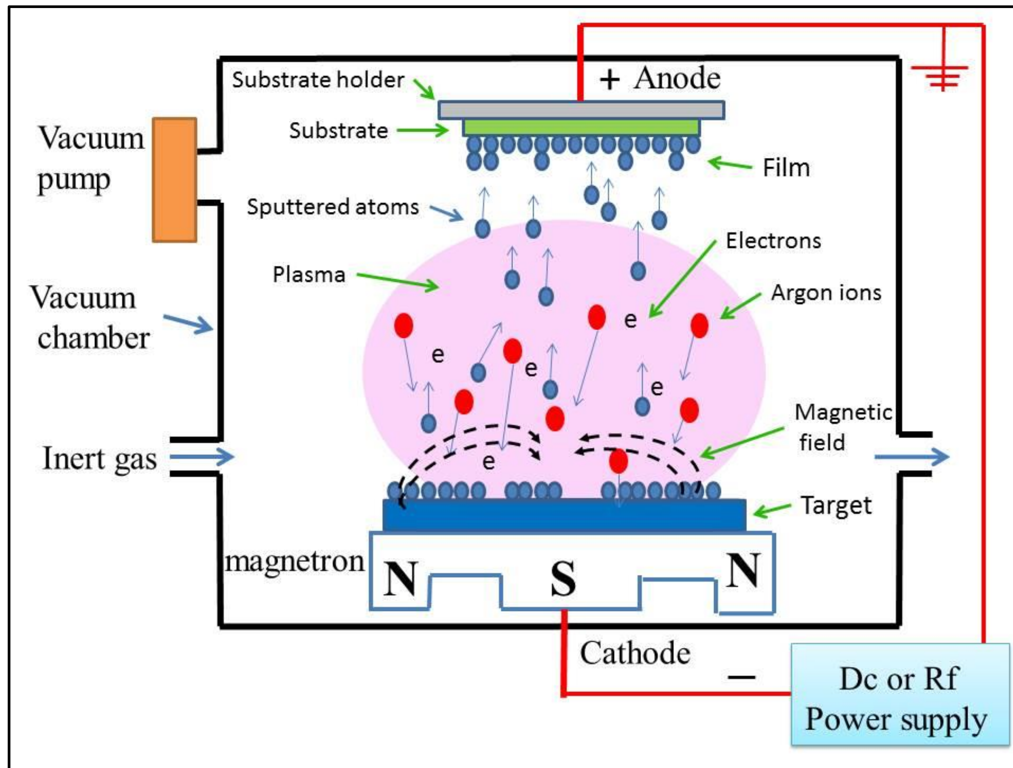

Figure 4.5 Schematic diagram of sputtering mechanism.

By applying a large negative voltage to the cathode and grounding the anode, as shown in **Fig. 4.5**, as the generated plasma has a very high conductivity, a larger magnitude of the applied voltage is dropped by the cathode; this will lead to an ion bombardment process. Another interaction occurs between the ions and the surface, which is the generation of secondary electrons. Therefore, at the surface of the sputtering target, ions and secondary electrons are emitted from the surface. The emitted electrons will accelerate into the plasma leading to more ionising collisions. Self-sustaining plasma is formed from the emitted secondary electrons. The collision of the sputter gas with free electrons leads to the ionisation of gas in the plasma.

The sputtering technique can be classified into two classes: DC and RF. DC sputtering uses a DC voltage generated by a power supply to provide both the target and the substrate with a suitable potential and is used to sputter conductive materials. RF (radio frequency) sputtering is used to sputter insulator materials. In the case of non-conductive materials, the charge of the ions stays localized after hitting the surface of the target and with time positive charges will accumulate on the target surface, leading to an infeasible additional bombard of the target surface. This problem can be solved by bombarding the non-conductive target material using both positive ions and electrons at the same time. To achieve that, an RF potential is

applied to the target. The RF potential works as an energy provider to the electrons to oscillate them in an alternative field, thus producing ionizing collisions in addition to maintaining the self-sustained discharge. This type of discharge, if the potential gradient is high enough will accelerate the free electrons to ionize the atoms by more collisions. In this case, due to the high mobility of electrons in comparison with the mobility of ions, more electrons reach the non-conductive target surface when the positive bias of the RF voltage is applied, while a few positive ions reach the target surface during the negative bias of RF voltage and then the target body becomes negative self-biased. This fends off the electrons from the near area of the target surface and builds up a casing having a high number of positive ions near the surface. In this case, the positive ions will bombard the target surface during sputtering process.

The efficiency of the sputtering process can be increased by increasing the number of collisions that are achieved by secondary electrons before they reach the anode. To achieve this, a magnetic field is applied, by using strong magnets, to confine the secondary electrons in a path close to the cathode. The configuration of the magnetic field is commonly generated by a planar magnetron. This uses magnets beneath the target at right angles to generate a magnetic field with a parallel component to the surface. The secondary electrons, which pass across the lines of the magnetic field, undergo a force to work them forward towards the target surface with a cyclical movement. Therefore, at the magnetron for sputtering, the magnetic field traps the electrons near to the target to promote the plasma density and thus sputtering rate. The sputtering system has the advantage that the deposited films are uniform, dense, and can have a very small grain size. The substrate temperature also changes the crystallinity and the density of the deposited films. The substrate temperature can be modified from room temperature to 500 °C.

4.7 Growth Parameters Which Effect Film Properties

In the sputtering method, the properties of the deposited film depend on several deposition parameters.

4.7.1 Gas Pressure

Typically, the pressure is used to provide the required inert gas to the sputtering process. In addition, it can work as a moderator to the sputtered atoms from the target. The pressure is an essential parameter, which can influence the structure and magnetic properties of the films, therefore, changing and controlling the pressure will affect these properties. In sputtering, it is possible to apply a low pressure, which leads to the sputtered and reflected atoms having higher energies compared with the plasma ions on reaching the substrate. In this case, the sputtered atoms reach the substrate with a high surface mobility. While at higher pressure, the sputtered atoms increase thermally [7] as a result of the increase in the amount of collisions by the plasma ions before reaching the substrate surface. Therefore, the sputtered atoms will have low surface mobility. As a result of the effect of pressure on the sputtered atoms during the deposition of film, this can lead to a noticeable effect on the structure and magnetic properties of the film.

4.7.2 Target-Substrate Distance

The distance, which separates the target and substrate, has an effect similar to the effect of the sputtering gas pressure on the growth mechanism. Reducing the distance between the target and substrate leads to an increase in the mobility of the sputtered atom at the substrate surface. While increasing this distance leads to a reduction in the mobility of the atoms at the surface.

4.7.3 Sputtering Target Power

The power can affect the sputtered atoms and hence the properties of the deposited film in a similar way as described for the sputtering gas pressure. At a lower sputtering target power result in sputtered atoms with low kinetic energy and hence lower mobility on the substrate surface, which leads to a tensile stress in the film. Increasing the sputtering target power leads to an increase in the kinetic energy of the sputtered atoms, thus an increase in the mobility of the atoms at the substrate surface, which leads to a compressive stress within the film.

4.7.4 Sputtering Rate

The deposition rate of the sputtering process increases with the increasing sputtering target power and decreases with decreasing power. Increasing the target power leads to an increase in the potential of the cathode and hence increase in the bombardment process. This leads to an increase in the number of sputtered atoms from the target and hence an increase in the deposition rate. Also, the deposition rate can be affected by the sputtering gas pressure, as increasing the pressure leads to an increase in the plasma density and hence the number of collisions between the sputtered atoms with the plasma ions. Thus some of sputtered atoms will return back to the target, leading to a reduction in the number of atoms to reach the substrate thereby reducing the sputtering deposition rate. Further, using the magnetron in contact with the target leads to an increase in the deposition rate by producing a denser plasma on the target surface, which leads to an increase in the sputtering rate even in the case where the sputtering target power is constant.

4.8 Co-Sputtering and Evaporation Technique at Sheffield

4.8.1 Co-Sputter-Evaporation Deposition Chamber

The deposition chamber of the co-sputtering-evaporation technique [8], which was manufactured by Kurt J Lesker Company Ltd, includes two growth parts: one sputter target and one evaporator source to deposit thin films. The main parts of this chamber are shown schematically in **Fig. 4.6**. In this project, FeSiB and FeGaSiB thin films were fabricated. To produce the films, the FeSiB ribbon target was sputtered, while the gallium was evaporated because the gallium has a low melting point (30 ºC) and a high vapour point (1100 ºC). Both processes, the FeSiB sputtering and Ga evaporation, were done at the same time. In the current study, the growth parameters (sputtering power, Ar gas pressure, and Ga evaporation rate) were changed while the substrate-target distance was fixed at d = 60 mm. During the growth process, the substrate holder was rotated to remove any magnetic effects from the magnetron field and to get an uniform film thickness on the substrate. This rotation can also help the films to have uniform distribution of Ga atoms, hence uniform Ga composition, because the evaporation crucible is located at the side of the deposition chamber as shown in **Fig. 4.6**. For growth under different temperatures or annealing the samples under high vacuum, the substrate can be heated up to 500 ºC [9]. From above, the system can manufacture the FeSiB and FeGaSiB thin films over a range of growth parameters.

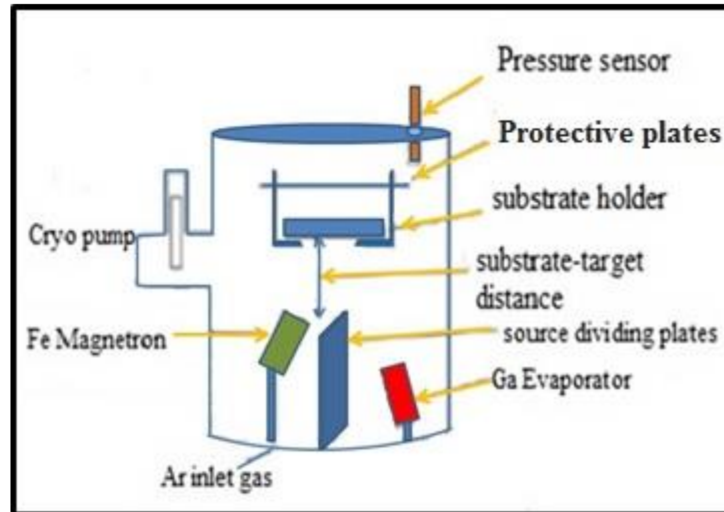

Figure 4.6 Schematic diagram of the co-sputtering-evaporation chamber edited from reference [8].

4.8.2 Co-Sputtering and Evaporation

The co-sputtering-evaporation system is designed to use the sputterer and the evaporator either individually or working at the same time. The DC sputterer is used to deposit the FeSiB thin film with different growth parameters, such as power density, to control the FeSiB deposition rate. The DC magnetron gun of this system has a diameter 50.8 mm and a FeSiB ribbon target is used in three layers with 23 μm thick for each. In the evaporator, changing the temperature of the Ga source controls the rate of Ga evaporation, for example, a higher amount of Ga is evaporated at a higher temperature. The stability of Ga rate is dependent on a stability of Ga temperature, which is controlled by applying power to the heater across the crucible. For this technique, computer software is used to control the film growth. The base pressure of the system is (8×10^{-6} mBar), the deposition rates of Ga source and FeSiB target are measured using rate thickness monitors located above them. Near the substrate, the film's thickness is determined from the FeSiB rate monitor reading, which is calibrated for FeSiB and FeGaSiB thin films. The properties of both films were affected by the growth parameters such as FeSiB power density (P_{FeSiB}), Ar gas pressure (p_{Ar}), substrate temperature, Ga evaporation rate (R_{Ga}), and substrate-target distance (d). Therefore, the properties of deposited films can be studied for a range of growth parameters, this can be considered as one of the advantages of this technique. The co-sputtering-evaporation mechanism is shown schematically in **Fig. 4.7**.

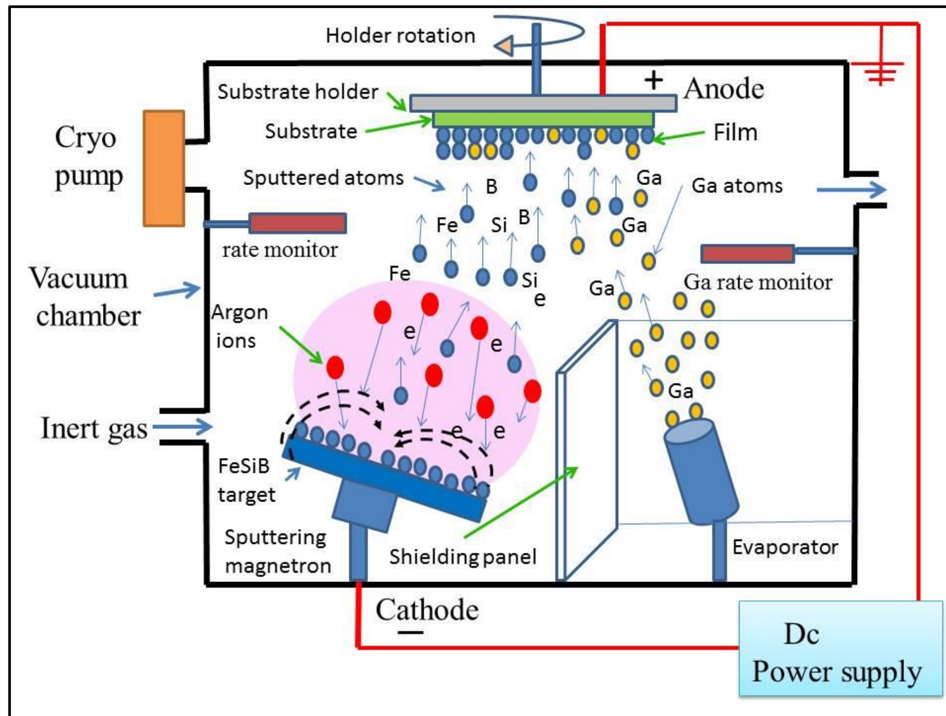

Figure 4.7 Schematic diagram of co-sputtering-evaporation mechanism.

4.9 Sample Preparation and Target

The co-sputtering–evaporation technique described in section (4.8) [8] was used to deposit FeSiB and FeGaSiB amorphous thin films. The formation of the amorphous films was made without rapid quenching methods. The films were grown on Si (100) substrates with dimensions 10 mm × 15 mm, which were washed using acetone and isopropanol (IPA) before deposition. Three Si substrates were used per film growth, attached to a glass slide using polymethyl methacrylate (PMMA). To determine the thickness of the films accurately, a PMMA blob was put on one Si substrate before growth using a small stick of wood (toothpick). After growth, the PMMA blob was washed away using acetone, to leave a sharp edge, so that the film thickness could be measured. The ferromagnetic amorphous thin films investigated in this thesis were sputtered from an amorphous Metglas 2605SA1 ribbon with composition $Fe_{85}Si_{10}B_5$. The starting ribbon was 15.2 cm in width and 23µm in thickness. The targets prepared for the sputter technique involved three 5 cm diameter thin discs cut from the Metglas ribbon material. The three thin discs were placed on the target sputter gun, with a 2 mm Fe target between the Metglas target and the gun electrode to intensify the sputtering rate. The three Metglas targets were used to avoid damage, which can be produced from the plasma on the surface of the first top target such as pinholes which can be covered

by the next target underneath, hence avoiding to sputtering the iron plate underneath. The holder including the substrate is shown schematically in **Fig. 4.8**.

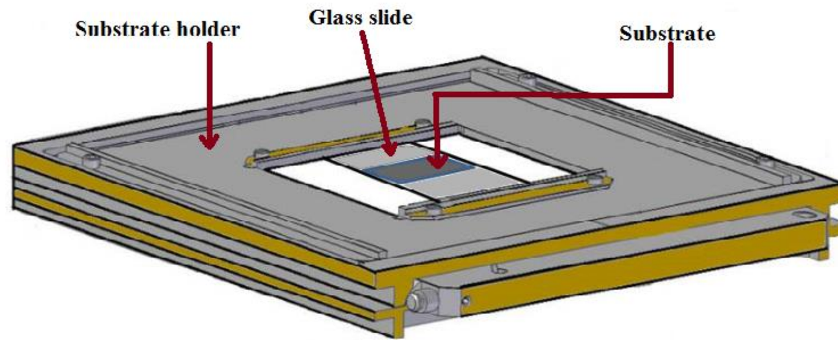

Figure 4.8 Schematic diagram of the substrate holder of the co-sputtering-evaporation chamber.

4.9.1 Growth of Amorphous FeSiB Thin Films

In this part: The first study of the experimental work was to investigate the influence of the FeSiB thin film thickness. The first film set was grown with a thickness range from 24 to 100 nm. The films were grown at a chamber pressure (p_{Ar}) of 4 μbar and sputter power (P_{FeSiB}) of 20 W by sputtering only Metgles $Fe_{85}Si_{10}B_5$ ribbon with the evaporator turned off. The second film set was to grow the films with a range of gas pressure from (4 to 8) μbar, keeping all other parameters constant (sputtering power at 20 W, thickness at 50 nm, and the Ga evaporation rate at zero). The third film set was growing the films with a range of powers from 20 W to 70 W and keeping all other parameters constant (gas pressure at 4 μbar, thickness at 50 nm, and the Ga evaporation rate at zero). The fourth set was to grow thicker FeSiB films with a range of thickness (290, 425, and 668) nm to study the mechanical properties using nanoindentation technique. The gas pressure was at 4 μbar, sputtering power at 20 W, and R_{Ga} = set to be zero.

4.9.2 Growth of Amorphous FeGaSiB Thin Films

The second part was fabricating FeGaSiB thin films by sputtering Metgles $Fe_{85}Si_{10}B_5$ ribbon and using Ga as a source material in the evaporator. Five sets of FeGaSiB thin films have been grown by the co-sputtering-evaporation technique with different conditions. In this technique, there are two sensors, rate monitors, used **Fig. 4.7**; one is placed upper the sputtering to measure the sputtering rate of FeSiB atoms and the second one is placed upper

the evaporator, used to measure the evaporation rate, with the evaporation power being varied to achieve a constant rate during growth. The first set was growing the films with different thicknesses ranging from 24 nm to 100 nm at the sputtering power (P_{FeSiB}) of 20 W, Argon gas pressure (p_{Ar}) of 4 µbar and Ga evaporated with a constant arbitrary rate, $R_{Ga} = 0.2$. The second set was growing the films with a range of gas pressure start from 4 µbar to 8 µbar and keep other parameters constant (sputtering power at 20 W, thickness at 50 nm, and $R_{Ga} = 0.2$). The third set was growing the films with a range of sputtering power starting from 20 W to 70 W and keeping all other parameters constant (gas pressure at 4 µbar, thickness at 50 nm, and $R_{Ga} = 0.2$). The fourth set was growing the films with range of Ga evaporation rates start from 0.2 to 0.6 and keeping other parameters constant (gas pressure at 4 µbar, sputtering power at 20 W, and the thickness at 50 nm). The fifth set was to grow thicker FeGaSiB films with a range of thickness (283, 450, and 640 nm) to study the mechanical properties using nanoindentation technique. The gas pressure was at 4 µbar, sputtering power at 20 W, and $R_{Ga} = 0.2$.

4.10 Characterization Techniques

A range of structural and magnetic characterization techniques were used to characterize the different film sets.

4.10.1 X-Ray Diffraction

X-ray diffraction (XRD) is a structural characterization technique [10] used for investigating the structure of materials in bulk, powder, and thin film form. The incident X-ray beam on the material is scattered by the atomic planes or it is transmitted through the material. The diffraction of incident X-rays from the atomic planes creates constructive interference when the path differences conform to Bragg's Law, $2d \sin\theta_i = n\lambda$ [10], where d refers to the interplane space, n refers to the order of reflection, θ_i is the incident angle, and λ refers to the wavelength of the X-ray used. The incident X-ray transmits the material and interacts with its atoms [11]. The negatively charged particles (electrons) of the material's atoms will interact directly with the electromagnetic field of the transmitted X-ray; this will lead to scattering of the X-ray elastically in direction away from the tested material [11], **Fig. 4.9**. Further, the electrons of the atoms oscillate as a result of the field associated with the incident X-ray and leading to the generation of electromagnetic waves which match in wavelength and phase to the used X-ray [11].

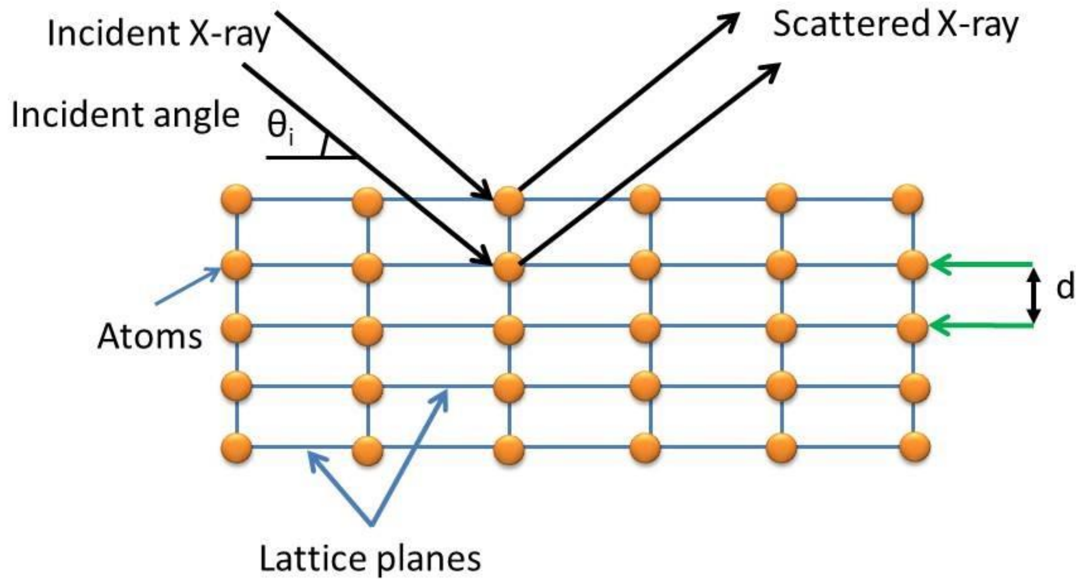

Figure 4.9 Schematic diagram of the interaction between X-ray and material adapted from reference [12].

In the case of thin film measurements, the X-ray passes through the substrate and measures both the film and the substrate. The X-ray beam passes through divergence slits before it is incident on the sample and reaches the detector after passing through a receiving or detector slit of width 0.6 mm. Properties such as the structure, phase identification, grain size, and texture can be measured by the XRD. In this thesis, the Bruker D2 phaser technique with Cu $K_{\alpha 1}$ radiation (wavelength 1.54184 Å) was used in standard scan type 2θ/θ geometry, as shown in the schematic diagram of the X-ray diffractometer **Fig. 4.10**, to analyse the film's structure. The XRD technique was used to check whether the films grown by the co-sputtering-evaporation technique were fully amorphous or if they contained nanocrystalline clusters within the amorphous matrix or they were polycrystalline. The X-ray generator was worked at 30 kV and 10 mA and by running the X-ray diffractometer at small step size of 0.02^o and a scan speed of 0.1 deg/min, the X-ray pattern was obtained. In this thesis, the 2θ range from 30 to 80° was used to check the structure of the films (for bcc Fe 2θ ~ 45° and for bcc Fe-Ga 2θ ~ 45°) and silicon substrate (2θ = 69.8°, 61.7°, and 33°), and the 2θ range from 35 to 55° was used to avoid the Si substrate peak.

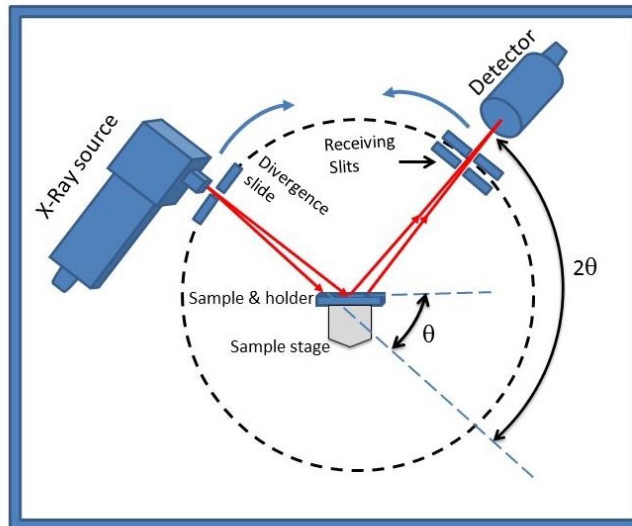

Figure 4.10 Schematic diagram of XRD technique in standard scan type θ/2θ geometry adapted from reference [12].

For cubic crystalline materials, the lattice parameters of the materials are calculated using the formula:

$$a = \frac{\lambda\sqrt{h^2+k^2+l^2}}{2sin\theta} \qquad (4.1)$$

Where λ is the x-ray wavelength, θ is the angle of Bragg's reflection, and (h, k, l) are the Miller parameters of the diffraction planes.

Measuring the grain size (D_{grain}) of materials by XRD data can be achieved by the Scherrer equation [13]:

$$D_{grain} = \frac{0.9\,\lambda}{\beta\cos\theta} \qquad (4.2)$$

Where β is the full width of the half maximum (FWHM) of the peak, θ is the Bragg angle of the reflection, and λ is the XRD wavelength.

4.10.2 Atomic Force Microscopy

The atomic force microscope (AFM) is designed as a scanning probe microscope to measure surface properties such as thickness, topography, and roughness. The AFM is used to obtain an image by scanning the probe over a very small surface area of the sample. It measures the force between the probe tip and the sample surface. The probe consists of a sharp tip, which has a 3-6 µm high pyramid, including a 15-40 nm end radius. AFM can be utilized in contact mode, in non-contact mode, and in tapping mode [14]. In contact mode, the used tip is continuously in contact with the sample surface. In this mode, no oscillation measurements are required to gain the images of the surface features. When the tip scans the surface, the repulsive force leads to the cantilever deformation to assimilate the changes in surface height. A position-sensitive photo-detector is used to monitor the deformation which has occurred in the cantilever by sensing the reflected laser from the upper side of the cantilever related to changes in the surface. These changes are recorded as data and converted as the topography images of the surface. The disadvantage of this mode is that across the scanning process both the sample surface and the tip can be damaged as a result of the forces linked between them.

In non-contact mode, the cantilever tip oscillates near to the sample surface within a very small space around 10 nm. The oscillation frequency of the cantilever is about (100-400) kHz, which is close to the cantilever resonant frequency. The resonant frequency of the cantilever and oscillation amplitude are changed due to the attractive force between the sample surface and the tip. Again, these changes are recorded as data and converted as the topography images of the surface. Non-contact mode does not cause damage to the sample surface as is the case for contact mode, but the sample surfaces are contaminated in the air by a contamination layer, which can lead to a reduction in the image resolution. Consequently, an ultrahigh vacuum is best used in the non-contact mode for a high image resolution.

The operation of tapping mode (TM) is through tapping the surface by an oscillating probe tip. To overcome the restrictions of the contact and non-contact modes, tapping mode was used to remove the profiling forces that can affect the sample surface and the resolution of AFM image. The resonance frequency of the cantilever oscillation is usually about 300 kHz and the amplitude in the range from 20 nm to 100 nm.

In this work, a tapping mode AFM based on the Veeco Dimension 3100 was used. A standard Si-cantilever tip, coated by a reflecting layer of Aluminium to increase the laser reflectivity, was used at the resonance frequency of about 270-313 kHz. The radius of this tip is about 7

nm, which is less than the ideal grain size of thin films which is > 10 nm. The standard Si-cantilever tip was used to take the topographic image. From analysing the image by software, the root mean square (RMS) surface roughness of the film's surface can be determined. The cross-sectional analysis of the AFM is used to determine the grain size of the film. This is achieved by plotting three straight lines at different locations of the image. The schematic diagram of AFM is in **Fig. 4.11**. AFM was used to measure the thickness of the thin film, surface morphology, surface roughness, the grain size, and 3D surface topography. In tapping mode, AFM was utilized to determine the film thickness by producing an edge or step between the surface of the substrate and the fabricated films.

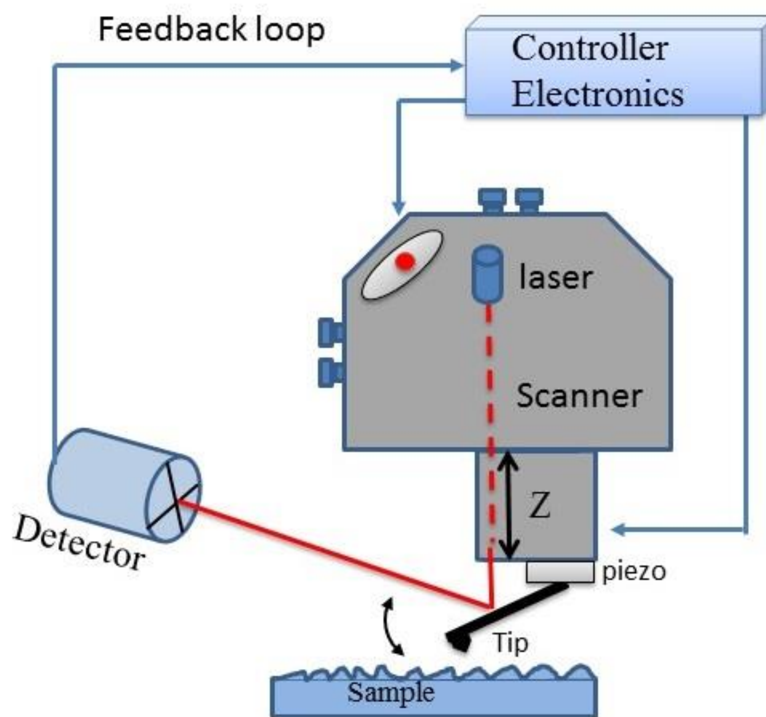

Figure 4.11 Schematic diagram of AFM in tapping mode.

For measuring the film's thickness, it was by creating a step on the surface of sample, to achieve that, a PMMA blob was put on the Si substrate before deposition as outlined in section 4.9. After the deposition process, the PMMA blob is washed away using acetone, to leave a sharp edge, so that the film thickness could be measured, as the AFM tip scans across the surface, therefore, it will scan two high levels (step height), the difference between these levels will give the height of the film which represents the measured thickness. As shown in **Fig. 4.12**, the film thickness was 86nm for FeGaSiB film.

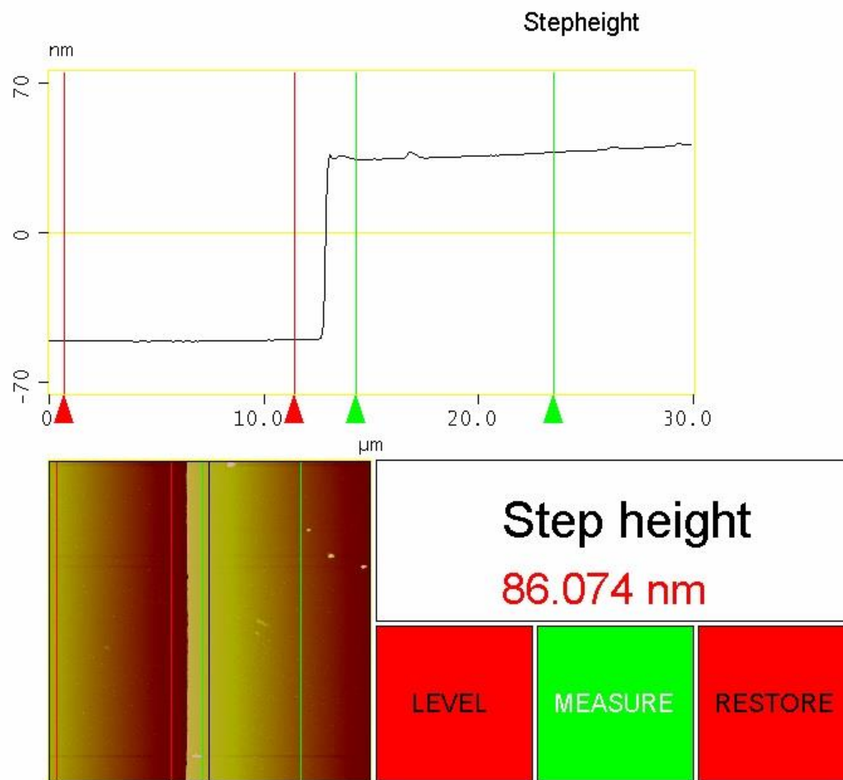

Fig. 4.12 AFM thickness measurement with scan area 30x30 µm^2. The two red lines moved to average the lower level of step and the two green lines moved to average the high level of step.

4.10.3 X-Ray Photoelectron Spectroscopy

X-ray photoelectron spectroscopy (XPS) is a surface analysis technique used for investigating and analyzing the chemistry of materials surface such as thin films. The XPS technique is able to measure the composition and chemistry of elements at the surface of materials. It is one of the quantitative techniques which has an ability to count the number of recorded photoelectrons for a specific transition, which is directly proportional to the number of atoms on or near the surface of the material. The detection region is within the top 10 nm from the surface. The main parts of XPS instrument, are electronic gun, energy analyzer, electronic lens, X-ray source, monochromatic crystal, charge neutralizer, detector plate, vacuum chamber, and UHV pump. As shown in **Fig 4.13**.

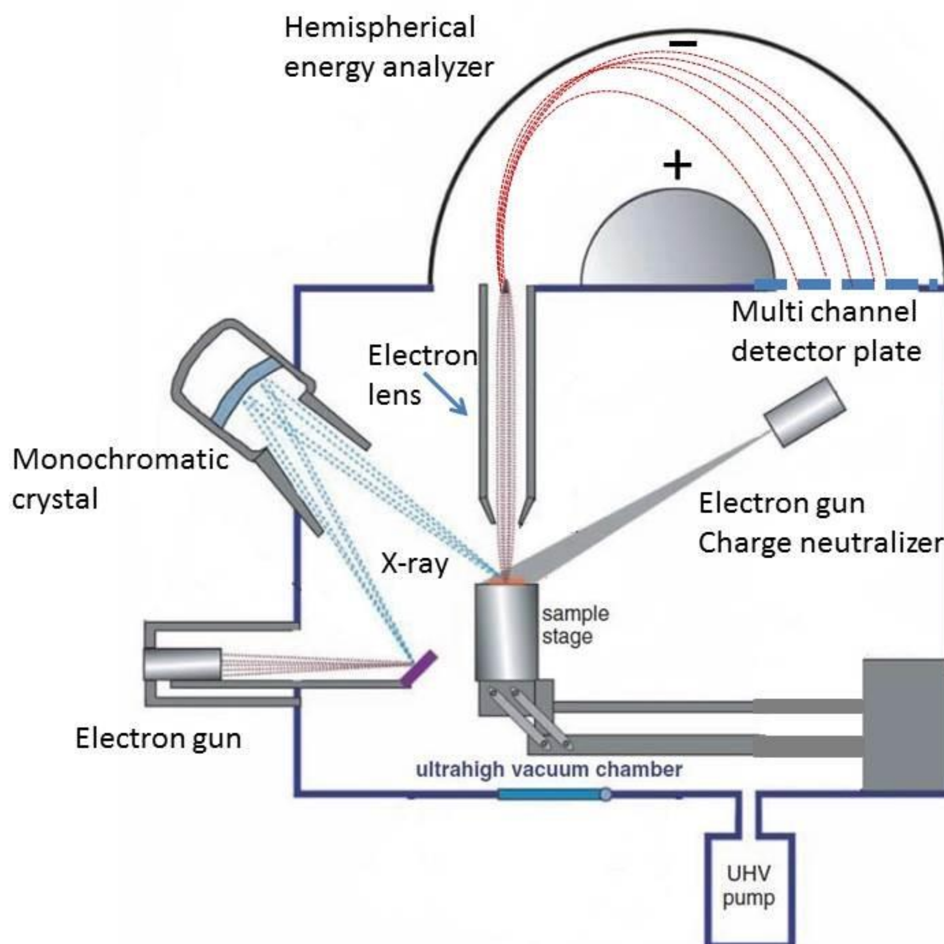

Figure 4.13 Schematic diagram of an XPS instrument adapted from reference[15].

The typical XPS technique involves X-ray source, ultrahigh vacuum chamber provided by UHV pump, an electron energy analyser, and data analysis system. To analysis the surface of a sample, the sample is located on a sample stage in the chamber under ultrahigh vacuum. X-ray photons, incident on the sample, are usually generated by hitting a high-energy electron beam, using electron gun, on an anode produced from Mg or Al elements. Water is used to cool the anode, which is heated by the incident electron energy. The photoelectrons, which have enough energy to leave the sample into the vacuum chamber, can be separated and the energy dispersive analyzer used to account for them.

The surface analysis of XPS can be applied on the material surface to: identify the elements presented at the surface (qualitative analysis), to determine the concentration of elements at the surface (quantitative analysis), and to identify the chemical bonding state of elements within the surface. Also the distribution of elements across the surface of material can be identified with elemental images and maps. Another study of the sample surface depth profile

XPS analysis, which includes removing layers from the surface of the sample during the measurement. In this way, the XPS analyses will provide the composition of the sample with increasing the depth moving from the surface to a deeper depth in the sample.

When a photon is incident on a material surface, there are three possible actions, which can occur within the material: firstly, the photon passes through the material without interaction; secondly, the photon can be scattered inelastically by an atomic orbital electron leading to it partially losing energy; finally, the photon energy can be absorbed by an atomic orbital electron causing the electron to be released from its atomic orbital. In the latter case, this interaction will lead to the photoelectric effect. The photoelectric process can occur just when the photon energy is higher than the binding energy of the ejected electron. Therefore, the main principle of XPS is based on the interaction between the electrons and the photons of the X-ray, the absorption of high energy X-rays by electrons allowing for the release of photoelectrons from the surface, which are detected. Two types of electrons can be ejected from the surface; photoelectrons and Auger electrons. The photoelectron process and Auger process are presented in **Fig. 4.14**. The photoelectron is affected directly by X-ray absorption, while the Auger electron occurs due to internal process which is independent of the X-ray.

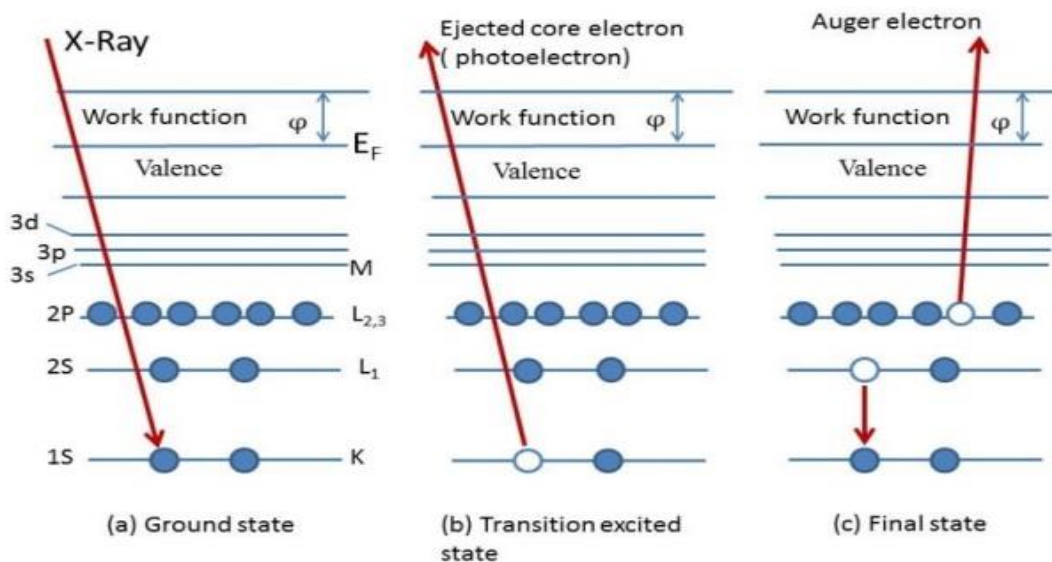

Figure 4.14 Schematic diagram of photoelectron and Auger electron process adapted from reference [16].

Experimentally, the XPS analyser measures the kinetic energy, KE, of any ejected photoelectron from the surface of the material and the binding energy, BE, which is important to identify the elements, is calculated after that from the equation:

$$BE = hv - KE - \phi \qquad (4.3)$$

Where BE is the binding energy, hv is the X-ray photon energy, KE is the kinetic energy of photoelectrons, and ϕ is the work function of the instrument.

The XPS spectrum is very important as it represents the number of photoelectrons at each energy, as the photoelectrons are measured according to their kinetic energy. From the spectrum, the identification of elements present can be achieved by the following steps: by detecting all the peaks in the spectra for one element, beginning with the maximum intensity peak to minimum one and matching the location of peaks with the standard data table. Once all the peaks for one element have been identified the steps are repeated for each element present. Once all the elemental peaks have been identified, then the composition is determined by the area of each peak in relation to the other peaks. This is done in the CasaXPS programme and gives the relative ratios for each of the peaks.

There are many problems which can affect the analysis of the data, these include peak overlap of two different elements, which comes from the relative intensities of peaks due to a change of X-ray type or change of the analyser resolution. Another problem comes from the electrical charge of the sample, which will present as a shift in the peak or the peak will be broadened. This can be solved by reducing the charging effect of the sample. Further, another problem is that the interaction of sample elements with chemical contamination, such as CO_2, O_2, and H_2 leads to the presence of extra peaks associated with the original peak of the element and a shift in the binding energies.

In this thesis, X-ray photoelectron spectroscopy (XPS), was carried out on a Thermo Fisher Scientific K-alpha+ spectrometer, used to measure the composition of the films. Samples were investigated via a micro-focused monochromatic Al X-ray source (72 W) over an area of around 400 μm. For high-resolution scan, recording of data was at pass energies of 150 eV for survey scans and 40 eV with 1 eV and 0.1 eV step sizes respectively. Charge neutralization of the sample was done by utilizing a combination of both low energy electrons and argon ions. Initial analysis of the samples revealed high levels of carbon attenuating the underlying metallic elements. To minimize this contamination all samples were cleaned with argon clusters of approximately 2000 atoms, from a Thermo MAGCIS source operating at 4

kV and restored over a 2 mm^2 area for a period of 30 seconds. The analysis of data was achieved by CasaXPS software with a Shirley type background. And Scofield cross sections, with an energy dependence of -0.6. The data was analysed at Sheffield.

4.10.4 Magneto-Optical Kerr Effect (MOKE) Magnetometer

The magneto-optical Kerr effect (MOKE) magnetometer is an instrumental device to understand and study the magnetic properties of thin films. There are three MOKE geometries, which can be used for measurement. They are dependent on the orientation of the magnetization with respect to the incident laser and the sample's plane: longitudinal, transverse and polar as shown in **Fig. 4.15**.

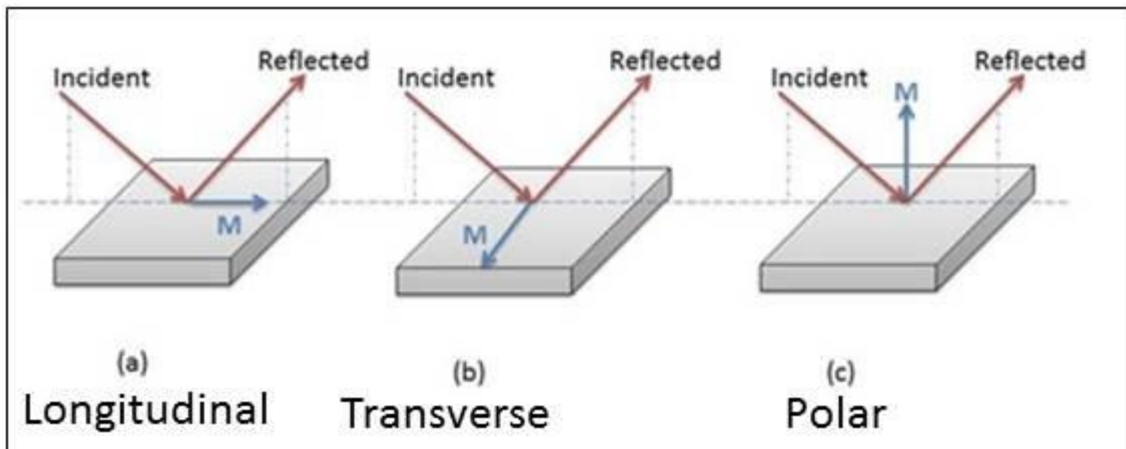

Figure 4.15 Geometries set up for MOKE (a) longitudinal (b) transverse and (c) polar. The red arrows denote the incident and reflected laser beam, while the blue arrow denotes the magnetisation vector M, adapted from reference [3].

In the longitudinal geometry, **Fig. 4.15 (a)**, the magnetization is aligned in-plane along the magnetic sample and in a parallel direction to the incident plane. In transverse geometry, **Fig. 4.15 (b)**, the alignment of the magnetization is in-plane and perpendicular to the incident plane, while in polar geometry, **Fig. 4.15 (c)**, the magnetization aligns in a perpendicular direction to the sample plane and is parallel to incident plane. Therefore, the difference between the three geometries arises from the direction of the magnetization alignment within the magnetic sample. The basic principle for all MOKEs is that the small change in the polarisation of incident light when reflected from the surface of magnetic materials is detected, which is proportional to magnetization of the film. In this study, a high field MOKE was used to measure the magnetic properties. The main components are a laser, polariser, a magnetic field produced by an electromagnet, a photodetector and analyser, as shown in the

Fig. 4.16. The laser light passes through the polarizer, which polarises the light, in this work, linear polarisation. The polarised laser light, after that, is incident on the magnetic sample with angle 45° and is reflected off the surface. A high magnetic field is applied in-plane, to the magnetic sample until magnetic saturation is reached. This change in magnetization affects the polarised laser light by interacting with it and changes the polarisation angle. By using an analyser, these changes in the rotation manifest as a changed in light intensity, which is detected by a photodetector. This is converted into a voltage signal and plotted against the applied magnetic field to produce a hysteresis loop. The main parts for MOKE are shown in the **Fig. 4.16**. In this study, for all sets of films, the magnetic properties were measured using a magneto-optical Kerr effect (MOKE) magnetometer, in the transverse mode, with the DC magnetic field being large enough to saturate the films (Max field applied was 39.78 kA/m). Normalized magnetic hysteresis loops were measured to characterize the films' magnetic properties. For each film, normalized hysteresis loops were measured by rotating the film within the magnetic field at different angles from 0° to 180° with 30° steps to study the magnetic anisotropy.

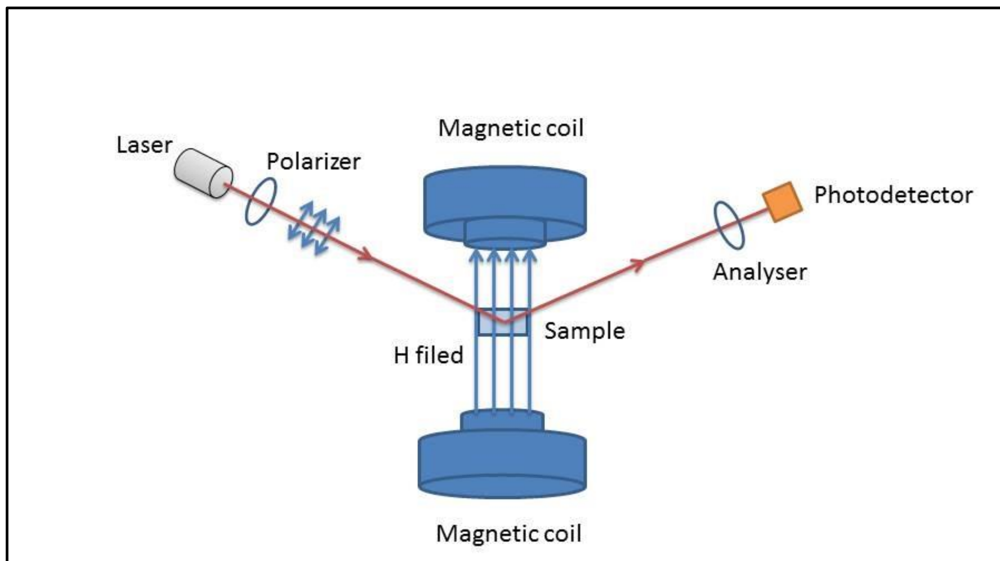

Figure 4.16 Schematic diagram of a magneto-optic Kerr effect (MOKE) magnetometer

4.10.5 Vibration Sample Magnetometer (VSM)

Simon Foner was the first designer of VSM in 1959 [17]. The basic operating principle of the VSM is based on Faraday's law and involves inducing an electromagnetic force (emf) in a coil due to a vibrating a magnetic sample. Basically, the regular vibration of a magnetic sample in a uniform magnetic field leads to an induced voltage in a stationary coil (detection

coil) which is measured. Therefore, due to the vibration of the magnetic sample, the induced voltage in the coil can be calculated by using the electromagnetic principles depending on a magnetic flux, Φ in the coil.

The magnetic flux in the coil is changed due to the vibration of the magnetic sample and the induced voltage, V_{ind} is calculated by:

$$V_{ind} = -N_{tu}\frac{d\Phi}{dt} \tag{4.4}$$

Where N_{tu} is the full number of turns in the coil.

Therefore, the induce voltage will depend on both the number of turns in the coil, the applied magnetic field and the magnetic moment of the sample.

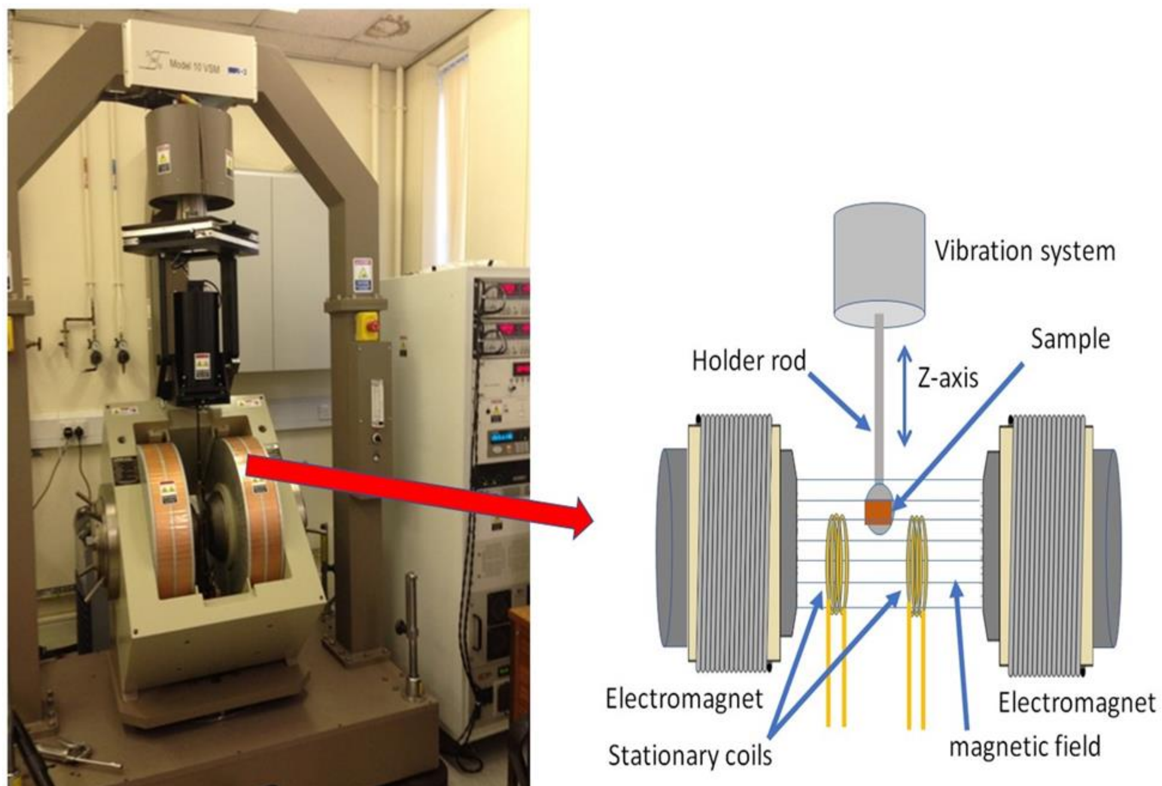

Figure 4.17 VSM technique picture and schematic diagram.

The main parts of the VSM technique are shown in **Fig. 4.17** and are:

1. A vibrating system is used to vibrate the holder rod in a harmonic vibration along z-axis, where the magnetic sample is attached to the rod. One end of the holder rod is connected to the vibration system and the other end is between the two magnetic poles. This allows the magnetic sample to move up and down at a frequency, normally about 85 Hz for this

measurment. The holder rod can be moved in different directions to obtain the required orientation of the magnetic sample to the uniform magnetic field. Also, the x, y, and z dimensions can be controlled by three knobs to centre the rod in the middle of the magnetic poles.

2. An amplifier is used to amplify the electric signal produced by the detection coils.
3. An electromagnet is used to produce uniform magnetic field
4. Detection coils are used to measure the induced voltage from the magnetic sample.
5. Temperature variation system, this unit is used to study the relation between the temperature and the magnetic moment of the magnetic sample. Studying the magnetization in a range of temperatures can help to study the effect of changing the phases of magnetic material under a magnetic field such as the magnetocaloric effect or determine the Curie temperature. The temperature variation in VSM system can be achieved by local heating and study the effect of changing the temperature on the magnetic properties of the films in this thesis does not achieved and all the films measured at room temperature.

4.11 Magnetostriction Measurement

For magnetic materials, the magnetostriction constant can be measured by different techniques designed for this purpose [18-21] (see section 3.7 chapter 3). These include the direct and indirect measurement methods. In this work, the magnetostriction constant (λ_s) was determined via the Villari effect [22] at room temperature. This involved using a set of bending tools, as seen in **Fig. 4.18**, with different radii (R), which induce a strain within the film, leading to a change in the magnetization of the films.

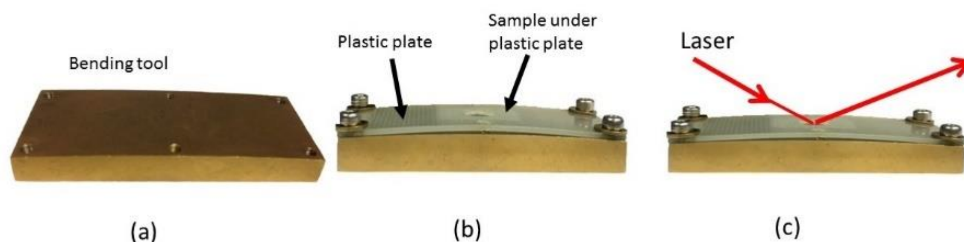

Figure 4.18 Images of the magnetostriction bending tool.

The film's hysteresis loops were measured for each bend radii on the MOKE magnetometer. The anisotropy field, $H_{k,}$ can be determined by different methods from the hysteresis loop.

These methods include the saturation method, the 90% method, and the straight-line method. In this study, the straight-line method, which is shown in **Fig. 4.19**, was used to determine the anisotropy field of both FeSiB and FeGaSiB films. For each bending radius, the anisotropy field (H_k), which is induced by the strain [23], can be determined directly by plotting straight lines; one along the straight part of the hysteresis loop and another parallel to the saturation part, the cross point of these lines represents the anisotropy field. For each loop, two anisotropy fields are determined, one at the upper side of the loop and another at the lower side, as seen in **Fig. 4.19**.

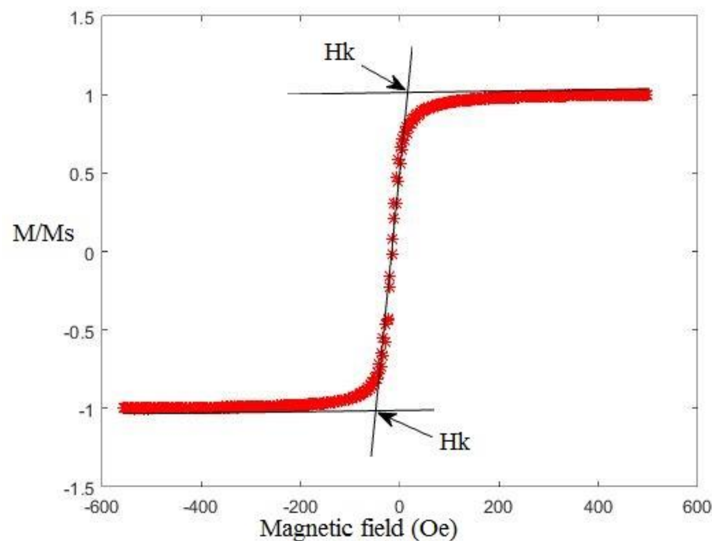

Figure 4.19 Schematic of the straight-line method to determine the anisotropy field (H_k)

The two values of the induced anisotropy field, H_k, are then are plotted as a function of the inverse bending radii (1/R) as seen in **Fig. 4.20**.

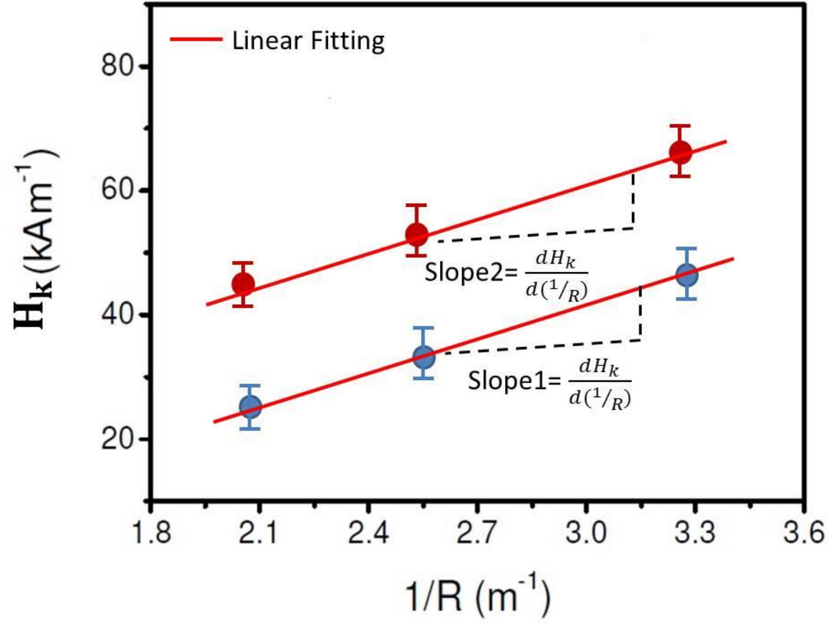

Figure 4.20 The changing of H_k as a function of 1/R. The slope is applied to the data.

Then a linear fit to the data is applied using the easyplot software, to find the slope of the two data sets, which represent the anisotropy fields, for the upper half and lower half of hysteresis loop for the three radii (300, 400, and 500 mm) of the bending tools.

After that, the first term in equation (4.5) is replaced by the slope value, and then the magnetostriction constant (λ_s) is calculated by using the equation; [22, 23].

$$\lambda_s = \frac{d(H_k)}{d\left(\frac{1}{R}\right)}\left\{\frac{2\mu_o M_s\left(1-v^2\right)}{3tE_s}\right\} \qquad (4.5)$$

Where the bend radii were R=300, 400 and 500 mm, μ_o is the permeability of space, M_s is the magnetization, and for the silicon substrate Young's Modulus, E_s=130 GPa, thickness of substrate, t =380 μm and Poisson ration of substrate, v=0.28.

The saturation induction of FeSiB films, $\mu_\circ M_s = 1.15\,T$, was used for all the FeSiB films, while the saturation induction of FeGaSiB films was measured via VSM for all the FeGaSiB films.

The result of this equation gives two values of λ_s, for each sample, as the anisotropy field was determined at two cross points on the loop (see **Fig. 4.19**). The deposition of each film was achieved by using three substrates therefore the result of λ_s as averaged over them and the standard error was determined by applying the standard deviation.

4.12 Nanoindentation Technique

Nanoindentation is an efficient technique, which can be used for determining the mechanical properties of materials at the nano and micro scales. In this thesis, a nanoindentation hysitron-Triboscope, **Fig. 4.21**, which is a scanning probe microscope, was used. Material parameters such as hardness and elastic modulus can be determined from the experimental measurements by applying a force in milli or micro-Newtons to the surface of the material. An indenter is used to penetrate the sample surface by applying a load, typically the penetration depth is in nanometers. Several types of tips can be used for creating an imprint into the materials surface. After applying a load in μN or mN on the indenter, the indenter tip will penetrate the original surface, **Fig. 4.22**, of the sample with a depth in nanometers at z-direction. The tip will contact the loaded surface in a contact area, which is very important for the data analysis, thus the contact area is calculated from measuring the tip area function. The tip area function can change if the tip is used for a long time. Therefore, a calibration of the area function is required, which is achieved by a standard material whose mechanical properties are known.

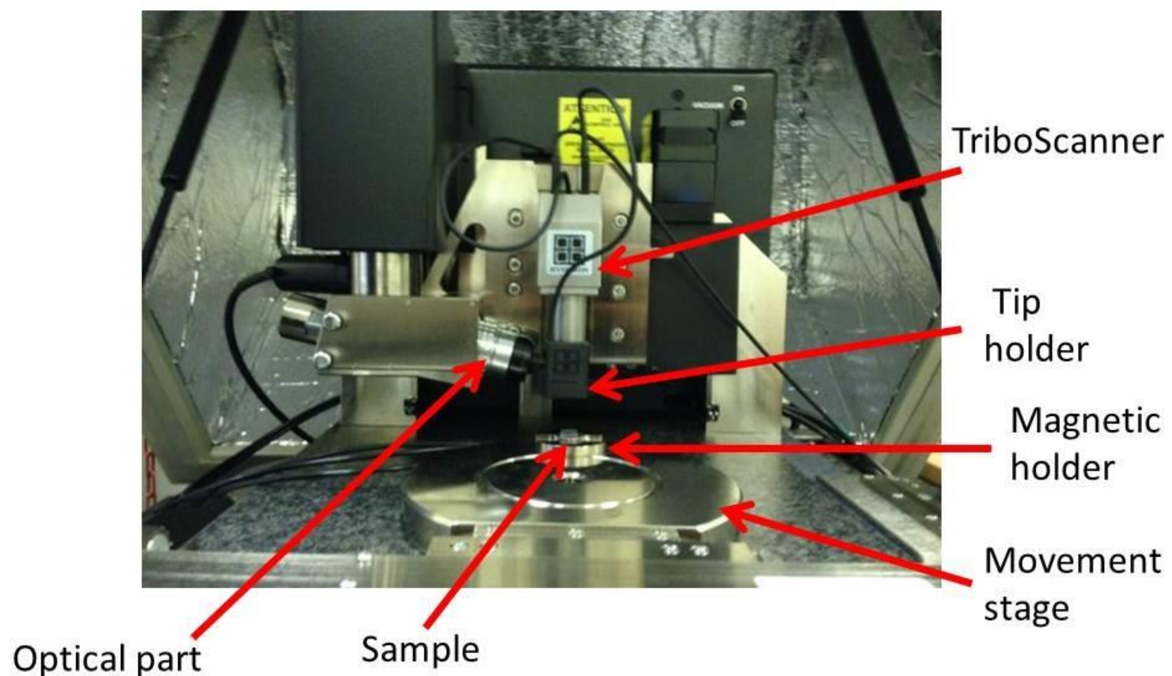

Figure 4.21 Optical image of the nanoindentation hysitron-triboscope used in this study.

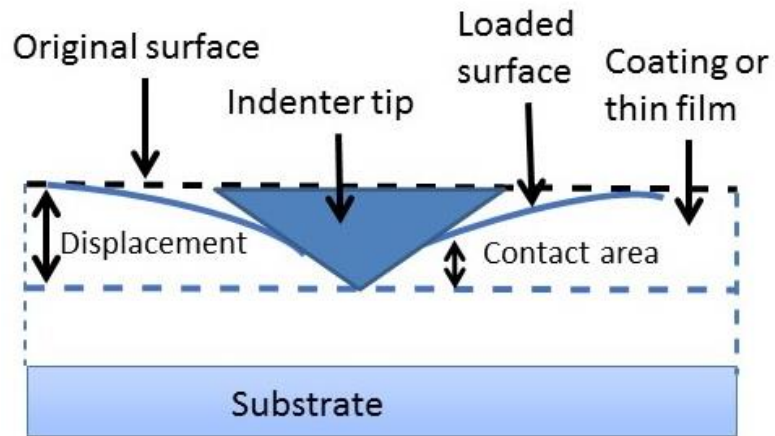

Figure 4.22 Schematic diagram of the indent process.

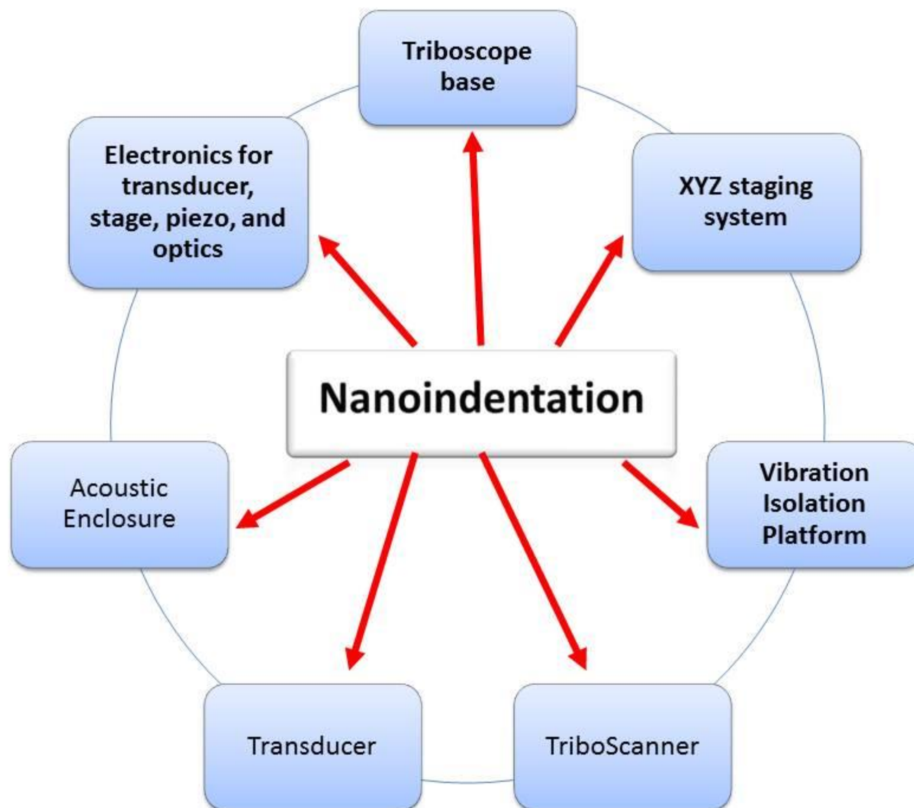

Figure 4.23 Main components of the nanoindentation technique.

The main components of nanoindentation technique are presented in **Fig. 4.23**, there include

- **The XYZ Staging System:** The XYZ staging system is used to control the sample and tip positions.
- **The Base:** The base is used to support other components of the system.
- **Triboscanner:** The Triboscanner is a very important component and is designed to produce a fine scale location of the indenter before and after performing the test. A three-axis piezo scanner is used to achieve the locating. The accuracy of the piezo scanner is considerably higher than that presented in the XYZ stage, therefore the definitive approaching of the tip from the sample surface is achieved with the scanner. Also, the Triboscanner can be set-up to measure an image of the sample surface before the test and after indentation process.
- **The Transducer:** The Hysitron Triboindenter transducer consists of three plates in a capacitor design as can be seen in **Fig. 4.24**. An indenter tip is fixed to the holder tip, which is placed in the middle of the centre plate. The middle plate is connected to the transducer frame by springs. When a DC bias is applied to the lower plate of this capacitive design, an indentation force is actuated in electrostatic effect leading to an electrostatic attraction between the middle plate with the lower plate. Hence this moves the middle plate including the tip down.

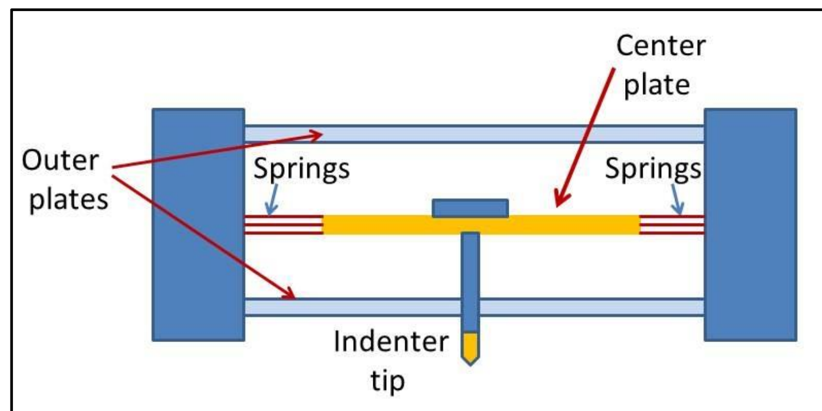

Figure 4.24 Schematic diagram of the standard transducer of a nanoindentation triboscaner.

- **The Vibration Isolation Platform:** The vibration isolation platform is a vibration system, which includes two stages with a control unit, placed below each side of the granite base and located within the acoustic enclosure. At any point, the piezoelectric accelerometers are working continuously to sense variations via an inner feedback loop.

- **The Acoustic Enclosure:** The acoustic enclosure is designed to reduce the acoustic noise coming from the environment around the system during the test.
- **The Electronics:** The electronics are divided into four separate systems, which are used to control many parts of the nanoindentation technique. They are: the piezo controller unit, transducer control unit, stage controller, and finally the optics electronics.

Nanoindentation measurements can be affected by many factors, for example: the instrument compliance, initial penetration depth, indentation size effect, indenter geometry, surface roughness, residual stress, tip rounding, sinking-in and piling-up, sample preparation, and thermal drift [24]. There are many steps, which should be taken before doing the test, including making sure the sample surface is flat by making the top and bottom surfaces parallel, cleaning the sample from dust and particles that can influence the tip and the measurements. The surface of the sample should be smooth and the roughness must be measured beforehand and should be less than the indenter depth. There are many ways to check the sample before taking measurements, including by optical microscopy or electron microscopy and checking the roughness by scanning the surface using AFM and to get 3D images. Typical, roughness between 10 to 50 nm will be suitable for indentation depth of 100 to 500 nm. In this thesis, the Berkovich tip was used and it is a very flat tip which has half angle 65.27^{o}, an included angle about 142.3^{o}, Young's modulus 1140 GPa, and Poisson's ratio 0.07. An image of the Berkovich tip is shown in **Fig. 4.25**.

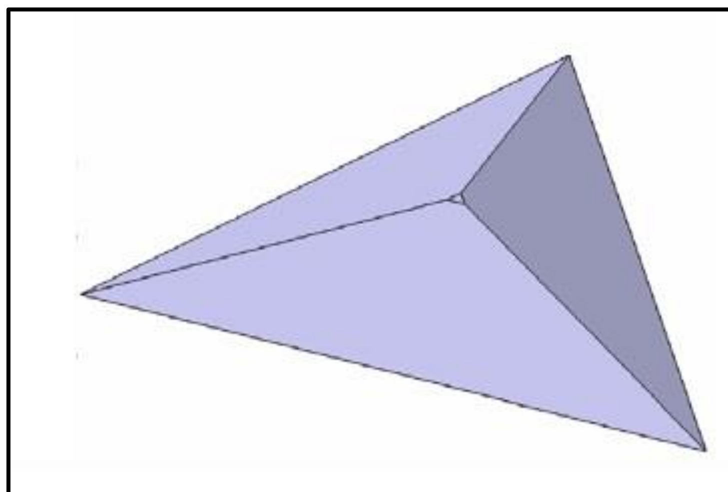

Figure 4.25 The Berkovich tip geometry taken from reference [25]

The geometry of this tip is suitable for use in standard nanoindentation for measurements of bulk and thin films at thicknesses greater than 100nm. There are many advantages of this tip: it is a sharp tip; it produces plastic deformation inside the surface of the material; and it is suitable to measure hardness and modulus parameters. The substrate can affect the measurement, therefore, to avoid the effect of the substrate the indenter depth should be ≤ 10% of the sample thickness. The effect of the substrate will be higher if the indenter goes too deep, this can affect the measurement by including measuring the substrate properties. In the thin films case, the measurement requirement is that the film needs to be ≥ 1 μm thick. Two types of test can be done, the first is to penetrate the surface with equal depths, using one cycle, in different places and the second is to partially indent with different cycles in one place as shown in **Fig. 4.26**.

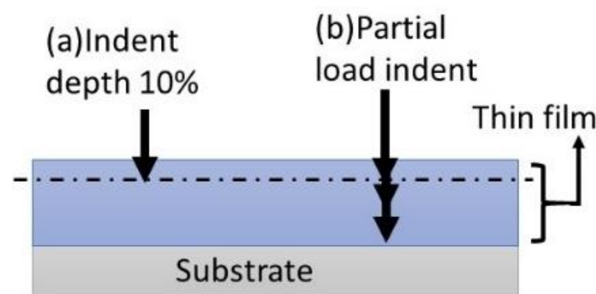

Figure 4.26 Schematic diagram of indenter depth 10% and partial load indenter of thin film.

The data can be analysed by two methods: Oliver & Pharr method [26] and Damir et al [27]. In this thesis, the Oliver and Pharr method was used to analyse the data as in **Fig 4.28**.

4.13 References

[1] K. Wasa, M. Kitabatake, and H. Adachi, Thin Film Materials Technology: Sputtering of Compound Materials, Springer: William Andrew Publishing, Inc., USA, 2004.

[2] J. A. Venables, G. D. T. Spiller, and M. Hanbücken, Rep. Prog. Phys. 47, 399, 1984.

[3] A. Javed, Ph.D. dissertation, Dept. of Materials Science and Engineering, Univ. Sheffield, Sheffield, U.K, 2010.

[4] Z. Yichena, S. Qingzhub, S. Zhulaib, Physics Procedia 32, 903 – 913, 2012.

[5] M. Ali, PhD thesis, University of Sheffield, UK, 1999.

[6] W. D. Westwood, Sputter Deposition, AVS Education Committee Book Series, Vol. 2, New York, USA, 2003.

[7] R.E. Somekh, J. Vac. Sci. Technol. A 2, (3), 1285, 1984.

[8] N. A. Morley, S.-L. Yeh, S. Rigby, A. Javed, and M. R. J. Gibbs, J. Vac. Sci. Technol. A 26, 581, 2008.

[9] Kurt J Lesker Company Ltd, Instructions Manual Issue 1, 2007.

[10] B. D. Cullity, Elements of X-ray Diffraction, Addison-Wesley Publishing Company, Inc. USA, 1977.

[11] R. W. Kelsall, I. W. Hamley, and M. Geoghegan, Nanoscale science and technology, Wiley online Library, 2005.

[12] N. Reeves Mclaren, MAT6665, Materials Processing and Characterisation, 2014, The university of Sheffield.

[13] B. E. Warren, X-ray Diffraction, Addison-Wesley Publishing Company, Inc. USA, 1968.

[14] Digital Instruments Veeco, Inc. Basic SPM Training Course, 2000

[15] Małgorzata Sowińska, Master of Science Engineer, Brandenburg University of Technology Cottbus – Senftenberg, 1986 in Gostyń (Polen).

[16] S. Tougaard, Reference Module in Chemistry, Molecular Sciences and Chemical Engineering, Elsevier, 2013,

[17] S. Foner, Rev. Sci. Instrum, 30, 548, 1959.

[18] P. T. Squire, Meas. Sci. Technol, 5, 67, 1994.

[19] N. B. Ekreem, A. G. Olabi, T. Prescott, A. Rafferty, and M. S. J. Hashmi, J. Mater. Proc. Technol. 191, 96, 2007.

[20] A. Rafferty, S. Bakir, D. Brabazon, and T. Prescott, Materials and Design 30, 1680, 2009.

[21] A. Raghunathan, J. E. Snyder, and D. C. Jiles, IEEE Trans. Magn. 45, 3269, 2009.

[22] N.A. Morley, A. Javed, M.R.J. Gibbs, J. Appl. Phys. 105, 07A912, 2009.

[23] A. Javed, N.A. Morley, M.R.J. Gibbs, J. Magn. Magn. Mater. 321, 2877–2882, 2009.

[24] Verena Maier, Benoit Merle, Mathias Göken, and Karsten Durst, J. Mater. Res., Vol. 28, No. 9, May 14, 2013.

[25] N.A. Sakharova, J.V. Fernandes, J.M. Antunes , M.C. Oliveira, International Journal of Solids and Structures 46, 1095–1104, 2009.

[26] W. C. Oliver, G. M. Pharr, J. Mater. Res., 7, 6, 1992.

[27] D. R. Tadjiev , R. J. Hand, S. A. Hayes, Philosophical Magazine, 90, 13, 1819–1832, 2010.

Chapter 5 Fabrication and Characterization of Magnetostrictive Amorphous FeSiB and FeGaSiB Films as a Function of Thickness

5.1 Introduction

The addition of Ga into a Fe crystal lattice strongly changes the functional magnetic properties (see section 3.4.1 of chapter 3), thus this chapter investigates the influence of Ga into an amorphous FeSiB film, to determine how it changes the structure, magnetic properties, and magnetostriction constant. The aim of this is to fabricate new films of FeGaSiB, which can have different properties compared to the original FeSiB films. As the thickness of thin film is a parameter which can influence the magnetic properties, this chapter describes the effect of adding Ga to FeSiB films and the effect the thickness has on both FeSiB and FeGaSiB thin films, allowing the results to be compared. The magnetostriction properties are measured via Villari effect by using the MOKE technique. The growth of amorphous magnetostrictive FeSiB and FeGaSiB thin films by co-sputtering-evaporation technique with their magnetic properties in comparison with those of rapid quench such as the FeSiB ribbons have been investigated.

5.2 Fabrication of The Films

5.2.1 Fabrication of FeSiB Thin Film

For the growth of FeSiB films, the co-sputtering–evaporation technique [1], as described in detail in chapter 4, was used. They were grown in a thickness range from 24 to 100 nm. The films were deposited on a Si substrate (100) with dimensions 10 mm x 15 mm, which is suitable for magnetostriction measurement without being broken by the bending tool as the Si wafer is a brittle material. The fabrication parameters for the FeSiB films were a fixed chamber pressure (p_{Ar}) of 4 µbar, sputter power (P_{FeSiB}) of 20 W, and Ga evaporation rate of zero. Three Si substrates were used per film growth, each attached to a glass slide using polymethyl methacrylate (PMMA). The sputter target was Metglas 2605SA1 with composition $Fe_{85}Si_{10}B_5$. This film composition was chosen for this study as it has soft

magnetic properties, as well as being amorphous and to compare its properties before and after adding the Ga atoms.

5.2.2 Fabrication of FeGaSiB Thin Films

For the growth of FeGaSiB films, the co-sputtering–evaporation technique [1], described in detail in chapter 4, was also used. Using the same technique to deposit both film sets will avoid any changes in properties due to use of different deposition systems, as the properties of films can change from one technique to another. The films were grown with a thickness range from 24 to 100 nm. The films were deposited on Si substrate (100) with dimensions 10mm x 15mm at a fixed chamber pressure (p_{Ar}) of 4 μbar, sputter power (P_{FeSiB}) of 20 W, and Ga evaporated with a constant rate, R_{Ga} = 0.2 (arbitrary unit). Again, three Si substrates were used per film growth, attached to a glass slide using polymethyl methacrylate (PMMA). The same Metglas 2605SA1 targets with composition $Fe_{85}Si_{10}B_5$ were used with a Ga (99.99%) ingot in the evaporator.

5.3 Thickness Calibration

For both sets of films, to determine the film thickness accurately, a PMMA blob was put on one Si substrate before growth using a toothpick. After growth, the PMMA blob was washed away using acetone, to leave a sharp edge, so that the film thickness could be measured. The thickness was measured by the AFM technique (section 4.9.2), in tapping mode.

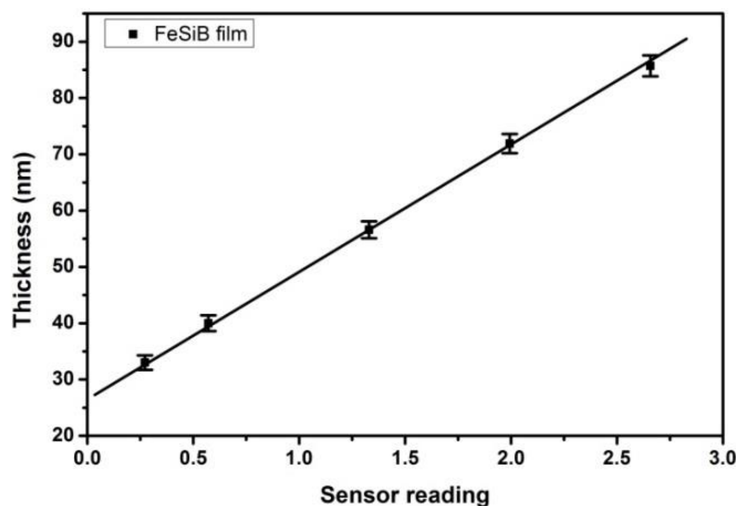

Figure 5.1 Thickness calibration of FeSiB films as a function of the chamber rate meter sensor reading.

Figure 5.1 shows the linear relation between the film thickness and the sensor reading of the rate of deposition of FeSiB films. This reading is achieved by the FeSiB rate monitor, placed nearby to the substrate, which has been calibrated for FeSiB films. For this set of films, the sputtering deposition rate was about 1.5 nm/s.

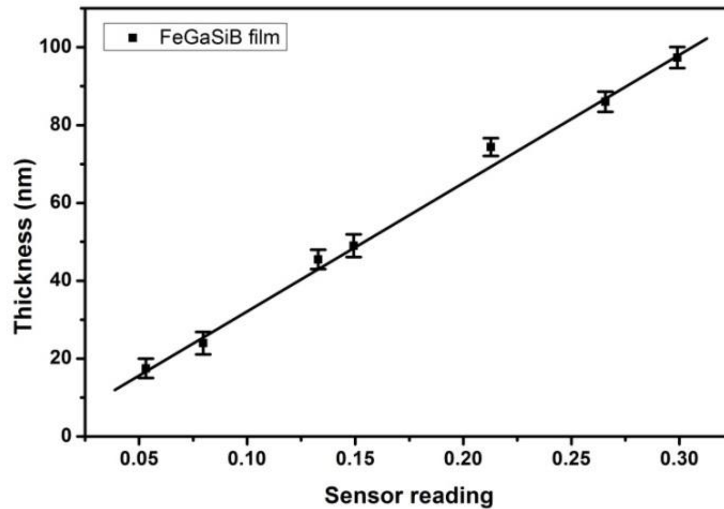

Figure 5.2 Thickness Calibration of FeGaSiB films as a function of chamber rate sensor reading.

Figure 5.2 shows the linear relation between the thickness in nanometres and the sensor reading of the deposition rate of FeGaSiB films. For this set of films, the sputtering deposition rate was about 0.1 nm/s. It was found that adding Ga atoms to FeSiB films decreased the deposition growth rate of the films. This could be due to the inelastic collisions of particles, which lead to the particle's speed decelerating down and hence reducing their kinetic energies arriving at the substrate.

5.4 Films Characterization

The Bruker D2 phaser technique, X-ray diffraction (XRD) with Cu $K_{\alpha 1}$ 1.54184 Å, in θ/2θ mode was used to analyze the film's structure. The 2θ range from 30 to 80° was used to check the structure of the film (for bcc Fe 2θ ~ 45° and for bcc Fe-Ga 2θ ~ 45°) and silicon substrate (2θ = 69.8°, 61.7°, and 33°) and to make sure that the film was positioned correctly in the machine, while the 2θ range from 35 to 55° was used to study the film structure at a higher resolution, so avoiding the Si substrate peaks. XRD analysis was carried out to determine whether the films were fully amorphous or if they contained nanocrystalline clusters within an amorphous matrix. X-ray Photoelectron Spectroscopy (XPS) using a

thermo theta probe, with parameters of pass energy of 40 eV, dwell time 100 ms (10 scans total for high resolution) and a monochromated Al K_{α} X-ray as a source was used to determine the composition of the films. For each film, three XPS runs were done in three different places on the film surface and an average was taken. Atomic force microscopy (AFM) was used, in tapping mode, to measure the thickness of the samples using the step produced in fabrication and to study the topography and roughness.

The DMS model 10 vibrating sample magnetometer (VSM) was used to determine the magnetic moment of the films at room temperature, using an applied field of 40 kA/m, from which the saturation magnetization was calculated. In the transverse mode, the magnetic properties of the two film sets were measured on a magneto-optical Kerr effect (MOKE) magnetometer, with the maximum magnetic field applied being 40 kA/m, which was sufficient to saturate the films. Characterization of the magnetic properties was carried out by measuring the normalized hysteresis loops. The magnetic anisotropy and saturation fields were determined by measuring the normalized hysteresis loops at different magnetic field directions with respect to the sample, with angles from 0° to 180°. To measure the magnetostriction constant (λ_s) [2] at room temperature, the inverse magnetostrictive effect (Villari effect) [3, 4] measurement was used.

5.5 Structural Properties

5.5.1 XRD Results

To understand the films structure and functional properties, the target material was also studied. A 23µm Metglas 2605SA1 sputter target in the Lesker system (see section 4.7) was cut from the Metglas 2605SA1 ribbon (dimensions 10mm x 15mm), with composition $Fe_{85}Si_{10}B_5$ and was measured using XRD.

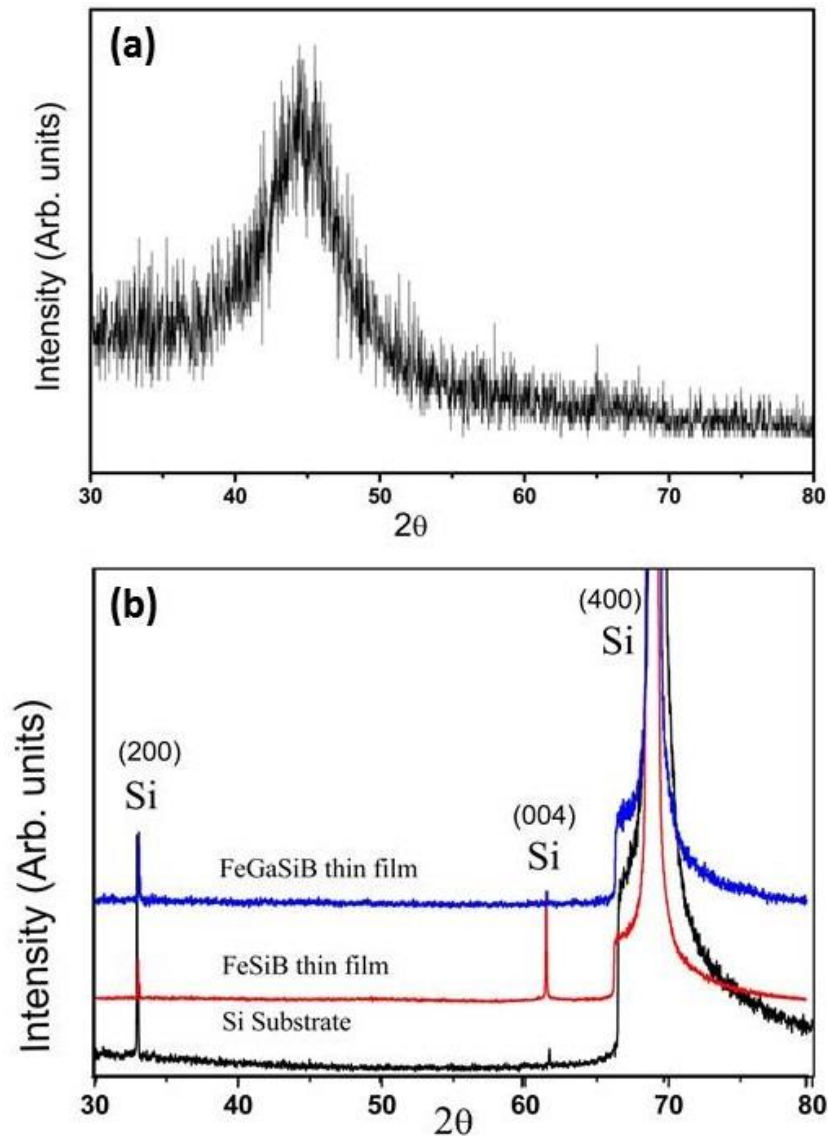

Figure 5.3 X-ray diffraction of (a) 23µm ribbon, the target of Metglas 2605SA1 with composition $Fe_{85}Si_{10}B_5$ (b) 86 nm FeSiB and FeGaSiB thin films and 380 µm Si substrate.

Figure (5.3) shows the XRD patterns of (a) 23 µm ribbon, the target of Metglas 2605SA1 with composition $Fe_{85}Si_{10}B_5$ and (b) 86 nm FeSiB and FeGaSiB thin films and 380 µm Si substrate. **Fig. 5.3 (a)** shows the XRD pattern of the target used in this study, a single broad peak is observed at $2\theta \approx 45^o$, as the amorphous phase has no long-range order, therefore the incident X-rays are dispersed randomly in different directions leading to no sharp narrow peaks present in the XRD pattern. Thus the target showed an amorphous bump, hence has an amorphous structure. **Fig. 5.3 (b)** presents the XRD results for 86 nm FeSiB and 86 nm FeGaSiB thin films deposited on 380 µm Si substrates, and the 380 µm Si substrate without film. It was found that both films were amorphous, as the only peaks observed were for the Si substrate and there was no evidence of crystalline peaks for either of the FeSiB and FeGaSiB films. It was found that the main diffraction peak of Si (100) was at $2\theta = 69.8^o$ corresponding to the Si (400) direction and other Si peaks found at 2θ 61.7^o and 33° corresponding to the Si (004) and (200) directions respectively.

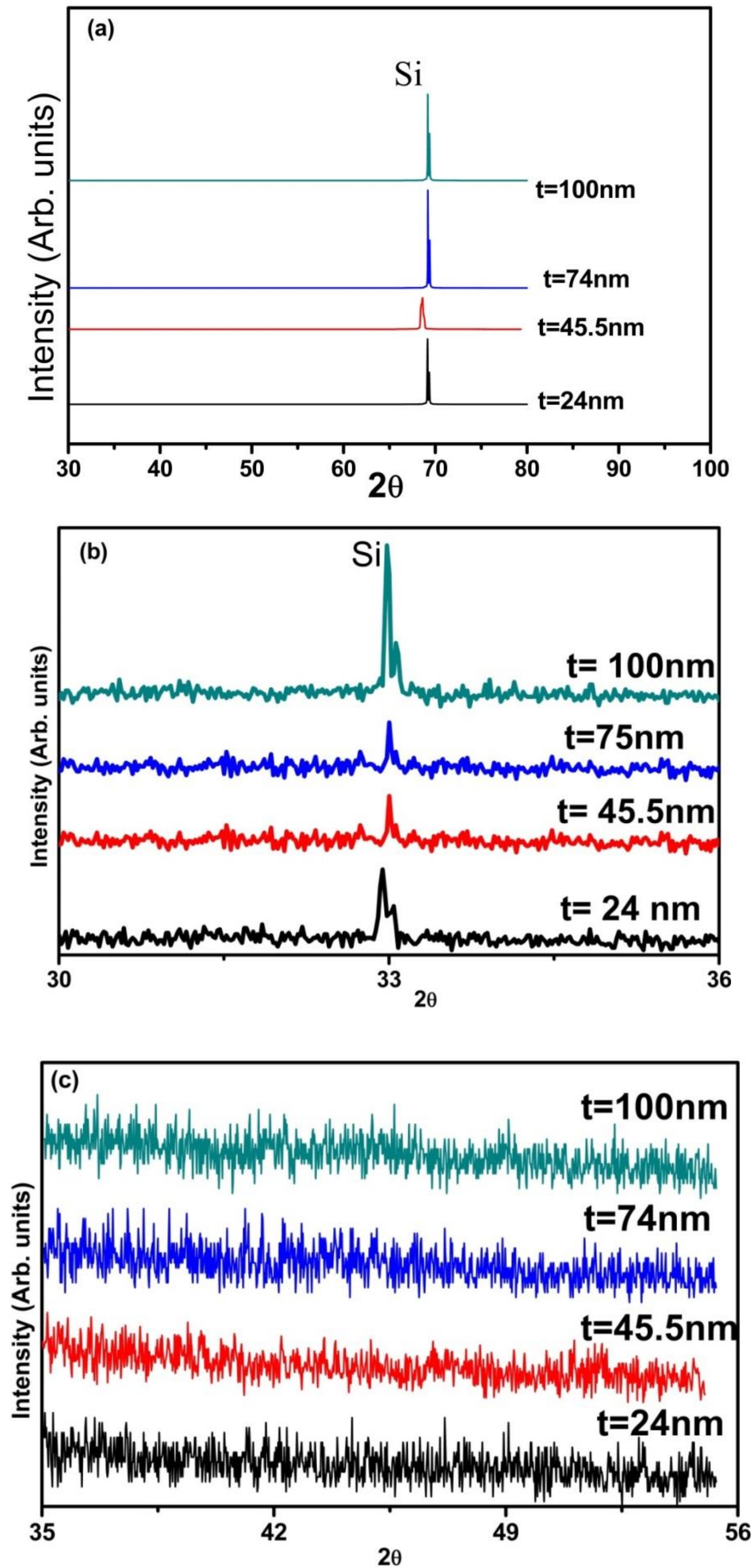

Figure 5.4 XRD patterns of (a) FeGaSiB thin films with increasing the thickness, (b) Si substrate peaks for the 2θ range from 30° to 36°, (c) XRD of FeGaSiB film for the 2θ range from 35° to 55°.

Figure 5.4 shows the XRD patterns for FeGaSiB thin films with increasing the thickness, **Fig. 5.4 (b)** represents the XRD of Si for the 2θ range from 30° to 36°, **Fig. 5.4 (c)** illustrates the XRD of FeGaSiB film for the 2θ range from 35° to 55°.

From **Figs 5.4 (a, b, c)**, it is observed that there are no peaks at 2θ ~ 45° for the thickness range from 24 nm to 100 nm of the FeGaSiB film, which is where the Fe-Ga films (110) texture peak would occur [5]. Thus, it is concluded that the addition of Ga into the FeSiB films for all thicknesses did not change the film morphology, as they were all amorphous. To be sure that the D2 phaser XRD technique able to detect the crystalline peaks of films with thickness 50 nm and to support that the films in **Fig 5.4** are amorphous, it was necessary that to present the XRD results of FeCo film which was tested by the D2 phaser XRD technique (see **Fig. 5.5**).

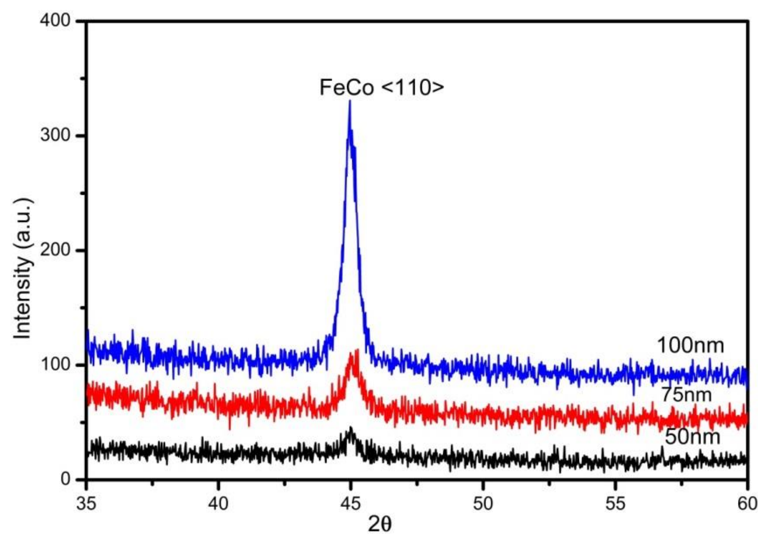

Figure 5.5 XRD patterns of FeCo film with different thicknesses tested by the D2 phaser technique.

5.5.2 XPS Results

From the XPS results, it was found that the FeGaSiB films had the composition $Fe_{82}Ga_7Si_5B_6$. It is clear for these fabrication parameters, that the Ga replaces more of the Si atoms than the Fe and B atoms in the $Fe_{85}Si_{10}B_5$ target. This could be due to the Ga being heavier than the Si, so causing more collisions within the plasma, hence allowing fewer atoms to reach the substrate. The fitting of data and more details about the calculation of the film's composition are presented in an appendix attached at the end of this thesis.

5.5.3 AFM Results

The AFM data determined that the films thickness range was from 24±2 nm to 100±2 nm. The thicknesses were also used to calibrate the growth sensor for the FeSiB and FeGaSiB films (see section 5.3).

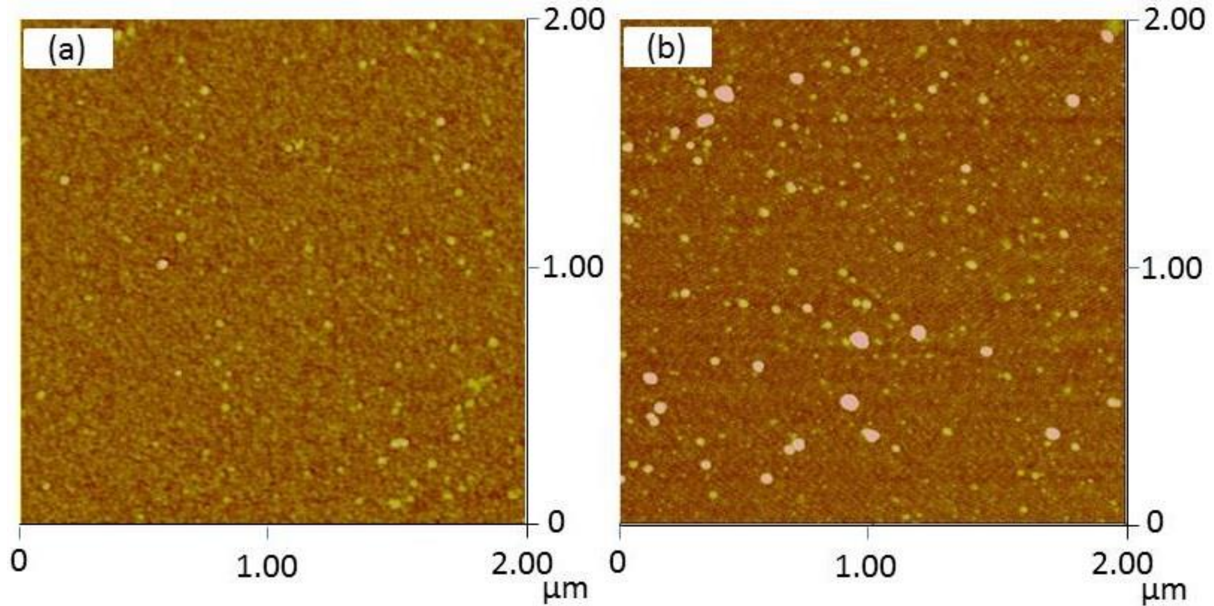

Figure 5.6 AFM image scan of the (a) 25 nm FeSiB film and (b) 24 nm FeGaSiB film. The scan size was 2x2 µm.

Figure 5.6 shows the surface topographic images of (a) 25 nm FeSiB film and (b) 24 nm FeGaSiB film. The film's surface of 25 nm FeSiB film had an average roughness (R_a) of 0.191 nm with a root mean square (Rms) surface roughness of 0.257 nm, while the film's surface of FeGaSiB film had an average roughness (Ra) of 0.376 nm with an average root mean square (Rms) surface roughness of 0.745 nm. The larger Ra and RMS of the FeGaSiB film were due to the 24 nm spots on the surface. Since both the films had a smooth surface, and no grains were observed, this confirms that the films were fully amorphous, when compared with AFM images of polycrystalline films such as FeGa [6]. The white spots observed are believed to be due to contamination on the surface, likely to be Ga, which has been observed before using this fabrication technique [6].

5.6 Magnetic Properties

5.6.1 Magnetic Properties Measured by MOKE

The magnetic properties were measured using a magneto-optical Kerr effect (MOKE) magnetometer, in the transverse mode, with the DC magnetic field being large enough to saturate the films (Max field applied was 40 kA/m). The MOKE magnetometer is a surface sensitive technique with a skin depth of ~20 nm [7] therefore, normalized magnetic hysteresis loops were measured to characterize the films' magnetic properties. This was done with the assumption that the loops measured were consistent for the full film thickness, although only ≈ 20 nm within the magnetic film surface was probed. For each film, normalized hysteresis loops were measured by rotating the film within the magnetic field at different angles from 0° to 180° with 30° steps to study the magnetic anisotropy, i.e. to see if they are magnetically isotropic or if they had magnetic anisotropy induced within them. This is done by measuring the hysteresis loops via MOKE magnetometer along with the chosen angles. If the films have magnetic anisotropy, then the strength of the anisotropy can also be determined. For example, if they exhibited a hard loop and an easy loop at 90° to each other, this means that the film has a strong uniaxial anisotropy. For each normalized loop, the loop was measured 10 times and an average taken.

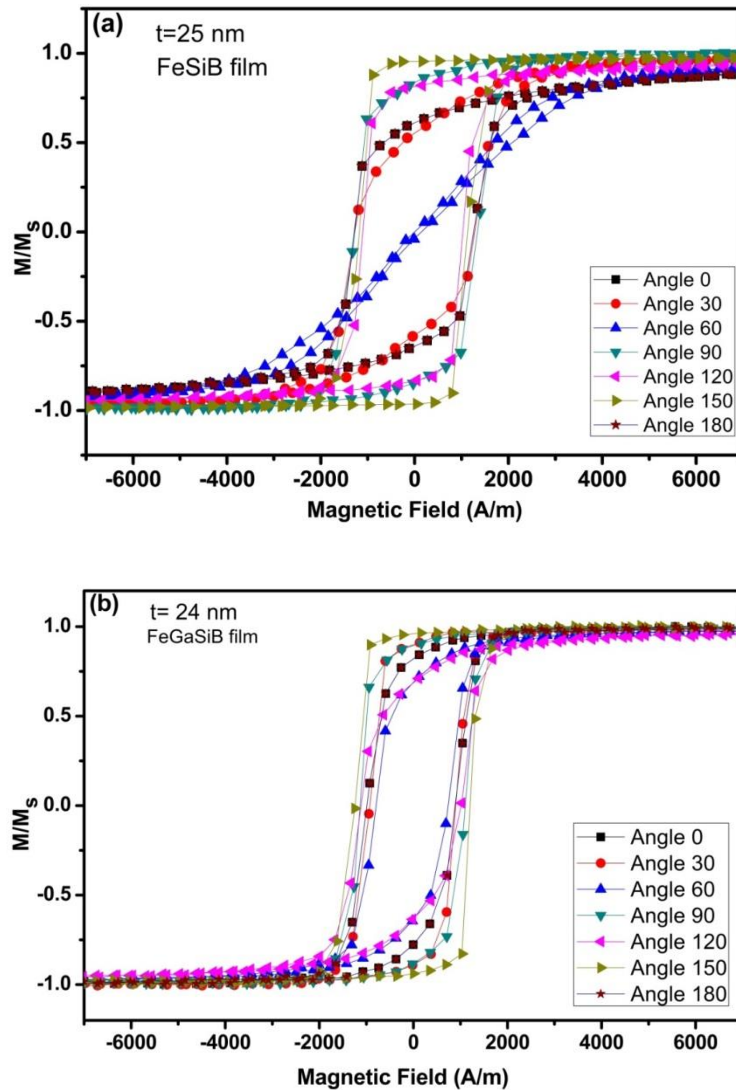

Figure 5.7 the hysteresis loops of (a) 25 nm FeSiB film and (b) 24 nm FeGaSiB film with different angles in degree unit.

Figure 5.7 compares the normalized hysteresis loops of 25 nm FeSiB film, at different angles of applied magnetic field and the normalized hysteresis loops of 24 nm FeGaSiB film. From **Fig. 5.7 (a)**, the 25 nm FeSiB film had a strong uniaxial anisotropy, with the hard loop at an angle 60° with anisotropy field (H_k) ≈ 4854 A/m and coercive field (H_c) 59 A/m. Therefore, for the film along the 60° direction, a higher magnetic field is needed to reach the saturation magnetization, while the easy loop at angle 150°, with anisotropy field, H_k, ≈2363 A/m and coercive field 1133 A/m, therefore the film along the 150° direction is easy to magnetize.

Figure 5.7 (b) shows the normalized hysteresis loops of 24 nm FeGaSiB film, and shows that adding 7% Ga (with Ga evaporation rate 0.2) into FeSiB, removed the strong uniaxial anisotropy from the film as no "hard loop" is observed, as can be seen for the FeSiB film at 60°. For the FeGaSiB film at 60°, the loop had saturation field of about 1949 A/m and coercive field (H_c) 939 A/m. The average coercive field for all the loops of the 24 nm FeGaSiB film was about 1024 A/m. This suggests that the presence of Ga within the film decreased the saturation field of the films. Hence, removed Ga doping the strong uniaxial anisotropy observed in the FeSiB film, and resulted in the FeGaSiB film having magnetically very weak anisotropy. The change in coercivity could be due to the change in stresses, which works as pinning sites to the domain wall movement, and is a reason for changes in the coercivity.

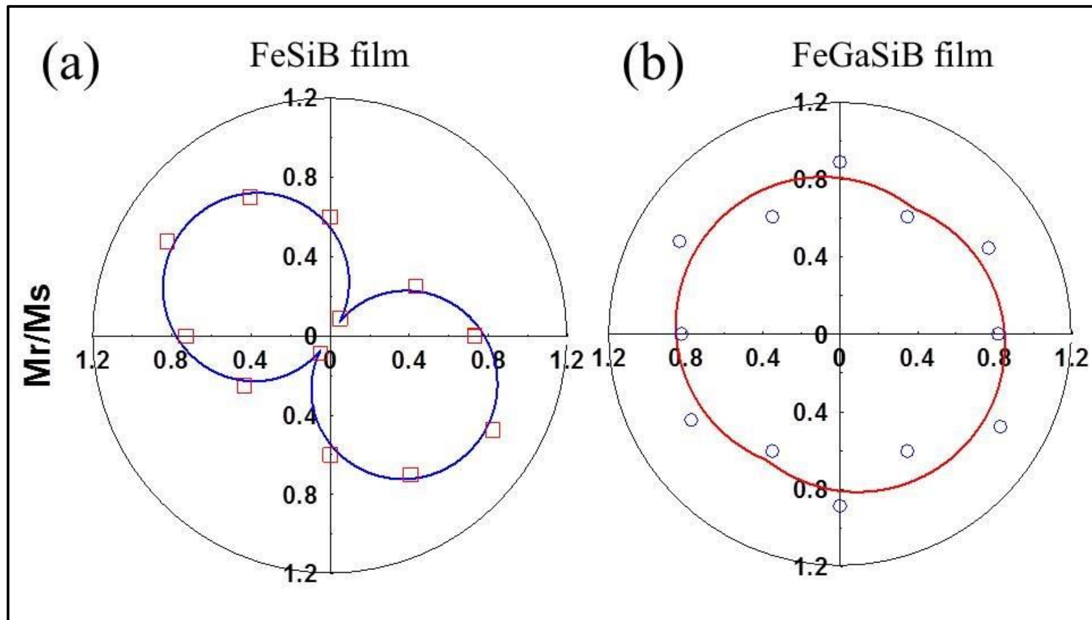

Figure 5.8 Angular plot of the remanence ratio (M_r/M_s) of (a) 25 nm FeSiB film and (b) 24 nm FeGaSiB film. The lines are a fitting to the M_r/M_s data using equ. (5.2).

The uniaxial anisotropy can be quantified by fitting the following equation [8] to the M_r/M_s as a function of angular data (**Fig. 5.8**):

$$\frac{M_r}{M_s} = D|cos\ (\theta_e - \theta_o)| + c \tag{5.2}$$

Where D refers to the strength of the uniaxial anisotropy, θ_e is the angle between the easy axis and the field, θ_o is the angle between the easy axis and the side of the film, and c is the

lowest measured ($\frac{M_r}{M_s}$). For an isotropic film, D = 0, as M_r/M_s is a constant, while for D < 0.5 the anisotropy within the film is weakly uniaxial and for D > 0.5, the anisotropy is strongly uniaxial.

Fig. 5.8 (a) shows the angular plot of normalized remanence magnetization (M_r/M_s) of 25 nm FeSiB film, it can be seen that a strong uniaxial anisotropy is observed with D = 0.83. While **Fig. 5.8 (b)** presents the angular plot of normalized remanence magnetization (M_r/M_s) of 24 nm FeGaSiB film, with D = 0.11, so exhibits very weak anisotropy. It is found that increasing the thickness of the FeSiB films decreases the anisotropy within the films to very weak anisotropy. While increasing the thickness of FeGaSiB film did not affect the magnetic anisotropy and it had a very weak anisotropy for all the thickness range. Thus adding Ga removed the strong uniaxial anisotropy of the FeSiB film to have magnetically very weak anisotropy where D = 0.11 for these films. Thus suggests that the presence of Ga, with increasing the thickness reduced the local stresses within the film, which is one source of uniaxial anisotropy.

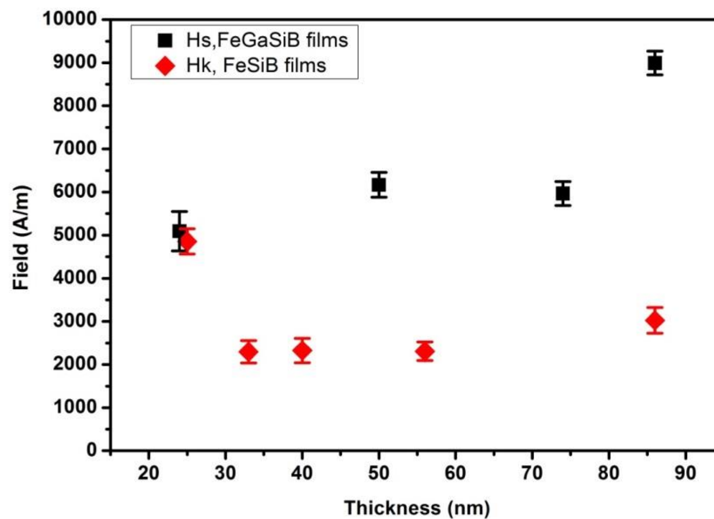

Figure 5.9 Anisotropy and saturation fields as a function of thickness, for the hard loop, for FeSiB and FeGaSiB thin films.

The magnetic anisotropy of the films can be influenced by the thickness and it can be changed from one film to another. Adding the Ga can affect the film magnetically. Therefore, as the FeGaSiB films had very weak anisotropy, a saturated field, H_s rather than anisotropy field from the hysteresis loops was determined. **Fig. 5.9** shows the comparison of the anisotropy and saturation fields as a function of thickness for the FeSiB and FeGaSiB thin

films respectively, prepared under the same growth conditions. The FeSiB films have uniaxial anisotropy, this means they have easy and hard loops as a function of applied field angle, thus an anisotropy field was determined from the normalized hard axis, as the field where the normalized magnetization reached 1 (or -1). It was observed that the anisotropy fields for the FeSiB films decreased with increasing thickness (**Fig. 5.9**). While the FeGaSiB films have very weak anisotropy, this means they have almost the same shape hysteresis loops for all applied field angles, thus a saturated field is determined from the hysteresis loops, again at the field where the normalized magnetization reached either 1 or -1. It was found that the FeGaSiB films saturation fields increased with the increasing thickness (**Fig. 5.9**). Thus the addition of Ga has not only changed the anisotropy from uniaxial to very weak anisotropy [9] but has also changed the distribution of the magnetic atoms with increasing thickness leading to an increase in the saturation field.

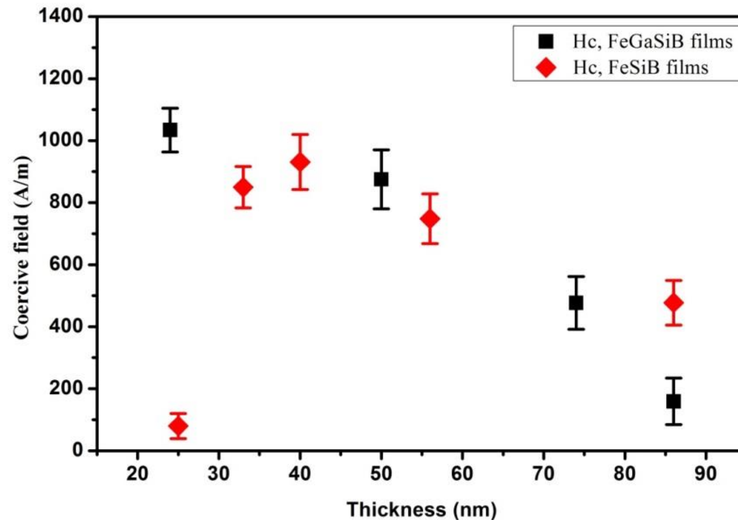

Figure 5.10 Coercive fields as a function of thickness, along hard loop, for FeSiB and FeGaSiB films.

Figure 5.10 shows the coercive fields for both film sets along the hard loop axis. For the FeSiB films, the coercive field increases with thickness up to 40 nm, then decreases for films thicker than 40 nm. While for the FeSiGaB film, the coercive field decreased as the thickness increased. Such that for the thicker films (>50 nm), the coercive field of the FeGaSiB films were lower, i.e. for the 86 nm FeGaSiB film, H_c = 0.159 kA/m which was a factor 5 smaller than the 86 nm FeSiB film (H_c = 4.775kA/m). The films deposited by the sputtering suffer most from two types of stresses: extrinsic stresses, which arise from the difference between the thermal expansion coefficients of the substrate and the film; and intrinsic stresses, which

arise due to the growth parameters of sputtering. It was found that the coercivity decreased from 1.3 kA/m to 0.3 kA/m when the thickness increased from 10 nm to 100 nm for amorphous FeSiBC films [10], suggesting that a reduction in coercivity with increasing the thickness could be due to reducing the residual and inhomogeneous stresses present with increasing the thickness of the films and reducing the pinning of domain walls [10].

5.6.2 Magnetic Properties Measured by VSM system.

The fabrication of amorphous magnetostrictive thin films by co-sputtering-evaporation technique with their magnetic properties in comparison with those of rapid quench such as melt-spun ribbons have been investigated using a VSM system. Two types of films, 86 nm FeSiB, and 86 nm FeGaSiB were compared with a 23 μm ribbon in this study. A VSM system was used to measure the saturation induction of the samples at room temperature (300 K) with an applied field of 39.788 kA/m. The VSM is a non-surface sensitive technique compared with MOKE, so measures the whole sample volume. For this measurement, samples with dimensions 3 mm x 3 mm were cut from the original film samples 10 mm x 15 mm and from the 23 μm FeSiB ribbon (the target in this study). The system measured the magnetic moment as a function of applied field. The saturation magnetization was calculated from the saturation magnetic moment per unit volume. Multiplying the saturation magnetization by permeability μ_o can give the saturation induction. From the saturation induction data measured, **Fig. 5.11**, it is observed that the saturation induction of the 23 μm Metglas FeSiB ribbon, which was used to produce both film sets, was $\mu_o M_s = 1.56\ T$, which is found to be the same as the data given by from the manufacturing company [11]. For the 86 nm FeSiB thin film, the saturation induction was $\mu_o M_s = 1.15\ T$, which is lower than the saturation induction of the target sample. This difference could come from the small differences in area of samples as the magnetic moment is affected by the size of the sample and the big difference in thickness, where the thickness can influence the magnetic properties of samples. For the 86 nm FeGaSiB thin film, the saturation induction was $\mu_o M_s = 0.96T$. Thus, adding Ga atoms, which are nonmagnetic into FeSiB films reduced the saturation induction from 1.56 T for the ribbon to 0.96 T. Another difference observed from this figure is the difference in the shape of the hysteresis loops, this difference of hysteresis loops has been observed by Ref. [10] for both of ribbon and amorphous FeSiBC films. The target loop is a “hard loop” i.e. one that has no coercive field and shows moment rotation of the magnetization within the ribbon. While both the FeSiB and FeGaSiB films showed “easy

loop", i.e. the magnetization switches direction abruptly and hysteresis is observed. This difference could come from in-plane applied field, along the hard direction to the target sample and easy direction for the FeSiB sample as these films had uniaxial anisotropy. Another reason identified, is that there is a domain wall pinning within the film, due to its thickness, but not in the target which is thicker.

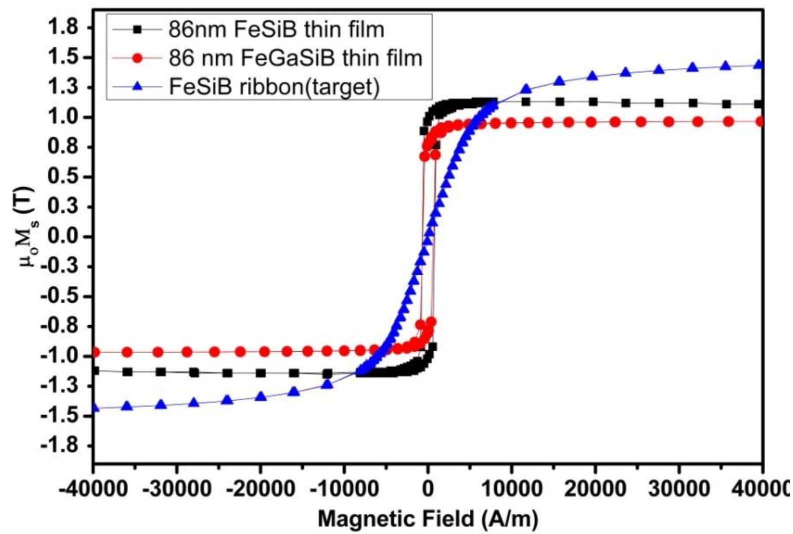

Figure 5.11 Saturation induction as a function of magnetic field at room temperature for the 86 nm FeSiB, 86 nm FeGaSiB film and 23 µm ribbon (Target) FeSiB.

The FeSiB ribbon (target) had a very low coercive field of about 47 A/m, while the 86nm FeSiB film and 86nm FeGaSiB film had coercivities of about 724 A/m and 628 A/m respectively.

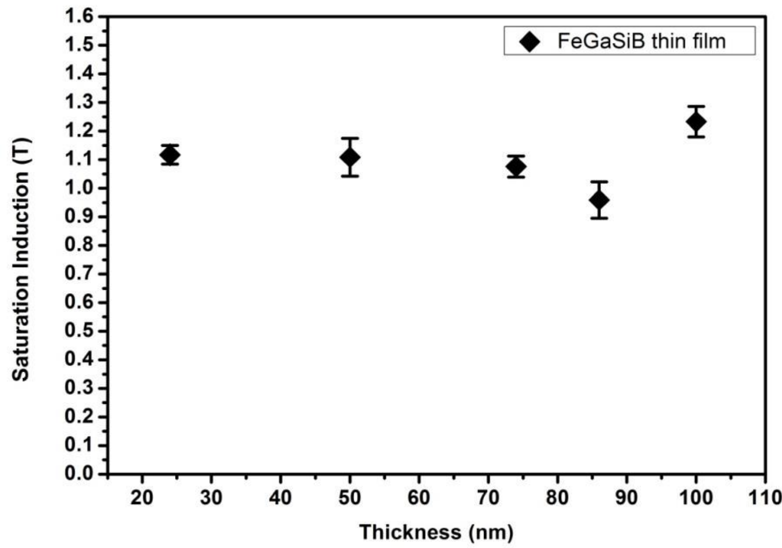

Figure 5.12 Saturation induction as a function of thickness of the FeGaSiB thin films.

Figure 5.12 shows the saturation induction for all the FeGaSiB thin films as a function of thickness. It can be seen that the saturation induction changed slightly with the thickness, from 1.1T for the 24 nm films to 0.96 T for the 86 nm film and then increased to 1.23 T for the 100 nm. This change in saturation induction as a function of thickness for the same composition is due to the amorphous nature of the films, as the atoms have no long-range order, only short-range order. This means that the nearest neighbour atoms change from film to film. The magnetic moment of Fe atoms depends on the nearest neighbours and the saturation magnetization is an average of the moments, which will change for each film. This effect of the nearest neighbour atoms is the likely reason that the 100 nm films has a higher saturation magnetization compared to the other films. A similar effect was observed for crystalline $Fe_{40}Co_{60}$, where the saturation induction is higher when the sample has an ordered bcc structure compared to a disordered fcc structure [12]. As the FeGaSiB films are amorphous and have no long-range order or set lattice constant, between films the nearest neighbours to the Fe will differ; this will change the saturation induction of the films.

5.7 Magnetostriction Properties

The magnetostriction constant (λ_s) was determined via the Villari effect [13] at room temperature (see section 4.10). This involved using a set of bending tools with different radii (R), which induce a strain within the film. The film's hysteresis loops were measured for each bend radii on the MOKE magnetometer. From the loops, the straight line method, determined in chapter 4, was used to determine the anisotropy field (H_k) induced by the strain [14]. The H_k was plotted as a function of the inverse bending radii (1/R) and magnetostriction constant (λ_s) was calculated using equation (4.5) chapter 4 [14, 15].

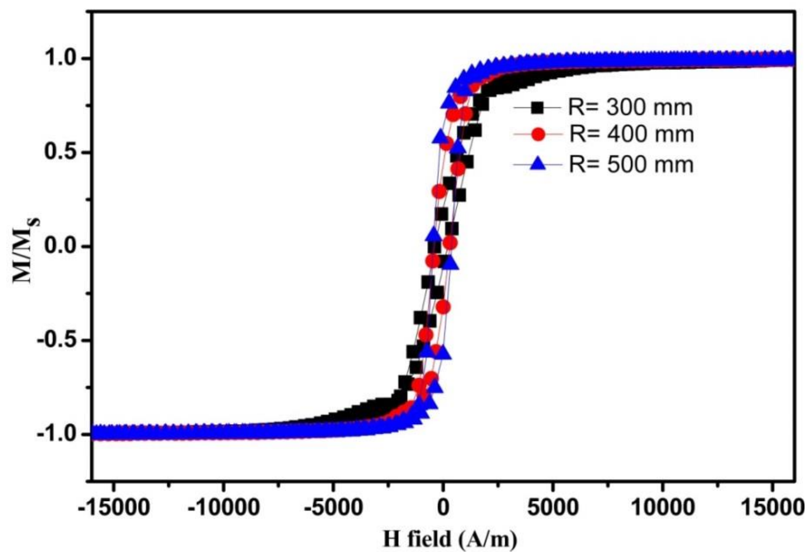

Figure 5.13 Magnetization curves for FeGaSiB thin film, a bended film with three bend radii.

Figure 5.13 shows the hysteresis loops, for three bend radii, R, (300, 400, and 500 mm) for the 74 nm FeGaSiB film, where it can be seen that there is a change in the loop shape. The difference is due to the effect of the strain on the magnetization of the film resulting from the bending. From these loops, the different saturation fields at each radius were determined and plotted against (1/R). The slope of this plot gives the result of the first term in equation (4.5).

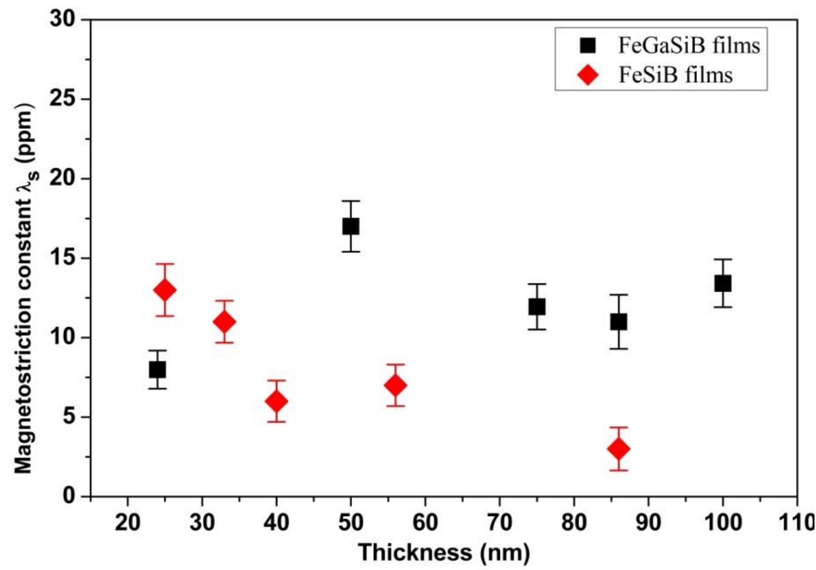

Figure 5.14 Magnetostriction constants for FeGaSiB and FeSiB films as a function of thickness.

Figure 5.14 shows the change in magnetostriction constant (λ_S) with thickness. It is observed that the FeGaSiB films have higher magnetostriction constants than the FeSiB films for thicknesses over 40 nm. The 50 nm FeGaSiB film had the largest λ_S of 17 ppm. For the FeSiB films, λ_S decreased with the increasing thickness, while for the FeGaSiB films with $t >$ 50nm, λ as approximately constant at 13 ppm but were still higher than the FeSiB films. This means adding Ga into the FeSiB thin films increased the magnetostriction constant by giving the amorphous structure dilation by increasing the space between the atoms because the radius of Fe atoms is slightly lower than the radius of Ga atoms. This would also reduce the inhomogeneous strain, which can be the reason the films anisotropy changed from uniaxial to almost isotropic. Compared to the crystalline Fe-Ga films, the saturation fields for the amorphous FeGaSiB films were a factor 50 smaller, while the magnetostriction constants were a factor 2.5 smaller. Thus the saturation field has been reduced, but so has the magnetostriction constant.

5.8 Summary

The FeSiB and FeGaSiB films, deposited under the same growth conditions by co-sputtering-evaporation technique, were studied. The structural, magnetic, magnetostriction properties of these films were investigated over a range of thicknesses. The aim of this work was to investigate the effect of adding the Ga to FeSiB film as a function of thickness. Different techniques were used to investigate these films including: XRD, XPS, MOKE magnetometry, and VSM.

The XRD showed that for both film sets, there was no sign of crystalline peaks observed, hence confirming an amorphous structure. The XPS result showed that the FeGaSiB film had a composition of $Fe_{82}Ga_7Si_5B_6$, which informs that the Ga was successfully added within the FeSiB film. The MOKE measurements of the magnetic properties showed that the FeGaSiB film had different magnetic properties of the FeSiB films, thus were affected by the addition of Ga.

The comparison between FeSiB and FeSiGaB films showed that the anisotropy and saturation fields increased as a function of thickness. For all the thickness range, the saturation field of the FeSiGaB films was higher than the anisotropy field of the FeSiB films. The comparison between FeSiB and FeSiGaB films showed that the coercive field decreased as the thickness increased. The comparison between the FeSiB ribbon, FeSiB film, and FeGaSiB film showed that adding Ga in at 7% reduced the saturation induction from 1.56T to 0.96T.

The saturation induction for the FeGaSiB thin films as a function of thickness showed that the saturation induction changed slightly with the thickness, from 1.1T for the 24 nm films to 0.96 T for the 86 nm film and then increased to 1.23 T for the 100 nm. This change is due to the amorphous nature of the films, as the atoms have no long-range order, only short-range order. This means that the nearest neighbour atoms change from film to film.

The result of magnetostriction properties, which were measured via Villari effect by the MOKE technique, showed that the FeGaSiB films have higher magnetostriction constants than the FeSiB films for thicknesses over 40 nm. The 50 nm FeGaSiB film had the largest λ_s of 17 ppm. For the FeSiB films, λ_s decreased with the increasing thickness, while for the FeGaSiB films with $t > 50$nm, λ_s ~13 ppm but were still higher than the FeSiB films.

5.9 References

[1] N. A. Morley, S. L. Yeh, S. Rigby, A. Javed, and M. R. J. Gibbs, *J. Vac. Sci. Technol. A*, vol. 26, no. 4, pp. 581–586, 2008.

[2] A. Javed, N. A. Morley, M. R. J. Gibbs, Journal of Applied Physics, vol. 107, p. 09A944, 2010.

[3] A. Javed, T. Szumiata, N.A. Morley, M. R. J. Gibbs, Acta Materialia, vol. 58, p. 4003-4011, 2010.

[4] B. Kundys, Yu. Bukhantsev, H. Szymczak, M.R.J. Gibbs, R. Zuberek, J. Magn. Magn. Mater., 258–259, 551–554, 2003.

[5] B. W. Wang, S. Y. Li, Y. Zhou, W. M. Huang, S. Y. Cao, *J. Magn. Magn. Mater*., vol. 320, pp. 769-773, 2008.

[6] A. Javed, N. A. Morley, M. R.J. Gibbs, *J. Magn. Magn. Mater*., vol. 321, pp. 2877-2882, 2009.

[7] M. D. Cookea, M.R.J. Gibbsa, R.F. Pettifer, *J. Magn. Magn. Mater*. 237, pp. 175–180, 2001.

[8] E. Miskevich, F. K. Alshammari, W-G. Yang, J. Sharp, S. Baco, Z. Leong, Q. A. Abbas, N. A. Morley, *J.Phys. D: Appl. Phys.*, 51, p. 085001, 2018.

[9] D. Ozkaya L, R. M. Langford, W. L. Chan, and A.K. Petford-Long, *J. Appl. Phys*., vol. 91, p. 12, 2002.

[10] C. Shearwood, A.D. Mattingley, M.R.J. Gibbs, *J. Magn. Magn. Mater*., vol. 162, pp. 147-154, 1996.

[11] http://www.rotima.ch/fileadmin/downloads/Amorphe_Materialien/2605-SA1-techn-bulletin.pdf

[12] H. Ishibashia, K. Haradaa, M. Kogachia, S. Noguchib, J. Magn. Magn. Mater., vol. 272–276, pp. 774–775, 2004.

[13] J.W. Judy, *Smart Mater. Struct*. vol.10, pp.1115–1134, 2001.

[14] A. Javed, N. A. Morley, M. R.J. Gibbs, *J. Magn. Magn. Mater*., vol. 321, pp. 2877-2882, 2009.

[15] N. A. Morley, A. Javed, M. R.J. Gibbs, *J. Appl. Phys*., vol. 105, p. 07A912, 2009.

Chapter 6 Influence of Growth Parameters on The Structure, Magnetic Properties, and Magnetostriction Constants of FeSiB and FeGaSiB Films.

6.1. Introduction

The growth parameters such as Ar gas pressure and sputtering target power can affect the magnetic, structural, and magnetostrictive properties of deposited films [1]. For example, the sputtering pressure can induce intrinsic stresses, which can be either tensile or compressive depending on the Ar gas pressure [2].

This chapter describes the influence of growth parameters on the structure, composition, magnetic properties, and magnetostriction constants of FeSiB and FeGaSiB thin films. This chapter is divided into three parts, each focusing on different growth parameters of the deposition technique. These are: (i) the Ar sputter pressure (p_{Ar}), (ii) the sputtering target power (P_{FeSiB}), and (iii) the Ga evaporation rate (Ga rate). Studying the effect of growth parameters on the properties of FeSiB and FeGaSiB films allows a comparison of the results to understand the influence of Ga addition into the FeSiB films. The magnetostriction constant measurement of the amorphous magnetostrictive thin films grown on a rigid substrate is achieved by a bending technique, which is described in chapter 4. The influence of changing the growth parameters on the Ga composition is studied over a wide range of compositions. Comparisons of the anisotropy fields and the saturation magnetostriction constants with the Ga composition were achieved.

Understanding the strength of the induced uniaxial anisotropy in the different films was determined via two different methods. The first method, which is used in this thesis, involves eqn. (5.2), and studying M_r/M_s as a function of applied field angles. [3]

The second method involves determining the anisotropy constant from the anisotropy field [4], taken from the hard axis loop. For the second method the following equation is used:

$$K_u = \frac{\mu_o H_k M_s}{2} \quad (6.1)$$

Where K_u is the anisotropy constant, H_k is the anisotropy field, M_s is the saturation magnetization, and μ_o is the permeability of space $4\pi \times 10^{-7}$ H.m^{-1}.

Qayes A. Abbas, 2018 & Email: qayes.a.abbas@gmail.com

6.2 Fabrication of The Films

The influence of film thickness on the structure and magnetic properties of magnetostrictive films was described in chapter 5. In this chapter, the film thickness was chosen to be 50 nm as it was shown to have the maximum magnetostriction constant (see **Fig. 5.15**).

6.2.1 Fabrication of FeSiB Thin Film

For the growth of the FeSiB films in this chapter, two series of 50 nm thick films were deposited on 380μm thick Si (100) substrates with dimensions (10 mm x 15 mm), which is suitable for the magnetostriction measurement, as they do no break in the bending tool, using the co-sputtering–evaporation technique [5], (as described in detail in chapter 4). For all the FeSiB films, the substrate-target distance (d) was 60 mm and the Ga evaporation rate was zero as the evaporator was off for the depositions. The first set of these films was grown in the chamber pressure (p_{Ar}) range from 4 μbar to 8 μbar and at fixed sputter power (P_{FeSiB}) of 20 W. The second set was grown in the sputter power (P_{FeSiB}) range from 20 W to 70 W and at fixed chamber pressure (p_{Ar}) of 4 μbar. For all the films, three Si substrates were used per film growth, attached to a glass slide using polymethyl methacrylate (PMMA). Metglas 2605SA1 with composition $Fe_{85}Si_{10}B_5$ was used as the sputtered target. The composition of the film was chosen for this study as it has soft magnetic properties, also it is amorphous, which had not been done before. The substrate holder was rotated during the growth at 0.1 rps, to avoid the effect of the sputter gun magnetron field, which can induce anisotropy into the films.

6.2.2 Fabrication of FeGaSiB Thin Films

For the growth of the FeGaSiB films, three series of 50 nm thick films were deposited on 380μm thick Si (100) substrates with dimensions (10 mm x 15 mm), using the co-sputtering–evaporation technique [5], (chapter 4). Using the same deposition system to deposit both films' series was to avoid the films' properties varying due to different deposition system, as the properties of films can change from system/technique to another. Hence the substrate-target distance (d) was equal 60 mm and the same as the FeSiB films. The first set of films was grown in the chamber pressure (p_{Ar}) range from 4 μbar to 8 μbar, sputter power (P_{FeSiB}) of 20 W, and the Ga was evaporated with a constant arbitrary rate, R_{Ga} = 0.2 (arbitrary unit). The second set of films was grown at a fixed chamber pressure (p_{Ar}) of 4 μbar, sputter power (P_{FeSiB}) range from 20 W-70 W, and fixed Ga evaporation arbitrary rate, R_{Ga} = 0.2 (arbitrary

unit). The third set was grown at a fixed chamber pressure (p_{Ar}) of 4 μbar, sputter power (P_{FeSiB}) of 20 W, and the Ga evaporation rates range R_{Ga} = 0.2, 0.3, 0.4, 0.5, and 0.6 (arbitrary unit). Again, three Si substrates were used per film growth, attached to a glass slide using polymethyl methacrylate (PMMA). Metglas 2605SA1 with composition $Fe_{85}Si_{10}B_5$ was used as the sputtered target and the Ga (99.99%) material in the evaporator. Also, the substrate holder was rotated as described in section 6.2.1.

6.3 Characterization of The Films

The Bruker D2 phaser technique, X-ray diffraction (XRD) with Cu $K_{\alpha 1}$ 1.54184 Å was used to analyze the film's structure. The θ/2θ mode was used, the first range of 2θ from 30° to 80° was used to check the structure of the film (for bcc Fe 2θ ~ 45° and for bcc Fe-Ga 2θ ~ 45°) and silicon substrate (2θ = 69.8°, 61.7°, and 33°), and the second 2θ range from 35° to 55° was used to avoid the Si substrate peaks. XRD analysis was carried out to determine whether the films were fully amorphous or if they contained nanocrystalline clusters within an amorphous matrix. Atomic force microscopy (AFM) was used, in tapping mode, to measure the thickness of the samples using the step produced in fabrication.

X-ray photoelectron spectroscopy (XPS), was carried out on a Thermo Fisher Scientific K-alpha+ spectrometer, used to measure the composition of the films. Samples were investigated via a micro-focused monochromatic Al X-ray source (72 W) over an area of around 400 μm. For high-resolution scans, recording of data was at pass energies of 150 eV for survey scans and 40 eV with 1 eV and 0.1 eV step sizes respectively. The analysis of data was achieved by CasaXPS software with a Shirley type background. More details can be seen in section (4.10.3) and details of fitting data and calculations can be found in the appendix attached at the end of this thesis.

The DMS model 10 vibrating sample magnetometer (VSM) was used to determine the magnetic moment of the films at room temperature, using an applied field of 40 kA/m, from which the saturation magnetisation was calculated.

In the transverse mode, the magnetic properties of the two film sets were measured on a magneto-optical Kerr effect (MOKE) magnetometer, with the max magnetic field applied being 40 kA/m, which was sufficient to saturate the films. Characterization of the magnetic properties was carried out by measuring the normalized hysteresis loops. The magnetic anisotropy and saturation fields were determined by measuring the normalized hysteresis

loops at different magnetic field directions with respect to the sample, with angles from 0° to 180°. To measure the magnetostriction constant (λ_s) [6] at room temperature, the inverse magnetostrictive effect (Villari effect) [7 - 9] measurement was used.

6.4 Influence of Ar Gas Pressure on the Structure, Magnetic Properties, and Magnetostriction Constants of Amorphous FeGaSiB Thin Films

Ar gas pressure is an important growth parameter of the sputtering process, in addition to providing the inert gas atoms in the sputtering process, it is also can work as an auxiliary moderator for sputtered atoms from the sputtering target. In an individual sputtering chamber, the Ar gas pressure can affect both the structure and the magnetic properties of the deposited films. For the co-sputtering-evaporation technique, used in this work, in addition to the above, the Ar gas pressure can affect the percentage of the Ga atoms thermally evaporated and the percentage that reach the substrate, hence the composition of the deposited films.

For the FeSiB thin film set, during the growth the substrate temperature was around 19℃ while it was around 31℃ for the set of FeGaSiB thin films for the variation of Ar pressure (p_{Ar}). This variation in temperature should not change the growth mechanism and is likely to be due to using the evaporator for the FeGaSiB thin films as the Ga atoms are evaporated at a high temperature.

Figure 6.1 shows the sputtering deposition rates of both the FeSiB and FeGaSiB films. As the films were deposited with fixing all growth parameters excepting Ar pressure, the sputtering rate of FeSiB film deposition decreased with increasing of pressure **Fig. 6.1** while the sputtering rate of FeGaSiB film deposition was stable around 0.1 nm/s for all the variations of pressure. This suggests that presence of Ga atoms led to a reduction in the sputtering rate by reducing the kinetic energy of the atoms. Hence the growth of the FeSiB films was faster compared with the FeGaSiB films.

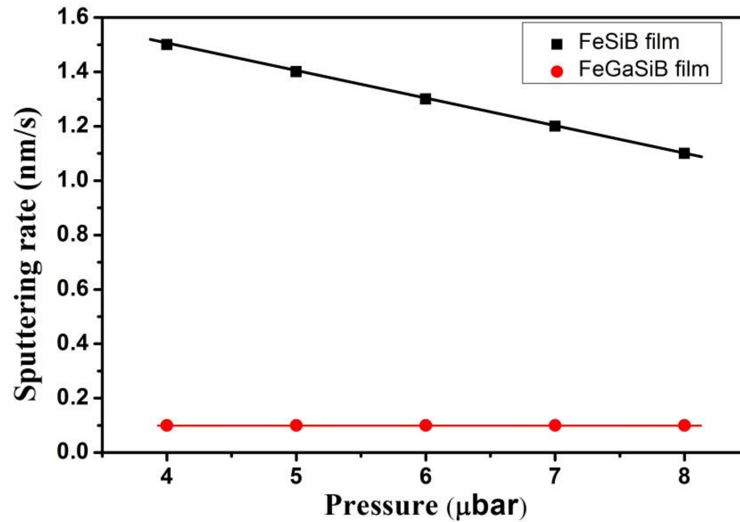

Figure 6.1 Sputtering rate of deposition the FeSiB and FeGaSiB films. The solid lines are a guide for the eye.

6.4.1 Structural Properties

Figure 6.2 (a) shows the XRD of the 50 nm thick FeGaSiB thin films for different (Ar) gas pressures (p_{Ar}). The results showed that all the films had an amorphous structure and all the peaks present were for the Si substrate. **Fig 6.2 (b)** shows the Si peaks at 2θ =33° and **Fig 6.2 (c)** shows the XRD pattern of the FeGaSiB thin films with a 2θ range (35° to 55°) to avoid the substrate peaks. It is clear from **Fig 6.2 (c)** there are no peaks present at 2θ ~ 45° to indicate the existence of crystalline Fe or FeGa. There is a broad peak at 2θ ~ 50°, which is expected for amorphous films. Hence all the films had an amorphous structure. It is found that the main diffraction peak of Si (100) is at 2θ= 69.8^{o} and other Si peaks found at 2θ 61.7^{o} and 33°. The results show that the adding of Ga into amorphous FeSiB thin films does not affect the morphology also changing the Ar gas pressure does not affect the film morphology. This means the film morphology is independent of pressure.

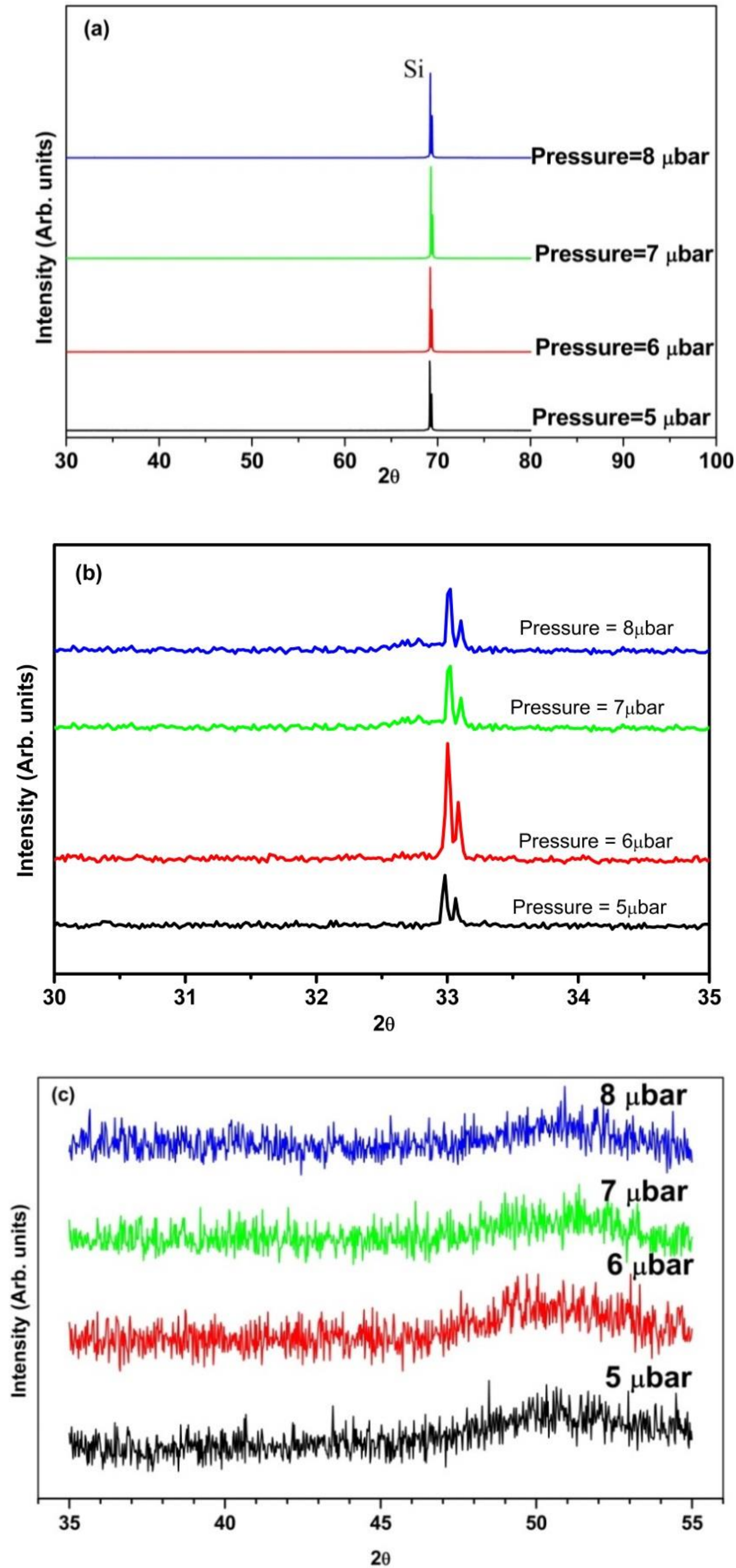

Figure 6.2 (a) XRD for the different pressures of 50nm FeGaSiB thin films, (b) The Si peaks 2θ range from 30° to 35°. (c) The FeGaSiB film without the Si peaks.

As described in chapter 4, the Ar sputtering pressure is one of the parameters of co-sputtering- evaporation chamber which can be varied to control the Ga composition. The effect of changing the Ar sputtering pressure has been investigated to achieve range of compositions. On the other hand, it has been informed [10-12] that the stress induced in films by sputtering deposition process can be induced by the changing the sputtering Ar pressure and the substrate-target distance, d. In this work the substrate-target distance was fixed at 60 mm, thus the stress can be influenced only by the Ar pressure. It is investigated to whether that the magnetic properties and the compositions of the magnetic films were strongly influenced by Ar pressure. The influence of Ar pressure on composition was determined by the XPS technique,as shown in **table 6.1**. From the XPS measurements, for all the FeGaSiB films, Ga was detected, also it is meant that the Ga atoms had enough energy to travel through the plasma, without being scattered.

Table 6.1 *summary of the XPS result of the film's composition as Ar pressure was increased.*

Ar pressure (μbar)	**Fe%**	**Ga%**	**Si%**	**B%**
4	82	7	5	6
5	81	8	5	6
6	83	4	7	6
7	83	7	5	5
8	83	4	6	7

Table 6.1 shows the result of the XPS measurements of the FeGaSiB films for different Ar pressures. The results showed that increasing the pressure does not scatter all the Ga atoms and the Ga was successfully added to FeSiB films. It is known that the increase of pressure is inversely proportional to the mean free path, l, of the sputter gas, where ($l \propto \frac{1}{p_{Ar}}$). An increase in Ar pressure leads to a decrease of the mean free path. Inelastic collisions between the Ga atoms and the sputter gas are increased with increasing the pressure and this leads to thermally increasing the Ga atoms during their movement from the source of evaporator towards the substrate.

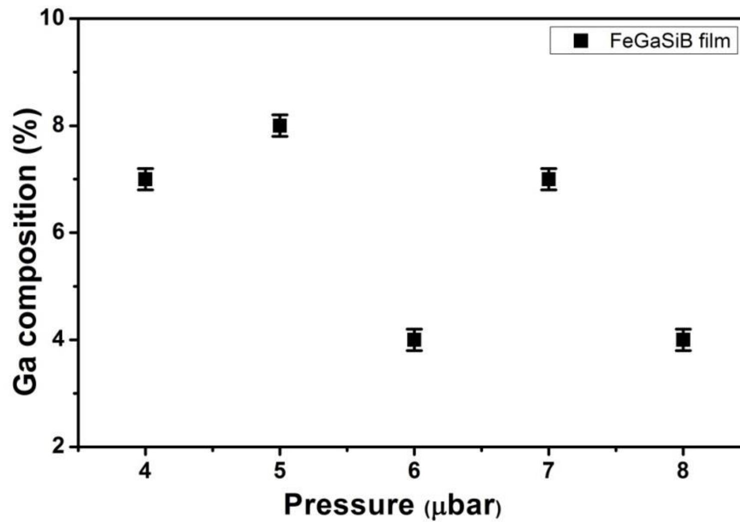

Figure 6.3 Ga compositions as a function of Ar pressure of FeGaSiB film.

Figure 6.3 shows the percentage of Ga composition as a function of Ar gas pressure of FeGaSiB film. It was found that for the Ar gas pressure range investigated, the Ga composition was changed by the variation of Ar gas pressure. The lowest values were at the pressure of 6 and 8 μbar while the maximum value was at a pressure of 5 μbar. Changing the pressure can affect the FeSiB:Ga ratio through scattering the Ga atoms away from reaching the substrate. By comparing the amorphous film of four elements (FeGaSiB), as shown result in **Fig. 6.3**, with the 50 nm thick binary crystalline FeGa in **Fig 6.4**, which was fabricated, with varying pressure, fixed power density of 9.87×10^{3} Wm^{-2} and Ga evaporation rate = 0.25, by the same chamber described in chapter 4, studied by Javed [13], it is found that there is a difference in the amount of Ga within the films. The binary FeGa film had a higher Ga percentage than the FeGaSiB film. This is likely to be due to the FeGaSiB films having four different element atoms, with different sizes, leading to a reduction in the Ga percentage, due to the Ga atoms having more collisions with those elements. In this case, the collisions of the four elements are more complex from those of binary system under increasing the pressure. For the pressure 5 μbar $\leq p_{Ar} \leq$ 7 μbar both film sets showed the same behaviour where the minimum valves were at the pressure of 6 μbar. For the pressure at 8 μbar, they did not include the result, but they suggested that the Ga atoms were scattered by the high pressure when the pressure was greater than 7 μbar as this was enough to reduce the amount of Ga atoms reaching the substrate. From **Fig. 6.3**, a similar suggestion could be made for the FeGaSiB films, where the percentage of Ga was too low at the pressure of 8 μbar.

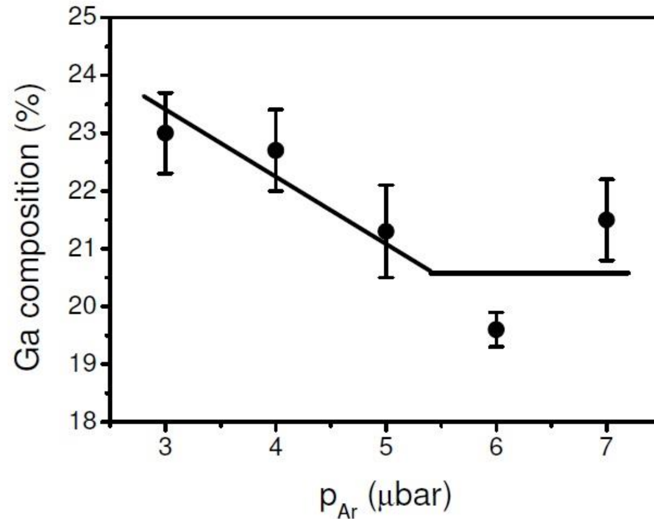

Figure 6.4 Ga composition of the binary FeGa film as a function of Ar pressure taken from reference [13].

6.4.2 Magnetic Properties

6.4.2.1 Magnetic Properties Measured by MOKE

For the selected range of pressure, the MOKE measurements of magnetostrictive FeSiB and FeGaSiB thin films were used to determine the main magnetic properties such as the normalized remanence, anisotropy/saturation fields, and coercivity.

Figure 6.5 shows the comparison of normalized hysteresis loops measured by the MOKE system (described in chapter 4) at different applied field angles of 50 nm FeSiB films prepared at different Ar gas pressures and fixed power 20 W and Ga rate = 0. From this figure, the effect of Ar gas pressure can be seen in the shape of the hysteresis loops. For example, in **Fig. 6.5 (a)** all the loops had the same shape, with equal coercivity and remanence values and an absence of a hard loop, hence an absence of an anisotropy field. Increasing the pressure > 4 μbar, (except at 6 μbar) induced an anisotropy in the plane of the films, which changed the coercivity and remanence values, suggesting that increasing the pressure induced a stress within the films. The normalized hysteresis loops for the film at pressure 6 μbar had, for all the different applied field angles, the same shape with a very low coercive field.

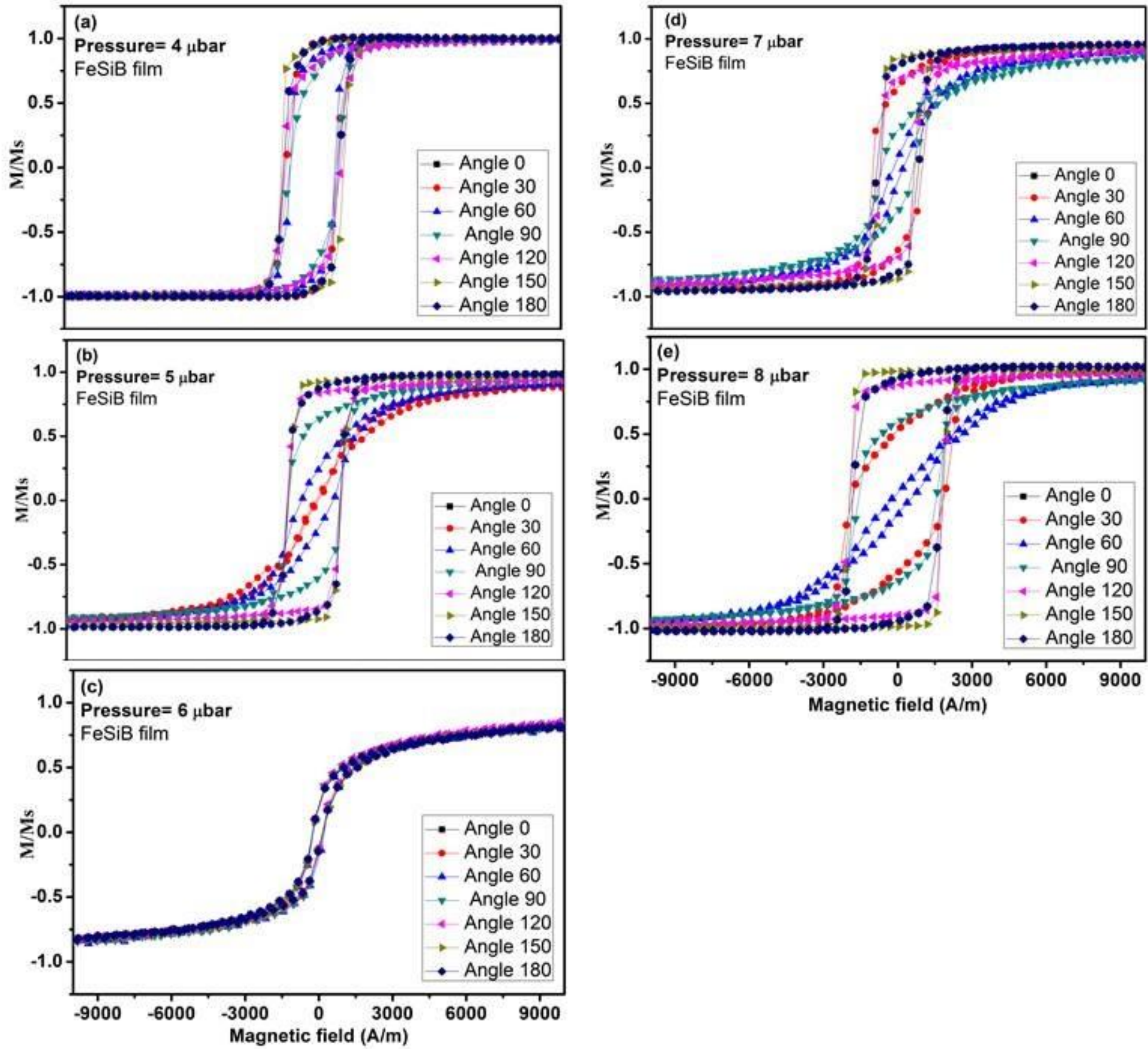

Figure 6.5 The normalized hysteresis loops, at different applied field angles, of 50 nm FeSiB films for different gas pressures. (a) Pressure 4 μbar (b) Pressure 5 μbar (c) Pressure 6 μbar (d) Pressure 7 μbar (e) Pressure 8 μbar.

Figure 6.6 shows the comparison of normalized hysteresis loops measured by MOKE (described in chapter 4) at different applied field angles for the 50 nm FeGaSiB films prepared at different Ar gas pressures and fixed power 20 W and Ga rate 0.2 (a.u). From **Fig 6.6**, the effect of Ar gas pressure in the shape of the hysteresis loops is shown. For example, **Fig. (a)** had different shape hysteresis loops with different anisotropy fields, coercivity and remanence values. It can be seen that increasing the pressure with the presence of Ga reduced the induced in-plane anisotropy of the films and affected the coercivity and remanence values, suggesting that increasing the pressure with Ga present reduced the induced stress within the films.

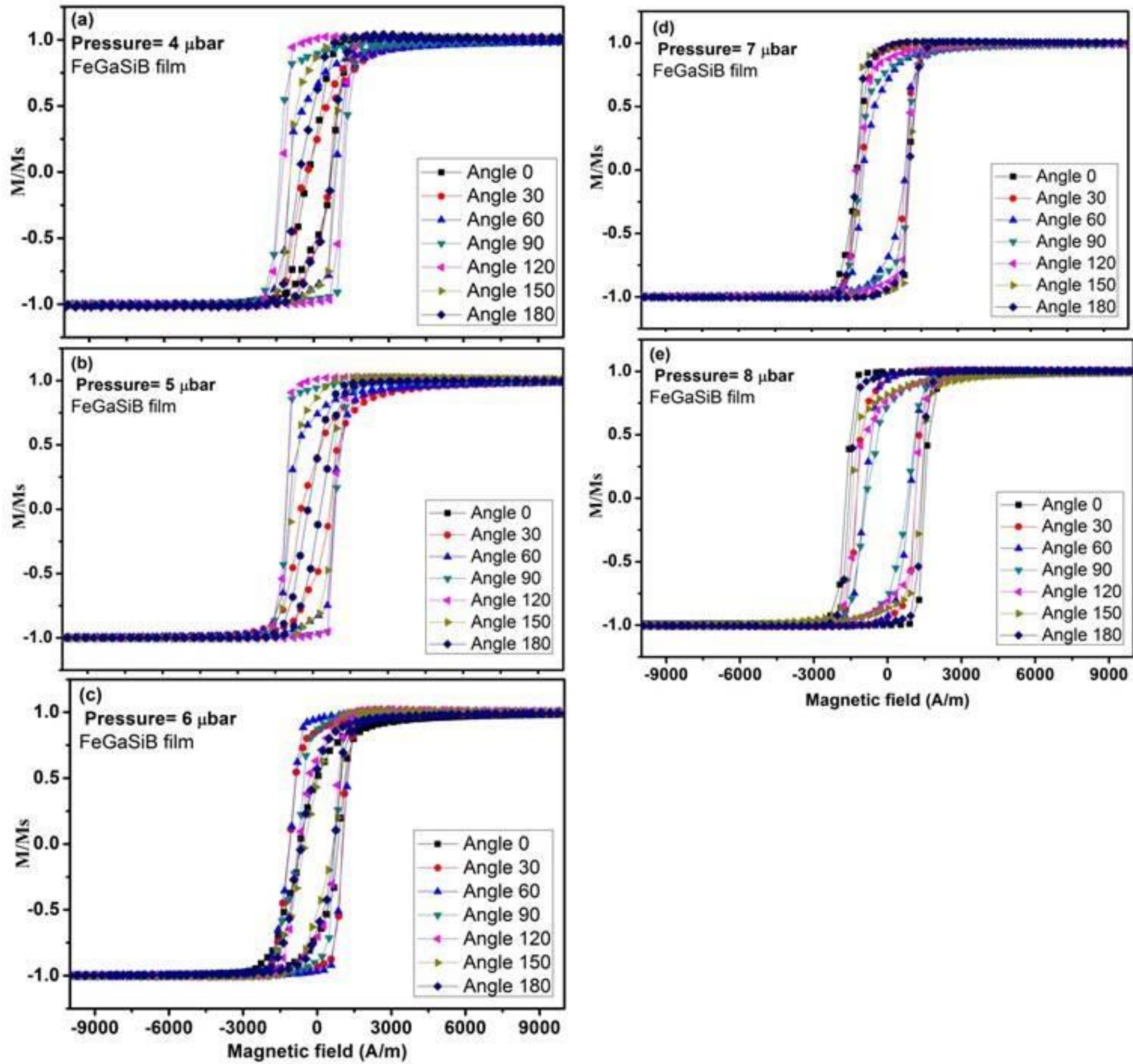

Figure 6.6 The normalized hysteresis loops, at different applied field angles, for 50 nm FeGaSiB films at different gas pressures. (a) Pressure 4 μbar (b) Pressure 5 μbar (c) Pressure 6 μbar (d) Pressure 7 μbar (e) Pressure 8 μbar.

Comparing the normalized hysteresis loops of the FeSiB and FeGaSiB films, **Figs (6.5 and 6.6)**, it can be seen that, for both film sets, changing the pressure affected the magnetic properties of the films, i.e. increasing the pressure increased the anisotropy of the FeSiB films and reduced it for the FeGaSiB films.

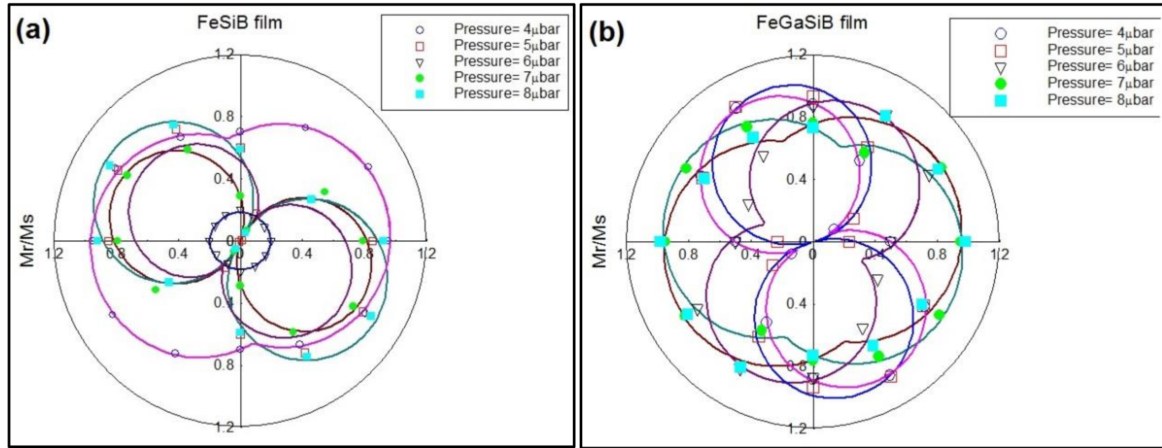

Figure (6.7) Angular plot of the remanence ratio (M_r/M_s) at different Ar gas pressures (a) FeSiB film (b) FeGaSiB film. The lines are a fit to the data.

Figure 6.7 presents an angular plot of the remanence magnetization ratio (M_r/M_s) of the selected Ar gas pressures for FeSiB and FeGaSiB films. The difference in the remanence magnetization ratio, M_r/M_s, along both the easy and the hard axes provides an indication of the strength of the uniaxial anisotropy. Therefore, the uniaxial anisotropy can be quantified by fitting the following equation (5.2) [3] to the M_r/M_s as a function of angle.
For the FeSiB film at low-pressure 4 µbar, D ≈ 0.3, so the film has weak uniaxial anisotropy, while a stronger uniaxial anisotropy is present in the films grown at 7 µbar and 8 µbar where D ≈ 0.9 and 0.93 respectively. Further, the film at 6 µbar is isotropic as D ≈ 0.01. For these films, the difference in M_r/M_s was influenced by the pressure. For the FeGaSiB films, **Fig 6.7 (b),** a weak uniaxial anisotropy at high pressures 7 µbar (7% Ga) and 8 µbar (4% Ga) was presented, where D ≈ 0.33 and 0.29 respectively, and a stronger uniaxial anisotropy at lower pressures 4 µbar (7% Ga) and 5 µbar (8% Ga) where D ≈ 0.87 and 1 respectively. The difference in M_r/M_s was influenced by both the pressure and Ga composition.

Magnetic properties of magnetic thin films such as the coercivity and anisotropy field can be affected by the pressure or the composition of the film. Deposition of films under pressure can induce a stress (compressive or tensile) overall the film and/or local stresses, within the film during the growth. This stress can strongly affect the coercivity and anisotropy field of the magnetic film. Another variable that changing the pressure can influence is the deposited film composition, such as the FeGaSiB film (see **table 6.1**). This change in composition can also affect the magnetization and anisotropy of the films. For the FeSiB film there was no change in its composition as they have the same target composition, hence approximately the

same composition. This indicates that the effect of the local stress is the dominate effect on the magnetic properties.

Figure 6.8 shows the effect of Ar pressure on the anisotropy field H_k and saturation field H_s for the FeSiB and FeGaSiB films respectively. For the FeSiB films, the H_k increased gradually as the pressure increased, suggesting that the local intrinsic stresses within the films increased with pressure. For the FeGaSiB films, the saturation field, $H_s \approx 4000$ A/m for all deposition pressures. This means the addition of Ga into FeSiB reduced the stress in the films, so giving stability to the saturation field over the pressure range. It is clear that the deposition rate of the FeGaSiB film was very low compared with a deposition rate of FeSiB film **Fig 6.1**, this resulted in reducing the kinetic energy of the atoms, which reduced the stress.

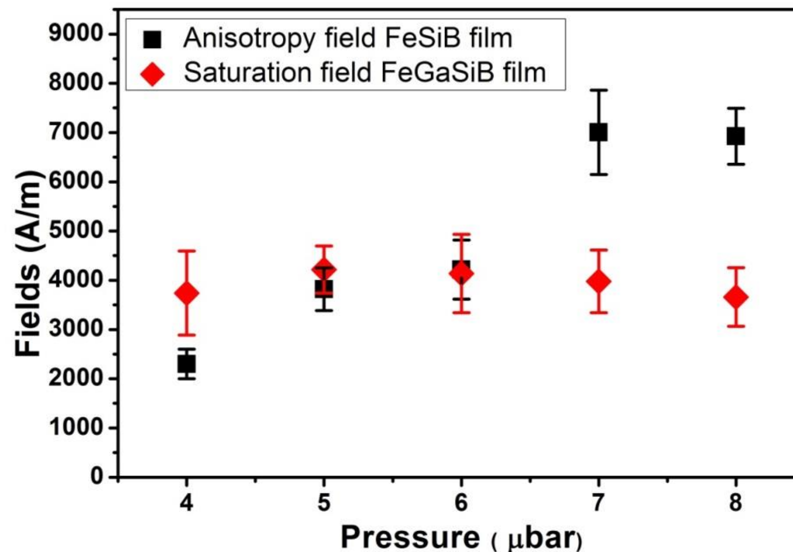

Figure 6.8 Saturation/Anisotropy Fields as a function of pressure for the FeSiB and FeGaSiB films

It was found that for the FeSiB films, the films had uniaxial anisotropy at pressures higher than 4 μbar, while the FeGaSiB films were isotropic at the pressure higher than 5 μbar. As all the films were amorphous, (see **Fig. 6.2**), the anisotropy will be dominated by the local stress within the films.

The coercive force is associated with the number of the domains, and how they are pinned, the grain size, and the internal stress within the material. As the films in this study were amorphous and there were no grains detected, the observed trend the coercive force indication that it was affected byninternal stress. Also, as the domains pin on the grains,

changing the coercivity, they can also pin on impurities and local stresses. As the response of the material to a magnetic field is due to either the rotation of magnetic moments or domain wall movement, restricting either can affect the coercivity. The stresses linked with, for example, dislocations inhibit the rotation of magnetic moments and/or the domain wall movement. Thus the intrinsic stresses influence magnetic properties of sputtered thin films and can affect the magnetic properties such as the coercivity.

Figure 6.9 shows the coercive fields as a function of Ar pressure for the FeSiB and FeGaSiB thin films. For both the film sets, H_c is less than 900 A/m and higher than 300 A/m showing that neither pressure nor Ga concentration changed the coercivity linearly. As discussed above the coercive field strongly depends on intrinsic properties such as the grain size, and as both film sets were amorphous, the films will contain no grains.

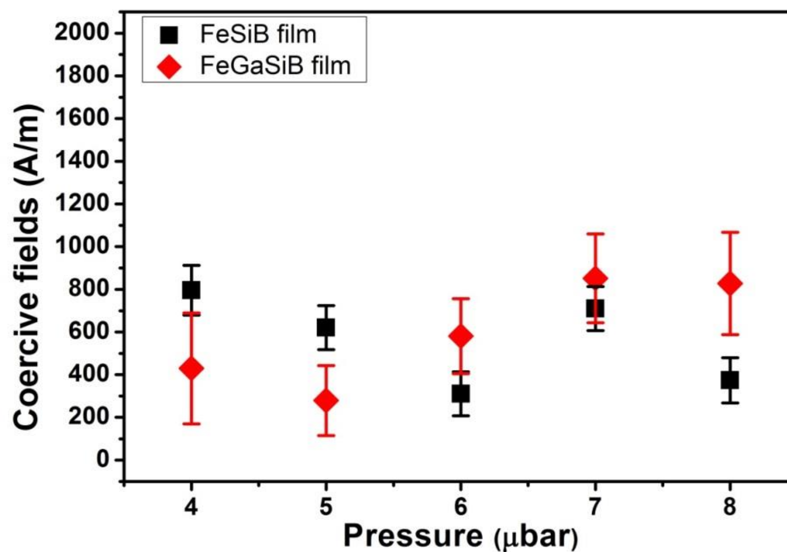

Figure 6.9 Coercive fields as a function of pressure for the FeSiB and FeGaSiB films.

6.4.2.2 Magnetic Properties Measured by VSM System

VSM measurements were used for the magnetostrictive FeGaSiB thin films to determine the magnetic moment, hence the saturation magnetization, the coercivity, and the normalized remanence.

Figure 6.10 shows the results of the VSM measurements for FeGaSiB thin films, which were measured at room temperature to avoid any thermal effects of high temperatures and to avoid annealing the films. From **Fig. 6.10**, it can be seen that the magnetization of the FeGaSiB

films decreases with increasing deposition pressure. This could be due to the Ar pressure creating a local stress and changing the percentage of non-magnetic atoms (Ga, Si, B) within the films due to complex collisions of atoms, so leading to a change in the composition of films [7, 15] (see **table 6.1**). Typically, the increase in pressure changes the mean free paths of all the atoms, as Ga is evaporated it is likely to have a higher energy than the sputtered elements, meaning that its mean free paths at higher pressures is longer than the other elements, so increasing the concentration in the films. This will change the local environment within the amorphous films, as the magnetic moment of Fe atoms depends on the nearest neighbours. Therefore, the saturation magnetization can be affected by the Ga concentration. From **Fig. 6.10**, it can be seen that the saturation magnetization decreased gradually with increasing the pressure, hence it is not dominated by the Ga percentage as the Ga percentage fluctuated with increasing the pressure (see **Fig. 6.3**). Therefore, it is suggested that the reduction in saturation magnetization is dominated by pressure increase.

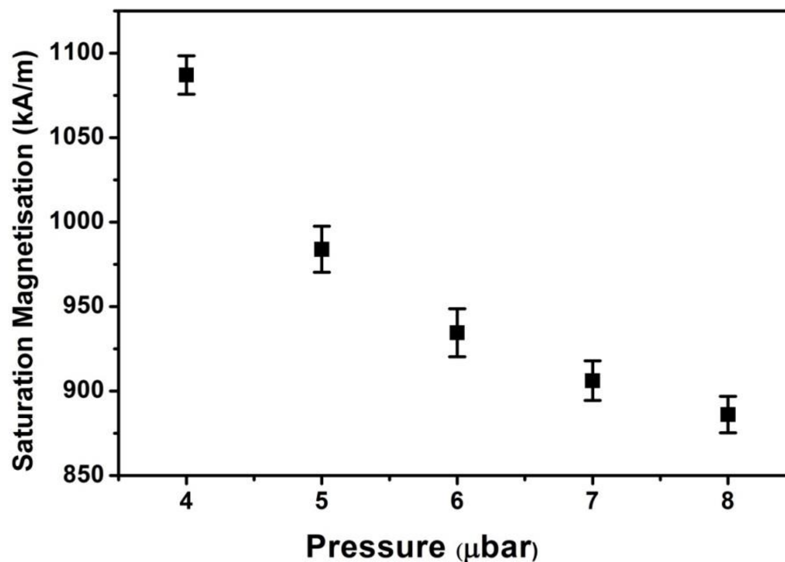

Figure 6.10 Magnetization as a function of pressure for the FeGaSiB films.

6.4.3 Magnetostriction Properties

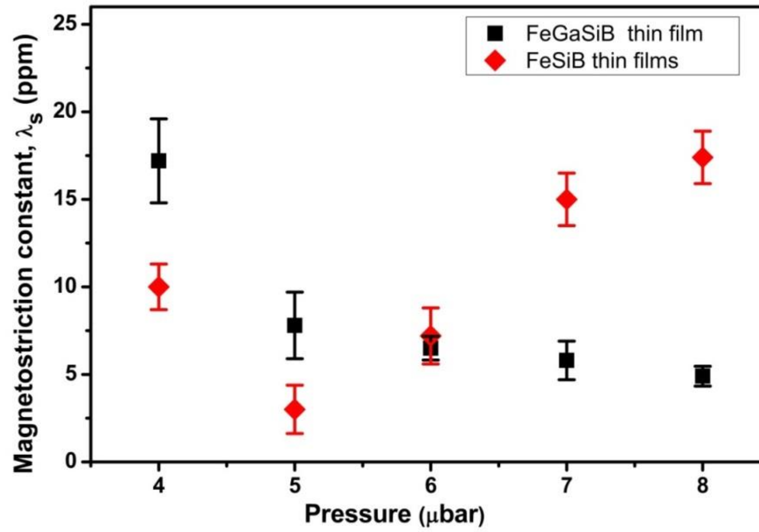

Figure 6.11 The comparison of the magnetostriction constant λ_s as a function of pressure for the FeSiB and FeGaSiB films at room temperature.

Figure 6.11 shows the comparison of the magnetostriction constant as a function of changing the Ar pressure for the FeSiB and FeGaSiB films at room temperature. From **Fig. 6.11**, it is observed that the magnetostriction constant of the FeSiB thin films increased with increasing the Ar pressure. From equation (4.5), it is observed that the magnetostriction constant, λ_s, is related to the intrinsic stress in the film. From previous work, the intrinsic stress is tensile as this leads to an increase in elastic properties, hence an increase in the magnetostriction constant, λ_s, [1]. Thus the increasing pressure causes an increase in tensile stress within the FeSiB films, which increased both the magnetostriction constant λ_s and anisotropy field. For the FeGaSiB films, the magnetostriction constant, λ_s, decreases with an increase of sputtering gas pressure. For $p_{Ar} \leq 5$ μbar, the magnetostriction constants were higher than those of FeSiB film and showed the higher magnetostriction constant, λ_s, at the lower pressures compared to the FeSiB film, with the maximum λ_s = 17.4 ppm, at 4 μbar with composition $Fe_{82}Ga_7Si_5B_6$. For p_{Ar}= 6 μbar, both films had the same values, with the film composition $Fe_{83}Ga_4Si_7B_6$. For $p_{Ar} > 6$ μbar, the magnetostriction constants of the FeSiB films were higher than those of films with compositions $Fe_{83}Ga_7Si_5B_5$ and $Fe_{83}Ga_4Si_6B_7$. Further, the minimum value of FeGaSiB film was 4.9 ppm at the high pressure of 8 μbar with composition $Fe_{83}Ga_4Si_6B_7$, while the minimum value for the FeSiB films was 3 ppm at 5 μbar. From the

anisotropy and saturation field measurements, it is concluded that the addition of Ga reduces the tensile stress within the films, thus these intrinsic stresses no longer dominate the magnetostriction constant, λ_s. The reduction in stress is due to the distribution of Ga atoms in the amorphous structure changing the local environment around the Fe atom. This means that the magnetostriction constant, λ_s, now depends on the saturation magnetization (refer to equations (2.32) and (2.36)), which depends on the Ga concentration, **Fig 6.10**, as both the saturation magnetisation and magnetostriction constant, λ_s, decrease with the increase in pressure. The effect of changing the gas pressure during sputtering, on the magnetic properties of magnetostrictive thin films has been studied and efforts achieved to investigate this effect. In the literature review (section 3.4.1), previous work found a large change in the magnetic properties of both polycrystalline FeGa [6, 13, 17] and amorphous FeGaB [16] films as a function of Ga concentration and argon pressure. For example, for the anisotropy within the FeGaSiB films, the results presented here show similar behaviour of result of Ref. [13], where increasing the pressure changed the anisotropy of the films from uniaxial to isotropic. The magnetostriction constant showed different behaviour for all the samples. Further, the results presented here show different behaviour of result of amorphous FeGaB films Ref. [16].

6.5 Influence of Sputtering Target Power on The Structure, Magnetic Properties, and Magnetostriction Constants of Amorphous FeGaSiB Thin Films

The sputtering target power is another important growth parameter of the deposition process. It can impact the properties of the films in a similar way as the sputtering gas pressure. Further, it can influence the deposition rate, the kinetic energy of sputtered atoms and consequently the surface mobility. In the co-sputtering-evaporation technique, the effect of changing the sputtering target power can affect the sputtering rate, which can affect the ratio of sputtered atoms to evaporated atoms. For the film growth, the Ga rate was fixed $R_{Ga} = 0.2$ and sputtering pressure $p_{Ar} = 4$ µbar, thus an increase in sputtering target power P_{FeSiB} leads to an increase in the FeSiB sputtering rate, **Fig 6.12** hence in principle a change in the FeSiB:Ga ratio in the films.

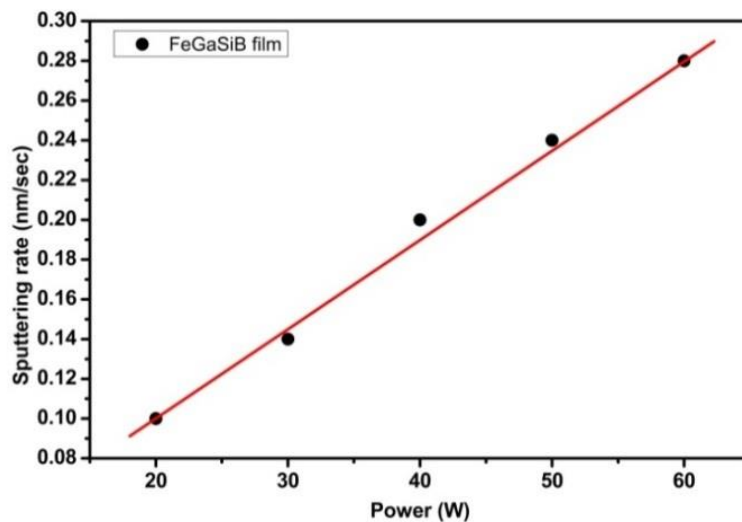

Figure 6.12 sputtering rate of FeGaSiB film as a function of increasing the power.

6.5.1 Structural Properties

Figure 6.13 (a) shows the XRD of 50 nm thick FeGaSiB thin films for different target power P_{FeSiB}. The results showed that all the films had an amorphous structure and all the peaks present were for the Si substrate. **Fig 6.13 (b)** shows the Si peaks at $2\theta = 33^{o}$ and **Fig 6.13 (c)** shows the XRD pattern of the FeGaSiB thin films with a 2θ range (35° to 55°) to avoid the substrate peaks. It is clear from **Fig 6.13 (c)** there are no peaks present at $2\theta \sim 45^{o}$ to indicate the existence of crystalline Fe or FeGa. Similar to the pressure study, it was found that the

samples had the same main diffraction peaks of Si (100). In this part, the results show that the adding of Ga into amorphous FeSiB thin films does not affect the morphology, also changing the target power P_{FeSiB} does not affect the film morphology. This means the film morphology is independent of power.

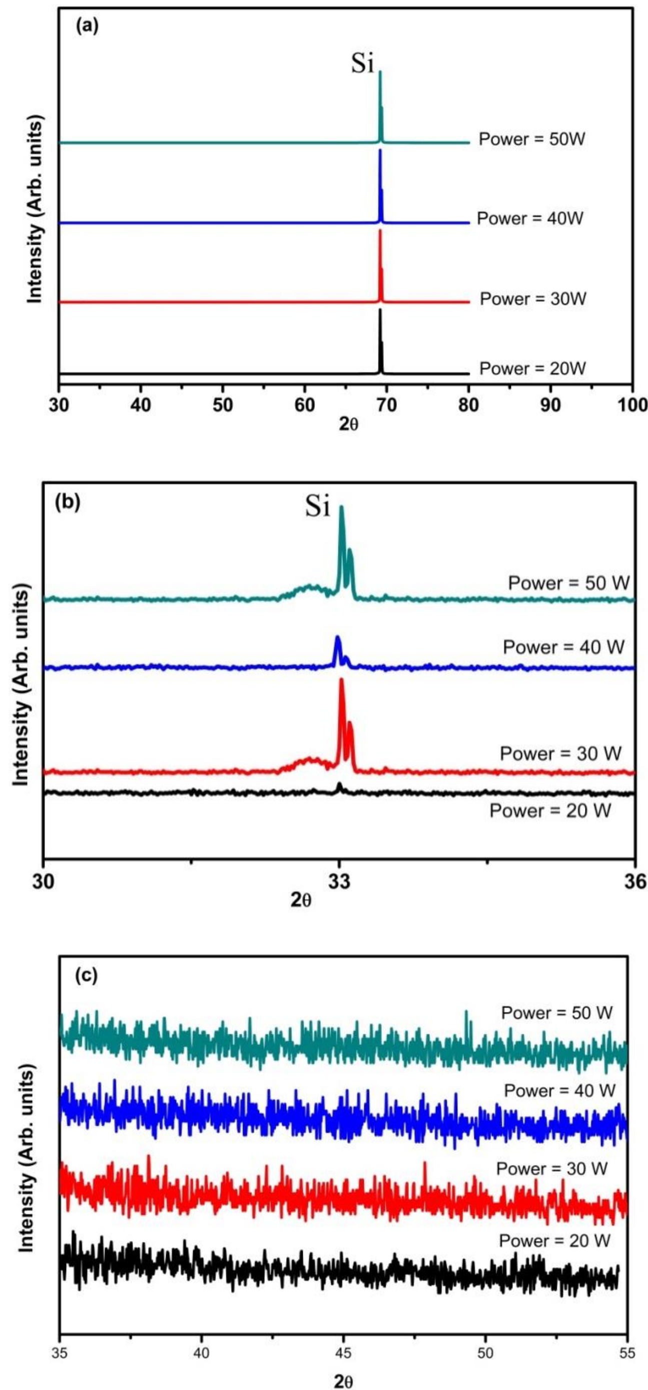

Figure 6.13 (a) XRD for the different powers of 50 nm FeGaSiB thin films. (b) The Si peaks. (c) The FeGaSiB film without the Si peaks.

Table 6.2 summary of XPS result for the film's composition of the increasing power.

power (W)	Fe%	Ga%	Si%	B%
20	82	7	5	6
30	81	4	8	8
40	82	7	6	5
50	81	8	6	5
60	85	5	3	7

Table 6.2 shows the result of the XPS measurements of the FeGaSiB films for different FeSiB target power (P_{FeSiB}). **Figure 6.14** shows the percentage of Ga composition as a function of the sputtering target power of FeGaSiB film. It is found that, for the range of power investigated, the Ga composition is influenced by varying of the sputtering target power. The lowest value was at the power of 30 W while the maximum value was at a power of 50 W. For fixed Ga evaporation rate and Ar pressure, an increase in the sputtering target power increased the FeSiB sputtering rate **Fig 6.12** hence increased the number and speed of sputtering atoms toward the substrate and this can influence the FeSiB:Ga ratio in film.

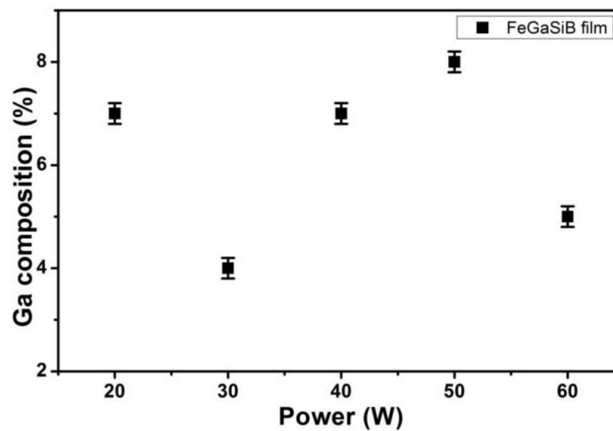

Figure 6.14 Ga compositions as a function of sputtering target power of FeGaSiB film.

By comparing the Ga concentration of the amorphous films with four elements (FeGaSiB), in **Fig. 6.14**, with the 50 nm thick of binary crystalline FeGa in **Fig 6.15**, fabricated with varying the power density, fixed pressure = 4 μbar and Ga evaporation rate = 0.3, by the same chamber described in chapter 4, studied by Javed [17]. It is found that there is a

difference in the amount of Ga within the films, including the binary films of FeGa having a higher Ga percentage than the FeGaSiB films. For the binary FeGa film, the Ga percentage decreased with increasing the power density, as increasing the power increases the number of Fe atoms and affects the percentage of Fe:Ga by decreasing the number of Ga atoms to reach the substrate. For the four element films (FeGaSiB) the Ga percentage fluctuated with increasing the power.

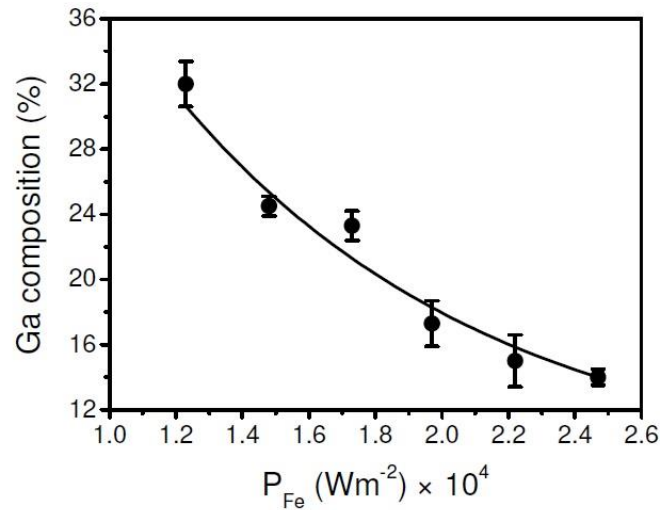

Figure 6.15 Ga composition of the binary FeGa film as a function of Fe power density taken from reference [17].

6.5.2 Magnetic Properties

6.5.2.1 Magnetic Properties Measured by MOKE

The MOKE measurements of the magnetostrictive FeSiB and FeGaSiB thin films were used to determine the essential magnetic properties such as the normalized remanence, anisotropy/saturation fields, and coercivity

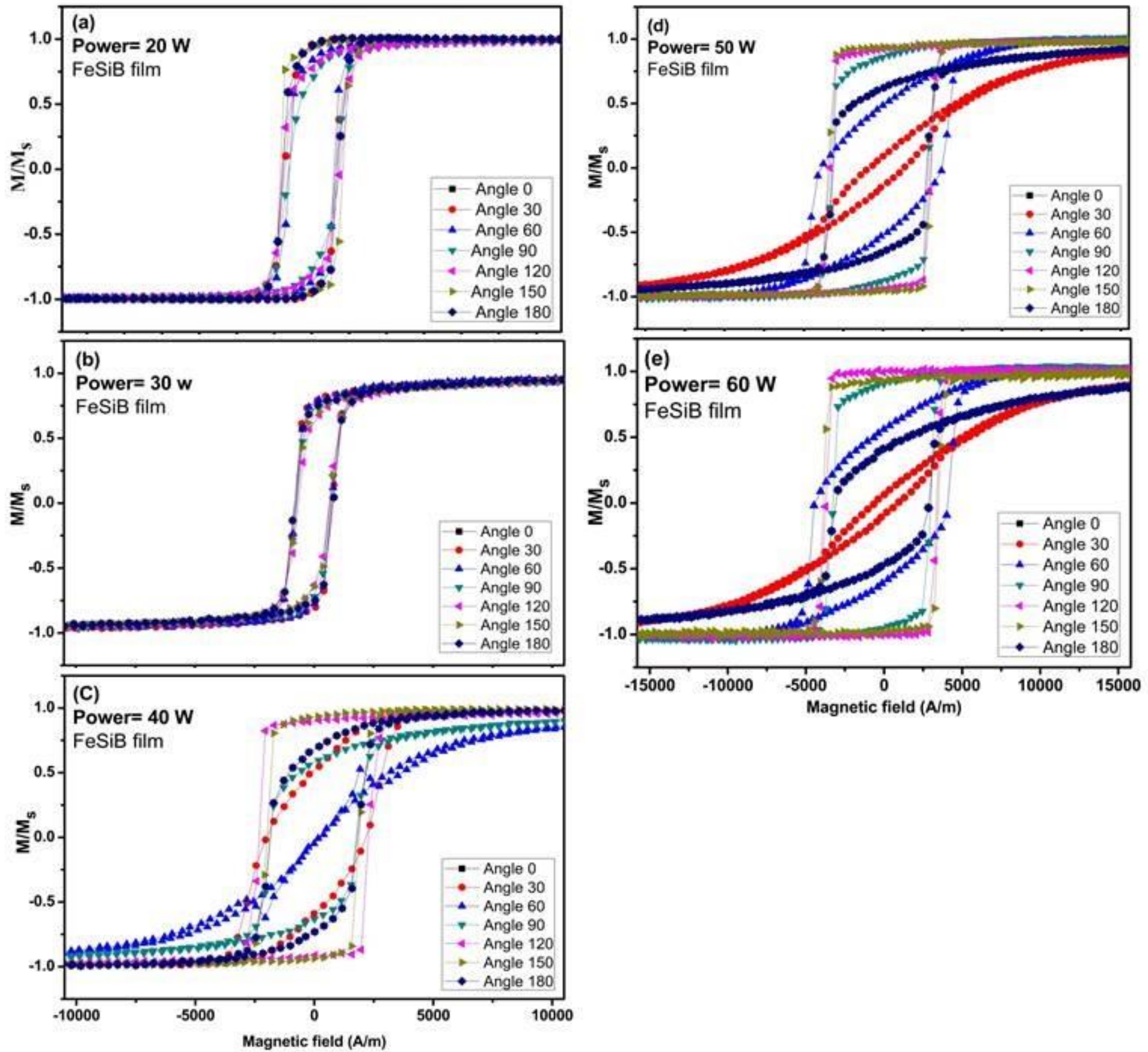

Figure 6.16 Normalized hysteresis loops at different applied field angles, for 50 nm FeSiB films a different sputtering target power. (a) 20 W (b) 30 W (c) 40 W (d) 50 W (e) 60 W.

Figure 6.16 shows the normalized hysteresis loops measured by the MOKE system (described in chapter 4) at different applied field angles for 50 nm FeSiB films prepared at different sputtering target power and fixed pressure at 4µbar and Ga rate set to = 0. In **Figs (a) and (b)** (20 W + 30 W) all the loops had the same shape and similar coercivities and

remanences values, with the absence of hard loops, hence absence of an anisotropy field. Increasing the power ≥ 40 W, induced an in-plane anisotropy within the films and affected the coercivity and remanence values, suggesting that increasing the power induced stress within the films. From **Fig. (c)**, it can be seen that the hard loop direction aligned at the angle 60° and the easy loop at the angles 120° and 150°. Therefore, this film had uniaxial anisotropy field as the difference in the angles of the easy and hard loops 90°. Also, it can be seen that increasing the power higher than 40 W changed the hard loop direction from 60° to 30°, **Figs. (d) and (e)**.

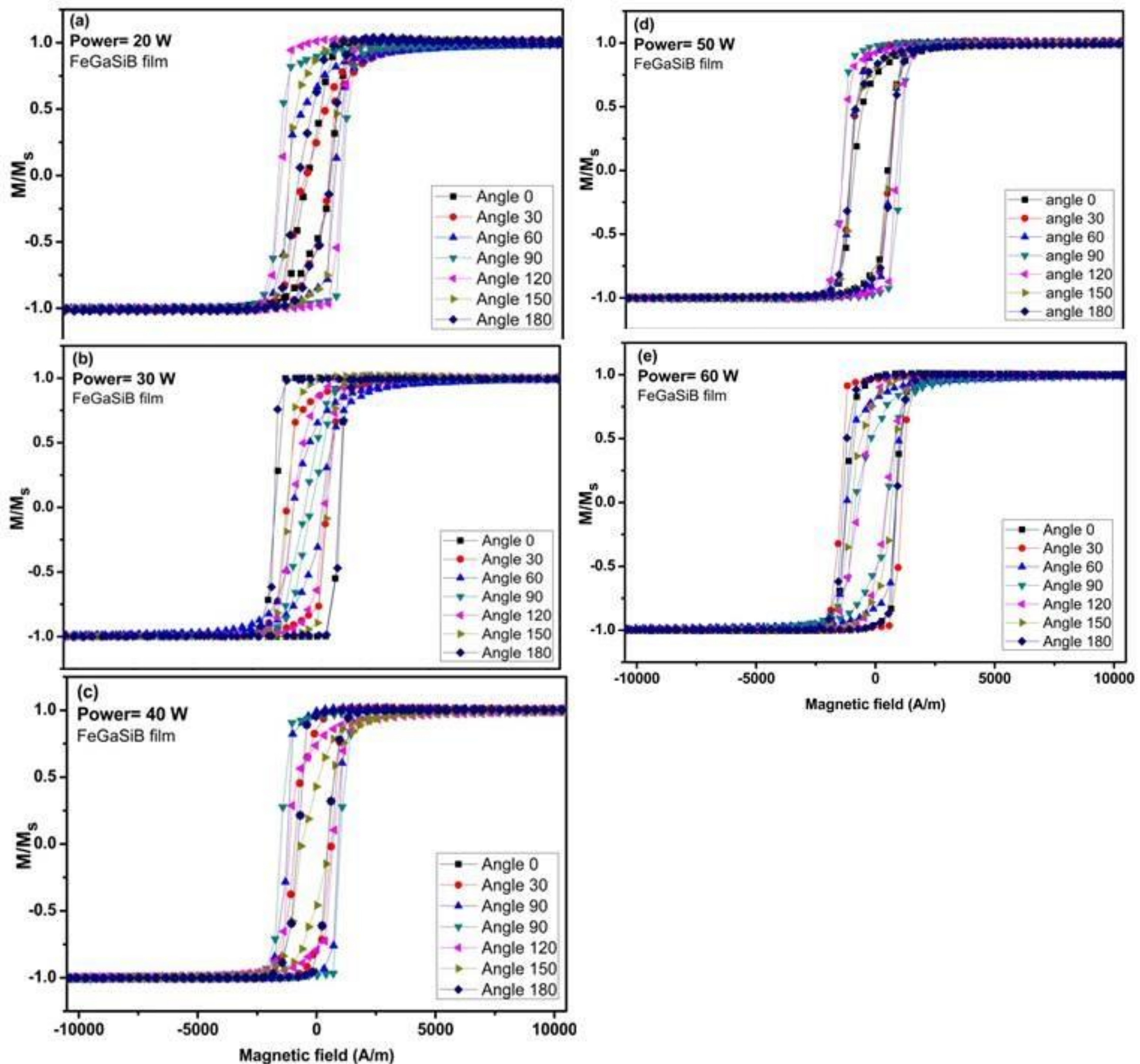

Figure 6.17 Normalized hysteresis loops, at different applied field angles, for 50 nm FeGaSiB films for different sputtering target power. (a) 20 W (b) 30 W (c) 40 W (d) 50 W (e) 60 W.

Figure 6.17 shows the normalized hysteresis loops measured by the MOKE system at different applied field angles for 50 nm FeGaSiB films prepared at different sputtering target powers and at a fixed Ar gas pressure and Ga rate 0.2 (a.u). From **Fig. 6.17**, the effect of sputtering target power on the shape of the hysteresis loops is shown, for example, **Figs. (a) and (b)** had different shape hysteresis loops with different anisotropy fields, coercivity and remanence values. It can be seen that increasing the sputtering target power with the presence of Ga, reduced the in-plane induced anisotropy field and affected the coercivity and remanence values. This suggests that increasing the sputtering target power with Ga reduces the induced stress within the films, so changing the anisotropy field. Thus, for sputtering target powers higher than 30 W, the anisotropy field was reduced.

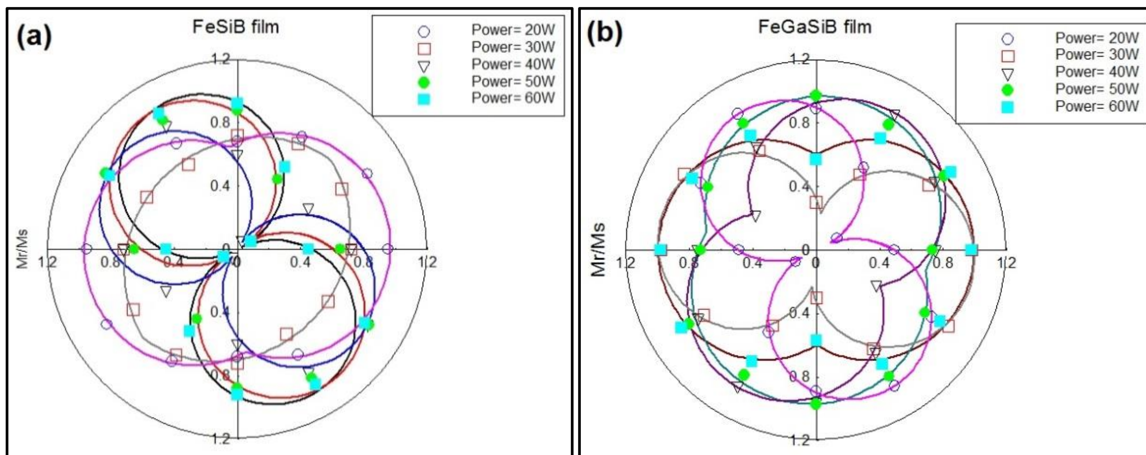

Figure (6.18) Angular plot of the remanence ratio (Mr/Ms) of different powers (a) FeSiB film (b) FeGaSiB film. The lines are a fitting to the data.

Figure 6.18 represents the angular plot of the remanence magnetization ratio (M_r/M_s) of the selected powers of both the FeSiB and FeGaSiB films. To examine the strength of the uniaxial anisotropy, from the remanence magnetization ratio (M_r/M_s), the fitting equation (5.2) is applied, the uniaxial anisotropy can be quantified [3] to the M_r/M_s as a function of angle data **Fig 6.18**.

For the FeSiB film at power 30 W, D ≈ 0.16, therefore the film has very weak anisotropy, while a stronger uniaxial anisotropy is present in the films of powers 40, 50, and 60 W where D ≈ 0.9, 0.94, and 1 respectively. For this film, the difference in M_r/M_s is influenced by the power. While for the FeGaSiB films, they all had weak uniaxial anisotropy at the $P_{FeSiB} \geq 40$

W when D < 0.5 and stronger uniaxial anisotropy at P_{FeSiB} 20 W (7% Ga) when D ≈ 0.89. For this film, the difference in M_r/M_s was influenced by the power and Ga composition.

Figure 6.19 shows the effect of sputtering target power (P_{FeSiB}) on the anisotropy/saturation fields for FeSiB and FeGaSiB films. For the FeSiB films, H_k increased sharply from 2000 to 14000 A/m with increasing the sputtering target power (P_{FeSiB}). For the FeGaSiB films H_s increased gradually from 4000 to 5000 A/m with increasing the sputtering target power (P_{FeSiB}) and was about a factor 2.8 lower than the anisotropy fields of FeSiB films for $P_{FeSiB} \geq$ 40 W. Thus suggests that, the addition of Ga into FeSiB film reduced the induced stresses within the films, so giving stability to the saturation field over the power range.

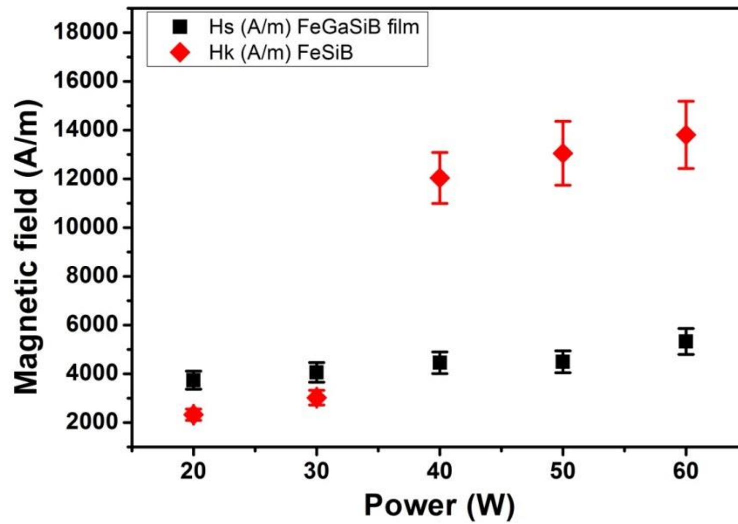

Figure 6.19 Saturation/Anisotropy Fields as a function of power for the FeSiB and FeGaSiB films.

Figure 6.20 shows the coercive fields as a function of sputtering target power (P_{FeSiB}) for FeSiB and FeGaSiB thin films. In general, the result showed that the coercivity H_c of FeSiB films were higher than the coercivity H_c of FeGaSiB films for all the powers, except the P_{FeSiB} = 40 W, which had a minimum value of 95 A/m. The maximum coercivity H_c of the FeSiB films was 1000 A/m at a power of 50 W, while the maximum coercivity H_c of the FeGaSiB film was 750 A/m. This means the FeGaSiB films had softer magnetic properties except at P_{FeSiB} = 40 W. For these two sets of films, the coercivity is influenced by changing the power.

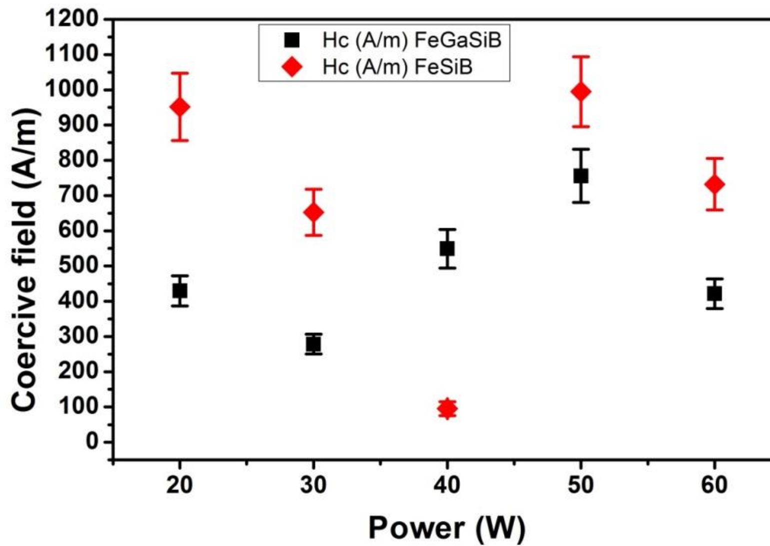

Figure 6.20 Coercive fields as a function of power for the FeSiB and FeGaSiB films.

6.5.2.2 Magnetic Properties Measured by VSM System

The VSM measurements of magnetostrictive FeSiB and FeGaSiB thin films were used to determine the magnetic moments hence the saturation magnetization, the coercivity, and the normalized remanence.

Figure 6.21 shows the saturation magnetization results of the VSM measurements for FeGaSiB thin films, which were measured at room temperature to avoid any thermal effects of high temperatures and to avoid annealing the films. From **Fig 6.21**, it can be seen that the saturation magnetisation of the FeGaSiB films increased slightly with increasing the power and then decreased with increasing the power > 30 W, and then at a power of 60 W the saturation magnetization increased again. It can be seen that the minimum value of the saturation magnetization was at the power of 50 W and the maximum saturation magnetization was at the power of 30 W.

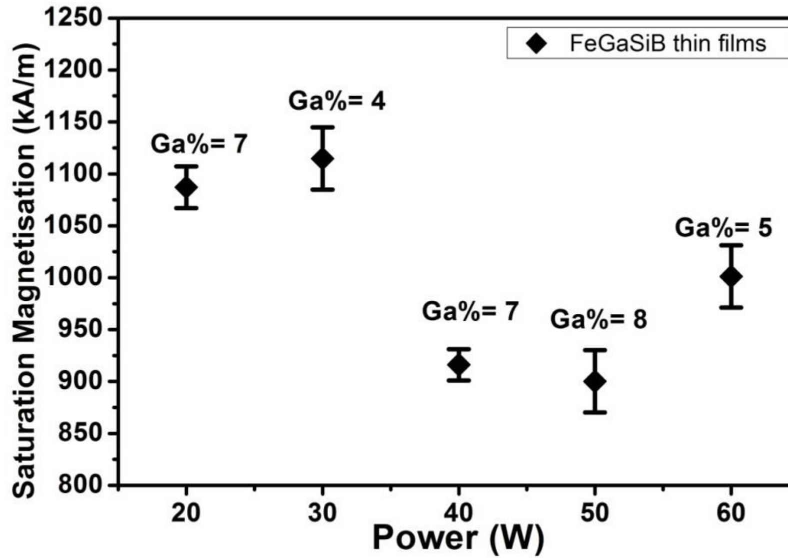

Figure 6.21 Saturation magnetization as a function of power for the FeGaSiB films.

From **Fig. 6.21**, it can be seen that the change in the saturation magnetization is not dominated by the power as the change in the saturation magnetization is not gradual with the power. While it is found that the Ga percentage was fluctuating with increasing the power (see **Fig.6.14**), it is suggested that the reduction in saturation magnetization is dominated by Ga percentage as the change in saturation magnetization follows the change in Ga percentage. It can be seen that the film, which has the highest saturation magnetization has the lowest Ga percentage of 4%, while the lowest saturation magnetization was for the film with the highest Ga percentage of 8%. Further, it is found that the saturation magnetization of the film with a power of 20W is not dominated by Ga percentage as suggested above, therefore this difference could be due to having this film a different stress compared with others.

6.5.3 Magnetostriction Properties

Figure 6.22 shows magnetostriction constant λ_s as a function of changing the sputtering target power, P_{FeSiB}, for the FeSiB and FeGaSiB films. From **Fig 6.22**, it is observed that the magnetostriction constant of the FeSiB thin films decreased from 10 ppm to 3 ppm with increasing the power $\leq$ 30 W and then increased for the powers > 30 W to reach the maximum 21 ppm value at the power of 60 W. For FeGaSiB film, the magnetostriction constant decreased from 17.4 ppm for the $Fe_{82}Ga_7Si_5B_6$ film (P_{FeSiB} = 20 W) to 5.2 ppm for the $Fe_{85}Ga_5Si_3B_7$ films (P_{FeSiB} = 60 W), as the power increased. The 20 W film ($Fe_{82}Ga_7Si_5B_6$) had a maximum value of 17.4 ppm, which was higher than the magnetostriction constant 10 ppm of FeSiB film deposited at the same power. While for the

films deposited at 60 W, the FeSiB film the magnetostriction constant was 21 ppm, which was higher than the 5.2 ppm magnetostriction constant, of the $Fe_{85}Ga_5Si_3B_7$ film. The $Fe_{82}Ga_7Si_6B_5$ film had a magnetostriction constant of 6.5 ppm, which was lower than the magnetostriction constant of the FeSiB film deposited at the same power (40 W). Further, Javed [17] found that the addition of Ga into Fe films, as a function of sputtering Fe target power, resulted in a lower Ga composition at the highest power P_{Fe} similar to the $Fe_{85}Ga_5Si_3B_7$ film, which had a lower magnetostriction constant at higher target power. He suggested that the Fe atoms have a higher energy reaching the substrate, which gave rise to a change in the local structure.

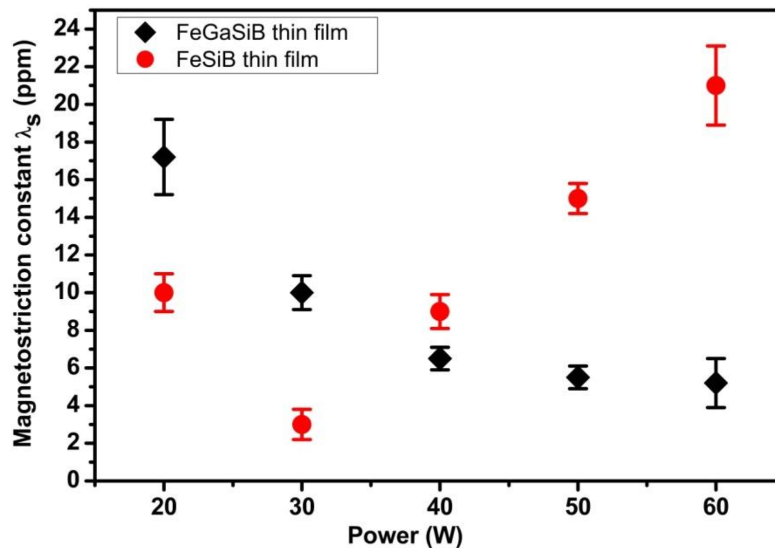

Figure 6.22 Magnetostriction constant λ_s as a function of power for the FeSiB and FeGaSiB films at room temperature.

6.6 Influence of Ga Evaporation Rate on The Structure, Magnetic Properties, and Magnetostriction Constants of Amorphous FeGaSiB Thin Films

In the co-sputtering-evaporation technique, the Ga evaporation rate is an important parameter to grow the films. It can influence the FeSiB:Ga ratio and the composition of the deposited films, as the films are deposited at fixed Ar pressure and sputtering target power. Quantitatively, the Ga evaporation rate cannot be calibrated, due to it being unachievable to manufacture pure Ga films, which can be calibrated at room temperature, as Ga has a melting point just above room temperature. Thus the rate is measured by a rate monitor placed inside the chamber.

6.6.1 Structural Properties

XRD measurements were taken to examine whether the films were completely amorphous or if they included crystalline cluster in an amorphous matrix. **Fig. 6.23 (a)** shows the XRD patterns of FeGaSiB films with varying Ga evaporation rates. It shows that all the films had an amorphous structure and all the peaks present were for the Si substrate. As previously done, to avoid the substrate peaks, the Si peaks at 2θ 33° are presented in **Fig 6.23 (b)**, the XRD measurement was repeated with a 2θ range (35° to 55°) as shown in **Fig 6.23 (c)**. It can be seen from **Fig 6.23 (c)** there are no peaks existing at 2θ ~ 45°, which would be due to the presence of crystalline Fe or the Fe-Ga (110) texture within the films [18]. Hence the films had an amorphous structure. Thus **Fig. 6.23 (a)**, **(b)**, and **(c)** show that varying the Ga evaporation rate does not influence the film morphology. This indicates that the film morphology is independent of the Ga evaporation rate, and hence the amount of Ga in the films.

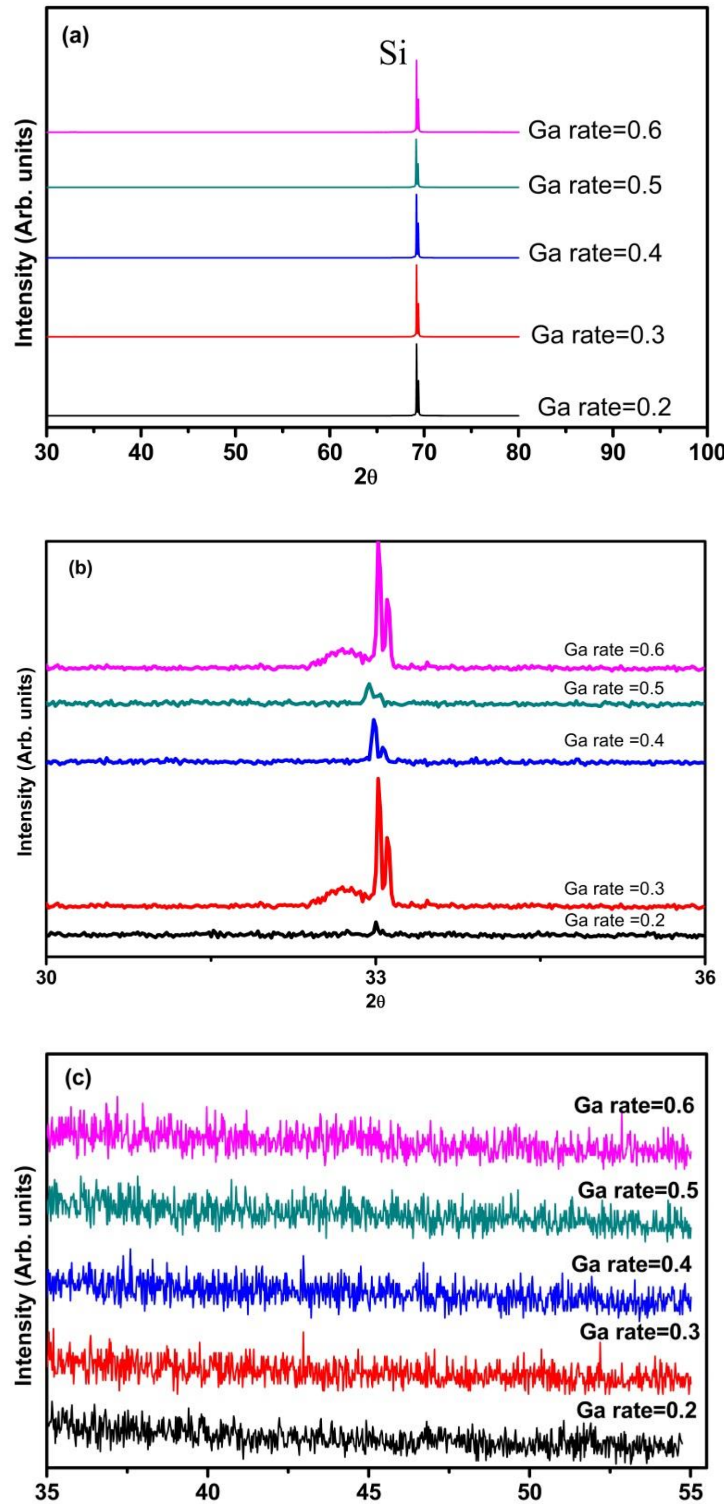

Figure 6.23 (a) XRD FeGaSiB thin films with different Ga evaporation rates. (b) The Si peaks. (c) The FeGaSiB film without the Si peaks.

Table 6.3 Summary of the XPS result of the film's composition via the Ga evaporation rate.

Ga evaporation rate	Fe%	Ga%	Si%	B%
0.2	82	7	5	6
0.3	83	8	4	5
0.4	79	11	5	5
0.5	79	12	5	4
0.6	77	14	5	4

Table 6.3 shows the result of the XPS measurements of the films for different Ga evaporation rates. The results showed that Ga was successfully added to FeSiB films by using the co-sputtering-evaporation technique, to fabricate the FeGaSiB films. For fixed pressure and power, the results also show that increasing the Ga evaporation rate led to an increase in the Ga concentration. This allows for control of the Ga percentage within the films. It can be seen in **Fig. 6.24** that the composition of Ga has a linear relation with Ga evaporation rate (R_{Ga}). Thus the Ga composition can be controlled over a range of Ga% by changing the Ga evaporation rate (R_{Ga}), whilst the remaining fabrication parameters remain constant. The data in **table 6.3** also show that the Fe and B concentrations decreased with increasing Ga concentration, while the Si concentration is maintained within the accuracy of the measurement.

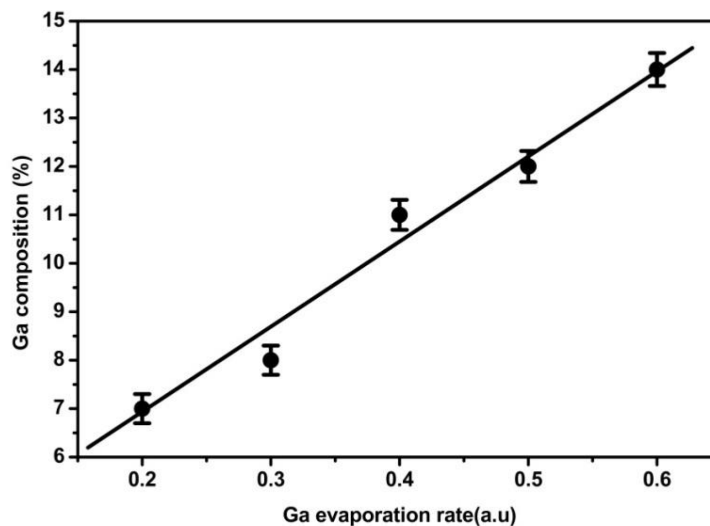

Figure 6.24 Ga compositions as a function of Ga evaporation rate under constant pressure 4 μbar and power 20 W. The solid line is a guide for the eye.

6.6.2 Magnetic Properties

6.6.2.1 Magnetic Properties Measured by MOKE

For the chosen range of Ga evaporation rate, the MOKE measurements of the magnetostrictive FeGaSiB thin films were used to measure the necessary magnetic properties including the normalized remanence, anisotropy fields, and coercivity.

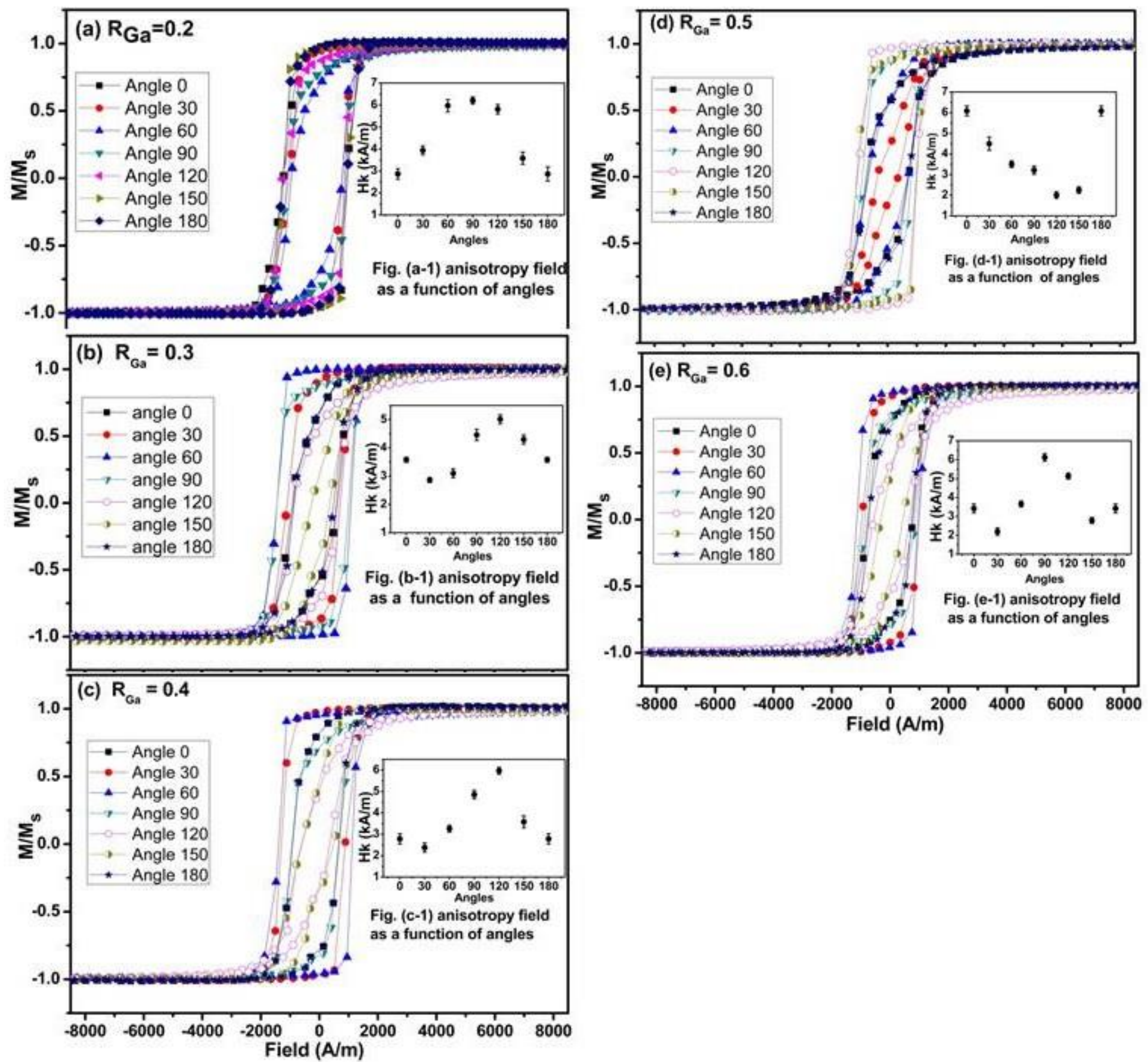

Figure 6.25 Hysteresis loops of FeGaSiB films for different Ga evaporation rates, where (a) R_{Ga} 0.2, (b) R_{Ga} 0.3, (c) R_{Ga} 0.4, (d) R_{Ga} 0.5, and (e) R_{Ga} 0.6. The right insert fig (a-1, b-1, c-1, d-1, e-1) sow the anisotropy fields H_k at different applied field angles.

Figure 6.25 (a, b, c, d, and e) shows the normalized hysteresis loops for FeGaSiB films where the anisotropy fields were determined as a function of the angles between the applied magnetic field and the designated film side.

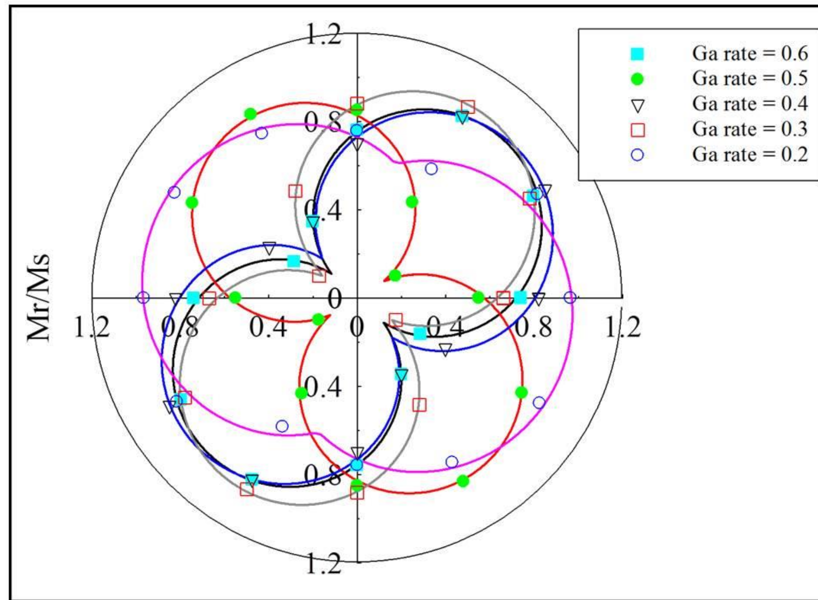

Figure 26 Angular plot of the remanence ratio (M_r/M_s) of different Ga Rates. The lines are a fit to the data.

The uniaxial anisotropy can be quantified by fitting the equation (5.2) [3] to the M_r/M_s as a function of angle, as shown in **Fig. 6.26**. Thus, for the film at 7% Ga, D ≈ 0.3, indicating a weak uniaxial anisotropy, while a stronger uniaxial anisotropy is present in the film at 8% Ga, where D ≈ 0.83. One reason for this could be that as all the films were amorphous the anisotropy will be influenced by the intrinsic stress within the films. Hence this suggests that the films with Ga > 7% had a larger intrinsic stress, compared to the 7% Ga film. Also, the increase in uniaxial anisotropy could be due to increasing the amount of Ga within the films from 7 Ga% to 14 Ga%, as Ga does not have a polarizable magnetic moment, which can modify the nearest neighbour interactions of the Fe-Fe atoms.

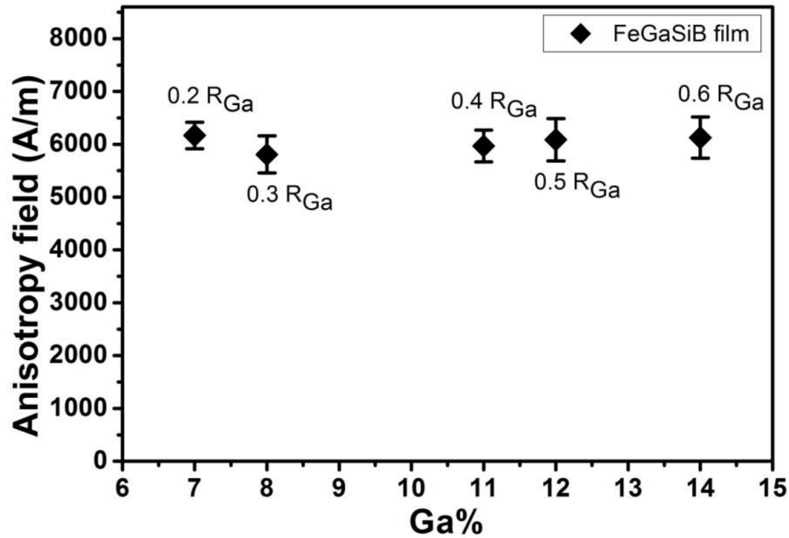

Figure 6.27 Anisotropy field as a function of Ga composition for FeGaSiB thin films.

Figure 6.27 presents the anisotropy field as a function of different Ga evaporation rates for FeGaSiB thin films. From **Fig. 6.27**, for all the films as the Ga evaporation rate was increased (Ga% from 7% to 14%), the $H_k \approx 6000$ A/m, along the hard axis loop remained. This shows approx constant that even with the increase of Ga within the films, the anisotropy field was maintained. The anisotropy energy depends on the anisotropy constant, which is given by $K = \frac{\mu_o H_k M_S}{2}$. From **Fig. 6.29**, it is observed that there is a change in M_s with Ga concentration. Thus the anisotropy constant of 7% Ga is K= 4212 Jm^{-3}, while the 14% Ga is K= 3353 Jm^{-3}. Hence a difference in anisotropy energy, but a difference compared in anisotropy as determined in **Fig. 6.25**. One reason is that the two methods are using different parameters from the magnetic hysteresis loop. The remanent magnetization depends on the pinning of domain walls in the film, while the anisotropy field is dependant on the dominated energy contribution. Thus this suggests that the 17% Ga film, has less pinning, so a small M_r/M_s, which leads to strong uniaxial anisotropy observed in **Fig 6.25**, but has a smaller M_s, thus the anisotropy constant is smaller. Comparing this to a 50 nm FeSiB film grown with the same fabrication parameters, $H_k \approx 2300$ A/m (see chapter 5), the FeGaSiB films all have a higher anisotropy field.

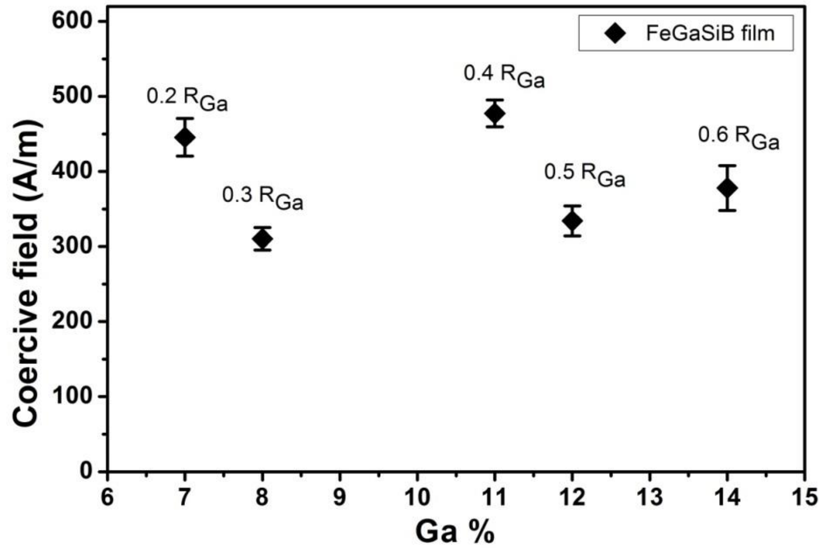

Figure 6.28 Coercive fields as a function of Ga composition for FeGaSiB thin films.

Figure 6.28 shows the coercive field, along the hard axis loop, as a function of the Ga evaporation rate for the FeGaSiB thin films. The coercive fields were in the range from 300 to 500 A/m, which are lower than the coercive field of a 50 nm FeSiB film, grown with the same fabrication parameters (see chapter 5) of $H_c \approx 800$ A/m. This means that the Ga addition has reduced the coercive field, suggesting that the coercive field depends strongly on the pinning in the material. A ferromagnetic material is taken to be soft when it has a low coercivity. Absence of grains and grain boundaries in amorphous alloys makes them to be homogeneous and this leads to them containing less defects. Thus as the number of defects is very small in amorphous material, the pinning can be less, resulting in a very soft material, with a small coercivity (<500 A/m).

6.6.2.2 Magnetic Properties Measured by VSM

For the designated range of Ga evaporation rate, the VSM measurements of magnetostrictive FeGaSiB thin films were used to measure the magnetic moments and hence the saturation magnetisation, the remanence, and the coercivity.

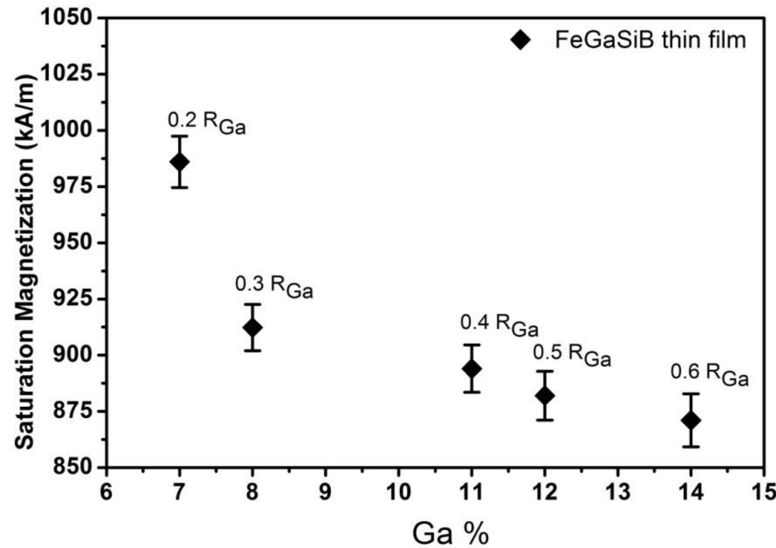

Figure 6.29 Saturation magnetization as a function of a Ga % of FeGaSiB thin film.

Figure 6.29 shows the saturation magnetization for FeGaSiB thin films measured by the VSM technique at room temperature. From **Fig 6.29**, it is noted that the magnetization of the films reduces with increasing Ga evaporation rate, hence an increase in Ga concentration, and decrease in Fe concentration (**Table 6.3**). As Ga is a non-magnetic element, it will decrease the magnetization of the films, along with changing the distribution of Fe atoms within the films, which can produce a variation in the films' composition [19], [15]. During evaporation, the amount of Ga atoms evaporated can be changed via the crucible temperature. By increasing the crucible temperature, the Ga evaporation rate increases, which is measured by thickness rate monitor. As the films were deposited at fixed Ar pressure (4 µbar) and sputtering power (20 W), such that the Fe, Si and B were sputtered at a fixed rate of 0.1, the ratio of Ga atoms will be proportional to the Ga evaporation rate. Thus more Ga atoms will reach the substrate compared with the sputtered Fe, Si, and B atoms. Also, as the deposition was done under low pressure, this will decrease the scattering of the Ga atoms by the Ar ions in the plasma and lead to a higher number of Ga atoms reaching the substrate. These conditions changed the concentrations of Fe, and Ga atoms within the films, which will lead to a distribution of the non-magnetic different atoms in the local environment within the

amorphous matrix, i.e. the nearest neighbours Fe atoms. As the magnetic moment of the Fe atoms is dependent directly on the nearest neighbours in the local environment, hence, the magnetization of the film will depend upon the atomic nearest neighbours. Due to the amorphous structure of FeGaSiB films, which have no long-range order or set lattice constant, this will influence the magnetisation of the films. In general, changing the amorphous distribution presents fluctuations in the exchange interactions, which impact the magnetic properties of the material. For example, the saturation magnetization of composition $Nd_2Fe_{11.5-x}Co_{2.5}Ga_xB$ decreases with increasing Ga content, as Ga is a non-magnetic element and will occupy certain the Fe sites, so changing the contribution of the Fe atoms [20].

6.6.3 Magnetostriction Properties

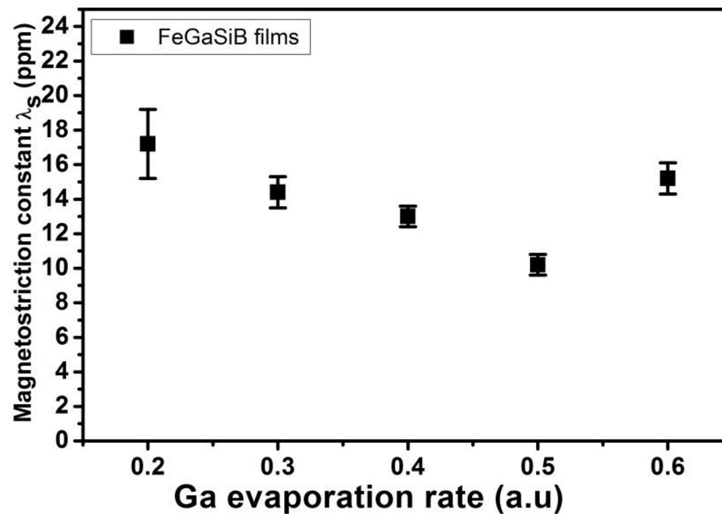

Figure 6.30 Magnetostriction constant as a function of Ga evaporation rate of FeGaSiB thin film.

Figure 6.30 shows the magnetostriction constant as a function of Ga evaporation rate of the FeGaSiB film. From **Fig 6.30**, it is observed that the magnetostriction constants of FeGaSiB thin films decreased with increasing Ga evaporation rate until R_{Ga} = 0.5 (Ga% =12), then increased for R_{Ga} = 0.6 (Ga% =14). The films have the highest magnetostriction constants, λ_s, at the lowest Ga evaporation rate with the maximum $\lambda_s = 17.2 \pm 0.3$ ppm, at R_{Ga} = 0.2 (Ga% =7). Compared with Ref. [16], for amorphous FeGaB films, they found that the addition of B into the bcc FeGa films in the range of 0-21% led to a change the content of Ga from 9 at% to 17 at% and the maximum value of the magnetostriction constant found to be

70 ppm at the boron content of 12at %. Further, Kobliska et al [21] found that the magnetostriction constant of amorphous films such as $Fe_{73}Si_6B_{21}$ had a saturation magnetostriction constant about 26 ppm, which is higher that the $Fe_{82}Ga_7Si_5B_6$ film in our study, while the amorphous $Fe_{62}Si_{19}B_{19}$ films had saturation magnetostriction constant of 14 ppm, which is lower than $Fe_{82}Ga_7Si_5B_6$ films. The minimum value of FeGaSiB films was λ_s = 10.2 ± 0.3 ppm in the $Fe_{79}Ga_{12}Si_5B_4$ film deposited at R_{Ga} = 0.5, which has Ga% = 12 and boron content 4 %. Compared with Ref. [16] for the FeGaB films, which had a minimum magnetostriction constant of about 46 ppm at the Ga content 17 at% and B content 21at%, it would seem that the Ga and B percentage in the films are important for the magnetostriction constant. In general, a higher B percentage is required to achieve the higher magnetostriction constants.

In addition, it was found that the FeGaSiB films minimum λ_s is higher than that the amorphous $Co_{79}Fe_5B_{14}Mo_2$ films, which has a magnetostriction constant equal to zero [21]. This nonlinear behaviour of magnetostriction constant as a function of nonmagnetic element's contents was also observed in other amorphous magnetic structures such as FeCoB [22]. According to Ref. [23], the reason for the magnetostriction nonlinear behaviour is due to a low amount of metalloid atoms such as Boron leading to creation of atomic pairs, for example, B-B and Ga-Ga that influence the magnetostriction behaviour. They suggest that increasing the content of metalloid atoms would lead to the formation of clusters that reduce the magnetostriction constant. Increasing the Ga evaporation rate from 0.2 to 0.6 increased the Ga percentage within the films from 7% to 14%, leading to changes in the local environment around the Fe atoms, hence changing the magnetic configuration and the exchange interaction of the Fe magnetic moments (**Fig. 6.29**). This can also affect the stress within the films due to changes in the distribution of Fe and Ga atoms in an amorphous matrix, which is the probable reason why the strength of the uniaxial anisotropy increased in the films with higher Ga%. Thus, the magnetostriction constant, λ_s, is influenced by both the saturation magnetization (**Fig 6.29** and equation 2.36), which depends on the composition and the stress present within the films.

6.7 Comparison of Fabrication Parameters

In this study, changing the growth parameters and adding the Ga were the main sources to influence the magnetic properties of the magnetostrictive amorphous thin films. Therefore comparing the effect of these parameters on the magnetic properties as a function of Ga

composition could help with understanding which parameter is dominating of these effects. From the XRD, it is found that all the growth parameters and adding the Ga did not affect the morphology of the films, as all the films had an amorphous structure.

The magnetocrystalline anisotropy caused by the long-range order in crystalline materials is absent in amorphous materials. Though, the local atomic order of amorphous materials can participate in a random anisotropy. Adding the Ga can affect the local atomic order of amorphous films. Therefore, a comparison between the anisotropy fields of the amorphous FeGaSiB films deposited by different growth parameters as a function of Ga composition could help to understand if the Ga percentage is dominating the change in anisotropy field. **Figure 6.31** shows anisotropy/saturation fields as a function of Ga composition for all the sets of FeGaSiB films. It is found that a slight increase in saturation field was observed over a range of Ga from 4% to 8% for varying the Ar pressure. While for varying the target power (P_{FeSiB}), the saturation field was found to fluctuate over a range of Ga from 4% to 8%. For the varying Ga evaporation rate, the anisotropy field increased with increasing the Ga % and found to be higher than saturation fields of varying both the Ar pressure and target power. The result of **Fig 6.31** shows that the lowest saturation field can be achieved at lower pressure and at low Ga composition (4%).

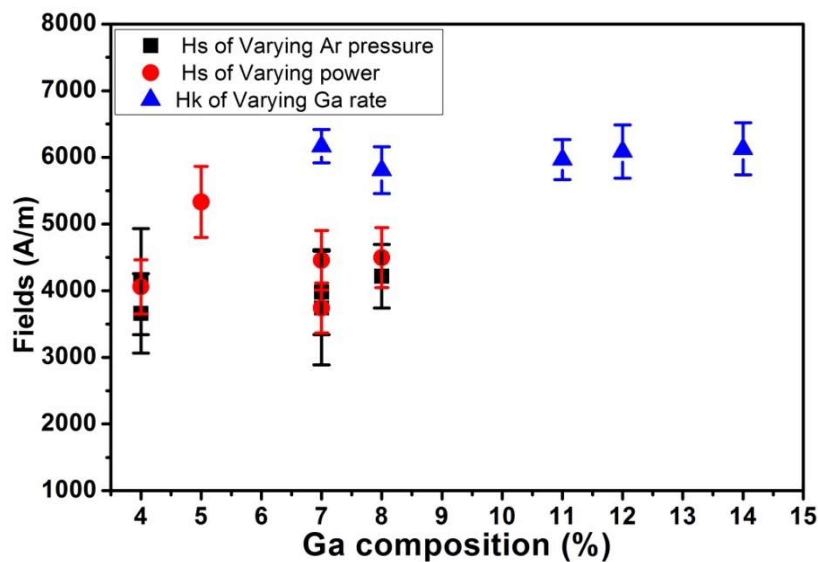

Figure 6.31 Anisotropy/saturation Fields as a function of Ga composition for FeGaSiB film (■) Varying Ar pressure, (●) Varying power (P_{FeSiB}) (▲) Varying Ga rate. The lines are a guide for the eye.

From **Figs.** (**6.11**, **6.22**, and **6.30**), the magnetostriction constant is plotted as a function of the growth parameters such as the Ar pressure, the target power, and the Ga evaporation rate. The maximum values of magnetostriction constant were at low pressure of 4 μbar, low power 20 W, and Ga evaporation rate of 0.2 (a.u.). Then the magnetostriction constants were decreased with increasing all the selected growth parameters.

Figure 6.32 shows the measured magnetostriction constant as a function of Ga composition for all the sets of FeGaSiB film. The comparison of magnetostriction constants for all the sets of FeGaSiB film (**Fig 6.32**) shows that for the film set of varying the Ga rate, all the magnetostriction constants were higher than both of the film sets for varying the Ar pressure and varying the target power when the Ga composition ≥ 7%. For all the FeGaSiB film sets, the highest magnetostriction was 17.4 ppm at the Ga composition of 7%. For the variation of Ar pressure, the magnetostriction constant increased with increasing the Ga composition while for the varying of target power, the magnetostriction constant decreased with increasing the Ga composition. From the **Fig. 6.32**, there was no evidence of peaks as detected in the binary FeGa film. [24, 25]

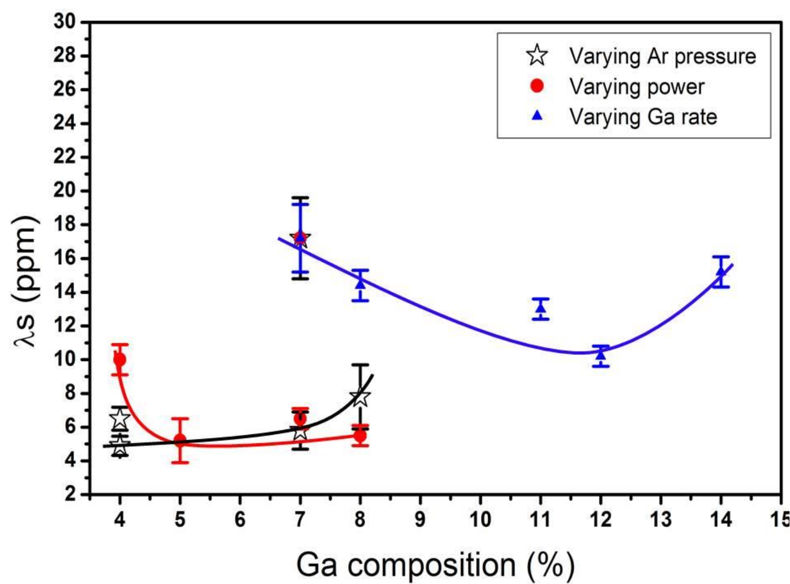

Figure 6.32 The dependence of magnetostriction constant on Ga composition for FeGaSiB thin films as a function of (■) Varying Ar pressure (●) Varying target power (♦) Varying Ga evaporation rate. The lines are a guide for the eye.

Due to the absence of crystalline structures and phases, which were expected to be formed in these films as a result of changing the growth parameters, all these films have an amorphous structure, which is verified by the XRD (see **Figs 6.2**, **6.13**, **6.23**). Therefore the structure does not dominate the effect of the magnetostriction constants. The structure of the film is an important property, which can affect the magnetostriction constant. Many studies in the literature show that magnetostriction constants are sensitive to the structure and changes in the crystalline phases. For example, Basumatary et al [26] studied the binary $Fe_{100-x}Ga_x$ film, which includes many phases such as (A2, DO_3, Ll_2, and B2). The film had an effective magnetostriction constant about 75 ppm at Ga composition of 17% as a result of forming a disordered A2 phase. While for Ga composition between 17% and 25%, the magnetostriction constant decreased as a result of forming the disordered $D0_3$ phase. They found that in case of more than one phase in the film being present, such as present both the ordered $D0_3$ and $L1_2$ phases into A2 matrix led to an additional decrease in the magnetostriction constant. Another example for the effect of structure is that was not fully amorphous. Z.G. Sun et al [27, 28] studied the amorphous $Fe_{78}Si_{10}B_{12}$ thin film of 100 nm thickness. They found that the film contained nanocrystalline structure such as αFe(Si) immersed in amorphous matrix [27]. It was found that the magnetostriction constant of the film was equal to 6.5 ppm, which was smaller than the magnetostriction constant 36 ppm for the fully amorphous $Fe_{78}Si_9B_{13}$ thin film. This reduction in the magnetostriction constant was due to the negative magnetostriction constant of the αFe(Si) nanocrystalline structure.

From **Fig. 6.32** it can be seen that some of the FeGaSiB films, which were fabricated at different growth parameters had a comparable Ga composition. Therefore the magnetostriction constants were influenced by the growth parameters such as the Ar gas pressure or sputtering target power. For the films with different Ga rates, the magnetostriction constants changed with increasing the Ga% within the films, therefore adding nonmagnetic element can influence the magnetostriction constants magnitude. Hall [29] reported that adding a nonmagnetic material such as aluminium into $Fe_{100-x}Al_x$ with composition range from 6% to 30%, at the room temperature, caused a remarkable increase in the magnetostriction constant. He found that the increasing of magnetostriction constant was sharp and had a peak at the Al composition of x= 0.19.

From **Fig. 6.32**, it can be seen that the fabrication technique and hence the growth parameters may affect the local environment of the Fe and Ga atoms. Therefore, to investigate the local environment of the Fe, Si, B, and Ga atoms, more experimental techniques are required, for

example, Extended X-ray Absorption Fine Structure (EXAFS) [30] which has been used to investigate the local environment of the Fe and Ga atoms in the binary $Fe_{80}Ga_{20}$ alloy. This technique has sensitivity to the first neighbour atom and can provide data about the chemical property of the nearest neighbours such as the number of atoms, the distance from them to the absorbing atom, and their static disorder related to the absorber atom. Another technique which could be used to investigate the films is Conversion Electron Mössbauer Spectrometry (CEMS) [31, 32]. From this technique, a more detailed investigation of amorphousity of the films by comparison of magnetic hyperfine field distribution in thin films as a function of Ga content can be obtained. Mössbauer spectrometry would be also helpful in determination of magnetic anisotropy.

6.8 Summary

X-ray diffraction (XRD) results of FeSiB and FeGaSiB films, for all the selected growth parameters, indicated that all the sets of both films had amorphous structure.

For all the growth parameters, the results showed that Ga was successfully added into FeSiB films without affecting the morphology of the films while the magnetic properties, and magnetostriction constant were influenced.

The magnetostriction constant, λ_s, decreased with increasing sputtering gas pressure from 17.4 ppm for the $Fe_{82}Ga_7Si_5B_6$ film to 4.9 ppm for the $Fe_{83}Ga_4Si_6B_7$ film. While the magnetostriction constant decreased from 17.4 ppm for $Fe_{82}Ga_7Si_5B_6$ to 5.2 ppm for $Fe_{85}Ga_5Si_3B_7$ with increasing the power, P_{FeSiB}. For the Ga evaporation rate, the films had the highest magnetostriction constants, λ_s, at the lowest Ga evaporation rate with the maximum $\lambda_s = 17.2 \pm 0.3$ ppm, at $R_{Ga} = 0.2$ (Ga% =7).

6.9 References

[1] M. Ali, Ph.D. dissertation, Dept. Phys. Astron., University of Sheffield, Sheffield, U.K., Sep. 1999.

[2] M. Chinmulgund, R.B. Inturi, J.A. Barnard, Thin Solid Films, 270, 260-263, 1995.

[3] E. Miskevich, F. K. Alshammari, W-G. Yang, J. Sharp, S. Baco, Z. Leong, Q. A. Abbas, N. A. Morley, Journal of Physics D: Applied Physics, 51, 085001, 2018.

[4] J. Yi-Jiao, He Wei, Ye Jun, Hu Bo, C. Zi-Yu, G. You-Hui, Z. Xiang-Qun, Y. Hai-Tao, C. Zhao-Hua, Chin. Phys. B Vol. 23, No. 1, 017502, 2014.

[5] N. A. Morley, S. L. Yeh, S. Rigby, A. Javed, and M. R. J. Gibbs, J. Vac. Sci. Technol. A, vol. 26, no. 4, pp. 581–586, 2008

[6] A. Javed, N. A. Morley, M. R. J. Gibbs, Journal of Applied Physics, vol. 107, p. 09A944, 2010.

[7] A. Javed, T. Szumiata, N.A. Morley, M. R. J. Gibbs, Acta Materialia, vol. 58, p. 4003-4011, 2010.

[8] N. A. Morley, A. Javed, M. R. J. Gibbs, Journal of Applied Physics, vol. 105, p. 07A912, 2009.

[9] B. Kundys, Yu. Bukhantsev, H. Szymczak, M.R.J. Gibbs, R. Zuberek, J. Magn. Magn. Mater., 258–259, 551–554, 2003.

[10] C. Hudson and R. E. Somekh, J. Vac. Sci. Technol. A 14,2169, 1996.

[11] C. Hudson and R. E. Somekh, Mater. Res. Soc. Symo. Proc. 239,145, 1992.

[12] R. E. Somekh and Z. H. Barber, J. Phys E: Sci. Instrum. 21,1029, 1988.

[13] A. Javed, N. A. Morley, and M. R. J. Gibbs, J. Magn. Magn. Mater., vol. 321, pp. 2877–2882, Sep. 2009.

[14] R.C. O Handley, Modern Magnetic Materials Principles and Applications, Wiley Inc, New York, 1999

[15] A. Javed, N. A. Morley, M. R. J. Gibbs, J Magn Magn Mater, vol. 321, p. 2877-2882, 2009.

[16] J. Lou, R. E. Insignares, Z. Cai, K. S. Ziemer, M. Liu, and N. X. Sun, Appl. Phys. Left., vol. 91, p. 182504, Oct. 2007.

[17] A. Javed, Ph.D. dissertation, Dept. of Materials Science and Engineering, University of Sheffield, Sheffield, U.K, 2010.

[18] B. W. Wang, S. Y. Li, Y. Zhou, W. M. Huang, and S. Y. Cao, Journal of Magnetism and Magnetic Materials, vol. 320, pp. 769–773, 2008.

[19] J.W. Judy, Smart Mater. Struct. vol.10, pp. 1115–1134, 2001.

[20] J. Q. Xie, C. H. Wu, and Y. C. Chuang, Solid state communications, vol.71, no. 5, pp. 329-332, 1989.

[21] R. J. Kobliska, J. A. Aboaf, A. Gangulee, J. J. Cuomo, and E. Klokholm, Appl. Phys. Lett., vol. 33, no. 5, pp. 473–475, 1978.

[22] L. P. Christopher, M. K. Minor, and J. K.Timothy, IEEE Transactions on Magnetics, vol. 37, no. 4, p. 2302, 2001.

[23] E. Clark, M.Wun-Fogle, J. B. Restorff, T. A. Lograsso, and J. R. Cullen IEEE Transactions on Magnetics, vol. 37, no. 4, p. 2678, 2001.

[24] A. E. Clark, K. B. Hathaway, M. Wun-Fogle, J. B. Restorff, T. A. Lograsso, V. M. Keppens, G. Petculescu, and R. A. Taylor, J. Appl. Phys. 93, 8621, 2003.

[25] T. A. Lograsso and E. M. Summers, J. Mater. Sci. Eng. A 416, 240, 2006.

[26] H. Basumatary, M. Palit, J. A. Chelvane, S. Pandian, M. M. Raja, and V. Chandrasekaran, Scripta Mater. 59, 878, 2008.

[27] Z.G. Sun, H. Kuramochi, M. Mizuguchi, F. Takano, Y. Semba, H. Akinaga, J. Magn. Magn. Mater. 272–276, 1160–1161, 2004.

[28] Z.G. Sun, H. Kuramochi, M. Mizuguchi, F. Takano, Y. Semb, H. Akinaga, Surface Science 556, 33–38, (2004).

[29] R. C. Hall, J. Appl. Phys. 28, 707, 1957.

[30] S. Pascarelli, M. P. Ruffoni, R. S. Turtelli, F. Kubel, and R. Grössinger, Phys. Rev.B 77, 184406, 2008.

[31] T. Szumiata, K. Brzózka, M. Gawroński, B. Górka, A. Javed, N.A. Morley and M.R.J. Gibbs, ACTA Physica Polonica A, Vol. 119, 2011.

[32] T. Szumiata, B. Górka, K. Brzózka, M. Gawroński, M. Gzik-Szumiata, A. Javed, N. A. Morley, M. R. J. Gibbs, Nukleonika, 58 (1): 27−30, 2013.

Chapter 7 Investigation of Mechanical Properties of Magnetostrictive Thin Films By Nanoindentation.

7.1 Introduction

In general, the mechanical behaviour of a material denotes its response to applied loads, where under an applied load, the material can be deformed. If the material deforms under small applied load, this could lead to elastic deformation, which means it will return to its original shape immediately after removing the applied load. In the case of applying very large loads, a plastic deformation in the material can occur. In this case, the material will not return to its original shape even after removing the load. It is known that amorphous materials are typically elastically isotropic, in spite of the fact that in some cases anisotropy can be produced either by processing methods or due to an external force, essentially in magnetic alloys and thin films [1, 2]. In isotropic materials, there are two significant elastic constants; these are the Young's modulus and Poisson's ratio. The nanoindentation technique is used to investigate the mechanical properties of materials in the form of bulk or thin films by applying a load in the range of mNewton on the material. In general, there is little information about the mechanical properties of crystalline or amorphous magnetostrictive thin films despite the wide use of these materials in applications. For example, amorphous magnetostrictive thin films have become of interest for micro-electro-mechanical systems (MEMS) such as magnetostrictive sensors [3, 4]. These applications require magnetostrictive thin films with good mechanical properties such as hardness and elastic modulus. If the mechanical properties of magnetostrictive thin films such as Young's modulus are measured, they can be used to calculate the magnetostriction constant of these films rather than use the mechanical properties of the substrate or the bulk values [5, 6]. This chapter describes the mechanical properties of two magnetostrictive thin films measured by the nanoindentation technique. The properties measured were hardness, reduced modulus, Young's modulus, and yield strength of magnetostrictive FeSiB, and FeGaSiB films. The films were grown in the same deposition chamber to allow comparison of the results. The influence of the addition of Ga into the FeSiB film was evaluated with the hardness, elastic modulus and yield strength of FeGaSiB films. Therefore, before investigating the mechanical properties of FeGaSiB film

Qayes A. Abbas, 2018 & Email: qayes.a.abbas@gmail.com

and understanding the effects of adding Ga on the mechanical properties of the magnetostrictive amorphous FeSiB film, it was necessary to investigate the mechanical properties of FeSiB film and compare the results.

To understand the mechanical properties of the magnetostrictive films and to avoid the effect of the substrate on the result, the Si substrate, which was chosen to grow the films on, was also studied, as the rigid substrate can affect the mechanical properties of the films [7]. Therefore, the mechanical properties of the Si substrate were measured by the nanoindentation technique. For a Si substrate of thickness 380 µm, the hardness was directly measured and plotted as a function of the indenter displacement. Further, to gain more information about the substrate effect, a glass substrate was used, to show the results of the thicker films. For both FeSiB and FeGaSiB films with a maximum thickness, comparison of mechanical properties between film/Si and film/glass substrates were achieved.

Nanoindentation tests have many problems; one of them is related to the tip. It is known that the tip shape changes considerably due to the use of the tip. This change can affect the tip radius and thereby its area function, hence the area function needs to be corrected occasionally. Therefore, by using the experimental determination method of the tip's area function [8], the real Berkovich indenter is not completely sharp. For example, Jaroslav et al [9], **Fig. 7.1 (a)** showed an image of the Berkovich indenter with three-sides of pyramidal symmetry by AFM technique. The correction of the area function can be achieved by using a material which has well-known mechanical properties. In this case, a standard calibration material is used to determine the area function [8]. This determination of the area function is typically achieved using fused silica [10], with elastic modulus and Poisson's ratio of 72 GPa and 0.17, respectively.

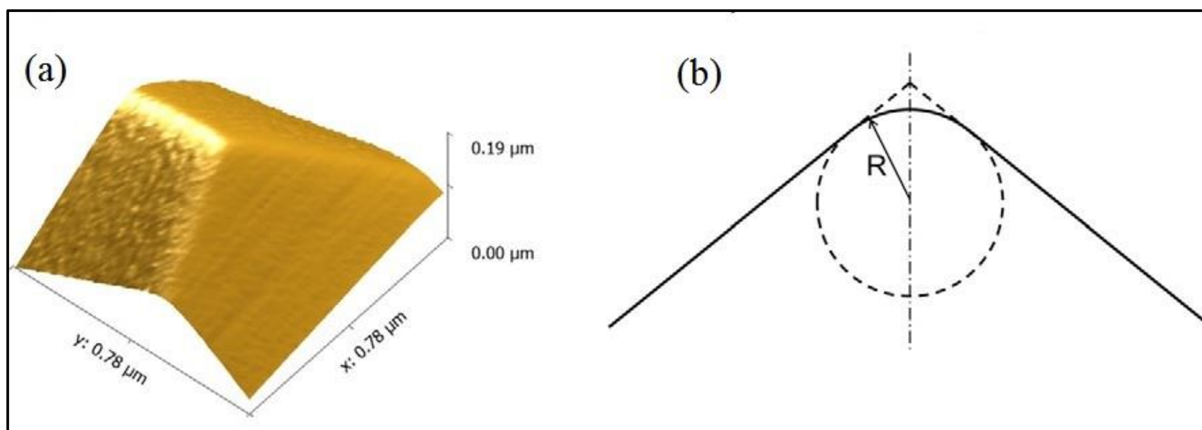

Figure 7.1 (a) AFM image of the Berkovich indenter, (b) schematic profile over the edge of the tip taken from reference [9].

Figure 7.1 shows the geometry of the Berkovich diamond tip normally used in nanoindentation tests, **Fig. 7.1 (a)** an image of the Berkovich indenter demonstrating the three-sides of pyramidal symmetry taken by AFM technique, **Fig. 7.1 (b)** the height profile plotted over the edge of the tip. The circle is fitting to have same radius of the tip. [9]

7.2 Fabrication of The Films

7.2.1 Fabrication of Thick FeSiB Films

For the growth of FeSiB films in this chapter, three thick films, 290, 425, and 660 nm were deposited on Si (100) and glass substrates with dimensions (10 mm x 15 mm), using the co-sputtering–evaporation technique [11], as described in detail in chapter 4. For all the films, the substrate-target distance (d) was 60 mm and the Ga evaporation rate was zero as the evaporator was off in this deposition, to achieve FeSiB films. All the films were grown with a fixed chamber pressure (p_{Ar}) of 4 µbar and at fixed sputter power (P_{FeSiB}) of 20 W. Three Si substrates were used per film growth, attached to a glass slide using polymethyl methacrylate (PMMA). Metglas 2605SA1 with composition $Fe_{85}Si_{10}B_5$ was used as the sputtered target. The substrate holder was rotated during the growth.

7.2.2 Fabrication of Thick FeGaSiB Films

For the growth of FeGaSiB films, three thick films, 283, 450, and 640 nm were deposited on Si (100) and glass substrates with dimensions (10 mm x 15 mm), using the co-sputtering–

evaporation technique [11], as described in detail in chapter 4. The substrate-target distance (*d*) was fixed at 60 mm. All the films were grown with a fixed chamber pressure (p_{Ar}) of 4 μbar, sputter power (P_{FeSiB}) of 20 W, and the Ga was evaporated with a constant arbitrary rate, R_{Ga} = 0.2 (arbitrary unit). Three Si substrates were used per film growth, attached to a glass slide using polymethyl methacrylate (PMMA). Metglas 2605SA1 with composition $Fe_{85}Si_{10}B_5$ was used as the sputtered target and the Ga (99.99%) material in the evaporator. The substrate holder was rotated during the growth.

7.3 Characterization of The Films

The Bruker D2 phaser technique, X-ray diffraction (XRD) with Cu $K_{\alpha1}$ 1.54184 Å was used to analyze the films' structure. The θ/2θ mode was used, the 2θ range from 35 to 55° to check the structure of the film (for bcc Fe 2θ ~ 45° and for bcc Fe-Ga 2θ ~ 45°) and used to avoid the Si substrate peaks (2θ = 69.8°, 61.7°, and 33°). XRD analysis was carried out to determine whether the films were fully amorphous or if they contained nanocrystalline cluster within an amorphous matrix. Atomic force microscopy (AFM) was used, in tapping mode, to measure the thickness of the samples using the step produced in fabrication and to check the topography.

The nanoindentation technique, (described in chapter 4) with a Berkovich indenter, which has radius 100 nm, Young's modulus 1140 GPa and Poisson's ratio 0.07, was used to investigate all the mechanical properties of the magnetostrictive films. The obtained curves were analyzed by the Oliver and Pharr method [12]. For preparing the sample for the nanoindentation test, there was significant sample preparation. Before the indentation test started, the specimen had to be held rigidly, to ensure that the measured displacement was at the correct penetration depth. Therefore, the use of a strong adhesive suitable for installation, such as a thin layer of glue was applied, to attach the sample to the holder. Other than that, the real measured displacement may have contributions from other displacements, related to the deformation of the substrate.

There are two load functions, which can be used to measure the mechanical properties of materials. The typical nanoindentation load function, which uses just one cycle curve to achieve a load-displacement curve. This involves applying a load, keeping the tip held, and then unloading the tip. The second load function, which can be used in nanoindentation measurements, is a partial load function. This type of load function involves a number of

cycles of load-displacement curves. The applied load is increased partially until reaching the maximum load. In this thesis, the partial load function was used to measure the mechanical properties of the films and substrates (see **Fig. 7.3**), as this method can provide information over a range of cycles for one indent, rather than the standard load function, which provides information from just one cycle. Therefore, to measure the mechanical properties, a partial load function was used with 50 cycles. The cycle involved loading for 5 seconds, at peak (maximum point) of the load the indenter was held for 5 seconds to remove any creep influence, and unloading for 5 seconds, with a maximum load of 10 mN. The results represent the total average of the indentations, which were set to be at least 14 per sample with error bars representing the standard deviation. Notice that in many places in the plots the error bars were smaller than the size of the curve symbols, leading them to disappear. The indentations were achieved in a perpendicular direction to the sample surface. For all the films and substrates, the Poisson's ratios were taken to be equal to 0.3 during analysis of the experimental data, as Ref. [13] presented indentation results that show that the Poisson's ratio leads to an insignificant influence. The estimation of the elastic modulus E_r is achieved from the unloading curve, which is supposed to be completely elastic. After determining the hardness data, the yield strength data can be calculated using Matlab data analysis software. In this study, the AFM images of the residual imprint of indentation were obtained by the indenter probe after finishing the indentation process and a sectional analysis was achieved to measure the height of the pile-up or sink-in material over the original surface of the film.

The Berkovich indenter used in this study had a radius of about 100 nm; therefore the indentation penetration depth should be higher than 1/3 of the radius tip, which in this case was about 33 nm. Before this value, the area function of the tip will break down and affect the measurements. This effect can be clear in the curves of hardness and elastic modulus when the values of the indentation penetration depth was less than about 33 nm. The Berkovich tip is blunt as described above, which causes the area function to increase sharply at small indentation penetration depths, hence the first part of all the hardness and Young's modulus curves will decrease or increase sharply at the small indentation depth. Increasing the indentation penetration depth greater than 33 nm should lead to horizontal and straight data curves of the mechanical properties. The contact area is very important to study for the mechanical properties and it can be determined, after unloading, from an analytical model of the load- penetration curve [12, 14].

7.4 Structural Properties

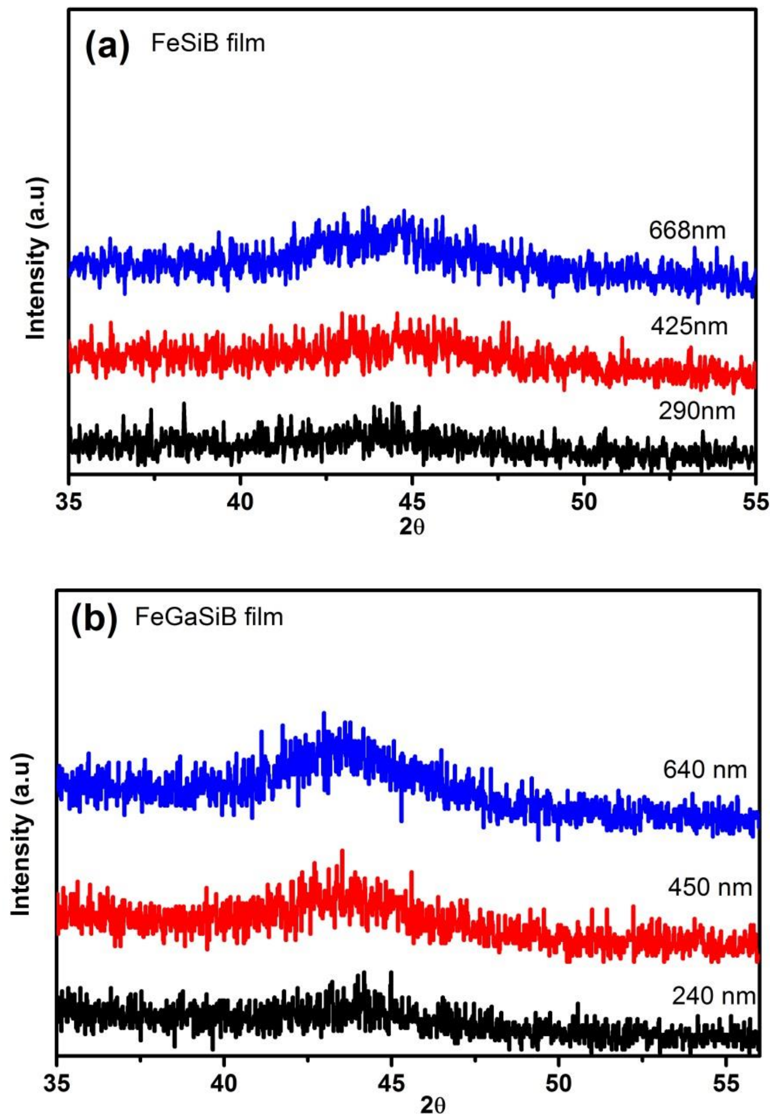

Figure 7.2 XRD of (a) FeSiB (b) FeGaSiB films with different thicknesses.

Figure 7.2 shows the XRD of FeSiB and FeGaSiB films of different thicknesses. For both films, it can be seen that a very broad peak is present. The size of this peak increases with the thickness. The broad peak was observed at $2\theta \sim 43^{o}$, which being indicative of absence the periodical atomic arrangement. From the XRD pattern, there was no sign of crystalline peaks observed, so confirms an amorphous structure.

7.5 Nanoindentation Test of Magnetostrictive Thin Films

In the nanoindentation test, during the pressing of the indenter into the material surface, elastic and plastic deformations are generated, leading to the creation of a residual imprint, which has the same indenter shape. During the unloading process, only the elastic part of the deformation is recovered. In a load-unload cycle of the indentation test, a load-displacement curve is obtained. This curve will be different from one material to another, depending on its response under the applied load. From this curve, the mechanical properties of materials are measured.

Figure 7.3 presents the experimental load-displacement curves, as examples of the three different materials (668 nm FeSiB film, 640 nm FeGaSiB film, and Si (100) substrate) used in this thesis, measured on the nanoindentation system using the partial load function method with 50 cycles and 10 mN a maximum applied load. It can be seen that there was a difference between the three curves; this difference is assumed to be due to the difference in the mechanical properties of these materials. As the Si substrate is harder than the FeSiB and FeGaSiB films, it has larger mechanical properties than both films. The mechanical properties of these materials will be presented and discussed later. The three curves have different indentation depth, which increased with increasing the applied load up to the maximum value. The curves show that the three materials had different maximum indentation depths at the same maximum applied load. The lowest penetration depth was for the Si substrate material of about 210 nm and the penetration depth of the 668 nm FeSiB film was about 300 nm, while the 640 nm FeGaSiB film had a maximum value of 370 nm. By analysing these three curves via Oliver & Pharr method [12], the mechanical properties were measured. Also from this figure, it can be seen that the difference in maximum penetration depth between the load-displacement curves of the FeSiB and FeGaSiB films for the same applied load was about 70 nm. This difference could be due to the addition of Ga. This means the addition of Ga into FeSiB film has changed the mechanical properties, which we will discuss in detail later.

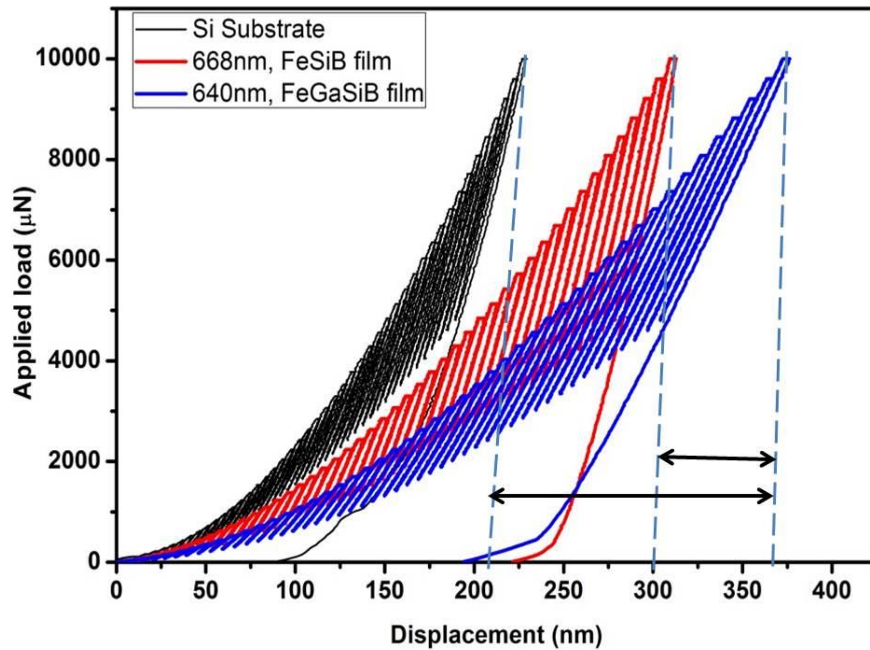

Figure 7.3 Experimental load-displacement curves of partial load function method with 50 cycles, applied load as a function of displacement, for FeSiB, FeGaSiB films and Si substrate.

Also from these curves, the amount of elastic recovery of these materials can be determined. This is the difference between the maximum value of the penetration depth and the final indentation depth, which appears after unloading the indenter. It can be seen that the unloading part of the curve is nonlinear; this because of the indenter is elastically unloaded, which leads to an increase in the contact area gradually up to the completed full cycle. Therefore, the elastic continuous variation in contact area is the reason why the unloading curves are nonlinear.

During the indentation test, there are two different effects, which can appear on the hardness data curve. The first is the nanoindentation size effect, which represents the decrease in the hardness values with increasing of the indentation penetration depth (increasing the applied load), and the second is the substrate effect, which represents an increase in the hardness values with increasing of the indentation penetration depth. If the hardness values do not change with increasing of the indentation penetration depth and appear as a horizontal straight line along with increasing the applied load, this means the hardness is not affected by either of the effects above. In the case of the indenter approaching the substrate, there can be an interaction between the substrate effect and the nanoindentation size effect. Therefore, by changing the thickness or the substrate, it can be seen, which one of these effects affects the result.

The theoretical calculation of the mechanical properties of the material presented in chapter 2 (section 2.8) showed that from the experimental data of load-displacement curves the stiffness, S, can be calculated from the slope of the initial part of the unloading curve by using equation (2.48). From the measured stiffness, the reduced modulus can be calculated using equation (2.50). The hardness, H_r, depends on the maximum applied load and the contact area and can be measured using equation (2.49). As the reduced modulus measurement includes the compliance of the indenter and the elastic modulus of the film, the Young's modulus of the films can be calculated from the equation (2.51) as the Young's modulus and Poisson's ratio of the Berkovich indenter are known and the Poisson's ratio of the films taken to be 0.3.

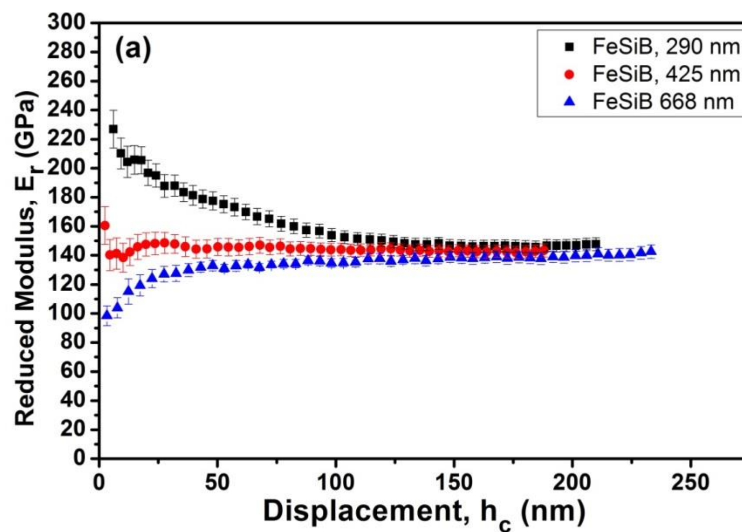

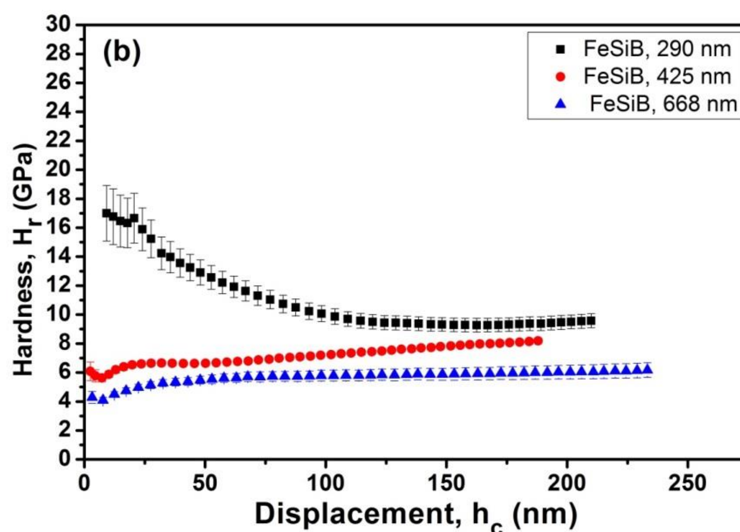

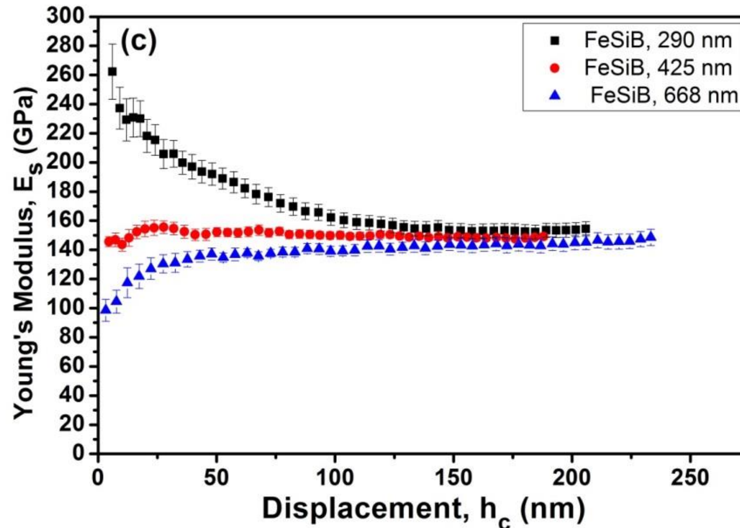

Figure 7.4 (a) Reduced modulus, E_r (b) hardness, H_r (c) Young's modulus, E_s, of FeSiB film for three different thicknesses as a function of displacement.

Figure 7.4 compares the reduced modulus, E_r, hardness, H_r, and Young's modulus, E_s, of the FeSiB film as a function of indentation penetration depth for three different thicknesses (290, 425, and 668 nm). **Fig. 7.4 (a)** shows the reduced modulus, E_r, of FeSiB film for three different thicknesses, it can be seen that the three films had different reduced modulus values, with the FeSiB film reduced modulus decreasing with increasing film thickness. Therefore the lower thickness 290 nm film had the highest reduced modulus values of about 160 GPa, which were affected by the substrate. While the highest thickness 668 nm film had the lowest reduced modulus values of about 140 GPa and was not affected by the substrate, as the data curve is a horizontal line.

Fig. 7.4 (b) presents the hardness, H_r, of the FeSiB film with three different thicknesses. It can be seen that there was no change in hardness for the highest thickness 668 nm film with an increase in indentation depth (displacement), as the data curve was a horizontal straight line at about 6 GPa value. While the hardness of the 425 nm film increased gradually from 6 GPa to 8 GPa with increasing indentation depth. The increasing hardness of this film is due to the effect of the substrate. Further, the smallest thickness 290 nm film showed an increase in hardness of about 10 GPa with increasing the indentation depth. This means that the film was affected by the substrate. The two smaller thicknesses, 290 nm and 425 nm of the FeSiB films showed hardness values higher than the 668nm film, this difference is taken to be due to the effect of the Si substrate. The effect of thickness on the Young's modulus, E_s, can be seen in the **Fig 7.4 (c)**, where the highest thickness 668 nm film had the lowest Young's

modulus values compare with the other thicknesses. From the **Figs 7.4 (a), (b)**, and **(c)**, the 668 nm film showed that the increasing of the applied load did not change the reduced modulus, hardness, and Young's modulus noticeably, as all the values for this film were a straight line. This means this thickness film was not affected by the substrate or by the indentation size. While the film with the smallest thickness, 290 nm, had a decrease in hardness with increasing the penetration depth until about 100 nm, this reduction in hardness was due to the indentation size effect.

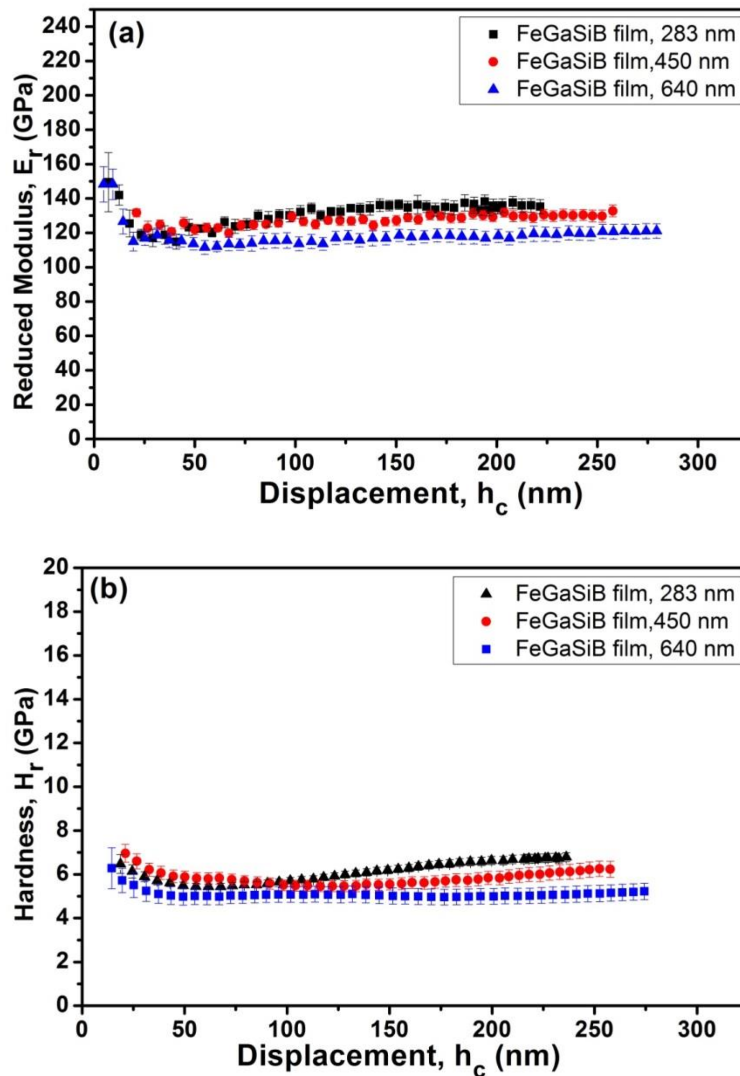

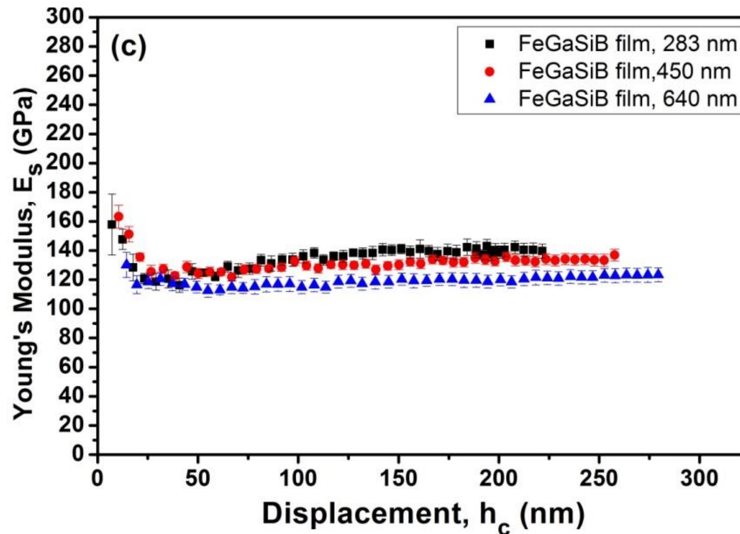

Figure 7.5 (a) Reduced modulus, E_r (b) hardness, H_r (c) Young's modulus, E_s, of FeGaSeB film with three different thicknesses as a function of displacement.

Figure 7.5 represents the mechanical properties of the FeGaSeB film with three different thicknesses (283, 450, and 640 nm) as a function of indentation penetration depth (displacement). From **Fig. 7.5 (a)**, it can be seen that the reduced modulus, E_r, of FeGaSiB films decreased with increasing thickness, which was the same behaviour as the FeSiB films. The lowest thickness 283 nm film had the highest reduced modulus value ~135 GPa, while the highest thickness 640 nm film had the lowest reduced modulus value ~115 GPa. From **Fig 7.5 (b)**, it can be seen that the films' hardness, H_r, decreased with increasing thickness. The 283 nm film had the highest hardness of about ~ 6 GPa, which increased with increasing applied load via the indentation penetration depth. This means that the film was affected by the substrate. The same thing was observed in the 450nm film, which had a hardness of about ~5.5 GPa, and increased with increasing the applied load. Further, the highest thickness 640 nm FeGaSiB film had the lowest hardness of about ~5 GPa, which was approximately constant with increasing the applied load. The influence of thickness on the Young's modulus, E_s, can be seen in **Fig 7.5 (c)**. The Young's modulus of FeGaSiB films decreased with increasing the thickness, where it can be seen that the highest thickness 668 nm film had a lower Young's modulus of about ~120 GPa, while the lowest thickness film Young's modulus value was of about~ 140 GPa. Also, from the **Figs 7.5 (a)**, **(b)**, and **(c)**, for the 640 nm FeGaSiB film, the increasing of the applied load did not change the reduced modulus, the hardness, and Young's modulus markedly, as all the values were constant, thus at this thickness the properties were not affected by the substrate.

In the soft film/hard substrate system, an increase in hardness can occur, when the applied load is enough to push the indenter forward towards the hard surface of the substrate through the soft film. This increase in hardness is due to combining the hardness of the film with the hardness of the hard substrate [15]. In our study, the limitation of the maximum applied load, which is 10 mN, was not enough to allow the tip to reach the substrate, therefore for each type of film, three different thicknesses have been studied to show the effect of the substrate on the results (**Figs. 7.4** and **7.5**). In the films with low thickness, the hardness was higher than the values for the thicker films. This is due to decreasing the thickness leading to an increase in the combined hardness, as it includes contributions from the hardness of both film and Si substrate, therefore the films with low thickness showed higher hardness values.

For both film sets in this study, the maximum values of both the hardness and Young's modulus at the maximum indentation depth, h_{max}, of each thickness have been chosen and plotted as a function of thickness to compare the data for FeSiB and FeGaSiB films with the hardness and Young's modulus values of Si substrate (**Figs. 7.6 (a)** and **(b)**).

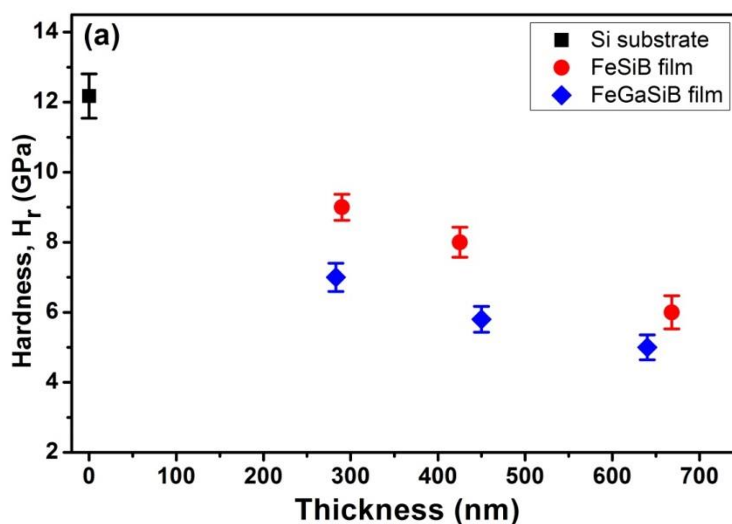

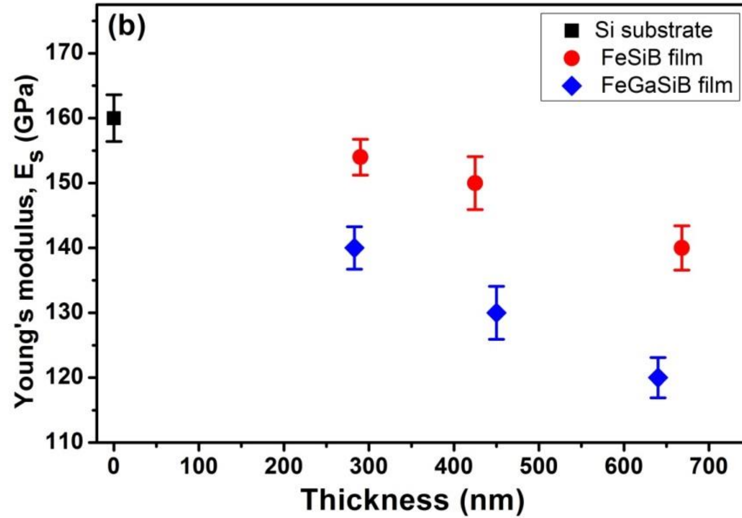

Figure 7.6 Comparison of (a) hardness, H_r (b) Young's modulus, E_s, of FeSiB film, FeGaSiB film, and 380 µm Si (100) substrate as a function of thickness.

Figure 7.6 shows the hardness, H_r, and Young's modulus, E_s, of the FeSiB and FeGaSiB films as a function of thickness in comparison with the hardness and Young's modulus of the Si substrate. It can be seen that the hardness in **Fig. 7.6 (a)** and Young's modulus in **Fig. 7.6 (b)** of FeSiB and FeGaSiB films increased with decreasing thickness, with the values approaching the hardness and Young's modulus values of the Si substrate, which have been selected from **Fig. 7.9**. This suggests that reducing the thickness can increase the substrate effect, which is very clear on the values for the low thickness films. It was found that although the films were deposited in the same growth conditions and all have an amorphous structure, over the thickness range, the hardness and Young's modulus values of FeSiB films were higher than the hardness and Young's modulus values of FeGaSiB films. This means that FeSiB films were more elastic than the FeGaSiB films over the thickness range.

From literature, it is found that changing the thickness of magnetostrictive crystalline FeCo film [16], deposited on a Si substrate, from 2 µm to 7 µm changed Young's modulus values from 165.5 GPa to 170 GPa, while the hardness decreased slightly from 5.5 GPa to 5.4 GPa. These measurements were made by the nanoindentation technique with a maximum load of about 200 mN. In a crystalline film, increasing the film thickness increases the grain size, which leads to generating the Hall-Petch effect or grain-boundary strengthening. This describes the relation between the inverse of the average grain size and the flow stress [17], which is defined as the required stress to continue the plastic deformation in a material. Therefore, changing the grain size leads to changes in the dislocation movement and the yield

strength. The grain-boundary strengthening can be explained as the effect of changing the grain size of the dislocation movement, which is impeded by the grain boundaries, which works as pinning points, **Fig 7.7**. Inside the grain, it is observed that the number of dislocations has an effect on crossing the dislocations through the grain boundaries and their movement from one grain to another. On the other hand, hindering the dislocation movement can impede the beginning of plasticity and lead to raising the yield strength of the material. Further, the growth of grains decreases the inter-particle spacing and hence the particles are unable to provide an effective barrier against shear band propagation or localized deformations.

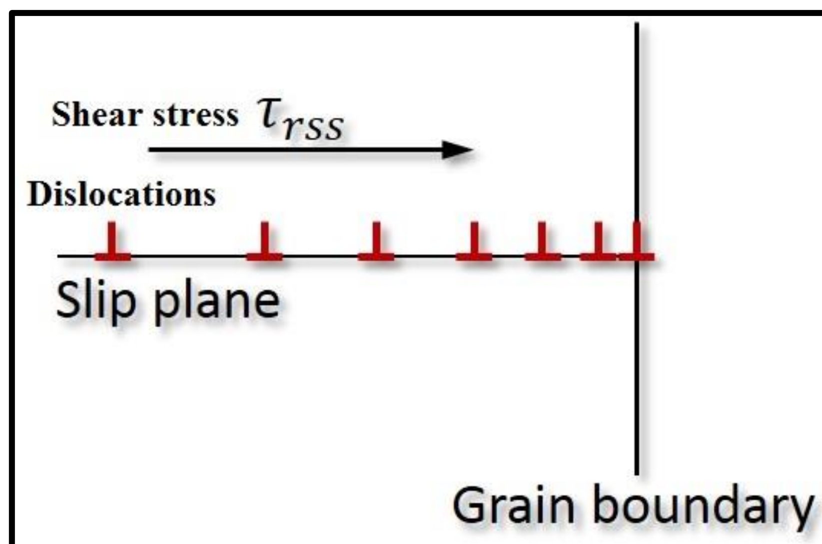

Figure 7.7 Schematic diagram of the affecting of grain boundary on the dislocation movement along the slip plane in a crystalline material under shear stress.

Figure 7.7 shows schematic diagram, which describes the effect of grain boundary on the dislocation movement along the slip plane in a crystalline material, where the symbol (⊥) represents the dislocation and τ_{rss} refers to shear stress. It can be seen that the grain boundary works as a barrier against the movement of the dislocations. It can also be seen that the distance between the dislocations decreases when they approach the boundary.

Further, it is known that the deposition of films by growth processes creates internal stress. Increasing this internal stress leads to a decrease in both the hardness and the elastic modulus of the films [18]. For example, increasing the internal stress by about 1 GPa leads to a decrease in the elastic modulus and hardness linearly by about 13%. Also, it was found that for films deposited by sputtering, an increase in the hardness was associated with increasing

compressive stress created by changing the pressure [19]. As the deposition of FeSiB and FeGaSiB films were carried out in the same chamber and was under the same growth conditions, this could lead to both film sets having the same internal stress effect, but adding Ga to FeSiB film can change the stress in the film due to rearrangement of the atomic distribution. Also, as the Ga atom is a larger size than the Si and B atoms, adding the Ga atoms can increase the interatomic spacing between the atoms and leading to a decrease in the hardness of the film. These are two possible reasons for the change in the mechanical properties between the FeSiB and FeGaSiB films.

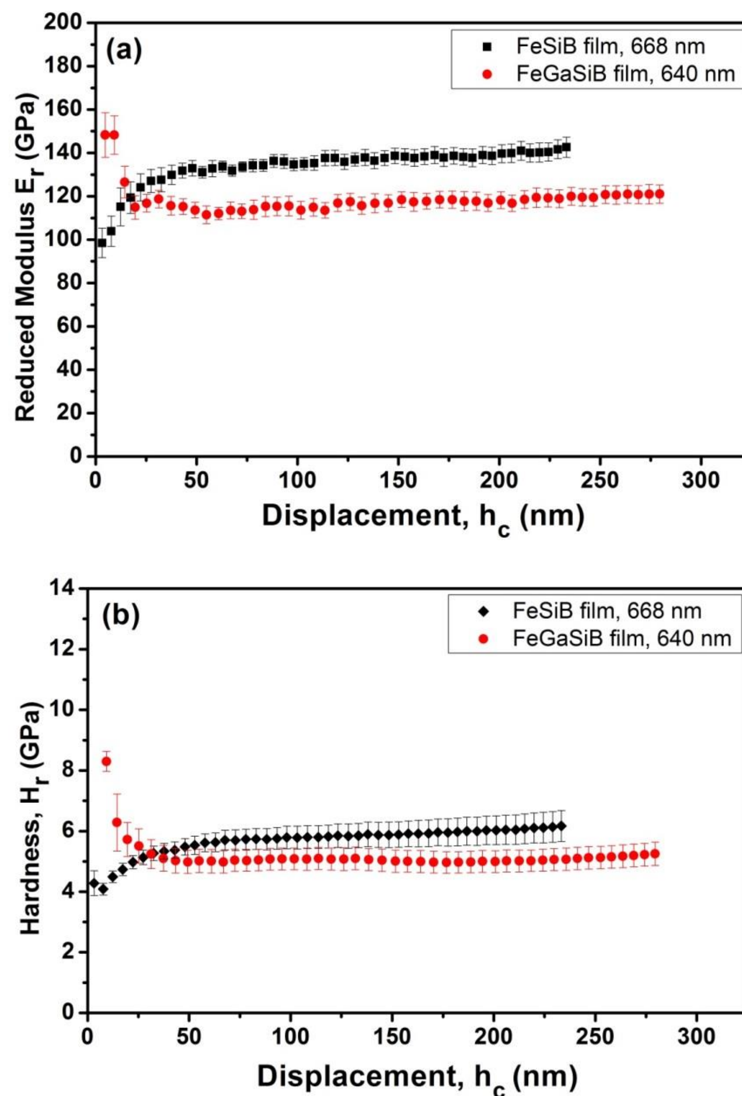

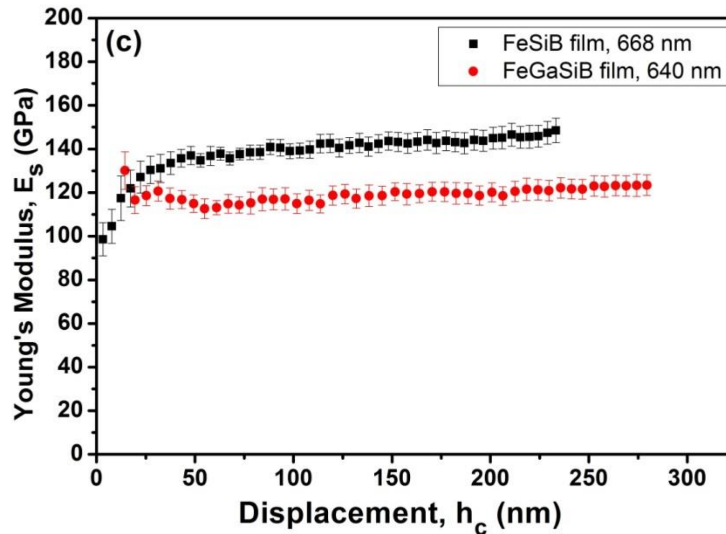

Figure 7.8 Comparison between (a) reduced modulus, E_r (b) hardness, H_r (c) Young's modulus, E_s, of 668 nm FeSiB and 640 nm FeGaSiB films deposited Si substrates.

Figure 7.8 illustrates a comparison between the mechanical properties of amorphous 668 nm FeSiB and amorphous 640 nm FeGaSiB films deposited on Si (100) substrate. To achieve the main goal of this study in this chapter, it was necessary to do the comparison between the two films without the substrate effect. The comparison of the films with the substrate is discussed next (see **Fig 7.9**). From this comparison, it can be seen that the FeSiB film reduced modulus, E_r, hardness, H_r, and Young's modulus, E_s, values were higher than the FeGaSiB film. From **Fig 7.8 (a)**, it can be seen that the reduced modulus of the FeSiB film was about ~130 GPa while the FeGaSiB film had a reduced modulus of about ~115 GPa. Further, from **Fig 7.8 (b)**, it can be seen that the hardness of the FeSiB film was about ~ 6 GPa while the FeGaSiB film had a hardness of about ~ 4.9 GPa. From **Fig 7.8 (c)**, it is noted that the Young's modulus, E_s, of the FeSiB film was about ~140 GPa while the FeGaSiB film Young's modulus, E_s, was about ~120 GPa. The mechanical properties of the films are generally influenced by the internal stresses that are generated by the growth parameters such as pressure and deposition rate [20-22], but both films had similar growth parameters and amorphous structures. As the films where deposited under the same pressure 4 µbar, but the deposition rate was changed by adding the Ga (see **Fig. 6.1**), the deposition rate of the FeSiB films was 1.5 nm/s, which is higher than the deposition rate 0.1 nm/s of the FeGaSiB films. Therefore, adding the Ga reduced the deposition rate (as discussed in chapter 6), of the films and hence affected the stresses within the films thereby influencing the mechanical properties of these films. Further, Satomi et al [23] found that changing the deposition rate can change

the stress within the film from compressive stress to tensile. While, Mani et al [24] studied the effect of internal stress on the mechanical properties of the film and found that the hardness increased with increasing the compressive stresses within the film. Also, this difference in the mechanical properties of the films can be attributed to the difference in the composition of the films. It can be seen that the addition of Ga into the FeSiB films reduced the mechanical properties such as the hardness and Young's modulus of the film.

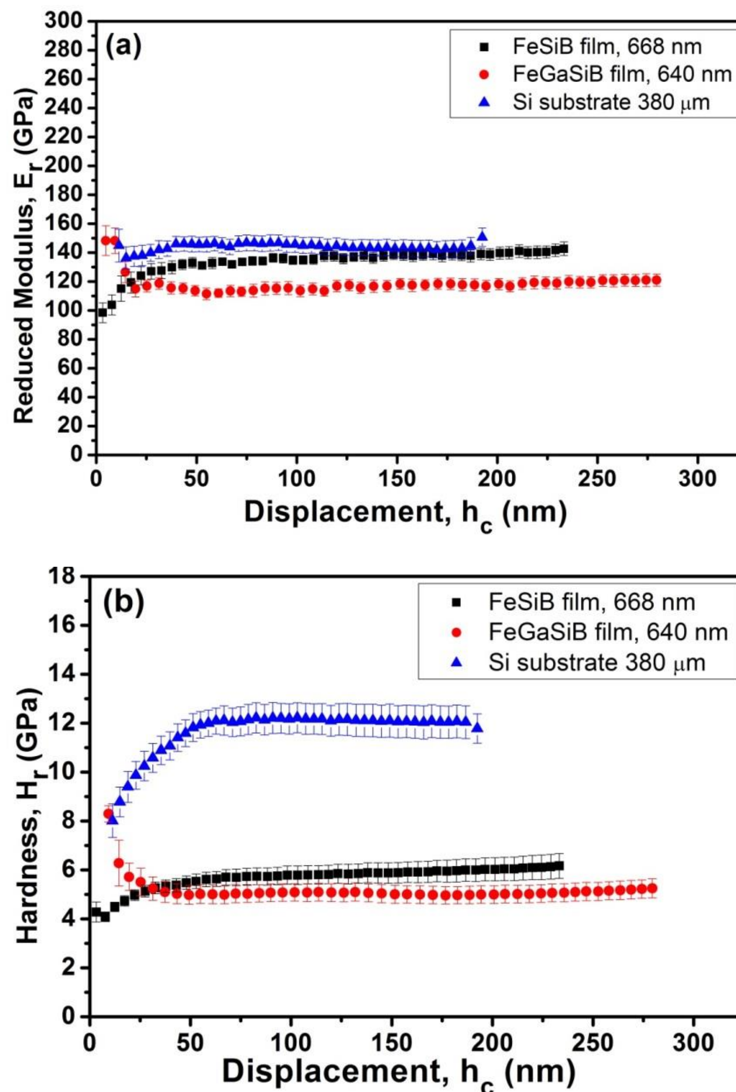

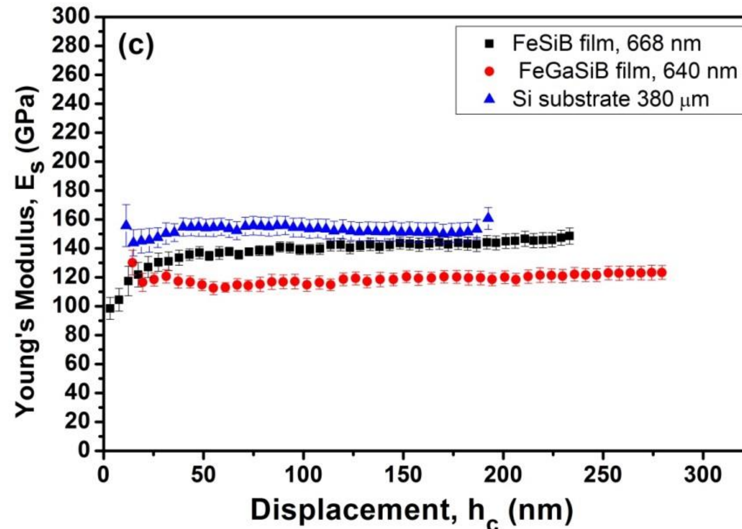

Figure 7.9 Comparison of (a) reduced modulus, E_r (b) hardness, H_r (c) Young's modulus, E_S, of 668 nm FeSiB film, 640 nm FeGaSiB film, and 380 µm Si substrate.

Figure 7.9 presents a comparison between the mechanical properties of 668 nm FeSiB film, 640 nm FeGaSiB film, and 380 µm Si substrate. After achieving the comparison of the mechanical properties between the films of FeSiB and FeGaSiB (see **Fig 7.8**), it was necessary to compare the mechanical properties of both films with the Si substrate, the reason was to check the substrate effect on the mechanical properties of the films and how far or near the values of the mechanical properties of the 668 nm FeSiB film and 640 nm FeGaSiB film were from the Si substrate. In general, from **Fig 7.9**, it can be seen that all the mechanical properties of the Si substrate were higher than both of the films. From **Fig 7.9 (a)**, the reduced modulus of Si substrate was about ~140 GPa, which was higher than the reduced modulus of both FeSiB and FeGaSiB films. From **Fig 7.9 (b)**, the hardness of the Si substrate was about ~12 GPa, which is higher than both of the films. From the **Fig 7.9 (c)**, Young's modulus of Si substrate was about ~155 GPa, which is higher than both of the films. Hence, both of the films had mechanical properties different from the mechanical properties of the Si substrate.

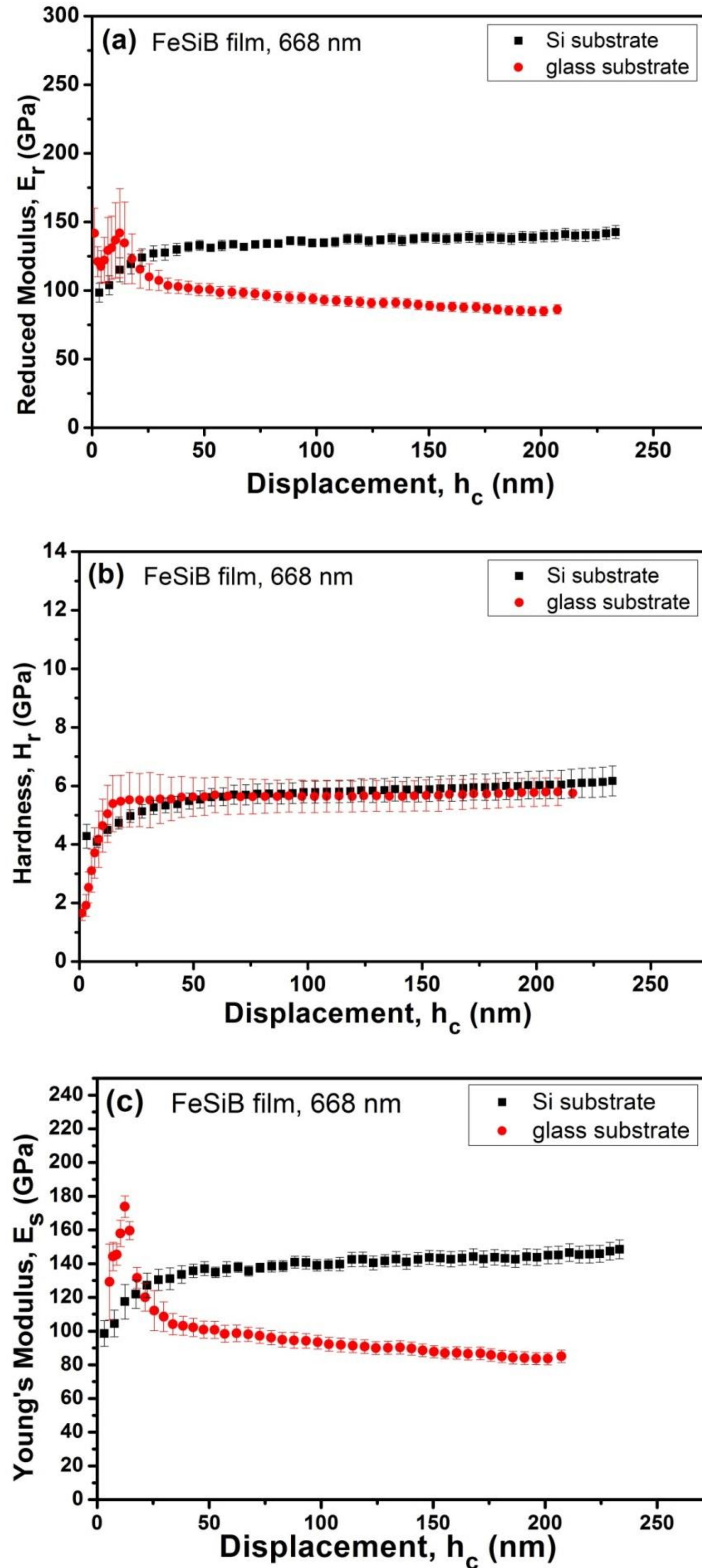

Figure 7.10 Comparison of (a) reduced modulus, E_r (b) hardness, H_r (c) Young's modulus, E_s, of 668 nm FeSiB film deposited on Si and glass substrates.

Figure 7.10 compares the reduced modulus, E_r, hardness, H_r, and Young's modulus, E_s, of 668 nm FeSiB films deposited on Si and glass substrates. From **Fig. 7.10 (a)**, it can be seen that the reduced modulus of FeSiB/Si film was about 110 GPa, which is higher than the reduced modulus of FeSiB/glass film, which also decreased from 100 GPa to 75 GPa with increasing indentation penetration depth. From **Fig. 7.10 (b)**, it can be observed that the hardnesses as a function of indentation depth for the amorphous FeSiB films with the same thickness grown on Si and glass substrates, both had the same value of 6 GPa within error with increasing indentation depth, with a horizontal line above 50 nm depth. Also, the hardness of FeSiB film showed no substrate effect, nor substrate type, again due to the film thickness being higher than the indentation penetration depth. The maximum depth was less than 230 nm for the FeSiB/Si film and less than 250 nm for the FeSiB/glass film, compare with the film thickness which was 668 nm. This is in agreement with the 640 nm FeGaSiB films, thus the hardness measurements were far enough away from substrates, so no influence occurred. From **Fig. 7.10 (c)**, it is observed that the Young's modulus of the FeSiB/Si and FeSiB/glass films of the same thicknesses moved away from each other with increasing indentation penetration depth. It was found that Young's modulus of FeSiB/glass film reduced from 130 GPa to 80 GPa with increasing of the indentation penetration depth. While the Young's modulus of the FeSiB/Si film was about 140 GPa, and was approximately constant with increasing indentation depth.

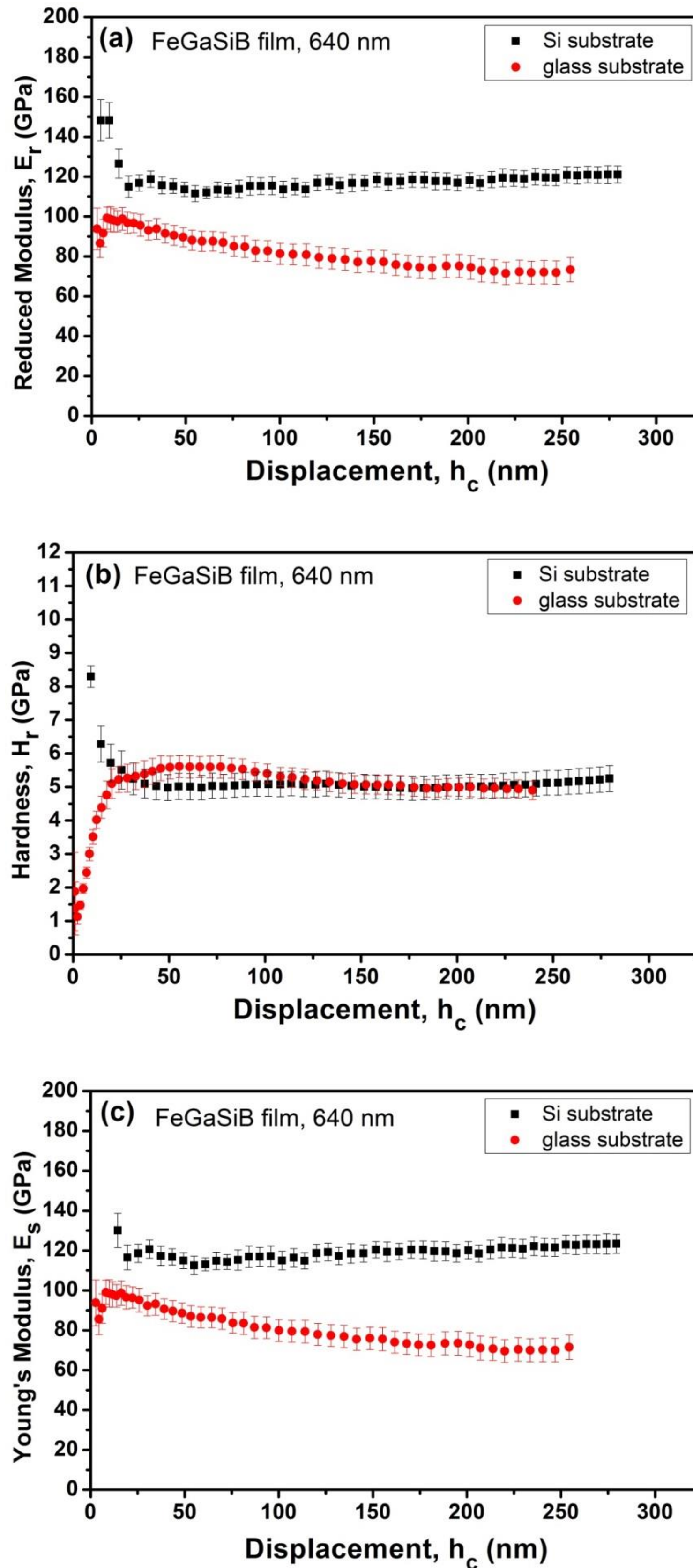

Figure 7.11 Comparison of (a) reduced modulus, E_r (b) hardness, H_r (c) Young's modulus, E_s, of 640nm FeGaSiB film deposited on Si and glass substrates.

Figure 7.11 compares the reduced modulus, E_r, hardness, H_r, and Young's modulus, E_s, of 640 nm FeGaSiB films deposited on Si and glass substrates. From **Fig. 7.11 (a)**, it can be seen that the reduced modulus of the FeGaSiB/Si film was about 120 GPa which is higher than the reduced modulus of the FeGaSiB/glass film, which decreased from 100 GPa to 75 GPa with increasing the indentation penetration depth. From **Fig. 7.11 (b)**, it can be seen that the plots of hardness against the indentation depth of amorphous 640 nm FeGaSiB films deposited on Si, which is a stiffer substrate, and glass, which is a softer substrate, showed the hardnesses was almost the same for both films with increasing indentation depth, as they are approximately a horizontal line. This means that the hardness was not affected by the substrate effect, or by the type of substrate at this film thickness. This is because film thicknesses were higher than the indentation depth, where the maximum depth was less than 300 nm for FeGaSiB/Si film and less than 250 nm for FeGaSiB/glass film, compare with 640 nm for the films. In these cases, the measurements were far from the substrate effect. From **Fig. 7.11 (c)**, it can be seen that Young's modulus of the FeGaSiB/Si and FeGaSiB/glass films of the same thicknesses diverge from each other with increasing indentation depth, and increasing applied load. This difference is due to the Young's modulus of FeGaSiB/glass film decreasing from 100 GPa to 70 GPa with increasing indentation depth up to 200 nm, then being approximately horizontal with indentation depth greater than 200 nm. While the Young's modulus of the FeGaSiB/Si film was about 120 GPa, with an approximately horizontal line with increasing the indentation depth. This means that the elastic modulus of FeGaSiB/glass film is more strongly affected by the glass substrate. The same behaviour in the elastic modulus was observed in the FeSiB/glass film, thus both were strongly affected by the glass substrate, due to the glass being softer in comparison to silicon. According to Ref. [25], the hardness and Young's modulus of glass are 6.8 GPa and 73 GPa respectively, therefore it is found that Young's modulus of the FeGaSiB/glass film reduced to be very near the glass value, hence the film was affected by the elastic properties of the glass substrate. Also, a deposited amorphous FeGaSiB film on an amorphous substrate (glass) showed different behaviour from the FeGaSiB film deposited on a crystalline substrate (Si).

It was reported that [26], if the film and the substrate are elastically homogeneous, which means they have the same values of Young's modulus, then the elastic modulus of the film, E_f equals the elastic modulus of the substrate, E_{sb}. If on the other hand they are not elastically homogeneous, then the film and the substrate will have different elastic modulus values. In this case, the measured elastic modulus of the film, E_f, will change from the actual

elastic modulus value of the film, E_f, to the elastic modulus value of the substrate, E_{sb}. This behaviour of the elastic modulus was observed in the result of both the FeSiB/glass and FeGaSiB/glass films, this means that both films were not in homogeneous elasticity with the substrate.

Further, it is found that for both 668 nm FeSiB and 640 nm FeGaSiB films deposited on Si and glass substrates, all the data curves of hardness presented in this study showed that the nanoindentation size effect, which is defined as the hardness decrease associated with increasing indentation penetration depth, was not observed. Therefore, increasing the applied load did not affect the hardness markedly. This effect was observed by Lashgari et al [27] on an amorphous ribbon of composition $Fe_{80.75}Si_8B_{11.25}$ and thickness 20 μm when the applied load increased from 10 to 70 mN [27]. The hardness decreased from 12.8 GPa to 11.8 GPa, and the elastic modulus decreased from 150 GPa to 110 GPa. Also, the same behaviour was found in other alloys when they add Cu to FeSiB alloy. In the 26 μm ribbon of composition $Fe_{85.2}Si_{0.9}B_{12.62}Cu_{1.28}$ for the same range of the load, the hardness decreased from 14.2 GPa to 10.8 GPa, and the elastic modulus decreased from 110 GPa to 60 GPa, while for the 35 μm ribbon of composition $Fe_{78.6}Si_{1.8}B_{17.75}Cu_{1.85}$, for the same load range the hardness reduced from 12.8 GPa to 10 GPa, and the elastic modulus reduced from 100 GPa to 60 GPa.

To understand the behaviour of material beneath the tip of the indentation, there are two models which have been designed to explain the plastic deformation mechanism in amorphous materials. One model is based on the mechanism of the shear transformation zone (STZ), where the local progression in the structural order occurs as a result of shear transformation zone effects, which can be accompanied by shear transformation zone processes such as redistribution of internal stresses and a rise in local heat. These have been suggested to explain the strain softening through plastic deformation [28, 29]. The second model is based on the local atomic jump, which suggests that in an amorphous material, the local distribution of free volume leads to control of the deformation form and these places support the local shear as the local atom jumps toward a vacancy. In other words, this mechanism can be described as a coalescence or accumulation of free volume through the shear localization [28, 30]. This leads to nucleation of shear bands, as a result of coalescing of excess free volume, which leads to dropping of the load suddenly during nanoindentation test.

Furthermore, in amorphous materials, the plastic deformation is not described as a result of dislocation slip due to the absence of grains and grain boundaries in their structure. On the other hand, in crystalline materials, reducing the defects and imperfections leads to an increase in the strength and elasticity modulus of the material [28]. In addition, in an amorphous material, the plastic deformation essentially focuses on shear bands or the strain localization and in this case, it will show strain softening behaviour instead of strain hardening behaviour, which appears in crystalline materials. These things can be related to the local reduction in the viscosity of the glassy material [28].

Additionally, in the nanoindentation test, it was found that after removing the indentation tip away from the material and finishing the indentation process, part of the material will move back from the maximum indentation penetration depth to the final indentation depth, h_f. The difference between the maximum depth, h_{max}, and the final depth, is defined as an elastic recovered part of the material. The elastic recovered part of the FeSiB and FeGaSiB films is presented in **Fig. 7.12**.

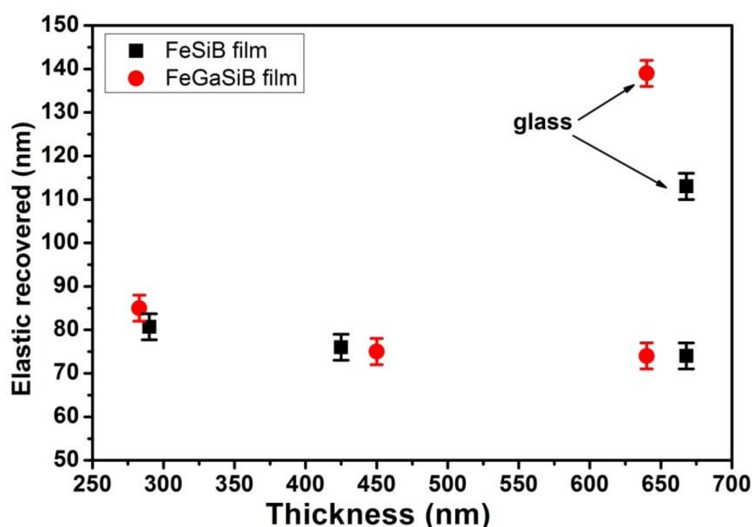

Figure 7.12 Elastic recovered FeSiB and FeGaSiB films deposited on Si and glass substrates as a function of thickness.

Figure 7.12 compares the elastic recovered part of the material after removing the indenter away, which means at zero applied loads on the FeSiB/Si and FeGaSiB/Si films as a function of thickness. It can be seen that for both films the elastic recovered part decreased with increasing the film thickness. While it was found that for the thicker films deposited on glass substrate showed high values of elastic recovered parts compared with the thicker films deposited on Si substrates. For example, the 668 nm FeSiB/glass film had elastic recovered

about 113 nm, which was higher than the elastic recovered value of 668 nm FeSiB/Si film by a factor 1.5. While the 640nm FeGaSiB/glass film had elastic recovered about 139 nm which was higher than the elastic recovered value of 640 nm FeSiGaB/Si film by a factor 1.8.

The ratio of h_f/h_{max}, where h_f is the final indentation depth and h_{max} is the maximum penetration depth at the maximum load, can be obtained simply from the unloading curve of nanoindentation test. There is a natural limitation of this ratio between zero and one, where $0 \leq h_f/h_{max} \leq 1$, and it can be used to determine the type of behaviour, i.e elastic or plastic, where the minimum value represents the full elastic deformation and the maximum value represents plastic deformation [31].

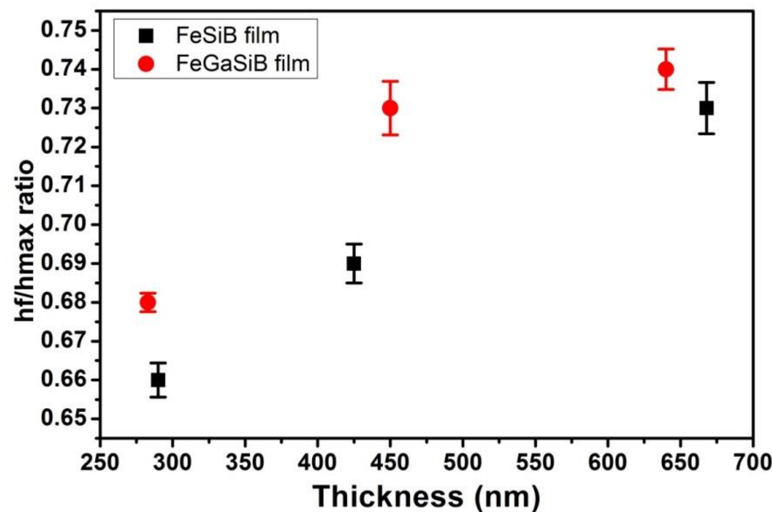

Figure 7.13 The ratio of (h_f/h_{max}) of FeSiB/Si and FeGaSiB/Si films as a function of thickness.

Figure 7.13 compares the ratio of the final indentation depth to the maximum penetration depth at the maximum load of FeSiB and FeGaSiB films deposited on Si substrates as a function of thickness. It can be seen that the ratio of (h_f/h_{max}) increased with increasing film thickness for both film sets. This means that the deformation becomes more plastic as the film thickness increases.

The yield strength of the films can be affected by many factors such as the grain size, grain boundaries, and film thickness [32]. As the films have an amorphous structure, the films have no grain size or grain boundary effects. In this work, the calculation of the yield strength is based on the model represented by equations (2.53 and 2.54) (chapter 2). The effect of thickness on the yield strength has been studied and the result presented in **Fig. 7.14**.

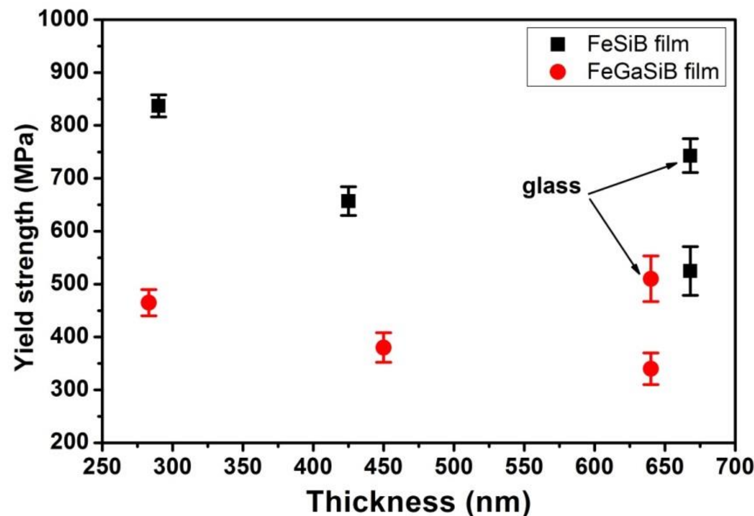

Figure 7.14 Yield strength of FeSiB and FeGaSiB films, deposited on a Si and the glass substrate, as a function of thickness.

Figure 7.14 compares the yield strength of FeSiB and FeGaSiB films deposited on a Si substrate as a function of thickness. From this figure, it can be seen that the yield strength of both films decreased with increasing thickness. Also, it is clear that the yield strength of the FeSiB/Si film were higher than the yield strength of the FeGaSiB/Si film over all the thickness range. This means that adding Ga into FeSiB films affected the yield strength of the film over all the thickness range. The yield strength point is the point which separates the elastic and plastic behaviour of the film. Therefore, it can be observed that the elastic part of FeSiB film was larger than the elastic part of the FeGaSiB film for all thicknesses. This means that FeSiB films have more elasticity than FeGaSiB films. Again, this decreased elasticity will be due to adding Ga into the FeSiB films and hence changing the chemical composition of the films in this case, the film will have four elements (Fe, Ga, Si, and B) instead of three (Fe, Si, and B). This could also affect the atomic spacing, which can affect the elastic properties of materials. While for the thicker films deposited on glass substrates, it was found that the 668 nm FeSiB/glass film had a yield strength of about 743± 32 MPa, which is higher than the yield strength of 668 nm FeSiB/Si film. Also it was found that the 640 nm FeGaSiB/glass film had a yield strength of about 510± 43 MPa, which was higher than the yield strength of 640 nm FeGaSiB/Si film, therefore for both films, the soft substrate (glass substrate) increased the yield strength of the films compared with the hard substrate (Si substrate). Further, it can be noted that the yield strength value of the 668 nm FeSiB/glass film was higher than the yield strength value of 640 nm FeGaSiB/glass film. This means that

the glass substrate affected the elasticity of both films, leading to an increase in the yield strength and hence increased the elastic parts of both films.

7.6 Material Influences

As described above, the measurements of the mechanical properties can be affected by many problems, such as changing the radius of the tip, which appears as an error in the first part of the data curve when the penetration depth was less than 33 nm, see for example (**Figs. 7.8** and **7.9**) and the substrate effects, where the mechanical properties of the substrate are higher than the film, which results in a gradual increase from the straight line to higher values approaching from the substrate data near maximum penetration depth (see **Fig. 7.5**). In addition to the above, there is another effect generated from the material itself. The hardness and elastic modulus can be affected by material effects: either a pile-up or a sink-in or both of material, which occurs on the sides of the indented edges. From the literature, the pile-up arises in films that have a compressive stress and is related to the increased amount of compressive stress, which results in the contact area deviating from the area measured [33]. Therefore AFM images and cross-sectional lines have been taken to show the material effects as shown in **Figs. (7.15** and **7.16)**.

Another possible material effect can be due to a changing in the density of dislocations over the material. It was noticed that during the measurements of, for example, the hardness over an indentation test on the sample surface, the results showed that all hardness values were not the same, but they were slightly different from each other. Therefore the result presented for the hardness was an average of a range of 14 indentation tests for each sample.

It was found by Lashgari et al [34] that the hardness and Young's modulus of FeSiB amorphous ribbon for one cycle of the load-displacement curve were 9.2 GPa and 165 GPa, but increased to 10 GPa and 170 GPa respectively, with increasing the number of cycles to 10. Annealing the sample at 500 ^{o}C for one hour increased the hardness and Young's modulus for one cycle to be about 10.5 GPa and 225 GPa respectively, which also increased to 11 GPa and 230 GPa respectively, with increasing the number of cycles to 10 [34]. Thus, this demonstrates changing the structure of the material by annealing can affect both hardness and the Young's modulus.

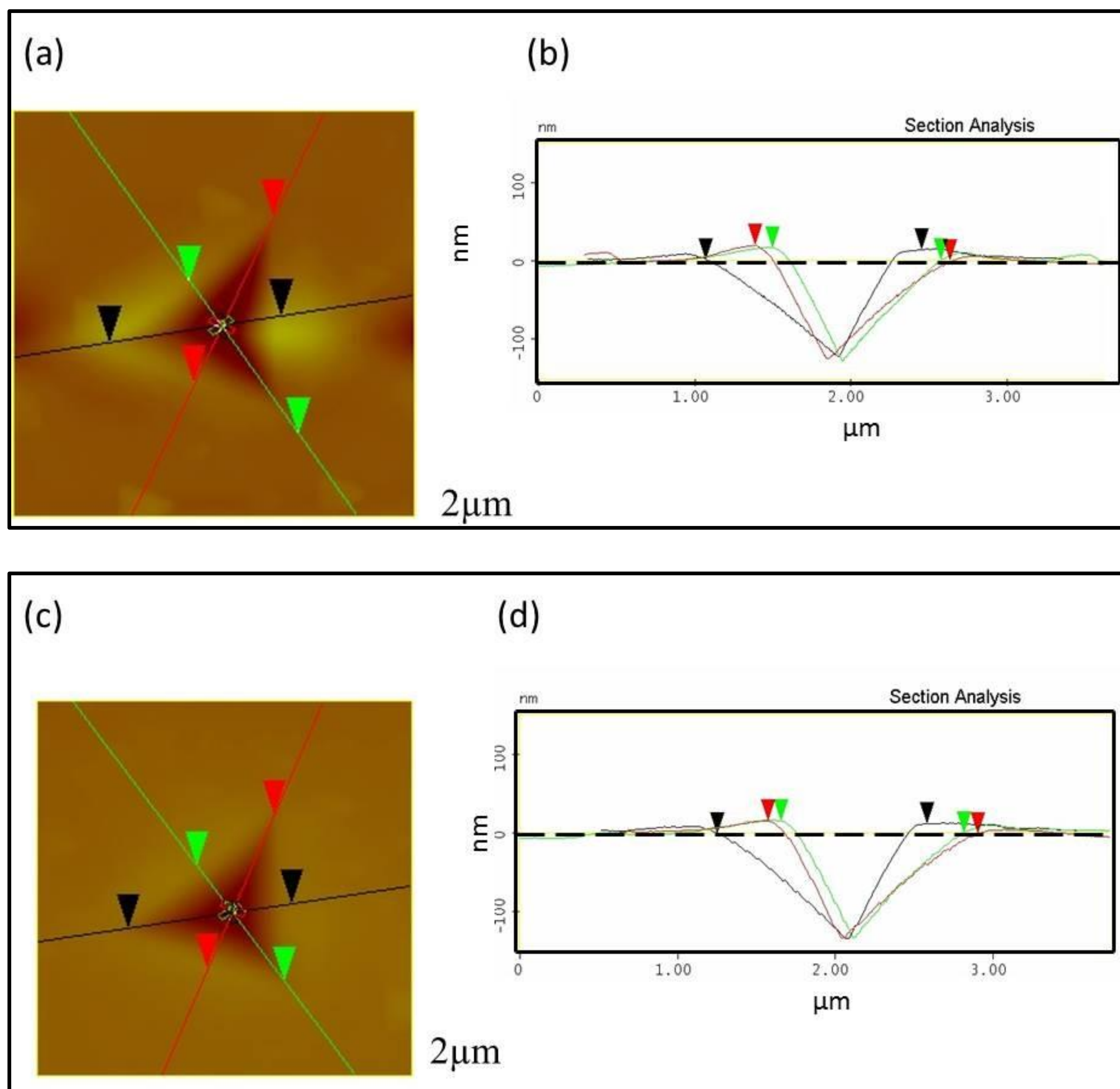

Figure 7.15 Indent surface features and section analysis, (a and b) AFM image (2x2µm) and section analysis of 668 nm FeSiB film/Si substrate; (c and d) AFM image (2x2µm) and section analysis of 668 nm FeSiB film/glass substrate.

Figure 7.15 presents AFM images and a sectional analysis (height profile) of an indented area on the surface of amorphous 668 nm FeSiB films deposited on Si and glass substrates. From **Figs 7.15 (b)** and **(d)**, both of the films showed that there was a small pile-up of material on three sides of the indent height profile represented by the arrows. The pile-up height of FeSiB/Si was in the range of about 12-19 nm, **Fig. 7.15 (b)**, and the height of FeSiB/glass was in the range of 13-16 nm **Fig. 7.15 (d)**. The pile-up effect around the sides of indenter could be due to the lack of the compressibility of the plastic deformation [27].

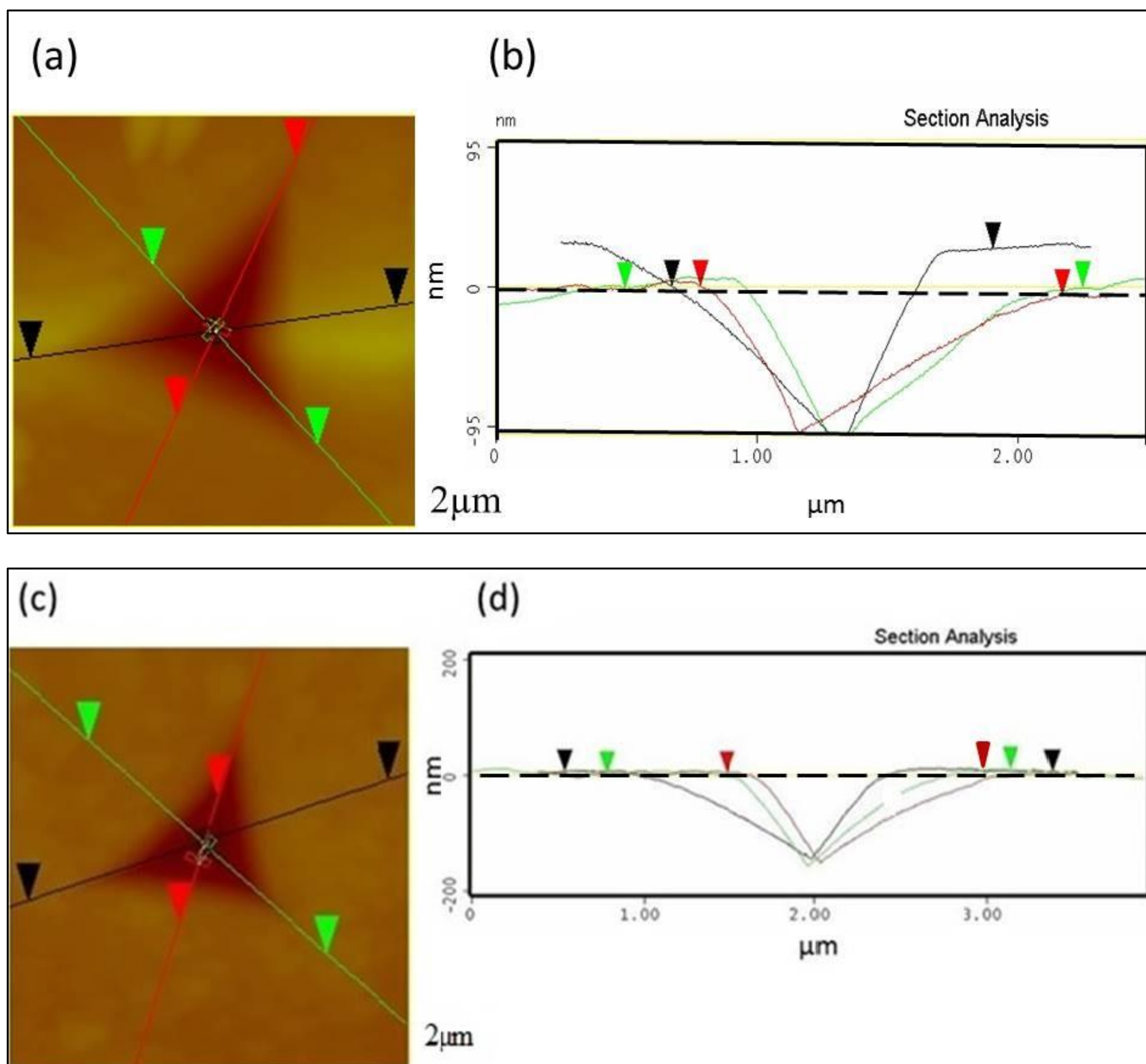

Figure 7.16 Indent surface features and section analysis, (a and b) AFM image (2x2µm) and section analysis of 640 nm FeGaSiB film/Si substrate; (c and d) AFM image (2x2µm) and section analysis of 640 nm FeGaSiB film/glass substrate.

Figure 7.16 shows AFM images and section analysis (height profile) of an indented area on the surface of amorphous 640 nm FeGaSiB films deposited on Si and glass substrates. In **Fig. 7.16 (b)**, the film of 640 nm FeGaSiB/Si showed a pile-up effect of the material of height 26 nm, on one side of the indent height profile represented by the black arrows compared with the 668 nm FeSiB/Si film, which showed the pile-up height on three sides with a range about 12-19 nm, **Fig. 7.15 (b)**, while the film of 640 nm FeGaSiB/glass does not show a pile-up effect of material as all the heights are levels, **Fig. 7.16 (d)**, and appear parallel to the original surface compared with the film of 668 nm FeSiB/glass which showed a small pile-up effect in the range of 13-16 nm **Fig. 7.15 (d)**.

From the above, the cross-sectional lines were used as a sectional analysis, which helps to measure the height of pile-up that occurred around the indentation edges. The arrangement of AFM images and section analysis showed that the amount of pile-up around the indentation edges was not symmetris, and their heights were altered from each other around the three sides of the indentation imprints. One reason for the testing material to pile-up around the sides of the indenter, in crystalline materials, is due to generation of dislocations underneath the applied indenter. These dislocations then propagate into the material due to the high shear stresses, which arise at around 45° to the applied load axis. Increasing stress can be enough to propagate these dislocations on the slip planes approaching the maximum shear, leading them to move downwards within the material. Therefore, in a soft material, which has no barrier to dislocation mobility, this will lead to continuing the dislocations within the material, which generates a sink-in effect around the sides of the indenter. If the material has strain hardening or work-hardening behaviour this will lead to a reduction in the mobility of these dislocations, so are limited in closeness to the surface. Thus a cross slip can arise on slip planes leading to the dislocations being able to propagate toward the surface and generating the pile-up effect. As a result of this, the amount of pile-up is influenced by the mobility of dislocations into the material and is not just related to the indentation load. In crystalline materials [34], the strain hardening behaviour is well known and working to control the plastic deformation. An interaction between the dislocations with each other leads to strengthening in a crystal, which can increase the resistance of the crystal to the plastic deformation.

In amorphous material such as the FeSiB and FeGaSiB films studied in this work, the strain hardening mechanism does not occur as a result of lacking the dislocations as well as grain boundaries because they have disordered, amorphous structure, in comparison with a crystalline material. Thus, even with their greater yield stress and strength, amorphous materials show a low toughness as a result of propagation of the shear bands [34]. Therefore, the plastic deformation, which occurs in amorphous FeSiB and FeGaSiB films, can be described depending on the mechanism of shear bands. On the other hand, amorphous materials commonly suffer a strong ability for shear localization and they tend to have a brittle structure after annealing at high temperatures. Therefore, there is evidence that amorphous materials are able to legitimate plastic shear flow in the range of the micro-scale [28].

7.7 Summary

The mechanical properties of magnetostrictive amorphous FeSiB and FeGaSiB films have been studied using the nanoindentation technique. The XRD results showed that for both film sets, there was no sign of crystalline peaks observed, so confirmed an amorphous structure.

The hardness and elastic modulus decreased with increasing the thickness for both FeSiB and FeGaSiB films. The film's hardness at lower thicknesses increased towards the substrate hardness, demonstrating the substrate effect. Due to the addition of Ga, the FeSiB and FeGaSiB films showed different mechanical properties. The films' comparison with Si substrate showed that the Si substrate had larger mechanical properties and that the measurement of the films' mechanical properties at higher thicknesses, were not affected by the substrate. The effect of different substrates was observed in the elastic modulus, but the films with different substrate showed the same hardness.

It was found that the elastic modulus of the films deposited on glass substrates decreased torward the elastic modulus of glass, as the films were not elastically homogeneous with the glass substrate.

For both films deposited on Si substrates, the elastic recovered decreased with increasing the film thickness. The comparison showed that the thicker films deposited on glass substrate had high values of elastic recovered parts compared with the thicker films deposited on Si substrates, i.e. the 668 nm FeSiB/glass film had an elastic recovered part of about 113 nm compared to 74 nm for the 668 nm FeSiB/Si film and the 640 nm FeGaSiB/glass film had elastic recovered part of about 139 nm compared to 75 nm for the 668 nm FeSiB/Si film.

In both films, it ws found that the ratio of h_f to h_{max} increased with increasing the thickness, meaning that the films become more plastic.

For both films, the yield strength decreased with increasing thickness. Also, the yield strength of the FeSiB/Si films was higher than the yield strength of the FeGaSiB/Si films over the whole thickness range. The comparison showed that for the thicker films deposited on glass substrates, the 668 nm FeSiB/glass film had yield strength of 743 ± 32 MPa which was higher than the 668 nm FeSiB/Si film yield strength of 525 ±46 MPa. Also, the 640 nm FeGaSiB/glass had a yield strength of 510± 43 MPa, which was higher than the 640 nm FeGaSiB/Si film yield strength of 340± 30 MPa. Further, it was found that the yield strength

value of the 668 nm FeSiB/glass film was higher than the yield strength value of 640 nm FeGaSiB/glass film. Thus the best film-substrate combination of high yield strength is in the films deposited on glass substrates.

The hardness and elastic modulus can be affected by material effects. These effects can be either a pile-up or a sink-in or both of material, which occurs on the sides of the indented edges. Both of the films deposited on Si substrates with higher thickness showed a pile-up effect. As the 640 nm FeGaSiB film/glass substrate sample did not show a pile-up effect, it suggests that the Si is a stiff substrate compared to the softer glass substrate, which means that the Si substrate resists the movements of the film material and enforces the material of film to move back to the surface. In conclusion, the FeSiB films had larger mechanical properties compared to the FeGaSiB films, thus the addition of Ga reduced the mechanical properties.

7.8 References

[1] H. Ogi, G. Shimoike, M. Hirao, K. Takashima, Y. Higo, J Appl Phys, 91:4857, 2002

[2] M. Kikuchi, K. Fukamichi, H. Kimura, T. Masumoto, Science reports of the Research Institutes Tohoku University. Ser A - Phys Chem Metall, 33:102, 1986.

[3] M. R. J. Gibbs, R. Watts, W.J. Karl, A.L. Powell, R.B. Yates, Sensors Actuators A, Physical, Vol. 59, no. (1-3), pp 229-235,1997.

[4] M. R. J. Gibbs, E. W. Hill and P. J. Wright, J. Phys. D: Appl. Phys. Vol. 37. P. R237–R244, 2004.

[5] M. Ali and R. Watts, J. Magn. Magn. Mater. 202, p 85, 1999.

[6] B Kundys, Yu Bukhantsev, H Szymczak, M R J Gibbs and R Zuberek, J. Phys. D: Appl. Phys. 35, 1095–1098, 2002.

[7] T. Y. Tsui and G. M. Pharr, J. Mater. Res., vol. 14, No. 1, p. 292-301, 1999.

[8] D. Chicot, M. Yetna N'Jock, E.S. Puchi-Cabrera, Alain Iost, M.H. Staia, G. Louis, G. Bouscarrat, R. Aumaitre, Thin Solid Film, 558, p. 259-266, 2014.

[9] Č. Jaroslav, P. Haušild, O. Kovářík, A. Materna, Materials and Design, vol. 109, 347–353, 2016.

[10] A.C. Barone, M. Salerno, N. Patra, D. Gastaldi, E. Bertarelli, D. Carnelli, and P. Vena, Microscopy Research and Technique, 73, P. 996–1004, 2010.

[11] N. A. Morley, S. L. Yeh, S. Rigby, A. Javed, and M. R. J. Gibbs, J. Vac. Sci. Technol. A, vol. 26, no. 4, pp. 581–586, 2008.

[12] W. C. Oliver, G. M. Pharr, J. Mater. Res, 7(6), 1564–83, 1992.

[13] S.D. Mesarovic, N.A. Fleck, Proc. R. Soc. Lond. 455, 2707, 1999.

[14] G. Hochstetter, A. Jimenez, J. Loubet. J. Macromol. Sci. Phys., B38 (5-6), 681–92,1999.

[15] R. Saha, Z. Xue, Y. Huang, W. D. Nix, J. Mechanics and Physics of Solids, 49, 1997 –2014, 2001.

[16] K. S. Chan, H. Ji, X. Wang, S. J. Hudak Jr. B. R. Lanning, Mater. Scie. and Engin. A, 422, 298-308, 2006.

[17] R. Venkatraman, J.C. Bravman, J. Mater. Res. 7 (1992) 2040.

[18] C. T. Chung, C. K. Chao, R. C. Chang, K. Y. Chu, J. mater. Proce. Technol., 201, 770-774, 2008.

[19] A. Mani, P. Aubert, F. Mercier, H. Khodja, C. Berthier, P. Houdy, Surf. Coat. Technol. 194, 190–195, 2005.

[20] C.T. Chuang, C.K. Chao, R.C. Chang, K. Y. Chu, J. mater. Proce. Technol., vol.201, pp. 770-774, 2008.

[21] D.T. Quinto, A.T. Santhanam, P.C. Jindal, Mater. Sci. Eng. A, vol. 105–106, pp. 443–452,1988.

[22] J. Gunnars, A. Alahelisten, Surf. Coat. Technol. Vol. 80, pp. 303–312, 1996.

[23] N. Satomi, M. Kitamura, T. Sasaki, M. Nishikawa, Fusion Eng. Des. vol. 39–40, pp. 493–497, 1998.

[24] A. Mani, P. Aubert, F. Mercier, H. Khodja, C. Berthier, P. Houdy, Surf. Coat. Technol, vol.194, PP. 190–195, 2005.

[25] R. Saha, W. D. Nix, Acta Materialia 50, 23–38, 2002.

[26] J.M. Antunes, J.V. Fernandes, N.A. Sakharova, M.C. Oliveira, L.F. Menezes, International Journal of Solids and Structures 44, 8313–8334, 2007.

[27] H.R. Lashgari, Z. Chen, X.Z. Liao, D. Chu, M. Ferry, S.Li, Materials Science & Engineering A, vol, 626, 480–499, 2015.

[28] C.A. Schuh, T.C. Hufnagel, U. Ramamurty, Acta Mater. 55 (12), 4067–4109, 2007.

[29] J.J. Lewandowski, A.L. Greer, Nat. Mater. 5 (1), 15–18, 2005.

[30] M. Ferry, T. Burgess, Mater. Today 12 (1–2), 24–32, 2009.

[31] W. C. Oliver, G. M. Pharr, J. Mater. Res., Vol. 19, No. 1, 2004.

[32] Y. W. Yu Denis and F. Spaepen, Journal of Applied Physics, Vol. 95, No. 6, 2004.

[33] Q.N. Meng, M. Wen, C.Q. Hu, S.M. Wang, K. Zhang, J.S. Lian, W.T. Zheng, Surface & Coatings Technology 206, 3250–3257, 2012.

[34] H.R. Lashgari, J.M. Cadogan, D. Chua, S. Li, Materials and Design 92, 919–931, 2016.

Chapter 8 Summary and Future Work

8.1 Summary

In summary, this thesis studied the magnetic properties, magnetostriction constant, and mechanical properties of magnetostrictive FeSiB and FeGaSiB films. The purpose of this study was to investigate the effect of adding Ga into FeSiB films on these properties. The thesis was divided into two parts, the first part investigated the magnetic properties of FeSiB and FeGaSiB thin films for a range of thicknesses and growth parameters. The second part investigated the mechanical properties of the magnetostrictive thick films (FeSiB, and FeGaSiB) by nanoindentation technique.

Both FeSiB and FeGaSiB films were grown on Si (100) substrates. The films were grown either by changing the film thickness or the growth parameters of the co-sputtering-evaporation chamber including the sputtering pressure, FeSiB target power P_{FeSiB}, and Ga evaporation rate R_{Ga}. The films investigated in this work were either different thicknesses (24 nm to 100 nm) or 50 nm thick. The structure, magnetic properties, and magnetostriction constant were investigated as a function of the film thickness, sputtering pressure, the power of the target, and the Ga composition.

For the experimental characterizations, several experimental techniques were used to investigate the structure, magnetic properties, magnetostriction constant, and mechanical properties. To investigate the structure, X-ray diffraction (XRD) was used, while atomic force microscopy (AFM) was used to investigate the surface and measure the thickness. The composition of the films was measured using X-ray photoelectron spectroscopy (XPS) and data analysis were performed in CasaXPS software. To investigate the magnetic properties and measure the magnetostriction constant, a magneto-optical Kerr effect magnetometry (MOKE) was used. The nanoindentation technique was also used to investigate the mechanical properties including the elastic modulus, hardness, and yield strength.

Qayes A. Abbas, 2018 & Email: qayes.a.abbas@gmail.com

From the experimental results shown in this thesis, the major findings are as follows:

- For all the parts of this thesis, the results showed that Ga was successfully added into FeSiB films by using the co-sputtering-evaporation technique and different compositions of FeGaSiB films were fabricated.
- From the XRD results, all the films had amorphous structure and the morphology of both the FeSiB and FeGaSiB films were independent of the growth parameters, film thickness, and the addition of Ga.
- The investigation of thickness (range: 24 nm – 100 nm) with adding Ga showed that the magnetic anisotropy of the films is influenced by the thickness. Adding the Ga affected the films magnetically. It was observed that the anisotropy fields for the FeSiB films decreased with increasing thickness, while the FeGaSiB films were isotropic and their saturation fields increased with the increasing thickness. Thus adding Ga atoms, which are nonmagnetic into FeSiB films reduced the saturation induction from 1.56 T for the ribbon to 0.96 T. For the FeSiB films, the saturation magnetostriction constant, λ_S decreased with the increasing thickness, while for the FeGaSiB films with $t > 50$nm, λ_S~13 ppm and was higher than the FeSiB films.
- For the range of Ar gas pressure investigated (4 μbar - 8 μbar), the Ga composition was influenced by Ar gas pressure. For the FeSiB films, H_k increased gradually as the pressure increased, suggesting that the intrinsic stresses within the films increased with the pressure, as the stress within the film affects the magnitude and direction of the magnetic anisotropy. For the FeGaSiB films $H_s \approx 4000$ A/m for all pressures. This means the addition of Ga into FeSiB reduced the stress in the films, so giving stability to the saturation field over the pressure range.

  The coercive fields of both FeSiB and FeGaSiB thin films were less than 800 A/m, showing that neither pressure nor Ga changed the coercivity. This is expected as the coercive field strongly depends on intrinsic properties such as the grain size, and as both film sets were amorphous, the films contained no grains.

  The saturation magnetization decreased gradually with increasing the pressure, hence it was not dominated by the Ga percentage, as the Ga percentage fluctuated with increasing the pressure. It was observed that the magnetostriction constant, λ_s, of the FeSiB thin films increased with increasing the Ar pressure, while for the FeGaSiB films, the magnetostriction constant, λ_s, decreased with an increase of sputtering gas

pressure.

- For the selected sputtering target powers (20 W – 60 W), the Ga composition was varied with the sputtering target power and was not affected by increasing the sputtering rate. For the FeSiB films, H_k increased sharply from 2000 to 14000 A/m with increasing the sputtering target power (P_{FeSiB}). For the FeGaSiB films H_s increased gradually from 4000 to 5000 A/m with increasing the sputtering target power (P_{FeSiB}) and was about 2.8 lower than the anisotropy field of FeSiB films for powers ≥ 40 W. This suggests that the addition of Ga into FeSiB reduced the induced stress in the films, so giving stability to the saturation field over the power range.
  In general, the results showed that the coercivity, H_c, of the FeSiB films was higher than the coercivity H_c of the FeGaSiB films for all powers except 40 W. The maximum coercivity, H_c, of the FeSiB films was 1000 A/m at a power of 50 W while the maximum coercivity, H_c, of the FeGaSiB films was 750 A/m at a power of 50 W.
  The saturation magnetisation of the FeGaSiB films increased slightly with increasing the power up to 30 W, then decreased with increasing the power> 30 W. The saturation magnetization increased again for a power of 60 W. Also, it was found that the minimum value of the saturation magnetization was at the power of 50 W, which had the highest Ga percentage of 8% and the maximum saturation magnetization was at the power of 30 W, which had the lowest Ga percentage of 4%.
  The magnetostriction constant of the FeSiB thin films decreased from 10 ppm to 3 ppm with increasing the power ≤ 30 W and then increased for the power > 30 W to reach the maximum 21 ppm value at the power of 60 W. For the FeGaSiB films, the magnetostriction constant decreased from 17.4 ppm for $Fe_{82}Ga_7Si_5B_6$ to 5.2 ppm for $Fe_{85}Ga_5Si_3B_7$, with increasing power, P_{FeSiB}.
- For the selected Ga evaporation rates (0.2-0.6 a.u.), the results showed that increasing the Ga evaporation rate led to an increase in the Ga concentration. This allowed for control of the Ga percentage within the films. For all the films, with increasing the Ga evaporation rate (Ga% from 7% to 14%), $H_k \approx 6000$ A/m, along the hard axis loops. This shows that even with the increase of Ga within the films, the anisotropy field was maintained. The coercive fields were in the range from 300 to 500 A/m. The magnetization of the FeGaSiB films reduced with increasing the Ga evaporation rate. The magnetostriction constants of FeGaSiB thin films decreased with increasing the Ga evaporation rate until R_{Ga} = 0.5 (Ga% =12), then increased for R_{Ga} = 0.6 (Ga%

=14). The films had the highest magnetostriction constants, λ_s, at the lowest Ga evaporation rate with the maximum λ_s = 17.2 ± 0.3 ppm, at R_{Ga} = 0.2 (Ga% =7).

- Thus the addition of Ga into FeSiB films affected the magnetic properties, magnetization, and saturation magnetostriction constant
- The second part was to investigate the mechanical properties of the magnetostrictive thick films, FeSiB, and FeGaSiB, by nanoindentation technique. The films had a range of thicknesses, FeGaSiB films (283, 450, 640 nm) and FeSiB films (290, 425, 668 nm).

  The XRD results showed a broad peak at 2θ ~ 43° for both films. The peak size increased with thickness. From the XRD pattern, there was no sign of crystalline peaks observed, thus confirming the amorphous structure.

  The difference in the experimental load-displacement curves means different mechanical properties for the FeSiB and FeGaSiB films. The hardness and elastic modulus decreased with increasing thickness of FeSiB and FeGaSiB films. The films' hardness with lower thicknesses increased towards the substrate hardness thus showing the substrate effect. Different elastic moduli were measured for the films grown on different substrates, while the hardness values of the films on different substrates were the same. The maximum thicknesses of the FeSiB and FeGaSiB films were suitable to measure the hardness without any effect from the substrate using the Berkovich indenter with a radius of 100 nm. For both film sets, the yield strength decreased with increasing the film thickness. Similarly, for both film sets, the elastic recovered part decreased with increasing the film thickness. Thus, for amorphous films, the mechanical properties where found to be affected by the thickness and the addition of Ga. Where it is found that adding the Ga into FeSiB films reduced their mechanical properties, suggesting that the presence of Ga has changed the distribution of atoms inside the film.

8.2 Future Work

To continue this study of amorphous magnetostrictive films, the following experiments and studies would be carried out.

1- After measuring the mechanical properties of these films such as Young's modulus of FeGaSiB films, it will be possible to recalculate the magnetostriction constants of these films without the use of the mechanical properties of the substrate which used in this thesis.

2- Use TEM and EDS to investigate the structure and composition of the films, to confirm the results presented in chapters 5 and 6.

3- Study the effect of annealing temperature and annealing field on the structural, magnetic, magnetostrictive properties of the films. As annealing can change the structure of films and influence the magnetic properties and magnetostriction constant, this will relax the stress within the films, which could work to improve the properties of the films. Further, applying an annealing field during the annealing process could produce uniaxial anisotropy property within the films.

4- Study the effect of heat treatment on the structural and mechanical properties of thicker FeGaSiB films, as the heat treatment can produce crystalline phases within an amorphous matrix and lead to growing grains thereby affecting the mechanical properties.

5- Study the effect of using flexible plastic substrates on the magnetic properties and the magnetostriction constant of the films. Where the deposition of films on a flexible plastic substrate can allow for bending the magnetic films and induce a mechanical strain within the films.

6- Use the Mössbauer (CEMS) to study the films. The main aim of the project would be to achieve a more detailed investigation of the amorphous structure. This includes studying the distribution of the magnetic hyperfine field in the amorphous films as a function of Ga composition to be compared with those of ribbons achieved by rapid quenching. Also, the magnetic anisotropy could be determined by Mössbauer spectrometry.

7- Use X-ray absorption fine structure (EXAFS), to investigate the local environment of the Fe and Ga atoms. This technique has sensitivity to the first neighbour atom and can provide data about the chemical property of the nearest neighbours such as the number of atoms, the distance from them to the absorbing atom, and their static disorder related to the absorber atom.

Appendix 1

XPS Fitting

The XPS spectra were fitted in the CasaXPS software. The spectra taken include a full survey spectrum of the whole binding energy range, which contains all the peaks of the different elements (Fig. 1). Once this has been done a set of different element peaks are taken at the different energies (Fig. 2).

To fit the XPS peaks, the CasaXPS software is used. An energy region is defined within the spectrum. The programme then automatically applies a background to the data (red line in Fig. 3). Using the quantification parameters component part, peaks are then created and fitted onto the data. For each peak, the relative sensitivity factors (r.s.f), which are a scaling factor to the peak area to determine the actual amount of material at the surface are added. If double peaks occur, then two peaks are fitted to the data. The programme then gives the percentage concentration of each peak fitted. Using these percentages, the total percentage of each element at the surface is determined.

Figure 4 shows the fitting of the survey data for all the elements for the Ga rate films. Figure 5 shows the fitting of the Ga, Si and B elements for the 140-210 eV binding energy. This gave another set of percentages for the ratio of the elements in the films.

Qayes A. Abbas, 2018 & Email: qayes.a.abbas@gmail.com

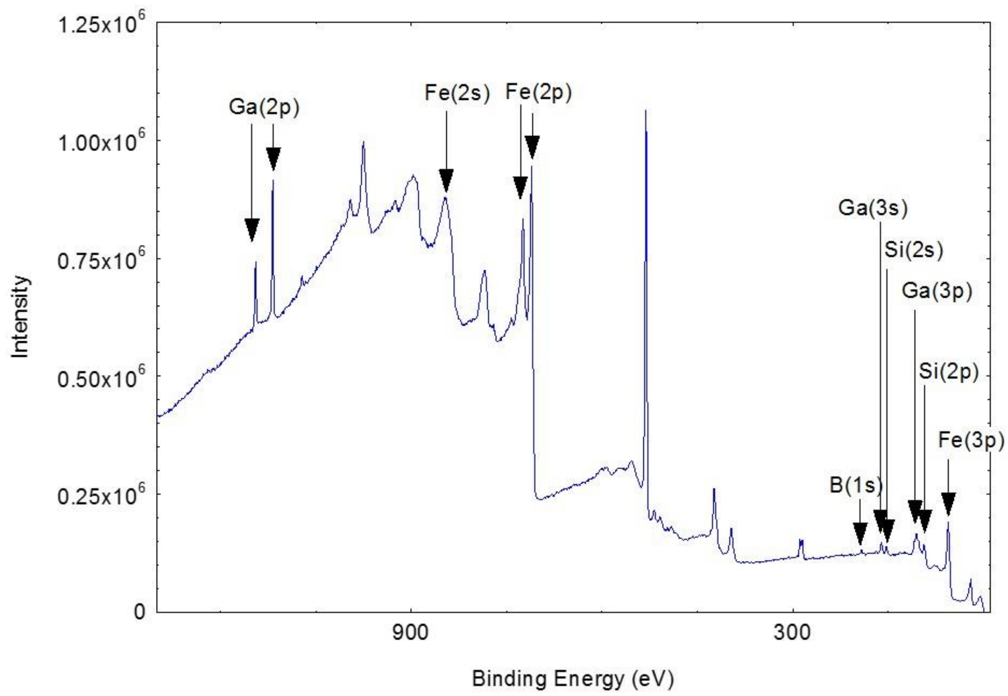

Figure 1 XPS binding energy survey for a FeGaSiB film. Labelled are the main element peaks.

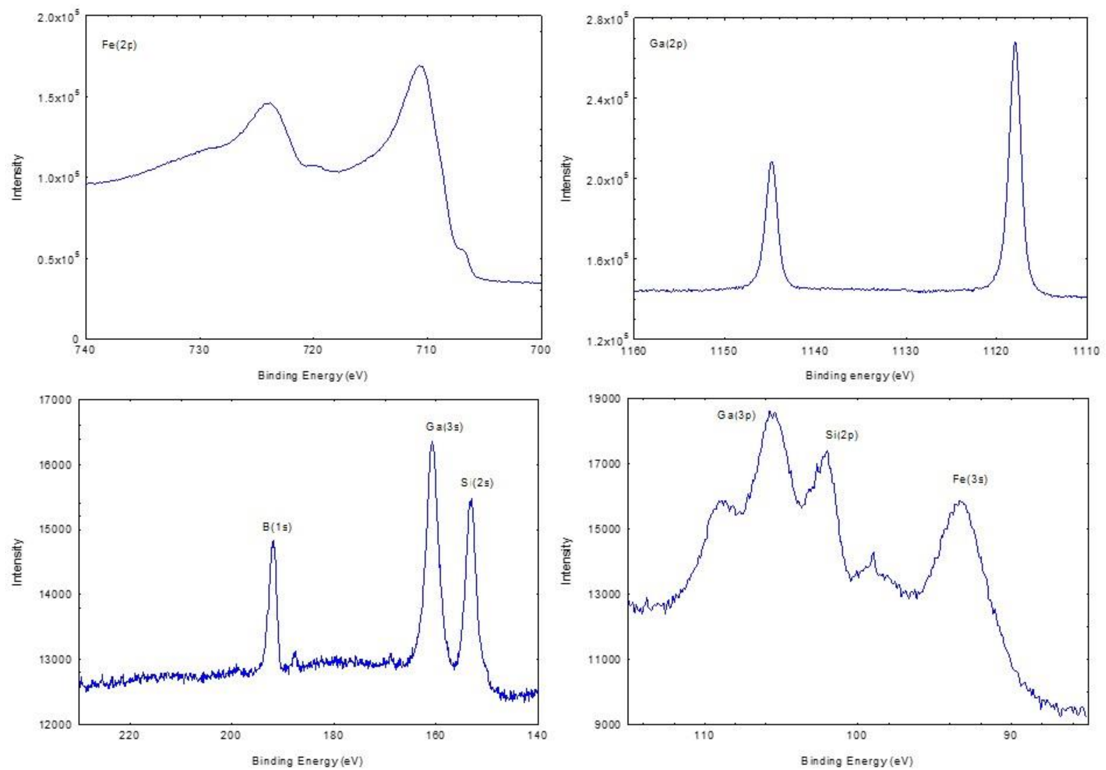

Figure 2 Selected elements XPS spectra for a FeGaSiB film.

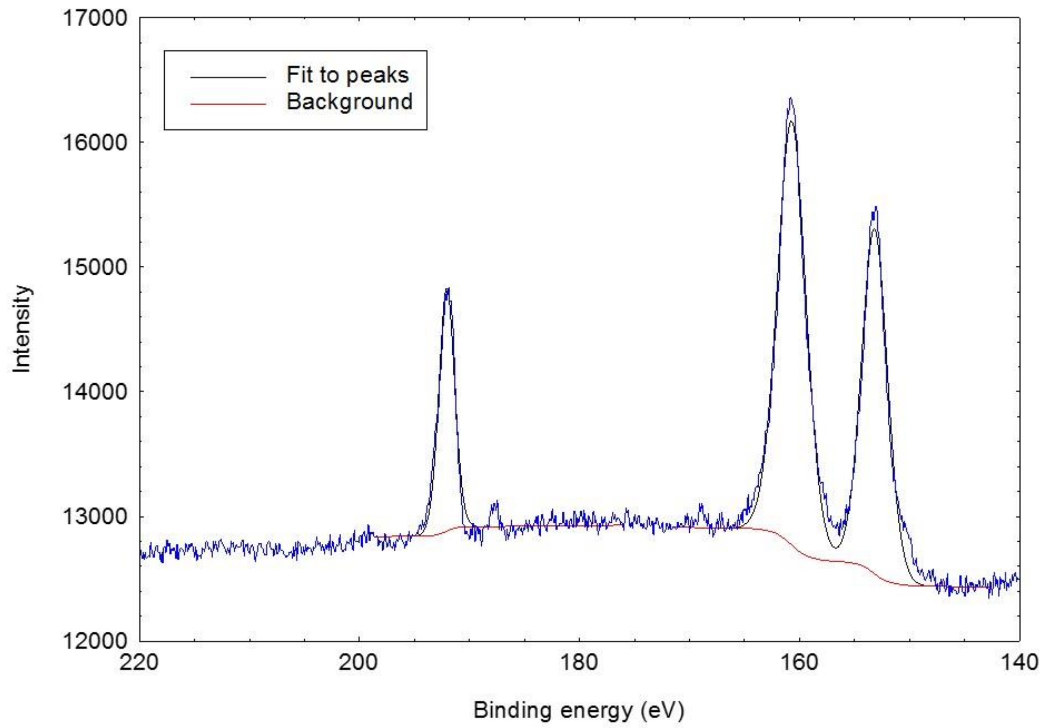

Figure 3 An example of fitting peaks to the XPS spectrum of a FeGaSiB film.

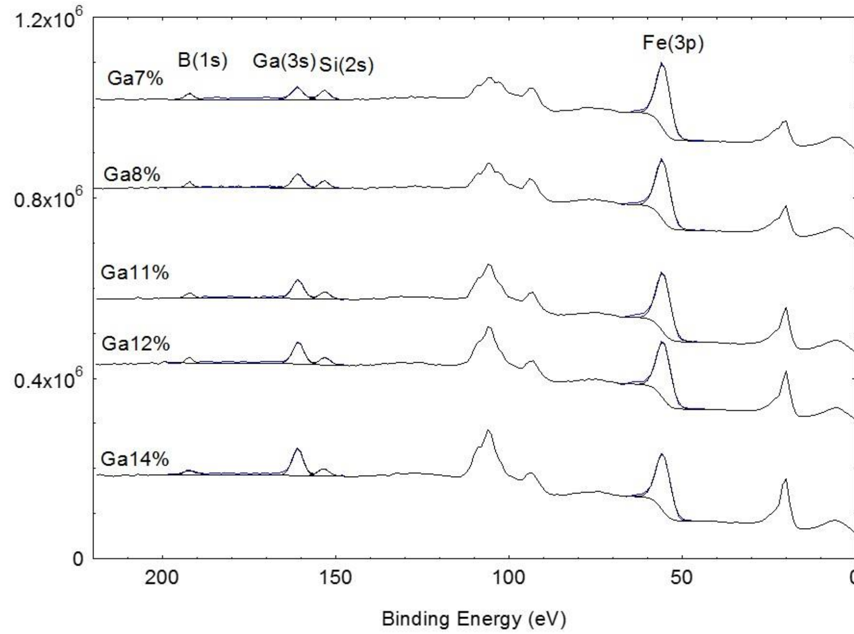

Figure 4 XPS survey spectra for the FeGaSiB films as a function of Ga rate.

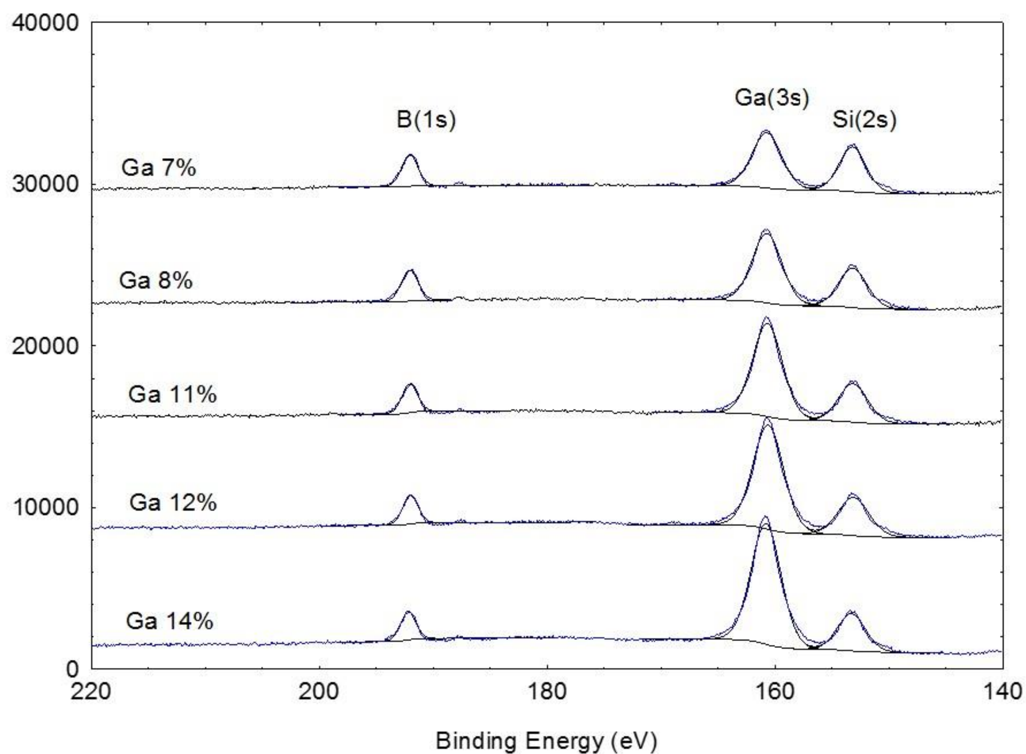

Figure 5 XPS spectra for the FeGaSiB films as a function of Ga rate focusing on the 140-220eV region.